



UNIVERSITAT DE
BARCELONA

Design and Engineering of Advanced Cathode Hosts for Lithium-Sulfur Batteries

Chaoqi Zhang



Aquesta tesi doctoral està subjecta a la llicència **Reconeixement- NoComercial – SenseObraDerivada 4.0. Espanya de Creative Commons.**

Esta tesis doctoral está sujeta a la licencia **Reconocimiento - NoComercial – SinObraDerivada 4.0. España de Creative Commons.**

This doctoral thesis is licensed under the **Creative Commons Attribution-NonCommercial-NoDerivs 4.0. Spain License.**

Tesi doctoral

**Design and Engineering of Advanced Cathode Hosts
for Lithium-Sulfur Batteries**

Autor:

Chaoqi Zhang

Director:

Andreu Cabot

Joan Ramon Morante



UNIVERSITAT_{DE}
BARCELONA

Design and Engineering of Advanced Cathode Hosts for Lithium-Sulfur Batteries

Memòria presentada per optar al grau de doctor per la
Universitat de Barcelona

Programa de doctorat en Nanociència

Autor:

Chaoqi Zhang

Director:

Andreu Cabot

Joan Ramon Morante

Tutor:

Joan Ramon Morante

Lloc on s'ha dut a terme la tesi

Institut de Recerca en Energia de Catalunya (IREC)



UNIVERSITAT DE
BARCELONA

Contents

Acknowledgments	1
List of publications	3
Authors' contributions	4
Preface	6
Summary of results	7
Resumen de Resultados	9
Abbreviation	11
Chapter 1	14
1.1 Introduction of LSB.....	14
1.2 Challenges.....	16
1.3 Host development process of LSBs.....	17
1.4 Host materials.....	18
1.4.1 Non-metallic materials.....	18
1.4.2 Metal.....	20
1.4.3 Transition metal oxides.....	21
1.4.4 Transition metal sulfides and selenides.....	22
1.4.5 Transition metal nitrides.....	23
1.4.6 Transition metal phosphides.....	24
1.4.7 Metallic carbides and borides.....	25
1.4.8 Single-atom catalysts.....	26
1.4.9 Metal-organic frameworks and covalent organic frameworks.....	27
1.5 Architecture optimization.....	28
1.5.1 Porous structure.....	29
1.5.2 Hollow structure.....	29
1.5.3 Self-standing architecture.....	30
1.6 Heterostructure engineering.....	31
1.6.1 Various-phase heterostructure.....	31
1.6.2 2D superlattice heterostructure.....	32
1.7 Objectives.....	33
1.8 References.....	34
Chapter 2	39
2.1 Abstract.....	39

2.2 Introduction.....	40
2.3 Experimental Section.....	42
2.4 Results and Discussion.....	46
2.5. Conclusions.....	70
2.6 References.....	70
Chapter 3.....	75
3.1 Abstract.....	75
3.2 Introduction.....	76
3.3 Experimental Section.....	78
3.4 Results and Discussion.....	83
3.5 Conclusions.....	114
3.6 References.....	115
Chapter 4.....	124
4.1 Abstract.....	124
4.2 Introduction.....	125
4.3 Experimental Section.....	127
4.4 Results and discussion.....	131
4.5 Conclusion.....	162
4.6 References.....	162
Result and Discussions.....	167
Conclusions.....	169
Future work.....	170
CURRICULUM VITAE.....	171
Annex.....	175

Acknowledgments

I made it!

终于! Finally! Por fin! Finalment! Long have I waited for this day!

Of course, I couldn't have done it without your help.

Five years ago, when I boarded the plane to Barcelona, I never thought my Ph.D. would be so amazing, so memorable, and so unusual. However, when this journey walked to the end, I sincerely thank all of you for your kind help and impressive edification in the last five years.

First of all, I would like to thank my director, Professor Andreu Cabot, with unparalleled gratitude. I am very lucky to have such a great director in my academic road, who uses his profound knowledge to guide me to appreciate the wonderful world of nanoscience and let me develop freely the fantastic energy materials. There is no doubt that he is a great model for my future academic life. In addition, I was fascinated by his cheerful personality and elegant academic style. He is not only my director, but also my good friend, and my best basketball friend during my years in Barcelona. Thank you!

Secondly, I would like to express my gratitude to Dr. Jordi Jacas, who open a door to my wonderful battery journey. With his cheerful smile and heart-warming communication, I overcame my initial shyness and nervousness. Through the hand-holding battery teaching, I mastered the initial battery technology and became better and better. He is so supportive of me, beyond battery research and even to my academic career. Thank you very much, Jordi.

In particular, I am very grateful to my master's supervisor, Prof. Hongbing Zhan, who is also my co-supervisor during the 2020-2021 academic year when I back to China due to the COVID-19. She is the one who initially helped me construct my academic thinking and strongly advised me to move forward bravely on the academic road. She was like a beacon for me when I was confused before I started my Ph.D. career, and also a refuge for me when COVID-19 affected my doctoral career. I will always remember her guidance and help to me.

Besides, I would like to thank my tutor, Prof. Joan Roman Morante, whose careful correction and in-depth discussion to my paper have benefited me a lot. My sincere thanks also goes to our friendly Functional Nanomaterials group and Energy Storage and Harvesting members in IREC: Doris, Taisiia, Pablo, Ievgenii, Alberto, Marcos, Sergi, Swapneel, Parizi, Ferando, Jesus, Paulina, Hamid, Felix, Elías, Prakasha, Nina, Mona, Marti, Miguel, Andreina,

Tandava, Viktoriia, Hemesh and especially the Chinese community including Zhishan, Yu Liu, Junfeng, Xiaoting, Peter, Junshan, Yong, Mengyao, Ruifeng, Congcong, Zhifu, Xiang, Dawei, Ke, Bingfei, Xuan Lu, Linlin, Gavin, Lili, Guifang, Chaoyue, Canhuang, all of you contributed to my happy and fulfilling these years in IREC, and wish you all the best in the future. I also need to thank the staff of IREC. Without your warm help and patient guidance, I could not have successfully completed many complicated experiments and instruments. Thank you for your hard work and kind help.

Also, I want to give my appreciation to Ting Zhang and Xu Han of Prof. Jordi Arbiol group in ICN2 for their professional work in HRTEM characterization, and also say thanks to Prof. Jordi Llorca group in UPC for their perfect XPS measurements and analysis. I am also grateful to Prof. Yingtang Zhou from Zhejiang Ocean University and Dr. Jiaao Wang from the University of Texas at Austin for their help in theoretical calculation. With your kind contributions, I can perfect my research to compete in high-impact journals.

I am also very grateful to the kind friends I met in Barcelona who cared for me and helped me, Hao Yu, Jiamei, Yafeng, Chengcheng, Yufen Chen, KiKi, Jing Li, Yang Song, Jing Liu, Bangxiao, Heyi, all of you made my life in a foreign country feel the warmth of friends. I will never forget the wonderful time we spent together, especially when we ate hot pot together. The financial support for my Ph.D. research work is from China Scholarship Council (No. 201706650011). Many thanks for giving me this precious opportunity!

Finally, I can't express my gratitude to my family in words. Without support from my family, I can't pursue my academic dream in here over 10,000 kilometers away from my hometown. They are always the refuge of my soul. I had dreamed of inviting them to the romantic city of Barcelona to complete this memorable event in my Ph.D. defense many times before, but now I can only hope to return to the beautiful Barcelona with them after the epidemic. I promise!

¡Muchas gracias a todos!

Barcelona, Spain

March 2022

Chao/张超琦

List of publications

My Ph.D. research work has been disseminated in three manuscripts, which have already been published in peer-reviewed journals. A full copy of each of the publications can be found in the Annex part. The following is the list of publications included in this thesis:

1. **Chaoqi Zhang**, Jordi Jacas Biendicho*, Ting Zhang, Ruifeng Du, Junshan Li, Xuhui Yang, Jordi Arbiol, Yingtang Zhou*, Joan Ramon Morante, Andreu Cabot*. *Combined High Catalytic Activity and Efficient Polar Tubular Nanostructure in Urchin-Like Metallic NiCo₂Se₄ for High-Performance Lithium-Sulfur Batteries*. *Advanced Functional Materials*, 2019, 29, 34, 1903842.

2. Ban Fei†, **Chaoqi Zhang**†, Daoping Cai*, Jingying Zheng, Qidi Chen, Yulan Xie, Longzhen Zhu, Andreu Cabot*, Hongbing Zhan*. *Hierarchical Nanoreactor with Multiple Adsorption and Catalytic Sites for Robust Lithium-Sulfur Batteries*. *ACS Nano*, 2021, 15, 4, 6849-6860.

3. **Chaoqi Zhang**, Ban Fei, Dawei Yang, Hongbing Zhan*, Jiaao Wang*, Jiefeng Diao, Junshan Li, Graeme Henkelman, Daoping Cai, Jordi Jacas Biendicho, Joan Ramon Morante, Andreu Cabot*. *Robust Lithium-Sulfur Batteries Enabled by Highly Conductive WSe₂-based Superlattices with Tunable Interlayer Space*. *Advanced Functional Materials*, 2022. DOI: 10.1002/adfm.202201322.

Authors' contributions

The work within this thesis was carried out at the Functional Nanomaterials group and Energy Storage, Harvesting and Catalysis Group in the Catalonia Institute for Energy Research (IREC). Chaoqi Zhang, as a doctoral candidate at the University of Barcelona, contributed to the experimental work, data analysis, and manuscript writing for all the publications presented in this thesis. The contributions of co-authors for each article are shown below. The impact factor in 2021 of the journals where the manuscripts were published is provided. All of the publications belong to the 1st quartile according to the Science Citation Index. None of these papers has been previously presented in any other Ph.D. thesis. In all the publications, Andreu Cabot conceived and guided the projects, participated in the experiment design and manuscript writing.

Chapter 2:

Chaoqi Zhang, Jordi Jacas Biendicho*, Ting Zhang, Ruifeng Du, Junshan Li, Xuhui Yang, Jordi Arbiol, Yingtang Zhou*, Joan Ramon Morante, Andreu Cabot*. *Combined High Catalytic Activity and Efficient Polar Tubular Nanostructure in Urchin-Like Metallic NiCo₂Se₄ for High-Performance Lithium-Sulfur Batteries. **Advanced Functional Materials**, 2019, 29, 34, 1903842.*

Impact factor 2021: **18.808**

In this work, C. Zhang designed the experiments, produced and characterized the nanomaterials, conducted the electrochemical test, and wrote the first draft of the manuscript. R. Du, J. Li participated in materials synthesis and structural characterization. J.J. Biendicho participated in experimental design and guided the electrochemical test. T. Zhang and J. Arbiol participated in HRTEM characterization, J. R. Morante contributed to logical framework modification. X. Yang and Y. Zhou participated in theoretical calculation. A. Cabot conceived and guided the project and supervised the work. The manuscript was corrected and improved by all authors.

Chapter 3:

Ban Fei†, **Chaoqi Zhang**†, Daoping Cai*, Jingying Zheng, Qidi Chen, Yulan Xie, Longzhen Zhu, Andreu Cabot*, Hongbing Zhan*. *Hierarchical Nanoreactor with Multiple*

Adsorption and Catalytic Sites for Robust Lithium-Sulfur Batteries. ACS Nano, 2021, 15, 4, 6849-6860.

Impact factor 2021: **15.881**

In this work, B. Fei and C. Zhang designed the experiments, produced and characterized the nanomaterials, conducted the electrochemical test, and wrote the first draft of the manuscript. D. Cai participated in experimental design and guided the electrochemical test. Y. Xie and L. Zhou participated in materials synthesis and structural characterization. J. Zhen participated in Raman spectrum characterization. A. Cabot and H. Zhan conceived and guided the project and supervised the work. The manuscript was corrected and improved by all authors.

Chapter 4:

Chaoqi Zhang, Ban Fei, Dawei Yang, Hongbing Zhan*, Jiaao Wang*, Jiefeng Diao, Junshan Li, Graeme Henkelman, Daoping Cai, Jordi Jacas Biendicho, Joan Ramon Morante, Andreu Cabot*. *Robust Lithium-Sulfur Batteries Enabled by Highly Conductive WSe₂-based Superlattices with Tunable Interlayer Space. Advanced Functional Materials*, 2022. DOI: 10.1002/adfm.202201322

Impact factor 2021: **18.808**

In this work, C. Zhang designed the experiments, produced and characterized the nanomaterials, conducted the electrochemical test, and wrote the first draft of the manuscript. B. Fei and D. Yang participated in materials synthesis and structural characterization. J.J. Biendicho participated in the electrochemical test and J. R. Morante contributed to logical framework modification. J. Wang, J. Diao, and G. Henkelman participated in theoretical calculation. H. Zhan and A. Cabot conceived and guided the project and supervised the work. The manuscript was corrected and improved by all authors.

Preface

The chapters in this Ph.D. thesis cover the work developed by the doctoral candidate Chaoqi Zhang at the Catalonia Institute for Energy Research (IREC) in Sant Adrià de Besòs, Barcelona, in the academic years 2017-2022, supported by China Scholarship Council (No. 201706650011). The thesis is particularly focused on advanced cathode host materials for lithium-sulfur batteries (LSBs).

This thesis contains 5 chapters, including an introductory chapter and 3 chapters of experimental work. In the introduction chapter, I briefly introduce the state of the art and working principle of LSBs. In view of the great challenges in achieving high-performance LSBs, I summarize the main research progress in designing and engineering advanced cathode hosts from the perspectives of materials, architecture, and interphases. I also discuss the key cathode parameters required in future commercial LSBs. Within the experimental chapters, the details of the design, synthesis, and characterization of three kinds of nanomaterials and their performance as cathode hosts for LSB are provided. In Chapter 1, I discuss the case of urchin-shaped NiCo_2Se_4 (u-NCSe) which was designed from the perspective of materials, to demonstrate the great advantage of selenides as S host. In Chapter 3, I provide the details from my work with Ag/VN@Co/NCNT nanoreactors as an advanced multi-component architecture to overcome the challenge of LSBs. In Chapter 4, NG/WSe₂ superlattice heterojunctions are designed and synthesized, that superlattices demonstrated that high performance LSBs can also be achieved by designing advanced Li-S reaction catalysts with heterogeneous interfaces. After these experimental chapters, I include a discussion of the results, the thesis conclusions, and the future work. Finally, I provide my CV and publications.

Summary of results

Lithium-sulfur batteries (LSBs) are regarded as the most promising candidate to replace lithium-ion batteries (LIBs) in next-generation energy storage systems. Compared with LIBs, LSBs are characterized by a sixfold higher theoretical energy density, 2500 Wh kg⁻¹, and a potentially lower cost and environmental impact for commercialization. Despite these attractive advantages, the electrically insulating character of sulfur/Li₂S and the shuttle effect of intermediate lithium polysulfides (LiPS) greatly limit the practical application of LSBs. Additionally, the serious volume changes (~80%) and slow redox kinetics during the charging/discharging process also reduce the cycling life and power density.

The rational design and engineering of the cathode host can effectively overcome the above challenges. In Chapter 1, I summarize the state of the art on advanced hosts for LSBs and detail the targeted requirements from three points of view: material, architecture, and heterogeneous interface. In Chapter 2, I detail my work on the design and engineering of urchin-shaped NiCo₂Se₄ (u-NCSe) nanostructures as efficient sulfur hosts to overcome the limitations of LSBs. u-NCSe provide a beneficial hollow structure to relieve volumetric expansion, a superior electrical conductivity to improve electron transfer, a high polarity to promote adsorption of LiPS, and outstanding electrocatalytic activity to accelerate LiPS conversion kinetics. Owing to these excellent qualities as LSB cathode, I demonstrated S@u-NCSe to deliver outstanding initial capacities up to 1403 mA h g⁻¹ at 0.1 C and retains 626 mAh g⁻¹ at 5 C with exceptional rate performance. More significantly, a very low capacity decay rate of only 0.016% per cycle was obtained after 2000 cycles at 3 C. Even at high sulfur loading (3.2 mg cm⁻²), a reversible capacity of 557 mA h g⁻¹ was measured after 600 cycles at 1 C. DFT calculations further confirmed the strong interaction between NCSe and LiPS, and cytotoxicity measurements prove the biocompatibility of u-NCSe. This work not only demonstrated that transition metal selenides can be promising candidates as sulfur host material, but also provided a strategy for the rational design and development of LSBs with long-life and high-rate electrochemical performance. This work was published in *Advanced Functional Materials* in 2019.

In Chapter 3, I explain my work on the design and production of multifunctional Ag/VN@Co/NCNTs nanocomposite with multiple adsorption and catalytic sites within hierarchical nanoreactors as a robust sulfur host for LSB cathodes. In this hierarchical nanoreactor, heterostructured Ag/VN nanorods serve as a highly conductive backbone

structure and provide internal adsorption and catalytic sites for LiPS conversion. Interconnected nitrogen-doped carbon nanotubes (NCNTs), *in situ* grown from the Ag/VN surface, greatly improve the overall specific surface area for sulfur dispersion and accommodate volume change in the reaction process. Owing to their high LiPS adsorption ability, outer Co nanoparticles at the top of the NCNTs catch escaped LiPS, thus effectively suppressing the shuttle effect and enhancing kinetics. Benefiting from the multiple adsorption and catalytic sites of the developed hierarchical nanoreactors, Ag/VN@Co/NCNTs@S cathodes display outstanding electrochemical performances, including a superior rate performance of 609.7 mAh g⁻¹ at 4 C and good stability with a capacity decay of 0.018% per cycle after 2000 cycles at 2 C. These properties demonstrate that there is great potential for improving electrochemical performance through proper design of the host architecture. This work was published in *ACS Nano* in 2021.

In Chapter 4, in view of the complexity and difficulty in the synthesis of superlattice materials, I detail a simple solution-based method to efficiently produce organic-inorganic PVP-WSe₂ superlattices and demonstrate that the pyrolysis of the PVP compound enables to continuously adjust their interlayer space in the range from 10.4 Å to 21 Å, resulting in N-doped graphene/WSe₂ (NG/WSe₂) superlattices with superior electrical conductivities. Both experimental results and theoretical calculations further demonstrate that NG/WSe₂ superlattices are excellent sulfur hosts for LSB, being able to effectively reduce the LiPS shuttle effect by dual-adsorption sites and accelerating the sluggish Li-S reaction kinetics. Consequently, S@NG/WSe₂ electrodes delivered high sulfur usages, superior rate performance, and outstanding cycling stability, even at high sulfur loadings, in lean electrolyte conditions, and at pouch cell level. Overall, this work not only establishes a cost-effective strategy to produce artificial superlattice materials but also pioneers their application in the field of LSBs. This work has been published in *Advanced Functional Materials* in 2022.

Resumen de Resultados

Las baterías de litio-azufre (LSB) se consideran el candidato más prometedor para reemplazar las baterías de iones de litio (LIB) en los sistemas de almacenamiento de energía de próxima generación. En comparación con las LIB, las LSB se caracterizan por una densidad de energía teórica seis veces mayor, 2500 Wh kg^{-1} , y un costo e impacto ambiental potencialmente más bajos para la comercialización. A pesar de estas atractivas ventajas, el carácter eléctricamente aislante del azufre/ Li_2S y la solubilidad de los polisulfuros de litio (LiPS) generados como productos intermedios de la reacción Li-S limitan en gran medida la aplicación práctica de las LSB. Además, los importantes cambios de volumen (80 %) y la lenta cinética redox durante el proceso de carga/descarga también reducen la vida útil y la densidad de potencia de las LSB.

Un diseño racional y una precisa ingeniería del cátodo pueden superar de manera efectiva los desafíos anteriores. En el Capítulo 1, resumo el estado del arte sobre hosts avanzados para LSB y detallo los requisitos específicos desde tres puntos de vista: material, arquitectura e interfaz heterogénea. En el Capítulo 2, detallo mi trabajo sobre el diseño y la ingeniería de nanoestructuras de NiCo_2Se_4 (u-NCSe) con forma de erizo como encapsulantes de azufre eficientes para superar las limitaciones de los LSB. u-NCSe proporciona una estructura hueca beneficiosa para aliviar la expansión volumétrica, una conductividad eléctrica superior para mejorar la transferencia de electrones, una alta polaridad para promover la adsorción de LiPS y una excelente actividad electrocatalítica para acelerar la cinética de conversión de LiPS. Debido a estas excelentes cualidades como cátodo LSB, demostré que S@u-NCSe ofrece capacidades iniciales sobresalientes de hasta 1403 mA h g^{-1} a 0,1 C y retiene 626 mAh g^{-1} a 5 C. Más significativamente, se obtuvo una disminución de capacidad muy baja de solo 0,016 % por ciclo después de 2000 ciclos a 3 C. Incluso con una carga alta de azufre ($3,2 \text{ mg cm}^{-2}$), se midió una capacidad reversible de 557 mA hg^{-1} después de 600 ciclos a 1 C. Los cálculos de DFT confirmaron la fuerte interacción entre NCSe y LiPS, y las mediciones de citotoxicidad demostraron la biocompatibilidad de u-NCSe. Este trabajo no solo demostró que los seleniuros de metales de transición pueden ser candidatos prometedores como material huésped de azufre, sino que también proporcionó una estrategia para el diseño y desarrollo racional de LSB con un rendimiento electroquímico de alta velocidad y larga duración. Este trabajo fue publicado en *Advanced Functional Materials* en 2019.

En el Capítulo 3, explico mi trabajo sobre el diseño y la producción de nanocompuestos multifuncionales de Ag/VN@Co/NCNT con múltiples sitios catalíticos y de adsorción dentro

de nanorreactores jerárquicos usados como huésped de azufre para cátodos LSB. En este nanorreactor jerárquico, las nanovarillas de Ag/VN heteroestructuradas sirven como una estructura de columna altamente conductora y proporcionan adsorción interna y sitios catalíticos para la conversión de LiPS. Los nanotubos de carbono dopados con nitrógeno (NCNT) interconectados, crecidos in situ a partir de la superficie Ag/VN, mejoran en gran medida el área de superficie específica general para la dispersión de azufre y se adaptan al cambio de volumen en el proceso de reacción. Debido a su alta capacidad de adsorción de LiPS, las nanopartículas de Co externas en la parte superior de los NCNT atrapan el LiPS escapado, lo que suprime de manera efectiva el efecto de lanzadera y mejora la cinética. Al beneficiarse de los múltiples sitios catalíticos y de adsorción de los nanorreactores jerárquicos desarrollados, los cátodos Ag/VN@Co/NCNTs@S muestran rendimientos electroquímicos sobresalientes, incluido 609,7 mAh g⁻¹ a 4 C y buena estabilidad con una capacidad de caída de 0,018 % por ciclo después de 2000 ciclos a 2 C. Estas propiedades demuestran que existe un gran potencial para mejorar el rendimiento electroquímico a través del diseño adecuado de la arquitectura del host de S. Este trabajo fue publicado en *ACS Nano* en 2021.

En el Capítulo 4, en vista de la complejidad y dificultad en la síntesis de materiales de superredes, detallo un método simple basado en soluciones para producir eficientemente superredes orgánicas-inorgánicas de PVP-WSe₂ y demuestro que la pirólisis del compuesto de PVP permite ajustar continuamente su espacio entre capas en el rango de 10,4 Å a 21 Å, lo que da como resultado superredes de grafeno/WSe₂ (NG/WSe₂) dopadas con N con conductividades eléctricas superiores. Tanto los resultados experimentales como los cálculos teóricos demuestran aún más que las superredes NG/WSe₂ son excelentes anfitriones de azufre para LSB, ya que pueden reducir eficazmente el efecto de lanzadera de LiPS mediante sitios de adsorción dual y acelerar la lenta cinética de reacción de Li-S. En consecuencia, los electrodos S@NG/WSe₂ permiten usar grandes proporciones de azufre, una velocidad superior de carga y descarga, y una excelente estabilidad, incluso con cargas altas de azufre, en condiciones de electrolito pobre y a nivel de celda de bolsa. En general, este trabajo no solo establece una estrategia rentable para producir materiales de superredes artificiales, sino que también es pionero en su aplicación en el campo de los LSB. Este trabajo ha sido publicado en *Advanced Functional Materials* en 2022.

Abbreviation

2D	Two-dimensional
3D	Three-dimensional
AMT	Ammonium metatungstate
BET	Brunauer–Emmett–Teller
C	Current rate
CNF	Carbon nanofiber
COF	Covalent organic framework
CP	Carbon paper
CTAB	Cetyltrimethylammonium bromide
CV	Cyclic voltammetry
DFT	Density functional theory
D_{Li^+}	Li diffusivity
DME	1,2-dimethoxy ethane
DMF	N, N-dimethylformamide
DOL	1,3-dioxolane
DOS	Density of states
E_b	Binding energy
EDX	Energy-dispersive X-ray
EELS	Electron energy loss spectroscopy
EIS	Electrochemical impedance spectroscopy
FT-IR	Fourier transform infrared
G	Graphene
GGA	Generalized gradient approximation

GLU	Glucose
GPA	Geometric phase analysis
HAADF	High-angle annular dark-field imaging
HRTEM	High-resolution transmission electron microscopy
LED	Light-emitting diode
LIB	Lithium-ion battery
LiPS	Lithium polysulfides
LiTFSI	Lithium bis(trifluoromethanesulfonyl) imide
LSB	Lithium-sulfur battery
MMT	3-(4,5-dimethyl-2-thiazolyl)-2,5-diphenyl-2-H-tetrazolium bromide
MOF	Metal-organic framework
NCNTs	Nitrogen-doped carbon nanotubes
NG	N-doped graphene
NW	Nanowire
PAN	Polyacrylonitrile
PBE	Perdew-Burke-Ernzerhof
PVDF	Polyvinylidene difluoride
PVP	Polyvinyl pyrrolidone
R _{ct}	Charge-transfer resistance
SDS	Sodium dodecyl sulfate
SEM	Scanning electron microscopy
TEM	Transmission electron microscopy
TGA	Thermogravimetric analysis
TMN	Transition metal nitride

TMO	Transition metal oxide
TMP	Transition metal phosphide
TMS	Transition metal sulfide
TMSe	Transition metal selenide
u-NCSe	Urchin-shaped NiCo ₂ Se ₄
UV-vis	Ultraviolet-visible
VASP	Vienna ab initio simulation package
XPS	X-ray photoelectron spectroscopy
XRD	X-ray diffraction
ΔE	Polarization potential
ν	Scan rate
σ	Electrical conductivity

Chapter 1

General Introduction

Advanced Lithium-Sulfur Batteries



1.1 Introduction of LSB

The rapid development of modern society, the emergence of electric vehicles, the integration of renewable energies and especially the rapid expansion of portable electronic devices (such as mobile phones, laptop computers, tablets, etc.) have completely changed people's lifestyles. These developments have stimulated people's demand for high energy density storage devices with long cycle life. Li-ion battery (LIB) technology occupies a dominant position in the current advanced commercial energy storage devices, but the present development of LIB has to face a series of difficulties related to its gradual approach to the theoretical energy density limitation and the high production cost.^[1] In this scenario, researchers have had to explore new electrochemical energy storage technologies and develop more efficient storage devices to meet the increasing demand for energy storage in the future.

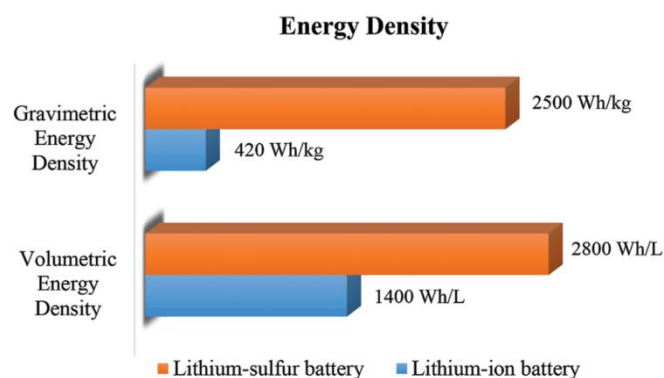


Figure 1. Energy density plots of lithium-sulfur vs. lithium-ion batteries (based on graphite anodes and $\text{LiNi}_{1/3}\text{Mn}_{1/3}\text{Co}_{1/3}\text{O}_2$ cathodes)^[4]

In the past decade, lithium-sulfur batteries (LSBs) have been identified by scientists as one of the most viable next-generation energy storage technologies.^[1-3] Compared with the current commercial LIBs, LSBs have a much higher theoretical specific capacity of 1675 mAh g⁻¹ and an overwhelming gravimetric energy density of 2500 Wh kg⁻¹,^[4] which is five times that of current LIBs (as shown in Figure 1). Moreover, LSBs have additional competitive advantages over LIBs related to the abundance of sulfur reserves, its low cost and environmental friendliness.^[5,6]

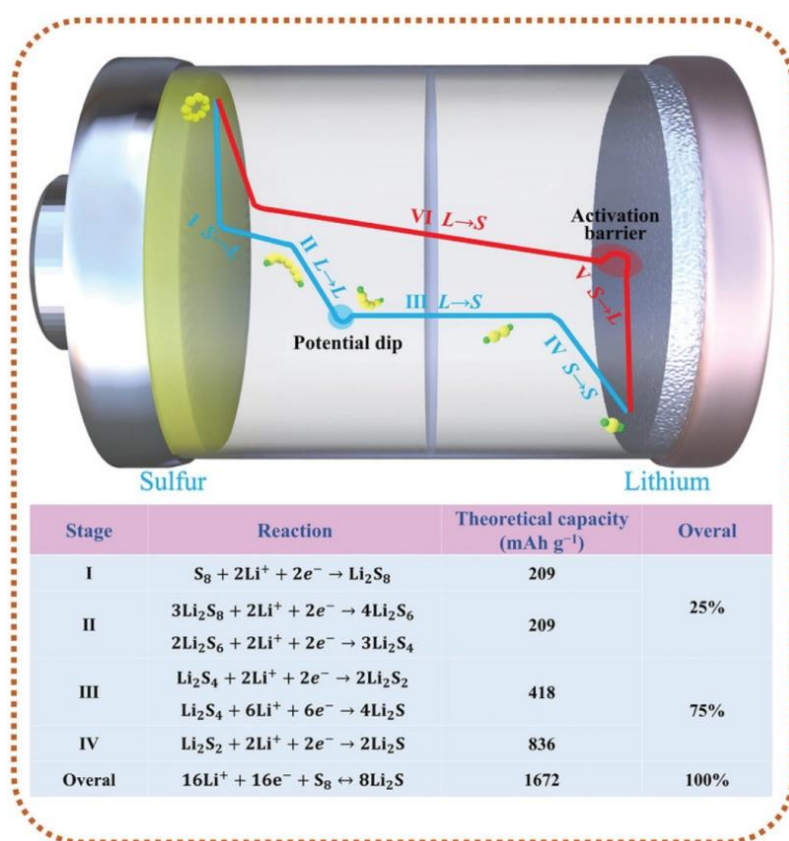


Figure 2 Schematic illustration and operating principles of LSBs.^[6]

The Li-S reaction can be split into a complex multi-step set of transformation reactions involving a variety of intermediate sulfur-containing species (Li_2S_n , $n \leq 8$), as shown in Figure 2. More specifically, during the lithiation process, elemental sulfur (S_8) produces a variety of soluble long-chained intermediates lithium polysulfide ($LiPS$, $S_8 \rightarrow Li_2S_8 \rightarrow Li_2S_6 \rightarrow Li_2S_4$).^[7,8] This process accounts for a quarter of the total amount of electron transfer in the reduction process, contributing up to 419 mAh g⁻¹ to the total capacity. The subsequent conversion to

insoluble products ($\text{Li}_2\text{S}_4 \rightarrow \text{Li}_2\text{S}_2 \rightarrow \text{Li}_2\text{S}$), accounts for a high 1252 mAh g^{-1} capacity. On the contrary, the delithiation process starts with Li_2S oxidization process until forms S_8 through multiple LiPS conversions.

It is worth noting that the electrochemical Li-S reaction principle mentioned above is a "solid-liquid-solid" reaction process based on ether-based electrolyte system, which is the main system attracting the most researchers' attention at present. In addition, there are some reports based on the "solid-solid" reaction process in the carbonate-based electrolyte, but the attraction is limited.^[9,10] Therefore, the following related discussions are based on the "solid-liquid-solid" reaction process with the ether-based electrolyte.

1.2 Challenges

Although Li-S reaction systems have numerous attractive advantages, their commercialization is severely hampered by various challenges, including:

1. The electrical conductivity of S and Li_2S at room temperature is only 5×10^{-30} and $3.6 \times 10^{-7} \text{ S cm}^{-1}$, respectively,^[11,12] and Li^+ transport in S and Li_2S is also very slow, which greatly limit electron and ion transport, making the reversible transformation of S and Li_2S difficult, and further leads to a low utilization rate of the active materials.
2. The volume expansion during lithiation process is up to 80% due to the significant density difference between Li_2S and S ($1.66 \text{ vs. } 2.07 \text{ g cm}^{-3}$).^[2,12] This large volume change, frequently aggravated by the structural collapse of the active material, is considered to be the main reason for the cathode powdering due to internal strain, and the subsequent loss of connectivity between the electrode and the current collector, thus greatly affecting the cyclic stability of the electrode.
3. The notorious "shuttle effect" caused by soluble LiPS leads to continuous loss of active material and electrochemical capacity, as well as diffusion to the anode causing serious corrosion behavior and low Coulomb efficiency.^[13,14]

4. The lithium dendrite caused by uneven lithium deposition/stripping has the potential to penetrate the membrane and create internal short circuits, potentially leading to safety accidents.^[15,16]

1.3 Host development process of LSBs

Due to the insulating ion/electronic character of sulfur, scientists are spending huge efforts to develop composite cathode materials that make LSBs feasible. A rational cathode design can not only solve the problem of electrical/ion conduction, but also provide a guarantee to the reversibility of LSBs in cycling.^[13] Figure 3 introduces the main milestones in the development of cathode hosts of LSBs. As early as 1960, Herbert and Ulam proposed the prototype of the Li-S battery in a patent.^[2] However, limited to the technology at that time, the poor reversibility of the battery greatly affected people's enthusiasm for exploration. With the booming development of nanotechnology in the 21st century, new hope to produce advanced LSBs was found. Wang et al. proved that the sulfur utilization and cycling stability of LSB can be effectively improved by using porous carbon as the host.^[17] A great breakthrough in the past decade was achieved by the Nazar group, who employed ordered mesoporous carbon (CMK-3) as sulfur host and achieved a high capacity of 1320 mAh g⁻¹ and stable LSBs.^[18] In the following years, the development of the cathode host of LSB attracted more and more attention, a large number of advanced materials were developed, and the enormous investigation delivered the rapid development of LSBs.

In this thesis, I summarize the previous reports about advanced cathode hosts to solve the challenges of the LSB from three aspects: the materials chosen, the host architecture, and the heterostructure interface construction.



Figure 3. Overview of the development of LSBs from the first proposal to the present. Inset in the lower right corner is the number of publications in recent years with the topic keywords of "Li-S battery" and "lithium-sulfur battery" in the Web of Science database, dated March 1st, 2022.

1.4 Host materials

From a material's engineering point of view, an advanced host material requires good electrical conductivity, strong polysulfide interactions, and high electrocatalytic activity.^[19,20] In the past decade, scientists developed a series of materials to promote the performance of LSBs, including carbon-based materials,^[21] transition metal oxides,^[22] sulfides,^[23] phosphides,^[24] etc. In the following sections, I discuss them from the perspective of the composition.

1.4.1 Non-metallic materials

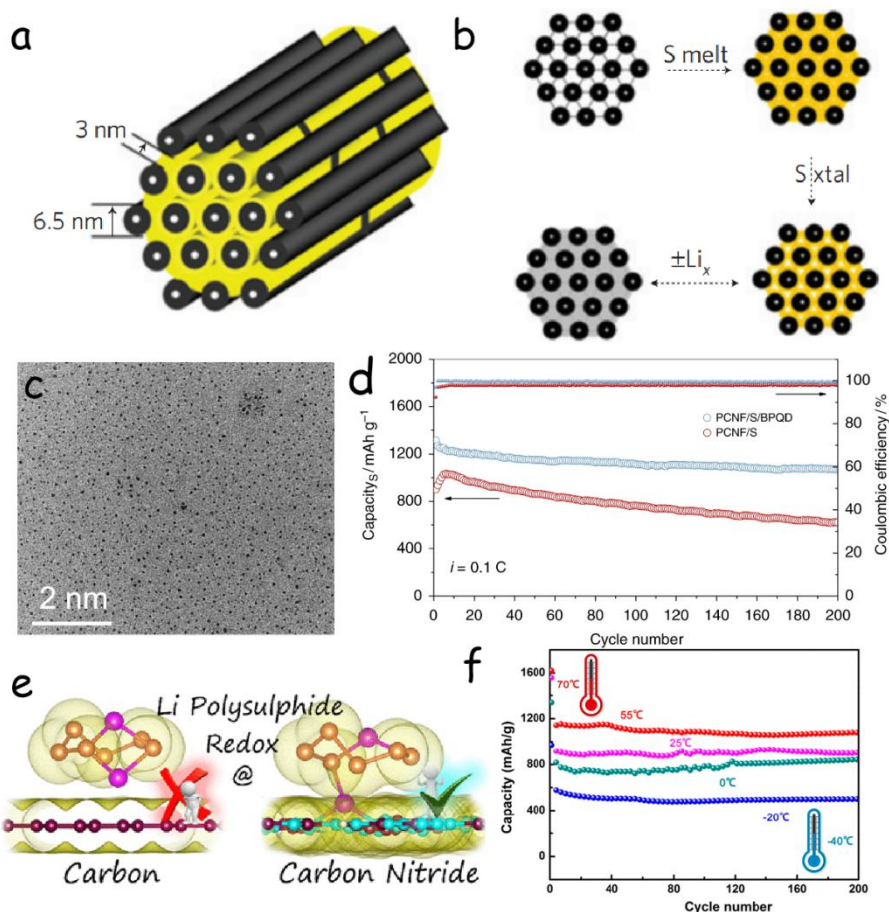


Figure 4. (a) Schematic diagram of the sulfur (yellow) confined in the interconnected pore structure of mesoporous carbon of CMK-3. (b) Schematic diagram of composite synthesis by impregnation of molten sulfur, followed by its densification on crystallization. The lower diagram represents subsequent discharging-charging with Li, illustrating the strategy of pore-filling to tune for volume expansion/contraction.^[18] (c) TEM image of black phosphorus quantum dots. (d) Cycling stability of PCNF/S and PCNF/S/BPQD electrode.^[25] (e) Interaction of LiPS with carbon or C₃N₄ surfaces.^[26] (f) The cycling stability at the different temperatures of graphene supported BN nanosheet composite as the cathode.^[27]

After Nazar group reported in 2009 that the use of highly ordered mesoporous carbon (CMK-3) as sulfur host (as shown in Figure 4a and 4b) greatly improved the cycling performance and specific capacity of LSBs by physically immobilizing LiPS,^[18] several other members of the family of carbon-based materials have been also tested as cathode host, including carbon nanotubes,^[28] graphene^[29], etc. These materials significantly improve the conductivity of the cathode and limit the shuttle effect of LiPS through the physical shield.^[19] Subsequent explorations found that heteroatom-doped carbon materials effectively enhance the interaction between metal-free hosts and LiPS, thus effectively confining soluble LiPS and

improving the cycle stability.^[30] For example, Nazar's group reported a nitrogen and sulfur co-doped carbon as sulfur host that greatly improves electrical conductivity, enhances affinity for LiPS, and facilitates the Li-S redox kinetics.^[31] These improvements were further demonstrated by theoretical calculations and combined X-ray photoelectron spectroscopy (XPS) studies, and the cathode based on a co-doped carbon host delivered a high capacity of 1370 mAh g⁻¹.

In addition to the traditional carbon materials, other non-metallic materials have been developed and shown charming results, such as black phosphorus (BP),^[25] boron nitride,^[27] and carbon nitride.^[26] These materials have good chemical stability and have excellent interaction with LiPS to regulate the diffusion and transformation process of LiPS during charge and discharge. For example, Lau and colleagues used BP quantum dots as efficient electrocatalysts for LiPS redox reactions.^[25] The edges of the BP quantum dots provide rich catalytic/adsorption active sites (as shown in Figure 4c and 4d), accelerate the reaction dynamics, and improve the chemical interaction with LiPS, which resulted in excellent cycling performance with a low decay rate (0.027% per cycle over 1000 cycles) and high specific capacity. Deng et al. developed a graphene/BN composite with high catalytic activity and promoted LiPS conversion in Li-S cells over a wide temperature range (-40 to 70°C, Figure 4f).^[27] Li and colleagues proved that C₃N₄ (Figure 4e) has a strong affinity for LiPS and can reduce the kinetic barrier of the redox reaction of LiPS, and the delivered performance exhibited a high capacity and low capacity decay rate of 0.037% per cycle.^[26] Although these materials show a strong ability to regulate the Li-S reaction, their semiconductor/insulator characteristics are not enough to meet the rapid electron transfer requirement of LSBs, thus the involvement of high-conductive carbon materials is necessary.

1.4.2 Metal

In the field of catalyst, noble metals such as platinum have proved superior catalytic properties in many applications.^[32] Accordingly, Arava et al. investigated the catalytic effect of platinum toward LiPS conversion (Figure 5a).^[33] Compared with pure graphene, graphene decorated with Pt nanoparticles greatly increased specific capacity by over 40% and delivered

a stable lifespan of more than 100 cycles with a high coulombic efficiency of 99.3%. Besides, the enlarged exchange current density during the charge/discharge process confirmed the accelerated LiPS redox kinetics in the presence of Pt. Non-noble metals also exhibited the promotion for LSBs. Qiao et al. reported a Co_xSn_y alloy (Figure 5b) modified hollow N-doped carbon nanobox with stronger LiPS affinity and redox kinetics than the control host.^[34] As a result, the stable cathode exhibited capacity retention of 81.2% after 500 cycles at 1 C. In addition, other bimetallic catalysts such as Co_3Fe_7 ^[35] and Fe-Ni^[36] are favorable for polysulfide shuttle inhibition. However, it is worth noting that, given the low surface area and high mass density of the metals, the cathode containing the metals must be supported by a light conductive material such as carbon.

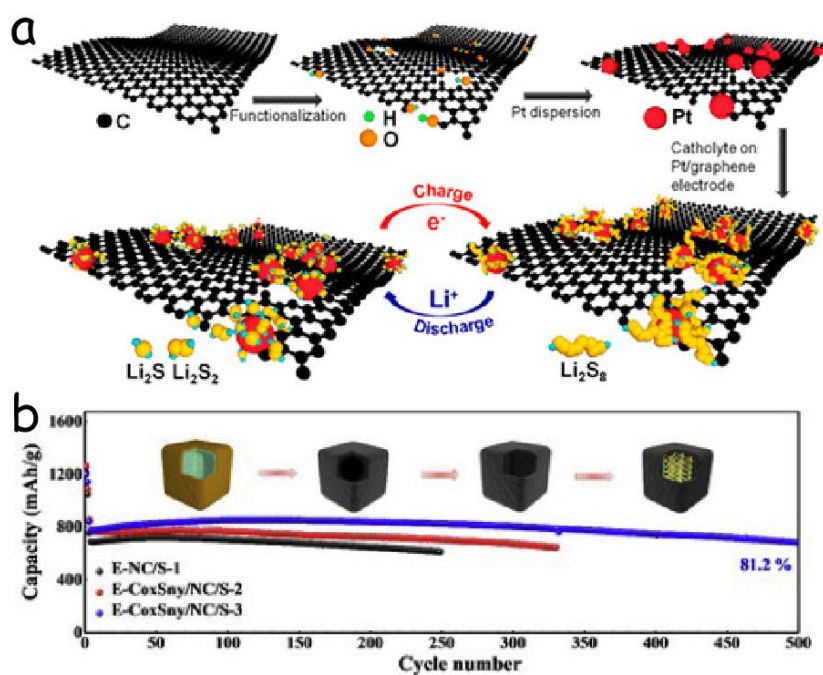


Figure 5. (a) Schematic illustration of Pt electrocatalyst anchored graphene nanocomposite preparation and its interaction with LiPS during charge/discharge process.^[33] (b) Co_xSn_y alloy modified N-doped carbon composite as the cathode host for Li-S batteries processes superior long-term cycling stability.^[34]

1.4.3 Transition metal oxides

Compared with carbon-based materials, transition metal oxides (TMOs) also have been widely explored as the sulfur host of LSBs.^[22] Based on Lewis acid-base theory, TMOs

provide a strong affinity for LiPSs by chemical capture,^[3] thus preventing LiPSs from cathode dissolving into the electrolyte. Cui group provided groundbreaking evidence of metal-oxide materials as polar hosts for LiPS absorption and improvement of lifespan (Figure 6a).^[37] In 2014, they reported that hydrogen-reduced TiO₂ host delivered high capacity retention of 81% after 200 cycles at 0.2 C with high coulombic efficiency of 99.5%. Subsequently, a series of host materials containing transition metal oxides were explored, including MnO₂,^[38] Fe₃O₄,^[39] Co₃O₄,^[40] etc. However, due to the intrinsic conductivity limitation, the rate performance based on TMO hosts is generally not particularly satisfactory.^[23]

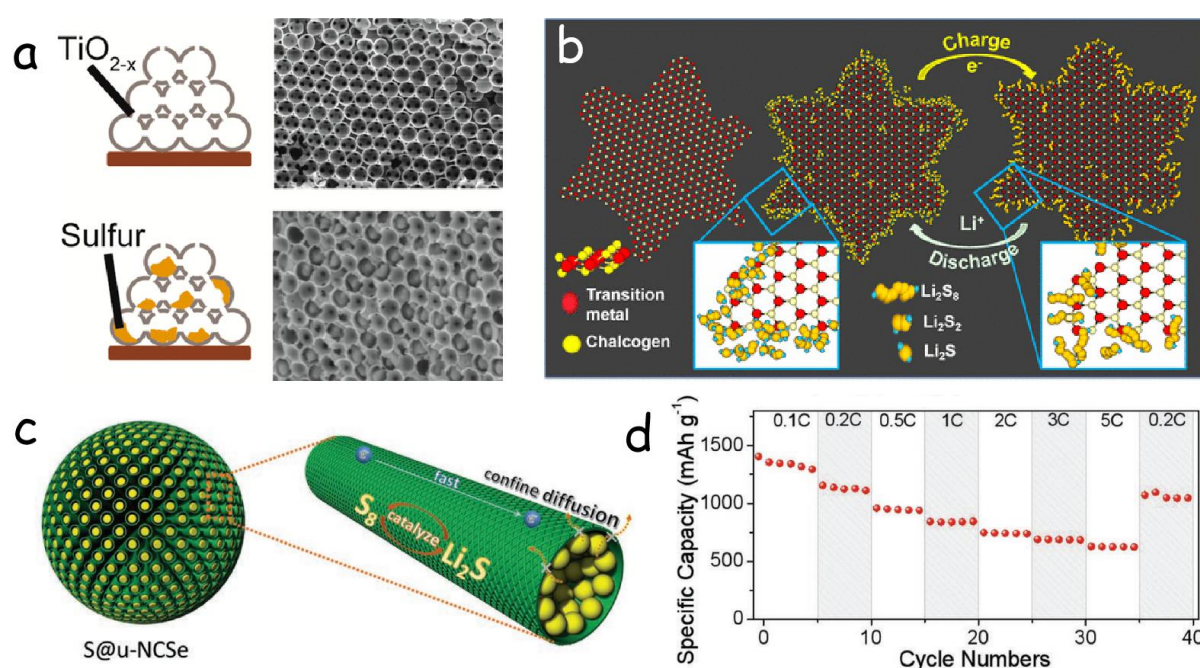


Figure 6. (a) Schematic illustration of sulfur cathodes with TiO_{2-x} inverse opal structure.^[37] (b) Schematic illustration of transition metal dichalcogenide nanosheets for LSB, showing confined deposition of lithium polysulfides at preferential catalytic sites and their conversions during discharge-charge processing in a catholyte solution.^[41] (c) Schematic illustration of the S@u-NCSe cathode for LSBs. (d) Rate capability at various current rates from 0.1 C to 5 C.^[42]

1.4.4 Transition metal sulfides and selenides

Transition metal sulfides (TMSs) generally exhibit higher electronic conductivity than TMOs and therefore have attracted large attention in the LSB community.^[7,23] The exposed crystal surface of TMSs provides a good platform for studying the interaction with LiPS from

theoretical calculation and experimental verification. In the case of WS_2 ,^[41] Arava et al. demonstrated that the unsaturated sulfur edge sites of WS_2 nanosheets have excellent regulation of LiPS (Figure 6b), not only could capture the higher-order LiPS at the edge, but also prove the transformation mechanism of long-chain to short-chain LiPS by thiosulfate compounds on the catalyst surface. After that, benefitting from the simple synthesis technology and efficient structural optimization, a series of TMS hosts have been developed as advanced cathode for LSB.

The transition metal selenides (TMSes) usually have a better conductive character than TMSs and retain a similar surface polarity.^[42–44] I have pioneered the use of TMSes as sulfur hosts for LSBs. As introduced in Chapter 2, I reported a hollow urchin-like NiCo_2Se_4 as host with high conductivity (Figure 6c and 6d), surface polarity, hollow structure, and high catalytic activity, which exhibited a high rate performance and long cycle life, e.g. 626 mAh g^{-1} at 5 C current rate and 0.016% capacity decay rate during 2000 cycles at 3 C.^[42]

1.4.5 Transition metal nitrides

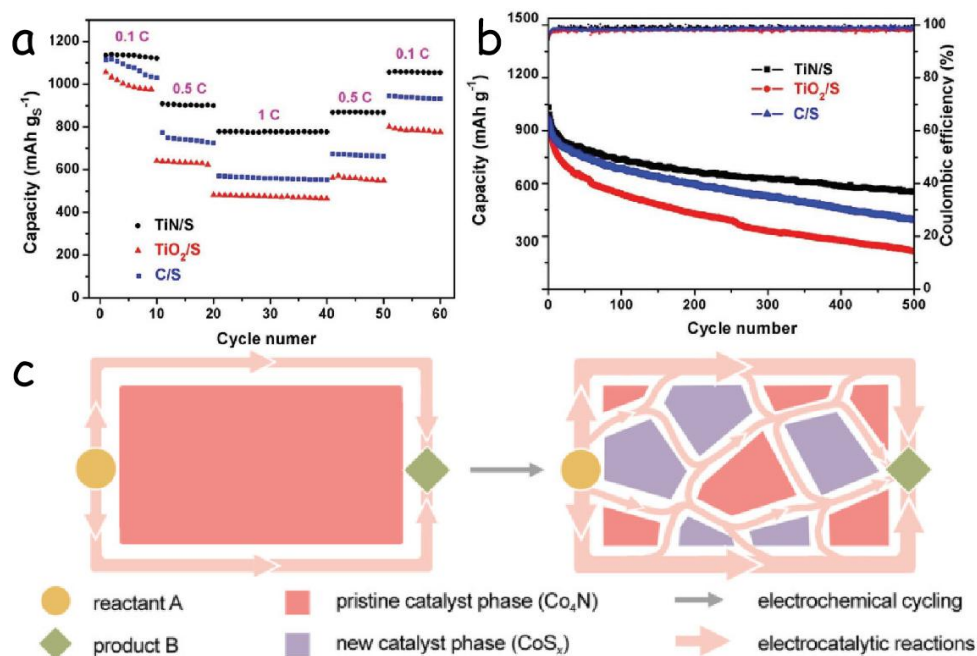


Figure 7. (a) Comparison of rate performance and cycle performance of TiN/S, TiO₂/S, and C/S cathode.^[45] (b) Representation of Co₄N as pre-catalysts undergo in situ mosaicking phase evolution in LSBs.^[46]

Goodenough et al. first developed the application of transition metal nitrides (TMNs) as cathode hosts in LSBs.^[45] Thanks to the high conductivity, robust porous skeleton, and good adsorption performance of the synthesized mesoporous TiN, the TiN-S electrode showed a high specific capacity and excellent rate performance, achieving a capacity decay rate of only 0.07% per cycle in 500 loops (Figure 7a and 7b). Subsequently, a series of TMNs, such as VN^[47] and WN^[48], were employed as the sulfur host. However, it is worth noting that although some TMNs achieve excellent electrochemical performance in LSBs, some of them are not stable in the Li-S reaction system. A typical example of this is that of cobalt nitride. Zhang et al. proved that under the action of LiPS, single-crystal Co₄N as the precatalyst could transform into polycrystalline CoS_x with abundant active sites (Figure 7c), thus achieving excellent catalytic performance.^[46]

1.4.6 Transition metal phosphides

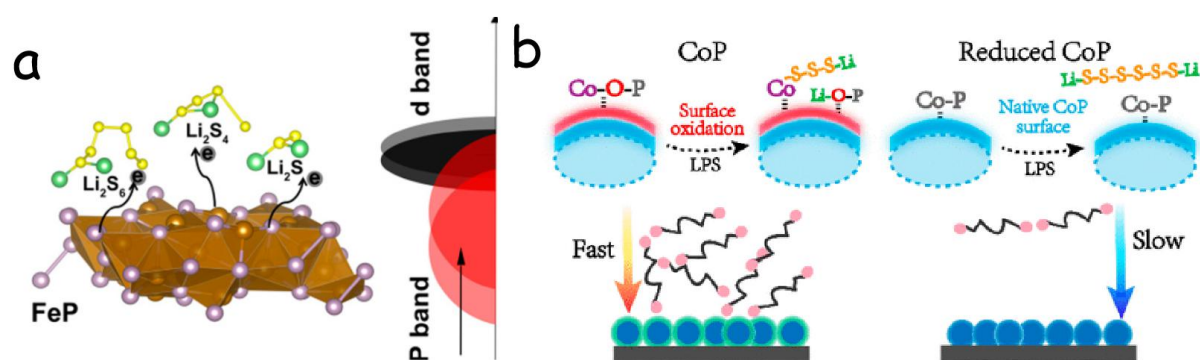


Figure 8. (a) Bandgap changes after FeP adsorbs LiPS.^[49] (b) LiPS-binding mechanism enabled by surface oxidation layers of CoP.^[50]

More recently, transition metal phosphides (TMPs) have been developed as sulfur hosts because of their distinct metallic character compared to TMO/TMSs and unique advantages in electrocatalysis.^[51,52] Zhu et al. reported FeP@C nanotube arrays (Figure 8a) as cathode host showed significantly improved electrochemical rate and cycling performance by comparing with Fe₃O₄@C host.^[49] In addition to the excellent LiPS adsorption capacity, DFT calculations probed that the position of the p-band center toward the Fermi level can influence redox reactions of the interface by adjusting the energy of electrons in the valence band. However, it is worth noting that the TMPs surface contained -P-O species caused by

inevitably natural oxidation in air. As the cathode host material, these species could greatly contribute to the adsorption and catalysis of LiPS, which has been discussed in detail in previous reports (Figure 8b).^[50]

1.4.7 Metallic carbides and borides

Metallic carbides and borides have excellent thermal/chemical stability, good electrical conductivity, and high mechanical strength to withstand internal stresses during the reaction process.^[53–56] In recent years, these compounds have attracted much attention in photo/electrocatalytic systems, as well as in the LSB community.

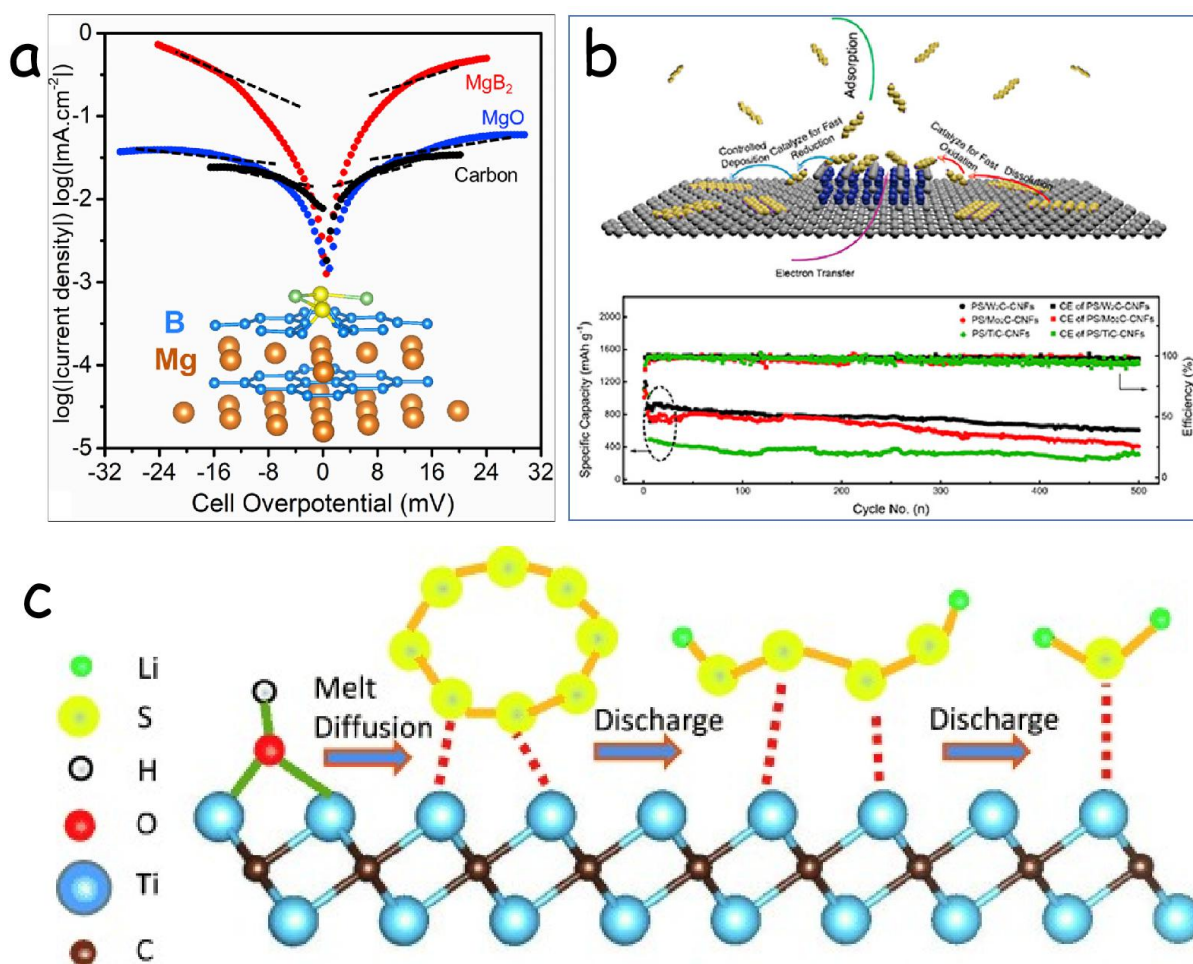


Figure 9. (a) The exchange current density plot of MgB₂, MgO, and carbon electrodes. The inset image is the adsorption configuration of Li₂S₂-MgB₂.^[57] (b) Schematic illustration of the MC NPs-CNFs hybrid electrode design to improve the performance of LSBs, and the stability during cycling tests.^[58] (c) Illustration replacement of the Ti-OH bond on the MXene surface with S-Ti-C bond on heat treatment or by contact with polysulfides.^[59]

The Nazar group reported the lightweight MgB_2 as the sulfur host (Figure 9a), which ensures good electron conduction and LiPS limitation.^[57] They demonstrated that their borides were unique because both superficial B and Mg could bind to the S_x^{2-} anion (not Li^+), thus improving electron transfer to the active S_x^{2-} anion. This surface-mediated LiPS conversion reaction increases the exchange current density compared to MgO and bare carbon. The cathode based on the MgB_2 host showed good electrochemical performance and stable cycling at a high sulfur load of 9.3 mg cm^{-2} .

Yu et al. reported a unique electrocatalyst of metal carbide nanoparticles decorated on carbon nanofibers (MC NPs-CNFS, Figure 9b).^[58] When MC NPs-CNFS were used in Li-S batteries, the cathode showed high rate performance, low hysteresis, and good cycle stability. The combination of experimental results and DFT calculation showed that the surface of MC NPs has a moderate affinity for LiPSs and also proved the catalytic performance for Li-S reaction. With these advantages, the host-based on W_2C NPs-CNFS exhibits a high reversible capacity of 1200 mAh g^{-1} at a rate of 0.2 C, with long cycle stability and a capacity decay rate of 0.06% per cycle over 500 cycles.

Another very unique metallic carbide family is that of the emerging 2D Mxenes, due to the various functional groups (-O, -F, -OH, etc.) attached on the surface during the synthesis process, this compound is expected to bind LiPS through polar-polar and Lewis acid-base interactions.^[59-61] In 2015, Nazar research group reported that Ti_2C Mxene host achieved a specific capacity of close to 1200 mAh g^{-1} at 0.2 C current rate with 70 wt % S load, and maintained 80% of the capacity by cycling for more than 400 times at 0.5 C (Figure 9c).^[59]

1.4.8 Single-atom catalysts

As an emerging catalyst system, single-atomic catalysts (SACs) revealed great potential in LSBs.^[62,63] The distribution of single atoms on the substrate maximizes the utilization efficiency of catalytically active atoms, and the unique electronic structure and unsaturated coordination environment,^[64,65] provide a guarantee to regulate LiPS and improve the Li-S performance. In 2018, Yang et al. first reported that Fe-SAC as a catalyst enables rapid transformation of LiPS (Figure 10a),^[66] which is in favor of the realization of high-rate and

long-cycle LSBs. Then, Wan et al. employed theoretical calculations and experiment verification to confirm that the Co-N-C coordination center acts as a dual-function electrocatalyst to promote the formation and decomposition of Li_2S during discharge and charge (Figure 10b),^[67] respectively, achieved a high specific capacity of 1210 mAh g^{-1} with high S mass ratio of 90 wt%. Even under the S load of 6.0 mg cm^{-2} , a lower decay rate is only 0.029% after 100 cycles. Subsequently, a series of SACs were developed as the sulfur cathode in LSBs, such as $\text{Fe}@C_2\text{N}$.^[68]

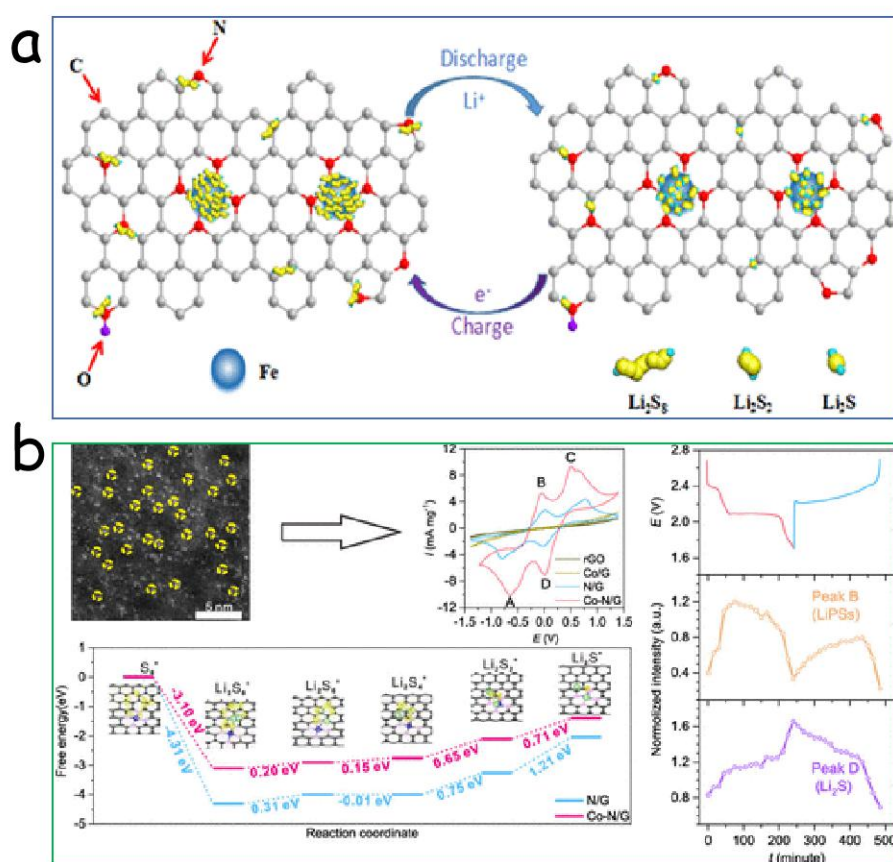


Figure 10. (a) Schematic illustration of the conversion process of LPS on the Fe-PNC surface with single-atomic iron catalytic sites.^[66] (b) Improved catalytic activity with the presence of Co-N-C coordination center.^[67]

1.4.9 Metal-organic frameworks and covalent organic frameworks

Metal-organic frameworks (MOFs) are promising candidates for efficient sulfur hosts due to their uniform structure, regular molecular framework, and controllable pore size.^[69–71] Lin et al. reported that MOFs/CNT thin films were constructed by using three different MOFs

(Figure 11a). Compared with MOF-5 and ZIF-8, the appropriate pore structure of HKUST-1 could effectively accommodate S₈ molecules and the open metal sites with positive charge provided an electrostatic attraction for polysulfide, and delivered a highly stable performance.^[72] However, it is worth noting that most of the MOF materials suffer from inherently poor electrical conductivity, which hinders electron transfer when they work as hosts. Therefore, the research on MOF hosts is still in the initial stage.

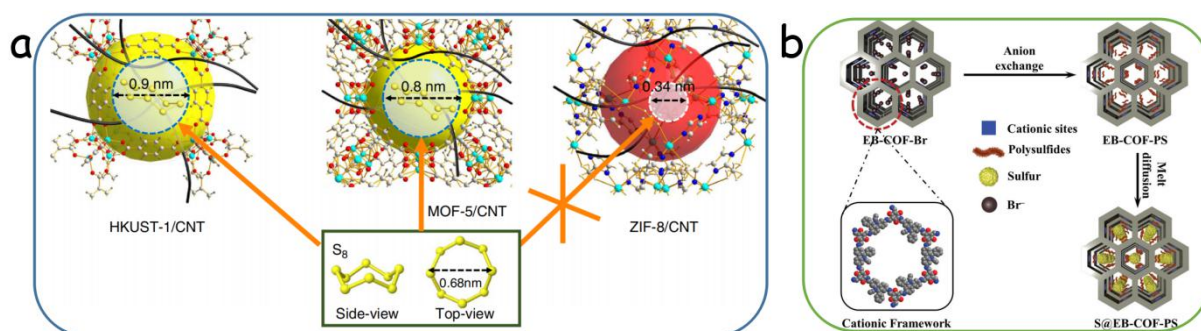


Figure 11. (a) Schematic diagram of S₈ molecule and MOFs/CNT structures with different pore sizes.^[72] (b) The diagram of the synthesis process of S@EB-COF-PS.^[73]

Another potentially interesting frame structure is that of the crystalline covalent organic framework (COF). COFs are composed of organic structural units and multifunctional groups covalently linked into an extended periodic arrangement.^[74–76] Due to their lightweight, uniform pore distribution, and favorable π -conjugated systems, COF can meet conductivity requirements, so they can be superior candidates of the sulfur host. Mak et al. utilized a cationic COF constructed by 1, 3, 5-triformylphloroglucinol and ethidium bromide as the polysulfides reservoir to inhibit the shuttle effect and improve the batteries performance (Figure 11b).^[73]

1.5 Architecture optimization

The rapid development of nanotechnology has brought revolutionary breakthroughs to the development of LSBs in the past decade. Improvements in the cathode architecture have achieved the reversible cycle in the earlier research. Still, currently, the development of new strategies to optimize the cathode architecture is gradually approaching LSBs towards

commercialization. Here, I summarize the general strategies of cathode structure design in LSBs.

1.5.1 Porous structure

Due to its good electronic conductivity and ionic conductivity, as well as the abundant void structure, porous hosts made of carbon-based materials provide the most feasible solution for the intrinsic challenges of the sulfur cathode.^[19,77,78] In 2009, the Nazar group first reported the use of ordered mesoporous carbon CMK-3 as a host to load sulfur, which successfully achieved high capacity (1320 mAh g⁻¹) and reversibility of LSB.^[18] The 2D space sandwiched into 2D host materials also significantly affected the Li-S electrochemical performance. The Cui group designed a highly torsional porous reduced GO with a horizontal arrangement for the efficient sulfur host (Figure 12a). Experimental results showed that higher tortuosity of the electrode may contribute to the geometrically extended outward mass transfer path to inhibit the LiPS shuttle effect and delivered an ultra-high area capacity of 21 mAh cm⁻² with a high capacity retention of 98.1% after 160 cycles.^[79]

1.5.2 Hollow structure

Hollow structure materials are currently widely studied in the cathode of LSBs, mainly because the holes' internal structure allows for a high sulfur load and has an effective buffer against volume expansion during the charge/discharge process. Besides, the outer shell could effectively limit soluble LiPS diffusion and improve cycle performance.^[19,81] In 2011, the Archer group developed a highly graphitized hollow carbon sphere as the sulfur host to accommodate 70 wt% sulfur, and delivered a high sulfur utilization of 1100 mAh g⁻¹ and stable lifespan as much as 100 cycles.^[82] Because the nonpolar carbon material could not provide effective chemical anchoring and catalytic conversion of LiPS, a series of hollow nanomaterials with surface polarity were developed, including heteroatom-doped and carbon transition metal compounds. The Cui group reported on yolk-shell sulfur-TiO₂ cathodes with the internal void space accommodating the volume expansion of sulfur (Figure 12b). These structures minimized the dissolution of LiPS and delivered a high specific capacity of 1030 mAh g⁻¹ at 0.5 C and 0.033% decay rate with more than 1000 cycles.^[80]

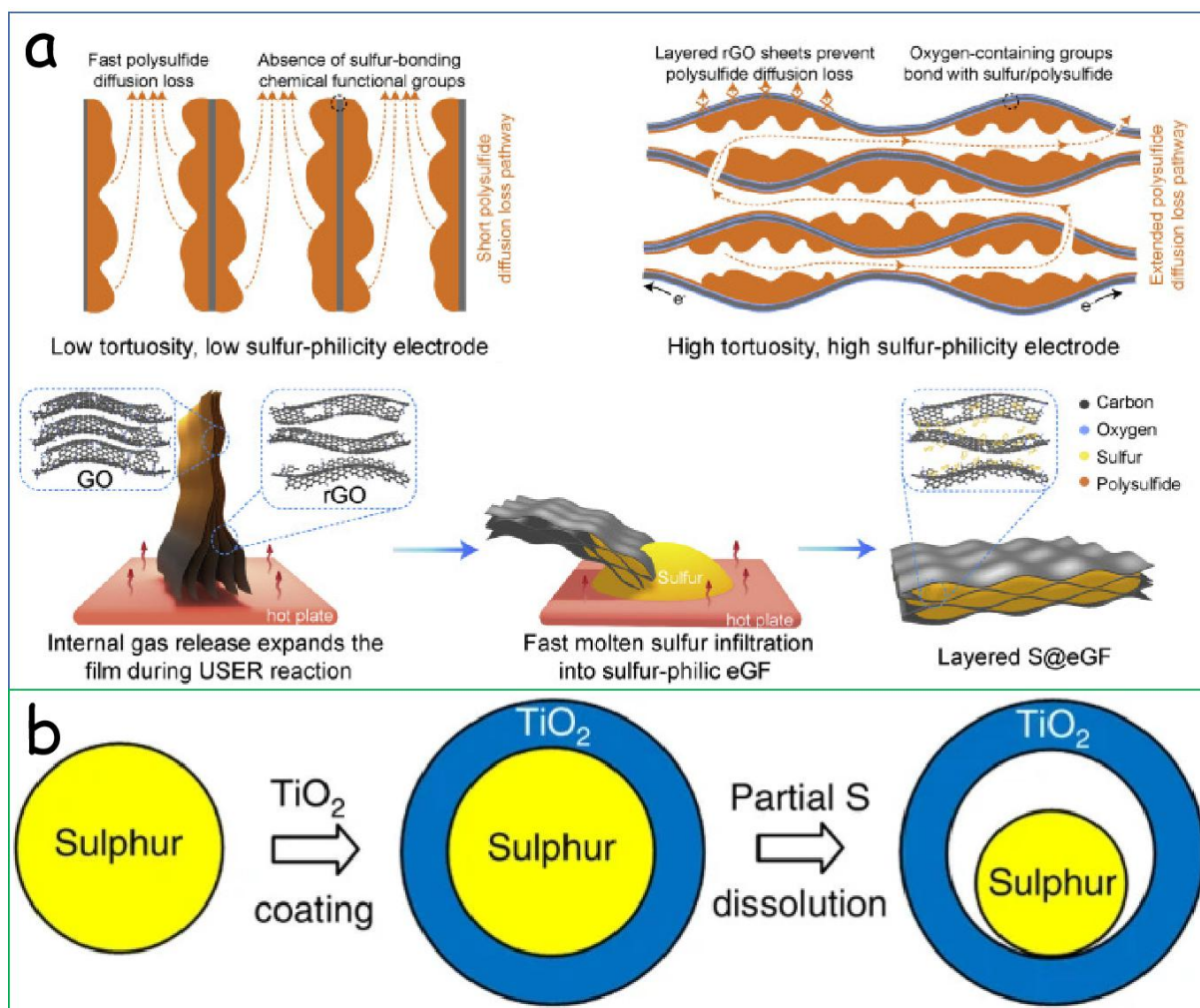


Figure 12. (a) Schematic of electrode design and fabrication of the higher tortuosity rGO electrode.^[79] (b) Schematic diagram of the synthesis process of yolk-shell sulfur-TiO₂ cathode.^[80]

1.5.3 Self-standing architecture

Generally, electrodes of various batteries are obtained by the doctor blade method for large-scale production. In such devices, the binder, conductive carbon, and current collector occupy a high gravimetric proportion, which greatly affects the energy density of batteries. In contrast, the self-standing electrode with a porous structure could effectively accommodate a large amount of active sulfur and provide favorable interconnection of the electronic and lithium-ion pathways.^[83] Therefore, it is highly desirable to prepare self-standing cathodes with a high sulfur load and excellent electronic/ion conductivity. In 2011, the Aurbach group reported that activated carbon fiber cloth with high sulfur content up to 6.5 mg cm⁻²

maintained 800 mAh g⁻¹ after 80 cycles.^[84] Since then, a mass of self-standing cathodes with high sulfur loads has been designed for high-energy-density LSBs. But it is worth noting that the current preparation method of the self-standing host (freeze-drying, filtration, or electrospinning) cannot meet the requirements of large-scale commercial production, and the welding problem between the self-supporting cathode and the tab for pouch cell has not been solved so far.

1.6 Heterostructure engineering

Due to the efficient LiPS chemical capture and excellent reaction kinetics promotion, employing a heterostructure host is one of the shortcuts to achieving advanced LSBs. Heterostructure refers to the composite constructed by different materials through physical contact or chemical bonding. By taking advantage of each component and the strong synergistic effect at the heterogeneous interface, heterostructure engineering provides a general strategy to solve the intrinsic challenges of LSB.^[85,86]

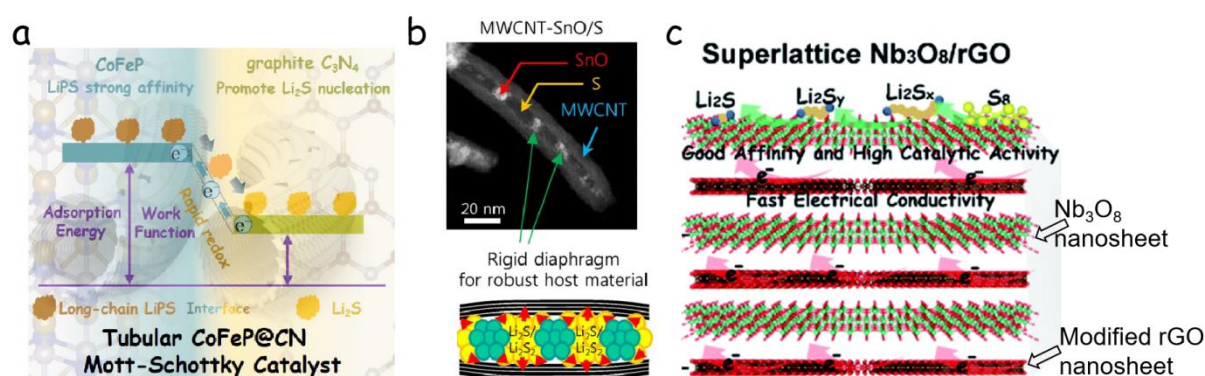


Figure 13. (a) Illustration of the CoFeP@CN Mott-Schottky heterojunction.^[87] (b) HR-TEM image of MWCNT-SnO/S and illustration of discharge state of the electrode.^[88] (c) Structure diagram of the Nb₃O₈/graphene superlattice as a three-in-one cathode host.^[89]

1.6.1 Various-phase heterostructure

In earlier studies, heterostructural design for LSBs typically focused on combining strong LiPS-adsorbing materials (e.g., metal oxides) with conductive carbon-based frameworks. The Lee group reported MWCNT-SnO heterostructure facilitated fast ion/electron transfer during the redox reactions (Figure 13b).^[88] Similarly, a range of other transition metal compound

materials has been developed for heterojunctions with carbon-based materials, including metal,^[90] TMS^[91], etc., which generally exhibit better electrical conductivity, moderate LPS affinity, and efficient catalytic conversion.

Later, it was found that combining nanomaterials with different bandgaps together allowed to achieve a Fermi energy balance at the interface and created a built-in electric field by charge transfer cross the interface, which could promote higher dipole-dipole interaction and faster electron transfer.^[92,93] A typical example is 2D MoN-VN heterostructure, which probed higher LiPS chemisorption capacity at the interface than the single compound.^[94] A similar effort has been proved by tubular CoFeP-C₃N₄ Mott-Schottky heterojunctions (Figure 13a).^[87] CoFeP nanocrystals were self-assembled onto C₃N₄ nanotubes by electrostatic adsorption to construct the heterojunction, which accelerated the rapid transformation of LiPS under the action of a built-in electric field at the heterogeneous interface, achieving a low decay of 0.014% per cycle and high rate performance of 630 mAh g⁻¹ under 5 C current rate.

1.6.2 2D superlattice heterostructure

Different from the above introduction of the various-phase heterostructure, 2D superlattice heterostructure is an artificial product obtained from different 2D monolayer sublattice nanosheets stacked together face to face with extraordinary control.^[95-97] These superlattices not only retain the advantages of the sublattice materials, but also maximize the heterogeneous interface providing some unique properties and performance beyond sublattices. Besides, the adjustable layer spacing as a critical character plays an important role in energy storage materials due to the promoted ion transfer.^[96] Considering the wide application of traditional 2D materials in LSBs, the emerging 2D superlattices can not only effectively make up for the deficiency of single component 2D materials in dealing with the challenge of LSB, but also maximize the heterojunction effect that effectively improves the performance of LSBs. Recently, the Sasaki group reported Nb₃O₈/graphene superlattice as a three-in-one cathode host to prevent the LiPS shuttle effect, accelerate Li-S conversion, and promote Li₂S nucleation, delivering superior electrochemical performance (Figure 13c).^[89] It is worth noting that the previously reported superlattice synthetic methods are characterized

by low throughput, such as layer-by-layer mechanical assembly or epitaxial growth by chemical vapor deposition, which make them incompatible with material-intensive applications. Other proposed methodologies, such as the flocculating self-assembly approach, still rely on the laborious precursor exfoliation step that limits the process scale-up. Therefore, it is urgent to develop a fast and efficient synthesis method of superlattice materials to meet the challenges of LSBs. In Chapters 4, I introduced a simple method with high-yield advantages and demonstrate its great potential in LSBs.

1.7 Objectives

To sum up, the goal of this thesis was to design and develop advanced cathode hosts so as to give play to the advantages of the preponderant theoretical capacity of the sulfur cathode, inhibit the shuttle effect, and realize the fast charge/discharge capability, which are the critical targets to meet the requirements for the next generation of energy storage devices. With these goals in mind, in order to achieve robust LSBs, the specific objectives of the thesis are defined as follows:

1. To demonstrate the potential of metal selenides as cathode host in LSBs. The exploration of advanced host materials is critical to achieving high-performance LSBs. Based on previous experience, excellent host materials need to meet not only the effective adsorption and chemical conversion of LiPS, but also in favor of the fast electron transport and accommodate volume change during the electrochemical reaction. Through theoretical analysis and practical verification, the development of advanced selenide-based host materials has great potential to achieve high-performance LSBs.

2. To demonstrate the potential of cathodes with a hierarchical nanoreactor architecture in LSBs. With a single-component host is difficult to meet the complicated challenges of LSB's cathode. The performance of LSBs can be effectively improved by effective collocation and structural regulation of different host materials. Rationally designed nanoreactors will provide a viable solution for an effective host of LSB.

3. To develop scalable procedures for the production of superlattices and demonstrate their potential as LSB cathode hosts. The heterojunction effect has been shown to efficiently regulate the adsorption and catalytic behavior of LiPS. In order to maximize the heterojunction effect, developing a simple and efficient synthetic strategy to large-scale and high yield produce the superlattice heterojunction not only play a great role for the high-performance LSBs, but also could provide potential effective materials for other applications in the field of energy storage and conversion.

In conclusion, the design and development of advanced cathode hosts through different strategies is of great significance for the realization of high-performance LSBs. In addition to the pursuance of high-level Li-S half-battery performance, some essential parameters to meet the commercial high-energy-density LSBs are worth considering. High sulfur content (5 mg cm^{-2}) and high area mass load (5 mAh cm^{-2}), low electrolyte/sulfur (E/S) ratio ($E/S < 5 \text{ mL g}^{-1}_{\text{sulfur}}$), and low negative/positive capacity (N/P) ratio ($N/P < 2$) have a critical effect to achieve high energy density of LSBs up to 500 Wh kg^{-1} .^[98-100]

1.8 References

- [1] A. Manthiram, Y. Fu, S.-H. Chung, C. Zu, Y.-S. Su, *Chem. Rev.* **2014**, *114*, 11751.
- [2] Y. Chen, T. Wang, H. Tian, D. Su, Q. Zhang, G. Wang, *Advanced Materials* **2021**, *33*, 2003666.
- [3] Q. Pang, X. Liang, C. Y. Kwok, L. F. Nazar, *Nat Energy* **2016**, *1*, 1.
- [4] Z. W. Seh, Y. Sun, Q. Zhang, Y. Cui, *Chemical Society Reviews* **2016**, *45*, 5605.
- [5] T. Liu, H. Hu, X. Ding, H. Yuan, C. Jin, J. Nai, Y. Liu, Y. Wang, Y. Wan, X. Tao, *Energy Storage Materials* **2020**, *30*, 346.
- [6] Y. Huang, L. Lin, C. Zhang, L. Liu, Y. Li, Z. Qiao, J. Lin, Q. Wei, L. Wang, Q. Xie, D.-L. Peng, *Advanced Science* **2022**, 2106004.
- [7] S.-F. Ng, M. Y. L. Lau, W.-J. Ong, *Advanced Materials* **2021**, *33*, 2008654.
- [8] T. Li, X. Bai, U. Gulzar, Y.-J. Bai, C. Capiglia, W. Deng, X. Zhou, Z. Liu, Z. Feng, R. Proietti Zaccaria, *Advanced Functional Materials* **2019**, *29*, 1901730.
- [9] X. Wu, Q. Zhang, G. Tang, Y. Cao, H. Yang, H. Li, X. Ai, *Small* **2022**, *18*, 2106144.
- [10] B. He, Z. Rao, Z. Cheng, D. Liu, D. He, J. Chen, Z. Miao, L. Yuan, Z. Li, Y. Huang, *Advanced Energy Materials* **2021**, *11*, 2003690.
- [11] W. Deng, J. Phung, G. Li, X. Wang, *Nano Energy* **2021**, *82*, 105761.

- [12]X. Yang, X. Li, K. Adair, H. Zhang, X. Sun, *Electrochem. Energ. Rev.* **2018**, *1*, 239.
- [13]Z. Li, H. B. Wu, X. W. (David) Lou, *Energy & Environmental Science* **2016**, *9*, 3061.
- [14]Y. Li, S. Guo, *Matter* **2021**, *4*, 1142.
- [15]T. Tao, S. Lu, Y. Fan, W. Lei, S. Huang, Y. Chen, *Advanced Materials* **2017**, 1700542.
- [16]Y. Zhao, Y. Ye, F. Wu, Y. Li, L. Li, R. Chen, *Advanced Materials* **2019**, *31*, 1806532.
- [17]J. L. Wang, J. Yang, J. Y. Xie, N. X. Xu, Y. Li, *Electrochemistry Communications* **2002**, *4*, 499.
- [18]X. Ji, K. T. Lee, L. F. Nazar, *Nature Materials* **2009**, *8*, 500.
- [19]A. Fu, C. Wang, F. Pei, J. Cui, X. Fang, N. Zheng, *Small* **2019**, *15*, 1804786.
- [20]M. Jana, R. Xu, X.-B. Cheng, J. Seok Yeon, J. Min Park, J.-Q. Huang, Q. Zhang, H. Seok Park, *Energy & Environmental Science* **2020**, *13*, 1049.
- [21]S. Li, B. Jin, X. Zhai, H. Li, Q. Jiang, *ChemistrySelect* **2018**, *3*, 2245.
- [22]X. Liang, C. Y. Kwok, F. Lodi-Marzano, Q. Pang, M. Cuisinier, H. Huang, C. J. Hart, D. Houtarde, K. Kaup, H. Sommer, T. Brezesinski, J. Janek, L. F. Nazar, *Advanced Energy Materials* **2016**, *6*, 1501636.
- [23]X. Liu, J.-Q. Huang, Q. Zhang, L. Mai, *Advanced Materials* **2017**, *29*, 1601759.
- [24]Z. Wang, X. Xu, Z. Liu, D. Zhang, J. Yuan, J. Liu, *Chemistry – A European Journal* **2021**, *27*, 13494.
- [25]Z.-L. Xu, S. Lin, N. Onofrio, L. Zhou, F. Shi, W. Lu, K. Kang, Q. Zhang, S. P. Lau, *Nat Commun* **2018**, *9*, 4164.
- [26]J. Liang, L. Yin, X. Tang, H. Yang, W. Yan, L. Song, H.-M. Cheng, F. Li, *ACS Appl. Mater. Interfaces* **2016**, *8*, 25193.
- [27]D. R. Deng, F. Xue, C.-D. Bai, J. Lei, R. Yuan, M. S. Zheng, Q. F. Dong, *ACS Nano* **2018**, *12*, 11120.
- [28]J. Guo, Y. Xu, C. Wang, *Nano Lett.* **2011**, *11*, 4288.
- [29]M. Yu, R. Li, M. Wu, G. Shi, *Energy Storage Materials* **2015**, *1*, 51.
- [30]T.-Z. Hou, X. Chen, H.-J. Peng, J.-Q. Huang, B.-Q. Li, Q. Zhang, B. Li, *Small* **2016**, *12*, 3283.
- [31]Q. Pang, J. Tang, H. Huang, X. Liang, C. Hart, K. C. Tam, L. F. Nazar, *Advanced Materials* **2015**, *27*, 6021.
- [32]N. Jung, D. Y. Chung, J. Ryu, S. J. Yoo, Y.-E. Sung, *Nano Today* **2014**, *9*, 433.
- [33]H. Al Salem, G. Babu, C. V. Rao, L. M. R. Arava, *J. Am. Chem. Soc.* **2015**, *137*, 11542.
- [34]Z. Qiao, F. Zhou, Q. Zhang, F. Pei, H. Zheng, W. Xu, P. Liu, Y. Ma, Q. Xie, L. Wang, X. Fang, D.-L. Peng, *Energy Storage Materials* **2019**, *23*, 62.
- [35]Z. Gu, C. Cheng, T. Yan, G. Liu, J. Jiang, J. Mao, K. Dai, J. Li, J. Wu, L. Zhang, *Nano Energy* **2021**, *86*, 106111.
- [36]J. He, A. Bhargav, A. Manthiram, *ACS Nano* **2021**, *15*, 8583.
- [37]Z. Liang, G. Zheng, W. Li, Z. W. Seh, H. Yao, K. Yan, D. Kong, Y. Cui, *ACS Nano* **2014**, *8*, 5249.

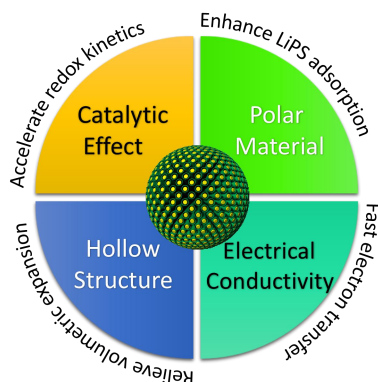
- [38]Z. Li, J. Zhang, X. W. D. Lou, *Angewandte Chemie International Edition* **2015**, *54*, 12886.
- [39]J. He, L. Luo, Y. Chen, A. Manthiram, *Advanced Materials* **2017**, *29*, 1702707.
- [40]J. Xu, W. Zhang, Y. Chen, H. Fan, D. Su, G. Wang, *Journal of Materials Chemistry A* **2018**, *6*, 2797.
- [41]G. Babu, N. Masurkar, H. Al Salem, L. M. R. Arava, *Journal of the American Chemical Society* **2017**, *139*, 171.
- [42]C. Zhang, J. J. Biendicho, T. Zhang, R. Du, J. Li, X. Yang, J. Arbiol, Y. Zhou, J. R. Morante, A. Cabot, *Advanced Functional Materials* **2019**, *29*, 1903842.
- [43]H.-J. Li, K. Xi, W. Wang, S. Liu, G.-R. Li, X.-P. Gao, *Energy Storage Materials* **2021**, DOI 10.1016/j.ensm.2021.11.024.
- [44]D. Yang, C. Zhang, J. J. Biendicho, X. Han, Z. Liang, R. Du, M. Li, J. Li, J. Arbiol, J. Llorca, Y. Zhou, J. R. Morante, A. Cabot, *ACS Nano* **2020**, *14*, 15492.
- [45]Z. Cui, C. Zu, W. Zhou, A. Manthiram, J. B. Goodenough, *Advanced Materials* **2016**, *28*, 6926.
- [46]M. Zhao, H.-J. Peng, B.-Q. Li, X. Chen, J. Xie, X. Liu, Q. Zhang, J.-Q. Huang, *Angewandte Chemie International Edition* **2020**, *59*, 9011.
- [47]J. He, A. Manthiram, *Advanced Energy Materials* **2020**, *10*, 1903241.
- [48]H. Liu, H. Shen, R. Li, S. Liu, A. Turak, M. Yang, *ChemElectroChem* **2019**, *6*, 2074.
- [49]J. Shen, X. Xu, J. Liu, Z. Liu, F. Li, R. Hu, J. Liu, X. Hou, Y. Feng, Y. Yu, M. Zhu, *ACS Nano* **2019**, *13*, 8986.
- [50]Y. Zhong, L. Yin, P. He, W. Liu, Z. Wu, H. Wang, *J. Am. Chem. Soc.* **2018**, *140*, 1455.
- [51]Y. Chen, W. Zhang, D. Zhou, H. Tian, D. Su, C. Wang, D. Stockdale, F. Kang, B. Li, G. Wang, *ACS Nano* **2019**, *13*, 4731.
- [52]S. Yu, W. Cai, L. Chen, L. Song, Y. Song, *Journal of Energy Chemistry* **2020**, DOI 10.1016/j.jechem.2020.07.020.
- [53]W. Bao, D. Su, W. Zhang, X. Guo, G. Wang, *Advanced Functional Materials* **2016**, *26*, 8746.
- [54]W. Cai, G. Li, K. Zhang, G. Xiao, C. Wang, K. Ye, Z. Chen, Y. Zhu, Y. Qian, *Advanced Functional Materials* **2018**, *28*, 1704865.
- [55]C. Li, X. Liu, L. Zhu, R. Huang, M. Zhao, L. Xu, Y. Qian, *Chemistry of Materials* **2018**, *30*, 6969.
- [56]J. He, A. Bhargav, A. Manthiram, *Advanced Materials* **2020**, *32*, 2004741.
- [57]Q. Pang, C. Y. Kwok, D. Kundu, X. Liang, L. F. Nazar, *Joule* **2019**, *3*, 136.
- [58]F. Zhou, Z. Li, X. Luo, T. Wu, B. Jiang, L.-L. Lu, H.-B. Yao, M. Antonietti, S.-H. Yu, *Nano Letters* **2018**, *18*, 1035.
- [59]X. Liang, A. Garsuch, L. F. Nazar, *Angewandte Chemie* **2015**, *127*, 3979.
- [60]W. Bao, L. Liu, C. Wang, S. Choi, D. Wang, G. Wang, *Advanced Energy Materials* **2018**, *8*, 1702485.

- [61] C. Xiong, G. Y. Zhu, H. R. Jiang, Q. Chen, T. S. Zhao, *Energy Storage Materials* **2020**, *33*, 147.
- [62] J. Wang, L. Jia, J. Zhong, Q. Xiao, C. Wang, K. Zang, H. Liu, H. Zheng, J. Luo, J. Yang, H. Fan, W. Duan, Y. Wu, H. Lin, Y. Zhang, *Energy Storage Materials* **2019**, *18*, 246.
- [63] Z. Liang, J. Shen, X. Xu, F. Li, J. Liu, B. Yuan, Y. Yu, M. Zhu, *Advanced Materials* **n.d.**, *n/a*, 2200102.
- [64] Y. Zhang, J. Yang, R. Ge, J. Zhang, J. M. Cairney, Y. Li, M. Zhu, S. Li, W. Li, *Coordination Chemistry Reviews* **2022**, *461*, 214493.
- [65] J. Xia, B. Wang, J. Di, Y. Li, S.-Z. Yang, H. Li, S. Guo, *Materials Today* **2022**, DOI 10.1016/j.mattod.2021.11.022.
- [66] Z. Liu, L. Zhou, Q. Ge, R. Chen, M. Ni, W. Utetiwabo, X. Zhang, W. Yang, *ACS Appl. Mater. Interfaces* **2018**, *10*, 19311.
- [67] Z. Du, X. Chen, W. Hu, C. Chuang, S. Xie, A. Hu, W. Yan, X. Kong, X. Wu, H. Ji, L.-J. Wan, *J. Am. Chem. Soc.* **2019**, *141*, 3977.
- [68] Z. Liang, D. Yang, P. Tang, C. Zhang, J. Jacas Biendicho, Y. Zhang, J. Llorca, X. Wang, J. Li, M. Heggen, J. David, R. E. Dunin-Borkowski, Y. Zhou, J. R. Morante, A. Cabot, J. Arbiol, *Advanced Energy Materials* **2021**, *11*, 2003507.
- [69] C. Zhou, Z. Li, X. Xu, L. Mai, *National Science Review* **2021**, *8*, nwab055.
- [70] M. Du, Q. Li, G. Zhang, F. Wang, H. Pang, *ENERGY & ENVIRONMENTAL MATERIALS* **2022**, *5*, 215.
- [71] B. Liu, V. Sara Thoi, *Chemical Communications* **2022**, DOI 10.1039/D1CC07087H.
- [72] Y. Mao, G. Li, Y. Guo, Z. Li, C. Liang, X. Peng, Z. Lin, *Nat Commun* **2017**, *8*, 14628.
- [73] X.-F. Liu, H. Chen, R. Wang, S.-Q. Zang, T. C. W. Mak, *Small* **2020**, *16*, 2002932.
- [74] S. Jin, O. Allam, S. S. Jang, S. W. Lee, *InfoMat*, **2022**, 10.1002/inf2.12277.
- [75] J. Zou, K. Fan, Y. Chen, W. Hu, C. Wang, *Coordination Chemistry Reviews* **2022**, *458*, 214431.
- [76] Q. Zhang, Q. Huang, S.-M. Hao, S. Deng, Q. He, Z. Lin, Y. Yang, *Advanced Science* **2022**, *9*, 2103798.
- [77] C. Wu, W.-H. Lai, X. Cai, S.-L. Chou, H.-K. Liu, Y.-X. Wang, S.-X. Dou, *Small* **2021**, *17*, 2006504.
- [78] Z. Li, Y. Huang, L. Yuan, Z. Hao, Y. Huang, *Carbon* **2015**, *92*, 41.
- [79] H. Chen, G. Zhou, D. Boyle, J. Wan, H. Wang, D. Lin, D. Mackanic, Z. Zhang, S. C. Kim, H. R. Lee, H. Wang, W. Huang, Y. Ye, Y. Cui, *Matter* **2020**, *2*, 1605.
- [80] Z. Wei Seh, W. Li, J. J. Cha, G. Zheng, Y. Yang, M. T. McDowell, P.-C. Hsu, Y. Cui, *Nature Communications* **2013**, *4*, DOI 10.1038/ncomms2327.
- [81] Z. Li, H. B. Wu, X. W. (David) Lou, *Energy & Environmental Science* **2016**, *9*, 3061.
- [82] N. Jayaprakash, J. Shen, S. S. Moganty, A. Corona, L. A. Archer, *Angewandte Chemie* **2011**, *123*, 6026.
- [83] J. Guo, J. Liu, *Nanoscale Advances* **2019**, *1*, 2104.

- [84] R. Elazari, G. Salitra, A. Garsuch, A. Panchenko, D. Aurbach, *Advanced Materials* **2011**, *23*, 5641.
- [85] Z.-W. Zhang, H.-J. Peng, M. Zhao, J.-Q. Huang, *Advanced Functional Materials* **2018**, *28*, 1707536.
- [86] S. Huang, Z. Wang, Y. Von Lim, Y. Wang, Y. Li, D. Zhang, H. Y. Yang, *Advanced Energy Materials* **2021**, *11*, 2003689.
- [87] C. Zhang, R. Du, J. J. Biendicho, M. Yi, K. Xiao, D. Yang, T. Zhang, X. Wang, J. Arbiol, J. Llorca, Y. Zhou, J. R. Morante, A. Cabot, *Advanced Energy Materials* **2021**, *11*, 2100432.
- [88] A.-Y. Kim, M. K. Kim, J. Y. Kim, Y. Wen, L. Gu, V.-D. Dao, H.-S. Choi, D. Byun, J. K. Lee, *Nano Res.* **2017**, *10*, 2083.
- [89] C. Wang, N. Sakai, Y. Ebina, T. Kikuchi, M. R. Snowdon, D. Tang, R. Ma, T. Sasaki, *J. Mater. Chem. A* **2021**, *9*, 9952.
- [90] S. Gu, Z. Bai, S. Majumder, B. Huang, G. Chen, *Nanoscale* **2019**, *11*, 20579.
- [91] N. Wei, J. Cai, R. Wang, M. Wang, W. Lv, H. Ci, J. Sun, Z. Liu, *Nano Energy* **2019**, *66*, 104190.
- [92] Y. Tian, G. Li, Y. Zhang, D. Luo, X. Wang, Y. Zhao, H. Liu, P. Ji, X. Du, J. Li, Z. Chen, *Advanced Materials* **2020**, *32*, 1904876.
- [93] Y. Wang, R. Zhang, J. Chen, H. Wu, S. Lu, K. Wang, H. Li, C. J. Harris, K. Xi, R. V. Kumar, S. Ding, *Advanced Energy Materials* **2019**, *9*, 1900953.
- [94] C. Ye, Y. Jiao, H. Jin, A. D. Slattery, K. Davey, H. Wang, S.-Z. Qiao, *Angewandte Chemie International Edition* **2018**, *57*, 16703.
- [95] Y. Huang, J. Liang, C. Wang, S. Yin, W. Fu, H. Zhu, C. Wan, *Chem. Soc. Rev.* **2020**, *49*, 6866.
- [96] P. Xiong, B. Sun, N. Sakai, R. Ma, T. Sasaki, S. Wang, J. Zhang, G. Wang, *Advanced Materials* **2020**, *32*, 1902654.
- [97] A. Khan, J. Azadmanjiri, B. Wu, L. Liping, Z. Sofer, J. Min, *Advanced Energy Materials* **2021**, *11*, 2100451.
- [98] A. Bhargav, J. He, A. Gupta, A. Manthiram, *Joule* **2020**, *4*, 285.
- [99] Y.-T. Liu, S. Liu, G.-R. Li, X.-P. Gao, *Advanced Materials* **2021**, *33*, 2003955.
- [100] S. Dörfler, H. Althues, P. Härtel, T. Abendroth, B. Schumm, S. Kaskel, *Joule* **2020**, *4*, 539.

Chapter 2

Combined High Catalytic Activity and Efficient Polar Tubular Nanostructure in Urchin-like Metallic NiCo₂Se₄ for High Performance Lithium Sulfur Batteries



2.1 Abstract

Urchin shaped NiCo₂Se₄ (u-NCSe) nanostructures as efficient sulfur hosts are synthesized to overcome the limitations of lithium sulfur batteries (LSBs). u-NCSe provides a beneficial hollow structure to relieve volumetric expansion, a superior electrical conductivity to improve electron transfer, a high polarity to promote absorption of LiPS, and outstanding electrocatalytic activity to accelerate LiPS conversion kinetics. Owing to these excellent qualities as cathode for LSBs, S@u-NCSe delivers outstanding initial capacities up to 1403 mA h g⁻¹ at 0.1 C, and retains 626 mAh g⁻¹ at 5 C with exceptional rate performance. More significantly, a very low capacity decay rate of only 0.016% per cycle is obtained after 2000 cycles at 3 C. Even at high sulfur loading (3.2 mg cm⁻²), a reversible capacity of 557 mA h g⁻¹ is delivered after 600 cycles at 1 C. DFT calculations further confirm the strong interaction between NCSe and LiPS and cytotoxicity measurements prove the biocompatibility of NCSe. This work not only demonstrates that transition metal selenides can be promising candidates as sulfur host materials, but also provides a strategy for the rational design and the development of LSBs with long-life and high-rate electrochemical performance.

2.2 Introduction

The low energy density and relatively high price of traditional lithium-ion batteries (LIBs) are dramatically limiting their application in large-scale energy storage systems, especially in the fast-growing field of electric vehicles.^[1,2] To overcome these two limitations, rechargeable lithium sulfur batteries (LSBs) have recently emerged as one of the most exciting alternatives to LIBs owing to their higher theoretical energy density (2600 W h kg⁻¹, 6 times higher than LIBs of 420 W h kg⁻¹) and lower cost.^[3,4] However, the practical application of LSBs requires overcoming important challenges. First, the electrical insulating character of sulfur and lithium sulfides involves a poor utilization of the active material.^[5] Besides, the severe volumetric variation (~80%) during charge/discharge processes leads to the rapid degradation of the electrode integrity.^[1] Moreover, the diffusion of soluble lithium polysulfides (LiPS) intermediates into the electrolyte results in poor cycling stability and low Coulombic efficiency.^[6] Additionally, the LiPS conversion reaction is generally characterized by slow redox kinetics, limiting the LSBs charge/discharge rate.^[7]

Several strategies have been developed to improve the electrochemical performance of LSBs. In terms of materials, one effective approach is to host sulfur at the cathode in carbon-based materials with high conductivity, such as porous structures of graphene,^[8] carbon spheres,^[9] carbon nanotubes,^[10] and nanofibers.^[11] These carbon-based materials can accelerate electron transfer, but are not able to suppress LiPS shuttling due to a weak chemical interaction between nonpolar carbons and polar LiPS. Therefore, LSBs based on carbon suffer from serious capacity fading.^[12] On the other hand, polar materials, such as TiO₂ and MnO₂, strongly bind LiPS and efficiently confine LiPS to the cathode, achieving notable improvements in cycling stability.^[13,14] However, such semiconducting oxides are characterized by insufficient electrical conductivities, what results in inferior rate capabilities. In terms of structure, hollow nanomaterials, like nanotubes, nanospheres or nanocubes, have been demonstrated advantageous in LSBs because of their large pore volumes and surface-to-volume ratios, which mitigate the detrimental effect of the volume expansion and provide an effective physical confinement for LiPS.^[5,15] Besides, the use of electrocatalysts have been demonstrated effective to accelerate the conversion of soluble long-chain LiPS into

solid phases of sulfur and $\text{Li}_2\text{S}_2/\text{Li}_2\text{S}$.^[16–18] Overall, high performance LSB cathodes require materials with excellent electrical conductivity, significant polarity to ensure a strong polysulfide affinity, high catalytic activity toward sulfide redox reactions and with hollow nanostructures to relieve volumetric expansion during charge/discharge (as shown in TOC).

Transition metal sulfides/selenides (TMS/TMSe) have attracted much attention for energy storage in recent years. TMS (e.g. CoS_2 , VS_2) have been proved as efficient catalysts in several energy conversion fields such as photovoltaics, solar-light to fuel photoconversion and electrochemical hydrogen evolution.^[19,20] Their high catalytic activity has been related to the abundance of defects on the surface of TMS due to the moderate electronegativity differences between transition metals and sulfur, the variable oxidation state of sulfur, and the potential formation of sulfur-sulfur and also metal-metal bonds.^[21,22] TMS are also highly stable catalysts in reactions involving sulfur.^[23] Besides, TMS have shown a strong bonding ability for LiPS owing to their polar character.^[17,24] TMSe display similar crystallographic structures, high defect densities and polar character to TMS owing to the relatively similar electronegativity and ionic radius of S and Se. However, the electrical conductivity of TMSe is much higher than the corresponding TMS. Se is characterized by electrical conductivities ($1 \times 10^{-3} \text{ S m}^{-1}$) many orders of magnitude higher than S ($5 \times 10^{-28} \text{ S m}^{-1}$).^[25] Thus, it is reasonable to speculate that TMSe would be promising hosts for LSBs because of their polarity, potential high catalytic activity, and high electrical conductivity. To our knowledge, this is the first work in which bimetallic selenides are reported as S host for LSBs.

NiCo_2Se_4 (NCSe) was specifically selected as the host material owing to its metallic nature and synergistic effect between Ni/Co atoms.^[26,27] The compound was prepared in the form of urchin like structures through a two-step hydrothermal process. We thoroughly studied the performance of LSBs based on urchin-like NCSe (u-NCSe) both experimentally and through theoretical calculations. Results presented in this manuscript show the benefits of a highly conductive and polar bimetallic selenide with a tubular structure for rapid electron transfer, enhanced confinement of LiPS, mitigation of volume expansion effects, and a catalytic enhancement of the electrochemical reaction kinetics.

2.3 Experimental Section

Synthesis of u-NCSe. u-NCSe was synthesized by a two-step synthesis process, from selenization of $\text{Ni}_{0.33}\text{Co}_{0.67}(\text{CO}_3)_{0.5}\text{OH}$ precursor obtained by a simple hydrothermal process. First, 5 mM $\text{NiCl}_2 \cdot 6\text{H}_2\text{O}$ (98%, Alfa Aesar) and $\text{CoCl}_2 \cdot 6\text{H}_2\text{O}$ (98%, Alfa Aesar) with molar ratio of 1:2 were dissolved into 30 mL of deionized (DI) water, and then 300 mg of urea (99%, Acros Organics) added, using an ultrasounds bath for 3 mins to form a homogeneous solution. This solution was then poured into a Teflon lined stainless steel autoclave of 50 mL volume and heated at 130 °C for 8 h. After naturally cooling to ambient temperature, the $\text{Ni}_{0.33}\text{Co}_{0.67}(\text{CO}_3)_{0.5}\text{OH}$ precipitate was centrifuged, washed, dried and recovered. Subsequently, 50 mg of as-obtained $\text{Ni}_{0.33}\text{Co}_{0.67}(\text{CO}_3)_{0.5}\text{OH}$ were dispersed in 25 mL of deionized water using an ultrasonic bath and then 150 mg of Na_2SeO_3 (99%, Alfa Aesar) and 4 mL of $\text{N}_2\text{H}_4 \cdot \text{H}_2\text{O}$ (98%, Sigma Aldrich) were incorporated under vigorous stirring. The mixture was finally poured into a Teflon-lined stainless steel autoclave of 50 mL volume and heated at 180 °C for 8 h. After cooling naturally to ambient temperature, the precipitate was centrifuged, washed, dried and recovered. NiSe and Co_3Se_4 nanostructures were synthesized following the same synthesis protocol.

Synthesis of b-NCSe. b-NCSe was obtained in just one synthesis step. 37 mg of $\text{NiCl}_2 \cdot 6\text{H}_2\text{O}$, 75 mg of $\text{CoCl}_2 \cdot 6\text{H}_2\text{O}$ and 150 mg of Na_2SeO_3 were dissolved into 25 mL of deionized water and then 4 mL of $\text{N}_2\text{H}_4 \cdot \text{H}_2\text{O}$ were dropped into the solution under vigorous stirring conditions. The resulting solution was finally poured into a Teflon-lined stainless steel autoclave of 50 mL volume and heated at 180 °C for 8 h.

Synthesis of S@u-NCSe and S@b-NCSe. u-NCSe and sulfur powder (99.98%, Sigma Aldrich) (1:3, weigh ratio) were mixed and heated at 155 °C for 12 h in a glass bottle under Ar atmosphere. In order to remove the redundant sulfur not incorporated into u-NCSe, the powder was immersed in a 10 mL CS_2 and ethanol solution (1:4, volume ratio) for 10 min twice. S@b-NCSe was obtained using the same process.

Synthesis of S@Super P. Super P (99%, Alfa Aesar) and sulfur powder (3:7, weigh ratio) were well mixed and heated at 155 °C for 12 h.

Materials Characterization: X-ray diffraction (XRD) patterns were recorded at room temperature using a Bruker AXS D8 Advance X-ray diffractometer with Cu K radiation ($\lambda = 1.5106 \text{ \AA}$) operating at 40 kV and 40 mA. The morphology and microstructure were examined by TEM (ZEISS LIBRA 120) and FESEM (ZEISS Auriga) equipped with an energy dispersive X-ray spectroscopy (EDS) detector operated at 20 kV. High-resolution TEM (HRTEM) and scanning TEM (STEM) studies were carried out using a field emission gun FEI Tecnai F20 microscope at 200 kV with a point-to-point resolution of 0.19 nm. High angle annular dark-field (HAADF) STEM was combined with electron energy loss spectroscopy (EELS) in the Tecnai microscope by using a GATAN QUANTUM filter. X-ray photoelectron spectroscopy (XPS) measurements were carried out in normal emission using an Al anode XR50 source operating at 150 mW and a Phoibos 150 MCD-9 detector. TGA (PerkinElmer Diamond TG/DTA instrument.) experiments were performed to estimate the content of S in prepared composites. The specific surface area and analysis of the pore size distribution were performed by Brunauer-Emmett-Teller method (Tristar II 3020 Micromeritics system). UV-vis absorption spectra were recorded on a PerkinElmer LAMBDA 950 UV-vis spectrophotometer. Electrical conductivities were measured using a four-point probe station (Keithley 2400, Tektronix).

Li-S cell assembly and measurements. S@host composites (S@u-NCSe; S@b-NCSe; S@Super P), Super P and PVDF binder (weight ratio = 8:1:1) were dispersed in N-methyl pyrrolidone (NMP, 99.5%, Acros Organics) to form a slurry which was coated on aluminum foils and dried at 60 °C overnight. The coated aluminum foil was then punched into small disks with a diameter of 12.0 mm. Sulfur loading was about 1.0-1.1 mg cm⁻². High-loading tests were applied using 3.2 mg cm⁻² of sulfur. Electrochemical measurements were conducted in standard 2032 coin-type cells. In LSBs assemblies, lithium foils were used as counter electrode and Celgard 2400 membranes as separators. The electrolyte used was 1.0 M lithium bis(trifluoromethanesulfonyl)imide (LiTFSI) (99%, Acros Organics) dissolved in a mixture of 1,3-dioxolane (DOL, 99.5%, Alfa Aesar) and 1,2-dimethoxy ethane (DME, 99%, Honeywell) (v/v = 1/1) and containing 0.2 M of LiNO₃ (99.98%, Alfa Aesar). For each coin cell, 20 μL of electrolyte was used, high-loaded coin cells added 45 μL . The cells were

galvanostatically cycled within a voltage range of 1.7-2.8 V using a Neware BTS4008 battery tester at different C rates. Cyclic voltammetry (CV) measurements were performed on a battery tester BCS-810 from Bio Logic at a scan rate of 0.1-0.4 mV s⁻¹ and electrochemical impedance spectroscopy (EIS) tests were performed using a sinusoidal voltage with amplitude of 10 mV in the frequency range 100 kHz to 10 mHz.

Preparation of Li₂S_x (like Li₂S₄, Li₂S₆, Li₂S₈, x=4, 6 or 8) solutions for adsorption test and kinetic study. Sulfur and Li₂S (99.9%, Alfa Aesar) in the molar ratio x-1:1 were added to appropriate amounts of DME and DOL (volume ratio of 1:1) under vigorous magnetic stirring overnight until a dark brown solution was formed. 20 mg of Super P, b-NCSe or u-NCSe were poured into 3.0 mL 10 mM Li₂S₄ solution, respectively, and mixtures stirred for homogenization overnight.

Symmetric cell assembly and measurements. Electrodes for symmetric cells were fabricated in the same way as electrodes for LSBs. Two pieces of the same electrode (average loading about 0.5 mg cm⁻²) were used as identical working and counter electrodes with 40 μL of electrolyte containing 0.5 mol L⁻¹ Li₂S₆ and 1 mol L⁻¹ LiTFSI dissolved in DOL/DME (v/v = 1/1). For comparison, symmetric cells with electrolyte 1 mol L⁻¹ LiTFSI dissolved in DOL/DME (v/v = 1/1) were also assembled and tested. In all cases, CV measurements were performed at scan rate of 40 mV s⁻¹.

Measurement of nucleation and dissolution of Li₂S.

The nucleation and dissolution of Li₂S were tested in 2032 coin cells, where 1 mg of u-NCSe or Super P loaded on the carbon papers was applied as work electrode, Li foil worked as the counter electrode, 20 μL of 0.25 M Li₂S₈ dissolved in DOL/DME (v/v=1:1) solution with 1.0 M LiTFSI was used as catholyte, and 20 μL of 1.0 M LiTFSI in DOL/DME (v/v=1:1) solution as anolyte. The cells were held at 2.19 V for 2 h to reduce higher order LiPS to Li₂S₄. And then held them at potential of 2.05 V until current decreased to 10⁻² mA for Li₂S nucleation and growth. In order to analyze the Li₂S dissolution, fresh cells were first discharged at a current of 0.10 mA to 1.80 V, and subsequently discharged at 0.01 mA to 1.80 V for full transformation of S species into solid Li₂S. After this discharge, cells were

potentiostatically charged at 2.40 V for the dissolution of Li₂S into LiPS until charge current was below 10⁻⁵ A.

Theoretical Computation. First-principle calculations were performed by the density functional theory (DFT) using the Vienna Ab-initio Simulation Package (VASP) package. The generalized gradient approximation (GGA) with the Perdew-Burke-Ernzerhof (PBE) functional were used to describe the electronic exchange and correlation effects. Uniform G-centered k-points meshes with a resolution of $2\pi \cdot 0.04 \text{ \AA}^{-1}$ and Methfessel-Paxton electronic smearing were adopted for the integration in the Brillouin zone for geometric optimization. The simulation was run with a cutoff energy of 500 eV throughout the computations.^[28] These settings ensure convergence of the total energies to within 1 meV per atom. Structure relaxation proceeded until all forces on atoms were less than 1 meV \AA^{-1} and the total stress tensor was within 0.01 GPa of the target value.^[29]

In order to optimize the stable configuration of Co₂NiSe₄ surface and the adsorbate Li-S molecules, a vacuum region of 15 \AA was also applied in the direction perpendicular to the (001) and (110) surfaces. The adsorption energy, $E_{(\text{ad})}$, was calculated by:

$$E_{(\text{ad})} = E_{(\text{Co}_2\text{NiSe}_4 + \text{Li/S})} - E_{(\text{Co}_2\text{NiSe}_4)} - E_{(\text{Li/S})}$$

where $E_{(\text{Li/S})}$ is the ground state energy of the free Hg atom in a (10 \AA) supercell; $E_{(\text{Co}_2\text{NiSe}_4)}$ is the total energies of the free Co₂NiSe₄ (001) and (110) surfaces, and $E_{(\text{Co}_2\text{NiSe}_4 + \text{Li/S})}$ is the total energy of the Li-S molecules being adsorbed on the Co₂NiSe₄ (001) and (110) surfaces in the optimized system.

Cell cytotoxicity evaluation. Cell cytotoxicity evaluation of 10% S@u-NCSe composite was conducted by 3-(4,5-dimethyl-2-thiazolyl)-2,5-diphenyl-2-H-tetrazolium bromide (MTT) assay with HepG2 cells.^[30] Firstly, 100 μL of HepG2 cells were seeded in a 96-well plates (1×10^4) and cultured at 37 °C for 24 h. Subsequently, the cells were treated with 100 μL of fresh medium containing different concentrations of 10% S@u-NCSe composite ranged from 0.01 $\mu\text{g mL}^{-1}$ to 1000 $\mu\text{g mL}^{-1}$. The medium was removed and the cells were washed several times after cultured 6 h, 24 h and 48 h. Then, cells were culture for 2 h at 37°C with 100 μL MTT solution (10% 5 mg mL^{-1} MTT with 90% medium). Finally, before determination at a

wavelength of 590 nm, cells were dissolved with 100 μ L dimethyl sulfoxide for 10 min after MTT solution removed. Cell viability (%) was measured according to following equation:

$$\text{Cell viability(\%)} = \frac{At}{Ac} \times 100\%$$

Where, At (a.u.) was the absorbance of S@u-NCSe treated cells, Ac (a.u.) was the absorbance of control. Regard of the control sample, we used HepG2 cells without S@u-NCSe treatment.

2.4 Results and Discussion

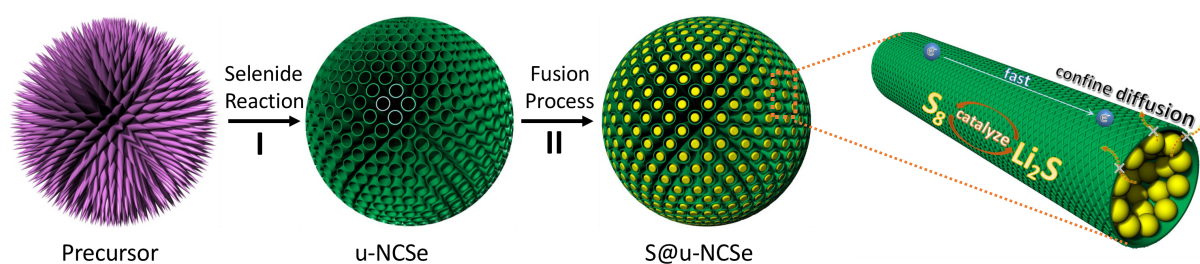


Figure 1. Schematic illustration of the fabrication process of S@u-NCSe composites as cathode for LSBs.

The synthesis strategy to produce S@u-NCSe is schematically shown in **Figure 1** (details can be obtained in the experimental section). u-NCSe was produced using two hydrothermal reaction steps.^[7,31] In the first step, $\text{Ni}_{0.33}\text{Co}_{0.67}(\text{CO}_3)_{0.5}\text{OH}$ urchin-like particles having an average diameter of 8-10 μm and containing solid nanoneedles of 200 nm diameter were produced (**Figure 2** and 3a).^[31] In a second step, such precursor nanostructures were selenized to u-NCSe (Figure 3b and 3c), which crystallized in the NiCo_2Se_4 phase, as indicated by XRD (JCPDS No. 81-4821) and HRTEM characterization (Figure 3e and 3h).^[27] u-NCSe displayed hollow tubular structures as observed from SEM and TEM micrographs (Figure 3c and 3d). The hollow structure was originated from the differential diffusivity of the metals and selenium through the growing NiCo_2Se_4 shell, *via* the nanoscale Kirkendall effect.^[32,33] The surface of the u-NCSe nanotubes is very rough, which translates into high effective surface areas and provides additional sites for electrochemical reactions as compared to the bulk counterpart (b-NCSe, **Figure 4**). Within the experimental error, energy dispersive spectroscopy (EDS) and electron energy loss spectroscopy (EELS) elemental maps showed

the relative atomic content of Ni, Co and Se to match well with stoichiometric NiCo_2Se_4 , with the three elements homogeneously distributed within u-NCSe (Figure 3f and 3g).

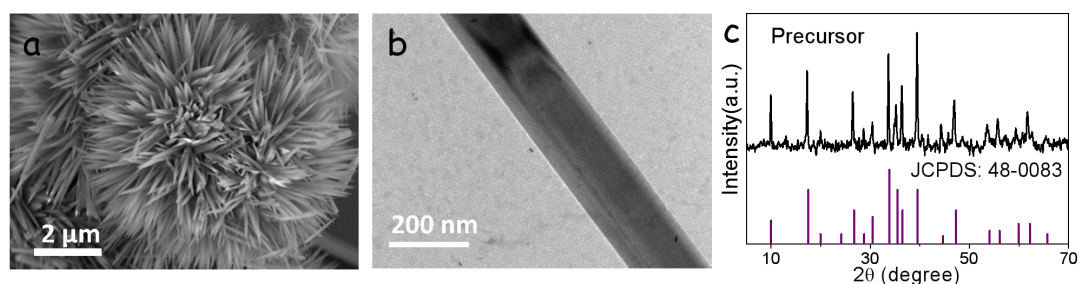


Figure 2. (a) FESEM, (b) TEM images and (c) XRD pattern of as-prepared precursor. Diffraction peaks are indexed to the JCPDS card 48-0083 corresponding to the phase $\text{Co}(\text{CO}_3)_{0.5}(\text{OH}) \cdot 0.11\text{H}_2\text{O}$

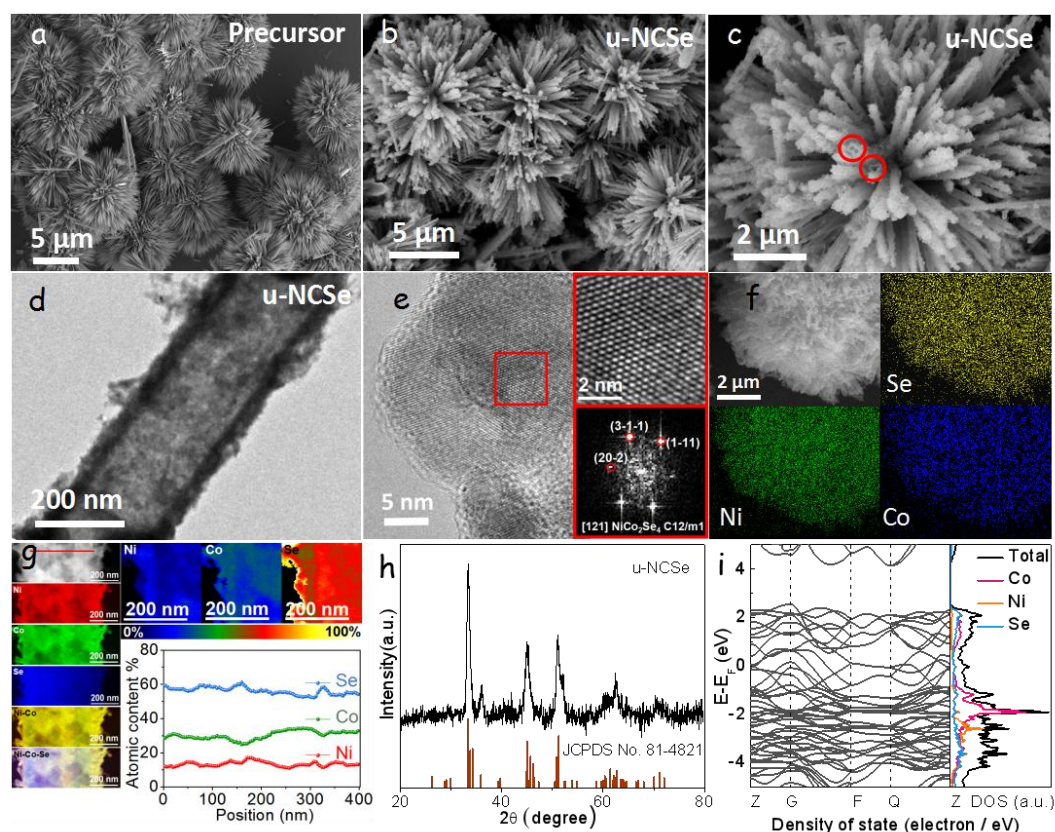


Figure 3. (a) FESEM image of urchin shaped precursor. (b, c) FESEM images and (d) TEM image of u-NCSe. (e) HRTEM image of u-NCSe and inset are images corresponding to FFT spectrum, which indicate that the material crystallizes in the monoclinic NiCo_2Se_4 phase, as visualized along the [121] direction. (f) EDX elemental mapping of Ni, Co, and Se elements collected from the selected area. (g) HAADF image and EELS chemical composition maps obtained from the STEM micrograph. Individual Ni L_{2,3}-edges at 855 eV (red), Co L_{2,3}-edges at 779 eV (green) and Se L_{2,3}-edges at 1436 eV (blue) as well as composites of Ni-Co and Ni-Co-Se (Left) are shown which give information of the relative compositions of

Ni, Co and Se in the elemental mapping. The scale bars for both panels (Ni, Co and Se) are the same. (right) Compositional line profile for Ni, Co and Se recorded along the red line (from left to right) in the STEM images. (h) XRD pattern of u-NCSe. (i) Band structure and density of state calculations for the NiCo₂Se₄ phase.

X-ray photoelectron spectroscopy (XPS) spectra of the samples exposed to air are shown in **Figure 5**. Ni 2p and Co 2p spectra display two pairs of spin-orbit doublets, 2p_{3/2} and 2p_{1/2}, and two shake-up satellite peaks (marked “Sat.”).^[34] In the Ni 2p spectra (Figure 5 a), the peaks located at 853.6 eV (Ni 2p_{3/2}) and 871 eV (Ni 2p_{1/2}) are assigned to Ni²⁺, and the peaks at 856.3 eV (Ni 2p_{3/2}) and 874.2 eV (Ni 2p_{1/2}) to Ni³⁺.^[31] Similarly, in the Co 2p spectra (Figure 5 b), the peaks located at 778.9 eV (Co 2p_{3/2}) and 793.9 eV (Co 2p_{1/2}) are related to Co³⁺ and those at 781.2 eV (Co 2p_{3/2}) and 797.5 eV (Co 2p_{1/2}) to Co²⁺.^[31] Se 3d peaks are located at 59.3 (Se 3d_{3/2}) and 54.8 eV (Se 3d_{5/2}) in agreement with Se²⁻ in a metal selenide environment (Figure 5c).^[35] The XPS spectra show the presence of occupied states at the Fermi level as it corresponds to a metal or a highly degenerated semiconductor (Figure 5d). Additionally, the calculated band structure and density of states of NCSe showed no gap of states at the Fermi level, demonstrating its metallic character (Figure 3i).^[27]

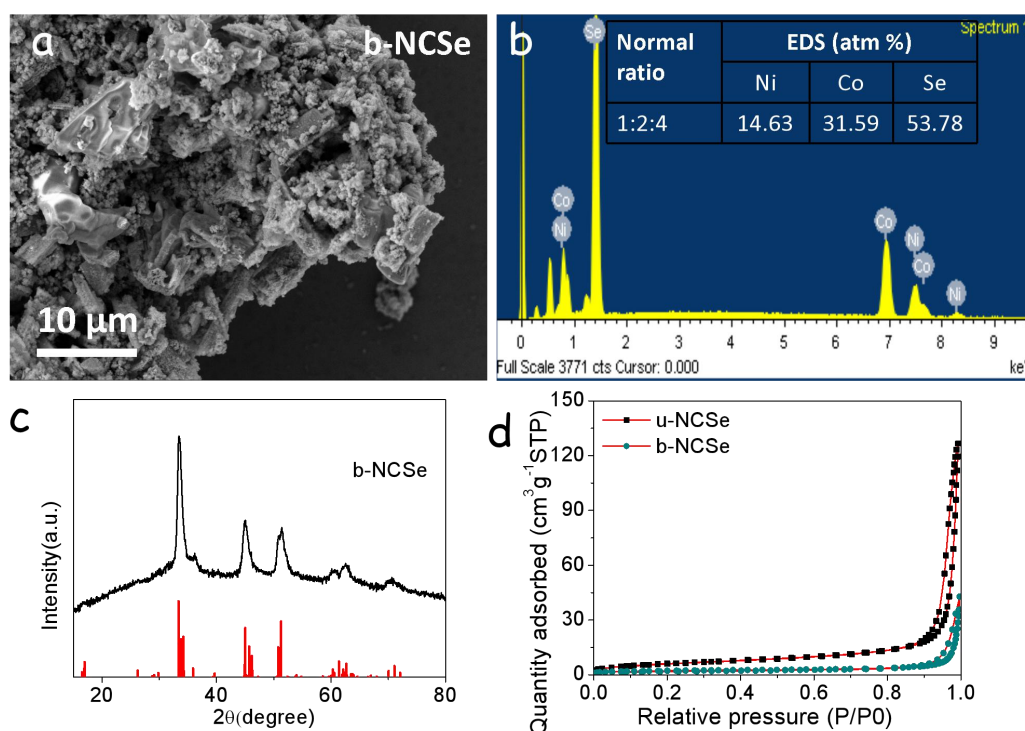


Figure 4. (a) FESEM image, (b) EDS results and (c) XRD pattern of b-NCSe (d) The N₂ adsorption-desorption isotherms of u-NCSe and b-NCSe. Calculated specific surface areas were 22.4 m² g⁻¹ and 7.8 m² g⁻¹ for u-NCSe and b-NCSe, respectively.

Sulfur was introduced within u-NCSe by a melt-diffusion process (see experimental section for details). The product or S@u-NCSe morphology resembles the original urchin-like structure of u-NCSe (**Figure 6a** and **6b**), but with the hollow structure partially filled with sulfur. Attempts to completely fill the tubes with sulfur were not considered since we believe that remaining internal voids in the porous structure are advantageous to accommodate the volumetric change during the charge/discharge process and trap polysulfides, favoring the cycling stability.^[36] XRD analysis demonstrates the presence of crystalline cubic sulfur (JCPDS No. 08-0247) within the S@u-NCSe nanocomposite (**Figure 6c**) and the retention of the NiCo₂Se₄ crystal structure.^[7] S@u-NCSe contains ca. 70 wt.% of sulfur as measured by thermogravimetric analysis (TGA, **Figure 6d**). In addition, with the incorporation of sulfur, the value of Brunauer-Emmett-Teller (BET) specific surface area reduced from 22.4 m² g⁻¹ (u-NCSe) to 1.7 m² g⁻¹ (S@u-NCSe), and the overall pore volume decreased from 0.20 cm³ g⁻¹ to 0.017 cm³ g⁻¹, indicating the successful filling of the u-NCSe porous structure by S (**Figure 7**). Four-point probe method was applied to obtain electrical conductivities of the host materials before and after sulfur fusion (**Figure 8**). u-NCSe and b-NCSe exhibited relatively high electrical conductivities, 287.7 and 295.1 S cm⁻¹, respectively, well above that of Super P (9.5 S cm⁻¹).^[37] After fusion with sulfur, S@u-NCSe showed electrical conductivities up to of 24.4 S cm⁻¹, well above that of S@b-NCSe (16.9 S cm⁻¹) and nearly six-fold above that of S@Super P (3.9 S cm⁻¹). The higher electrical conductivity of S@u-NCSe compared to S@b-NCSe can be explained by the hollow tubular nanostructure, which allows storing a large amount of sulfur but partially conserving a network of avenues for charge transport.

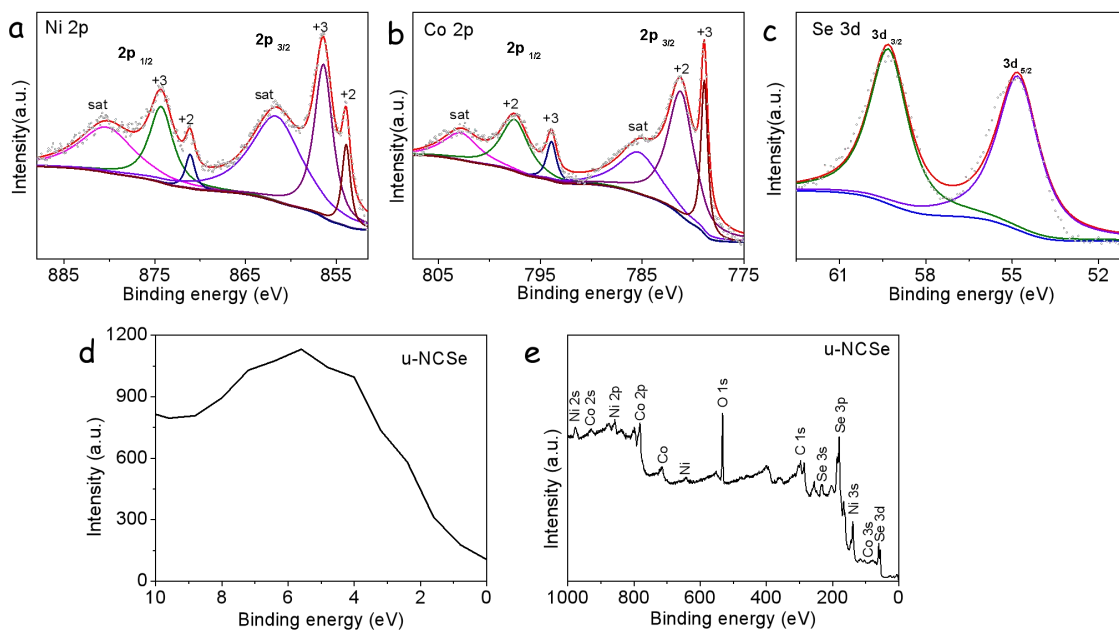


Figure 5. XPS spectra of u-NCSe, (a-c) Ni 2p, Co 2p, and Se 3d XPS spectra and (d, e) survey spectrum of u-NCSe.

The material adsorption ability plays a vital role in the confinement of LiPS. We tested this adsorption ability by immersing 20 mg of u-NCSe into a LiPS (\sim Li₂S₄, 10 mM) solution. For comparison the same test was carried out with b-NCSe and also with Super P, a carbon material typically used as an electrode additive. Upon immersion, clear differences in color were observed in as-prepared solutions (**Figure 9a**). This color change was quantitatively followed by UV-vis spectroscopy, monitoring the absorbance intensity in the 400-500 cm⁻¹ region associated to Li₂S₄ (**Figure 9b**).^[38-40] The color of Li₂S₄ solution after the addition of u-NCSe and b-NCSe was much lighter than that of the solution containing Super P, inferring a stronger chemical interaction of LiPS with NCSe.^[41] The color of the solution containing u-NCSe was clearer than that of b-NCSe, most probably due to the much higher surface area of the former. The colors of the solutions with or without addition of Super P were nearly the same, indicating the weak Li₂S₄ adsorption ability of Super P.

XPS analysis confirmed the strong interaction of LiPS with NCSe. **Figure 9c** and **9d** exhibit high-resolution Ni 2p_{3/2} and Co 2p_{3/2} XPS spectra of u-NCSe before and after adsorption test. The last denoted as u-NCSe/Li₂S₄. Compared with the original Ni 2p_{3/2} and Co 2p_{3/2} spectra, electron binding energies in u-NCSe/Li₂S₄ shifted to higher values, indicating the interaction of S with surface Ni and Co.^[42]

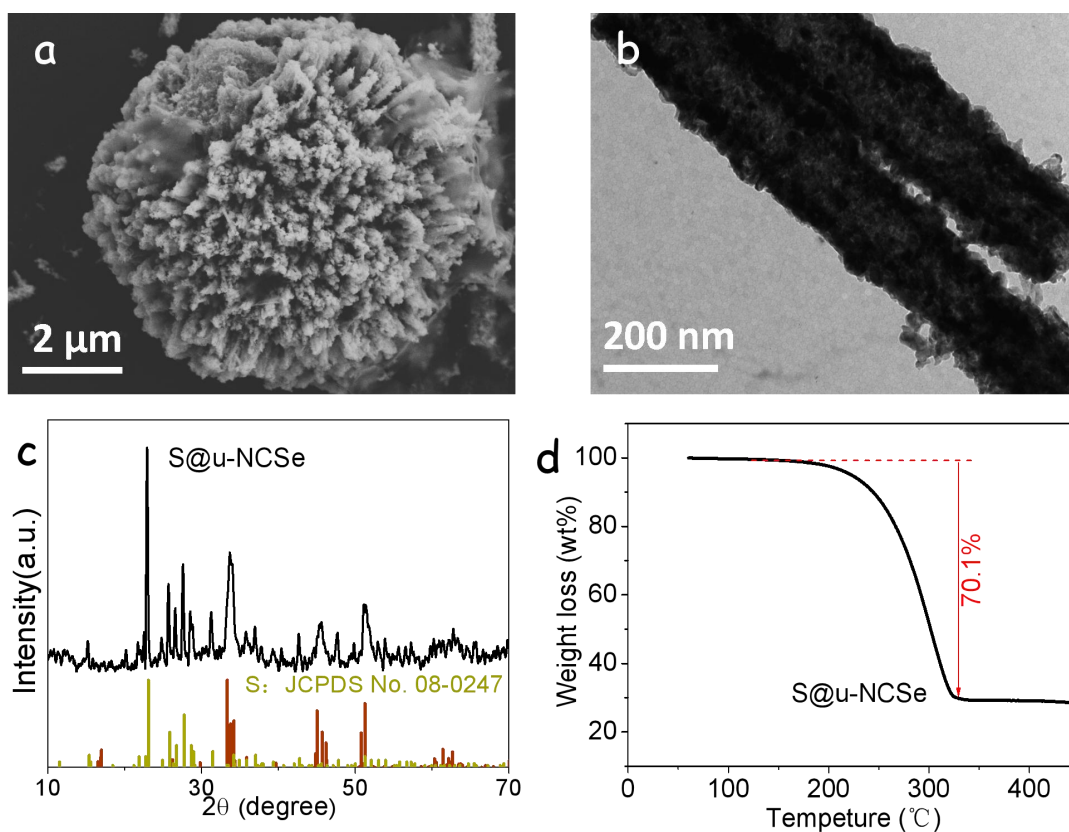


Figure 6. (a) SEM image and (b) TEM image of S@u-NCSe composite. (c) XRD pattern of S@u-NCSe. (d) TGA curve of S@u-NCSe composite measured in N₂, showing a large weight loss % during heating up, corresponding to a sulfur loading ratio of ~70.1 wt.%.

We further verified the strong interaction between NCSe and intermediate LiPS species by density functional theory (DFT). **Figure 10** exhibits the binding energies and atomic structures between LiPS (Li₂S₂, Li₂S₄, Li₂S₆) and the (110) and (001) surfaces of NCSe. Figure 9e displays the relaxed adsorption structure of Li₂S₄ on the two selected NCSe facets. Li preferentially binds to Se sites and S to Ni and Co ions. Compared with the previous reports on graphitic carbon,^[43] the lower sulfur binding energies on the surface of NCSe (Figure 9f) indicates a stronger adsorption of soluble LiPS, which favors an enhanced electrochemical performance. Interestingly, (110) surface shows lower binding energies than (001) surface, demonstrating a higher anchor strength to soluble LiPS of the former.

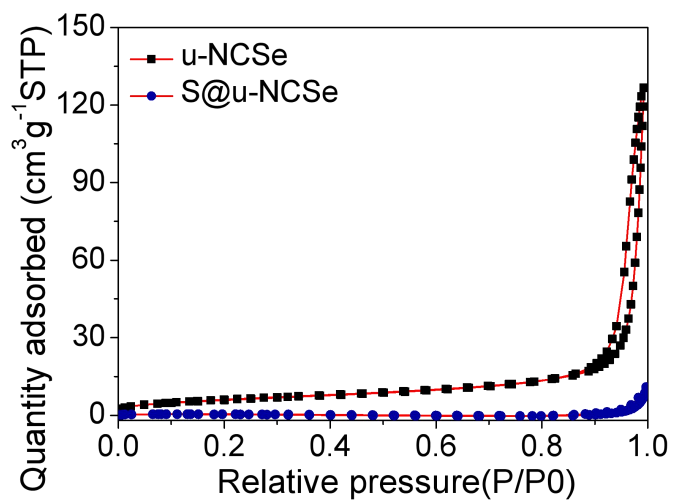


Figure 7. The N₂ adsorption-desorption isotherms of u-NCSe and S@u-NCSe.

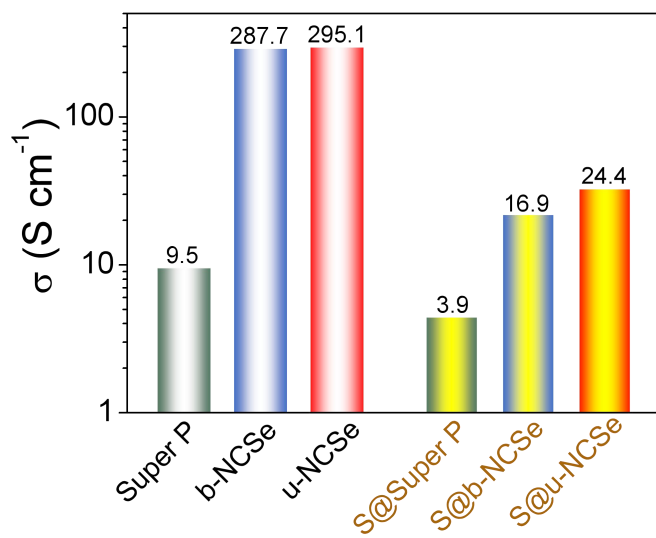


Figure 8. Electrical conductivity of the three hosts tested before and after fusion with sulfur.

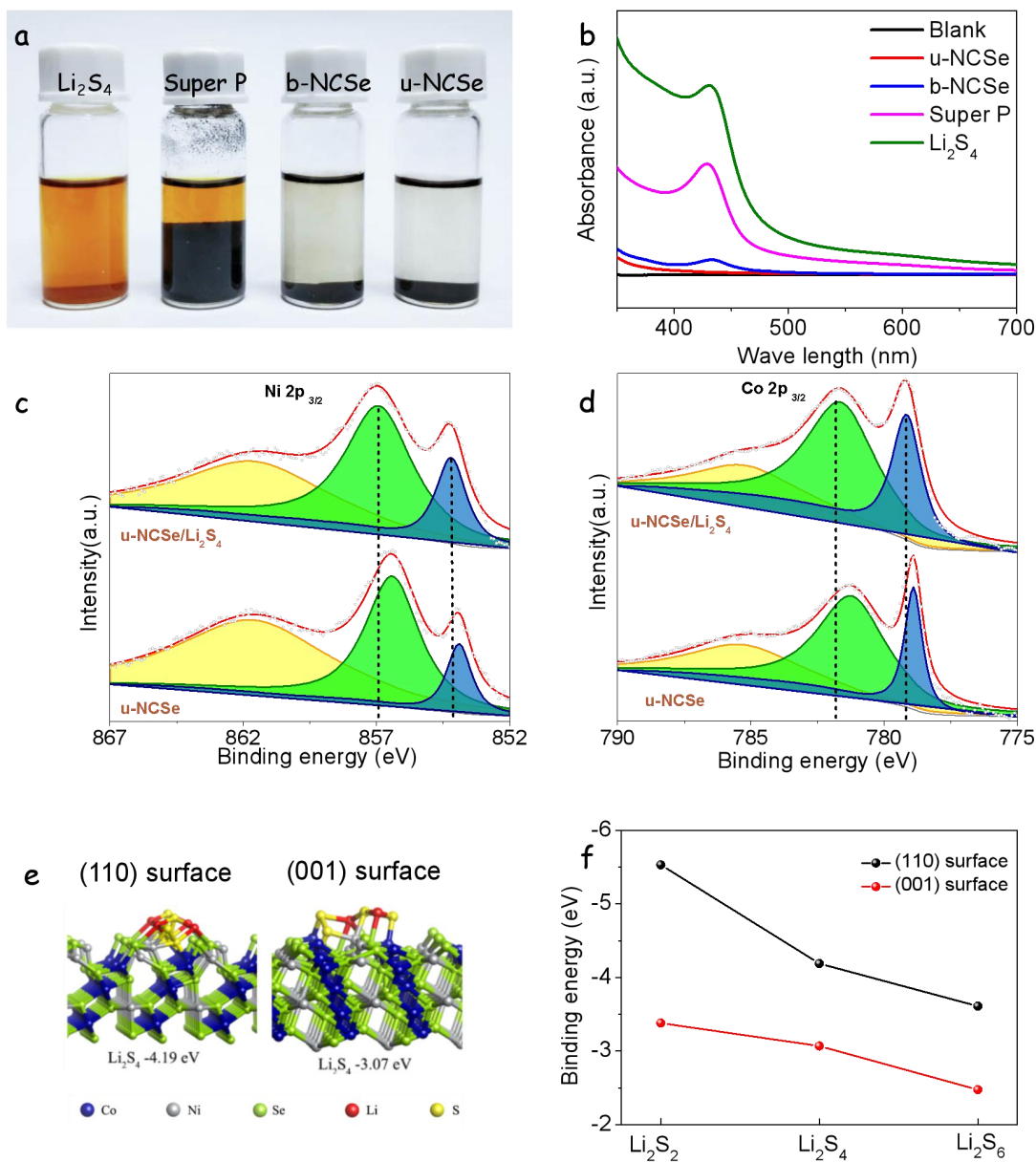


Figure 9. Strong static interaction between u-NCSe and LiPS. (a) Photograph and (b) UV-vis spectra of the polysulfide solution after exposure to the different adsorbers. (c, d) High-resolution XPS spectra of Ni $2p_{3/2}$ and Co $2p_{3/2}$ of u-NCSe before and after adsorption of Li_2S_4 . (e) Relaxed Li_2S_4 -adsorbed structures on both (110) (left) and (001) (right) surfaces of NiCo_2Se_4 calculated with DFT. (f) Calculated binding energy between LiPSs (Li_2S_2 , Li_2S_4 , and Li_2S_6) and NiCo_2Se_4 surfaces.

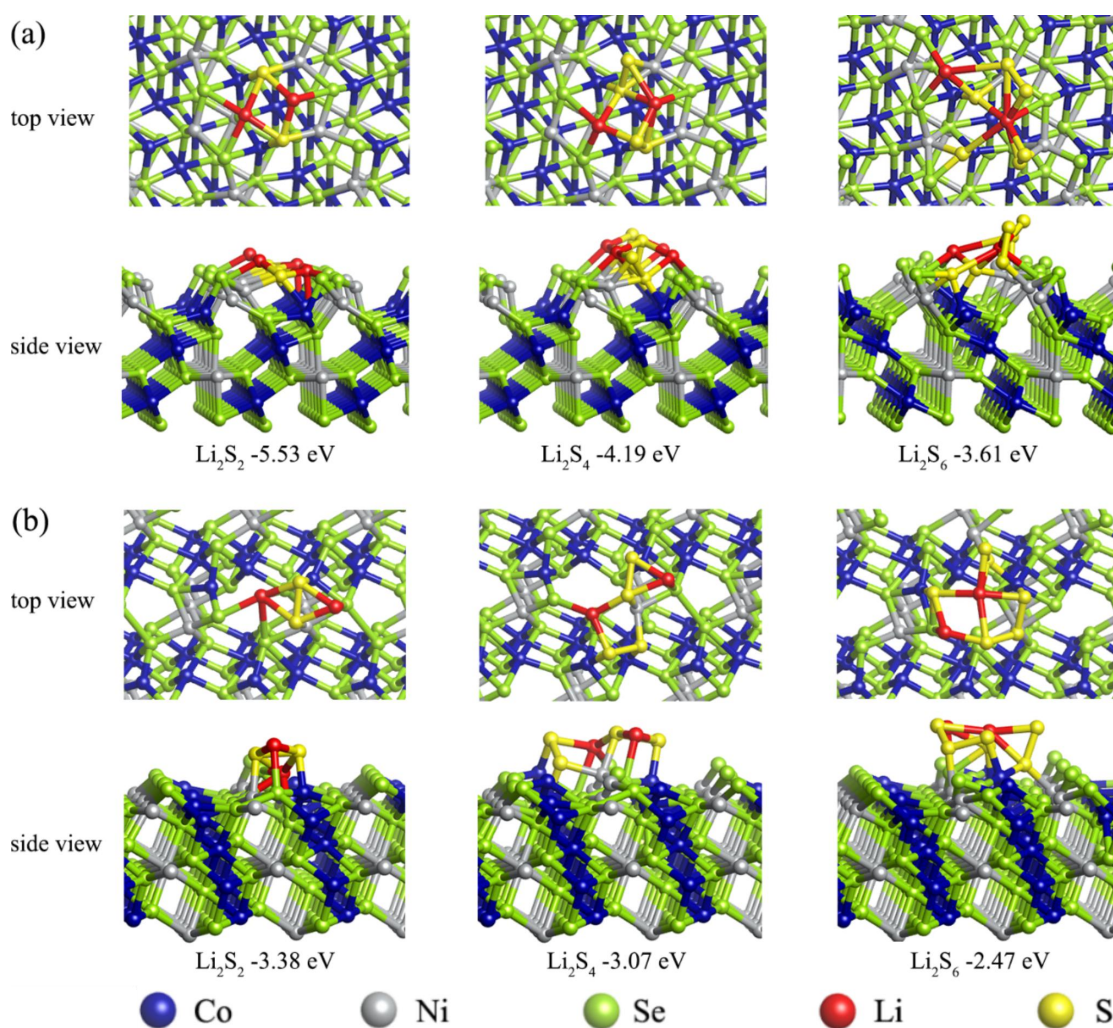


Figure 10. Relaxed LiPS (Li_2S_2 , Li_2S_4 , Li_2S_6) adsorbed structures on both (a) (001) and (b) (110) surfaces of NiCo_2Se_4 calculated with DFT.

To better understand the role of Ni and Co within u-NCSe, we produced and characterized the structural and functional properties of the selenides of the constituent elements. XRD patterns of Ni and Co selenides matched well with NiSe and Co_3Se_4 crystal phases (**Figure 11** e and f). Figure 11 shows the dandelion-like NiSe (and its precursor) and nanoneedle-shaped Co_3Se_4 (and its precursor) produced from the same process used to obtain u-NCSe.^[31] Notice the geometry of the elemental selenides significantly differed from that of u-NCSe, which can be considered a first main effect of combining both elements into a selenide. u-NCSe was characterized by higher electrical conductivities than NiSe and Co_3Se_4 (Figure 11 g), which is explained by a synergistic effect between the two transition metals, Ni and Co, as reported

previously.^[27,44,45] Besides, u-NCSe presented much higher LiPS adsorbabilities as displayed in Figure 11 h. This higher adsorbability can be explained by a higher concentration of defects in the bimetallic selenide, which could act as adsorption/catalytic sites.^[46,47] Overall, the combination of Ni and Co within a single selenide structure influence the morphology of the obtained materials and increased electrical conductivity and LiPS adsorbability.

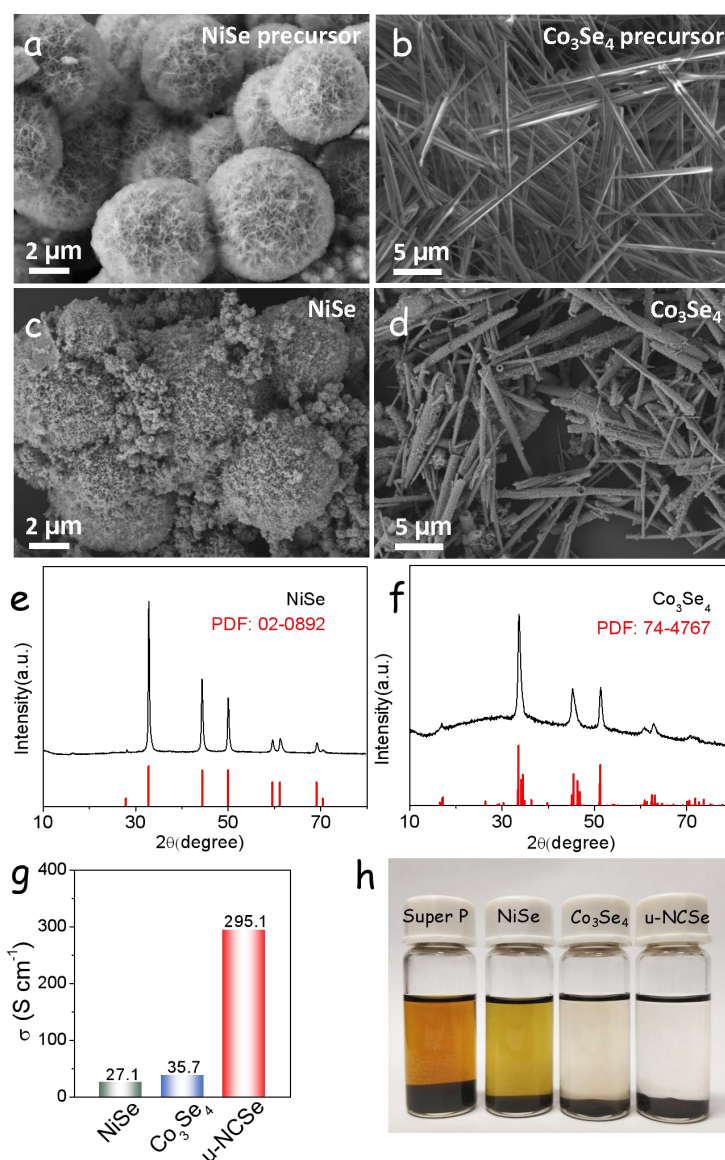


Figure 11. (a, b) SEM images of NiSe and Co₃Se₄ precursors. (c, d) SEM images of NiSe and Co₃Se₄. (e, f) XRD patterns of NiSe and Co₃Se₄. (g) Electrical conductivities of the three materials. (h) Photograph of the polysulfide solution after exposure to the different adsorbers.

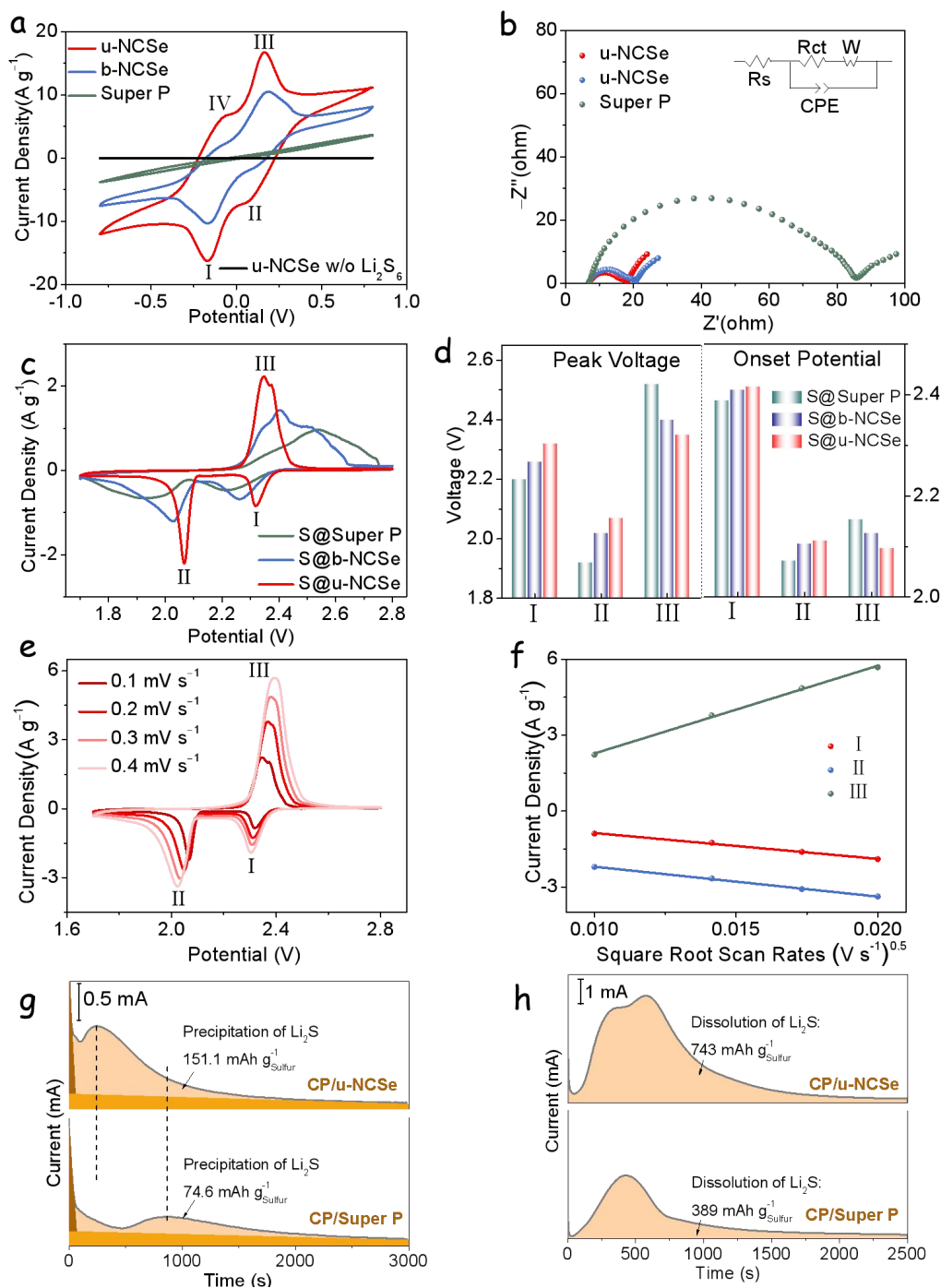
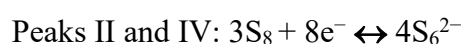
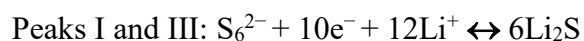


Figure 12. Polysulfide redox activity of u-NCSe (a) CV profiles and (b) EIS spectra of symmetrical cells with different host materials using an electrolyte containing $0.5 \text{ mol L}^{-1} \text{ Li}_2\text{S}_6$ and $1 \text{ mol L}^{-1} \text{ LiTFSI}$ dissolved in DOL/DME ($v/v = 1/1$). (c) CV profiles of Li-S cells with different electrodes. (d) Corresponding peak voltages and onset potentials of asymmetrical Li-S cells obtained from the CV curves. (e) CV curves of S@u-NCSe electrode at various scan rates. (f) Plot of CV peak current for peaks I, II, and III versus the square root of the scan rates. (g) Potentiostatic discharge profile at 2.05 V on different electrodes with Li_2S_8 catholyte. (h) Potentiostatic charge profile at 2.40 V for evaluating dissolution kinetics of Li_2S .

Cyclic voltammetry (CV) tests in symmetric cells using an electrolyte containing 0.5 mol L^{-1} Li_2S_6 and 1 mol L^{-1} LiTFSI dissolved in DOL/DME (v/v = 1/1) were carried out to study the electrocatalytic activity of u-NCSe, b-NCSe and Super P (see details in the experimental section). As illustrated in **Figure 12a**, u-NCSe and b-NCSe electrodes displayed two pairs of reversible redox peaks, named I, II, III, and IV, and associated to the following forward and reverse chemical reactions, respectively:^[16]



On the contrary, the linear-shaped CV of Super P did not show evident redox behavior. u-NCSe-based cells provided the highest peak current densities, indicating higher redox activity and accelerated reaction kinetics during liquid-to-solid ($\text{Li}_2\text{S} \leftrightarrow \text{S}_6^{2-} \leftrightarrow \text{S}_8$) conversion.^{38,39} This higher activity should have associated a reduction of soluble LiPS in the electrolyte, having a positive influence in the cycling stability of u-NCSe-based cells, as shown below. Besides, the CV curve of u-NCSe without Li_2S_6 addition exhibited a nearly rectangular shape (**Figure 13**) that indicated a pure capacitive contribution, thus pointing at Li_2S_6 as the unique electrochemically active specie. Electrochemical impedance spectroscopy (EIS) analysis of symmetric cells showed NCSe samples to be characterized by much lower charge transfer resistance (R_{ct}) than Super P, i.e. a much faster charge transfer at the NCSe-polysulfide interface than at Super P-polysulfide interface (**Figure 12b**).^[16,49]

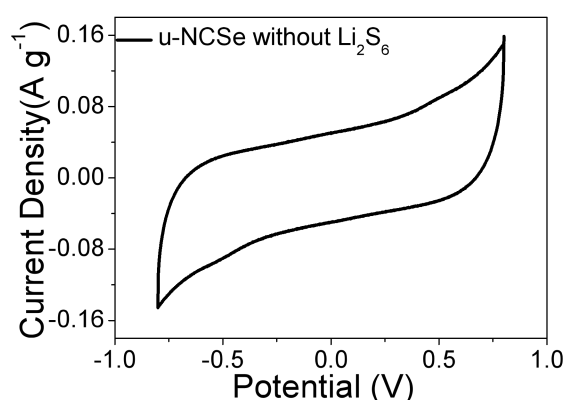


Figure 13. The CV curve of u-NCSe as electrode measured in symmetric coin cell configuration using an electrolyte containing 1 mol L^{-1} LiTFSI dissolved in DOL/DME (v/v = 1/1).

CV curves of Li-S coin cells based on S@Super P, S@b-NCSe and S@u-NCSe containing similar amounts of S (**Figure 14** and 15) were shown in Figure 12c. Two cathodic peaks (peak I and peak II) were identified during reduction of S₈ into long-chain LiPS (Li₂S_x, 4 < x < 8) and their subsequent conversion to insoluble products (Li₂S₂ and Li₂S), respectively. The anodic peak (peak III) accounts for the multistep oxidation conversion of short-chain Li₂S₂/Li₂S to LiPS and eventually to sulfur.^[49] Reduction peaks measured from cells based on S@u-NCSe systematically exhibited the highest potentials (peak I at 2.32 and peak II at 2.07 V) and current densities among the different materials tested (S@b-NCSe at 2.26 and 2.02 V, S@Super P at 2.2 and 1.92V), as shown in Figure 12d. However, the peak voltage and onset potential of oxidation peaks displayed inverse results, indicating that u-NCSe can effectively increase the polysulfides redox reaction kinetics.^[17,50] Besides, the enhanced catalytic activity of u-NCSe was also confirmed by changes in onset potentials, taken at a current density of 10 μA cm⁻² beyond the baseline current (**Figure 16**). As illustrated in Figure 12d, among the three kinds of electrode tested, S@u-NCSe exhibited the highest onset potentials of reduction peaks and the lowest onset potentials of oxidation peaks, evidencing the capacity of u-NCSe to electrocatalytically accelerate the reaction kinetics.^[17,51] CV curves of S@u-NCSe (**Figure 17 a**) almost overlapped in the first cycle, showing no obvious peak shifts or current changes, which indicated good stability and high reversibility.^[52]

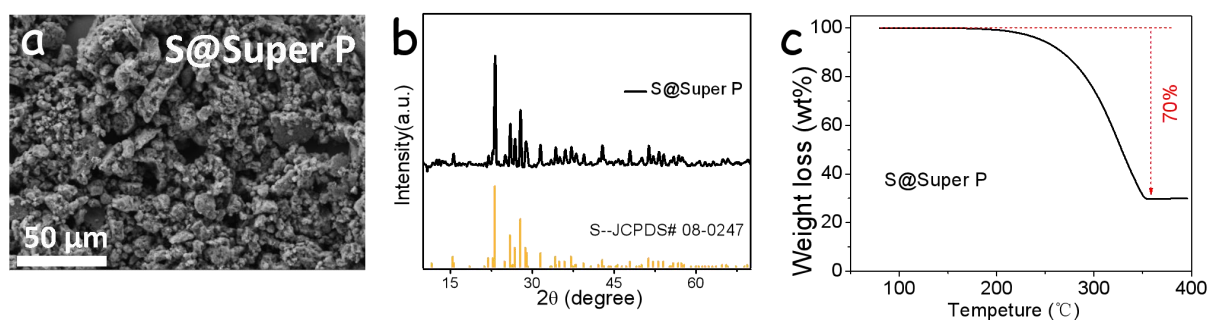


Figure 14. (a) SEM image, (b) XRD pattern and (c) TGA curve of S@Super P.

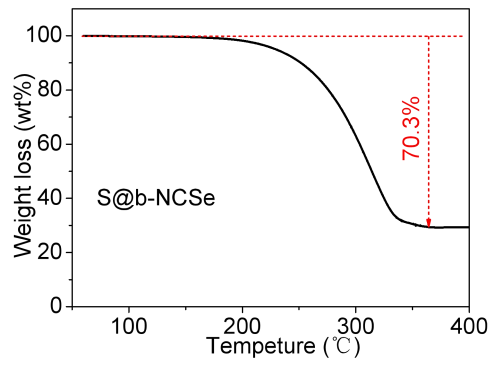


Figure 15. TGA curve measured in N₂ of S@b-NCSe.

The lithium ion diffusion coefficient was evaluated qualitatively from CV tests under different scanning rates, in the range from 0.1 mV s⁻¹ to 0.4 mV s⁻¹ (Figure 12e and 12f). A linear relationship was obtained between the reduction and oxidation peak currents and the square root of scanning rates, demonstrating the reaction to be diffusion-limited. Thus the lithium ion diffusivity can be calculated using the classical Randles-Sevcik equation:^[41,50]

$$I_p = (2.69 \cdot 10^5) n^{1.5} A D_{Li^+}^{0.5} C_{Li^+} \nu^{0.5}$$

where I_p is the peak current, n is the number of charge transfer, A is the geometric electrode area, D_{Li^+} is the lithium ion diffusion coefficient, C_{Li^+} is the concentration of lithium ions in the cathode, and ν is the scan rate. S@u-NCSe electrodes showed the sharpest slopes (**Figure 18**), thus the highest lithium ion diffusivity. We hypothesize this higher lithium ion diffusivity to be related to the relief of the shuttle effect and the improved catalytic activity of the u-NCSe host towards LiPS conversion demonstrated above, avoiding the high viscosity electrolyte caused by LiPS dissolution and the deposition of a thick insulating layer on the electrode.^[41]

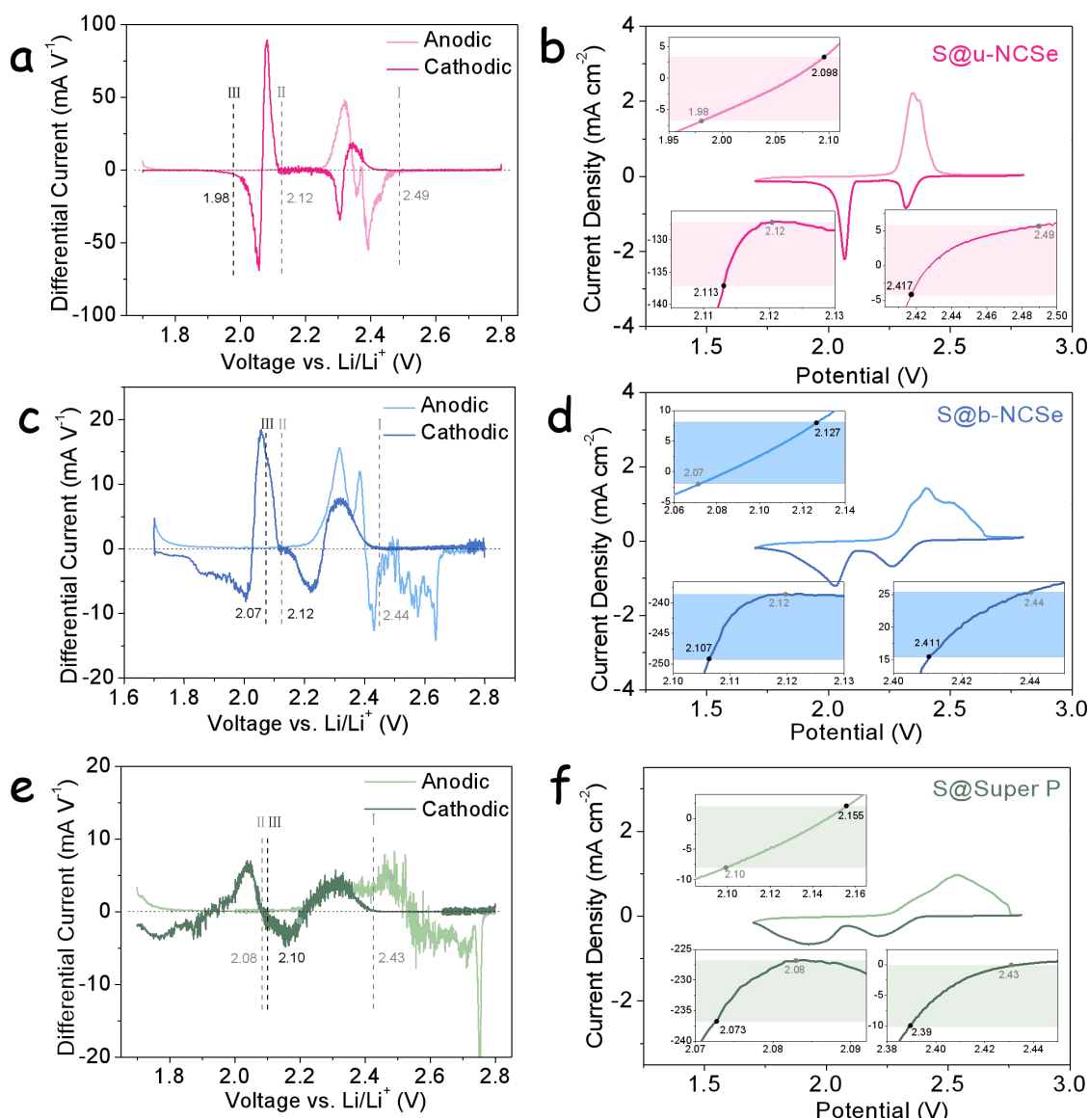


Figure 16. Onset potential for Li-S redox reactions. Differential CV curves of (a) S@u-NCSe, (c) S@b-NCSe and (e) S@Super P. The baseline voltage and current density are defined as the value before the redox peak, where the variation on current density is the smallest, namely $dI/dV = 0$. Baseline voltages are denoted in gray for cathodic peak I, II and in black for anodic peak III, respectively. CV curves and corresponding onset potentials of redox peak I, II, and III (inset): (b) S@u-NCSe, (d) S@b-NCSe and (f) S@Super P. Following a common definition employed in electrocatalysis, the onset potential is determined when the current density is $10 \mu\text{A cm}^{-2}$ beyond the corresponding baseline current density (more specifically, $10 \mu\text{A cm}^{-2}$ more negative than baseline current density for cathodic peaks or $10 \mu\text{A cm}^{-2}$ positive than baseline current density for anodic peaks). As shown in the inset of b, d, and f, the baseline voltages are the same as in a, c, and e while the colored region indicates the gap in current density ($10 \mu\text{A cm}^{-2}$)

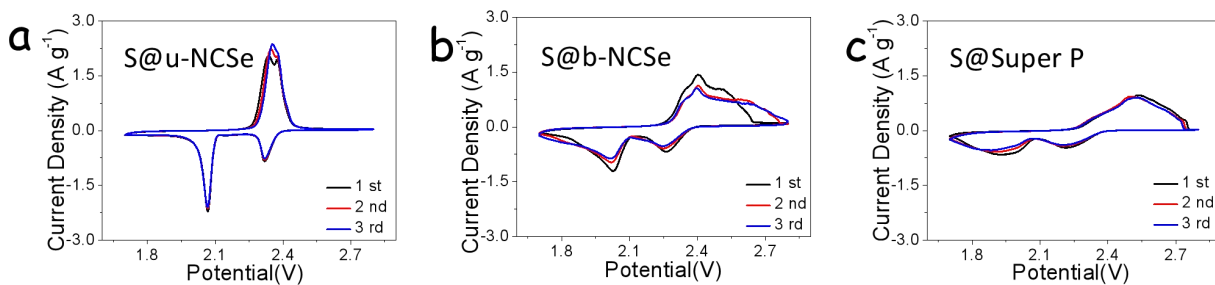


Figure 17. CV curves of (a) S@u-NCSe, (b) S@u-NCSe and (c) S@Super P measured at 0.1 mV s^{-1} in the voltage range 1.7-2.8 V versus Li/Li⁺. Three cycles are shown for each sample.

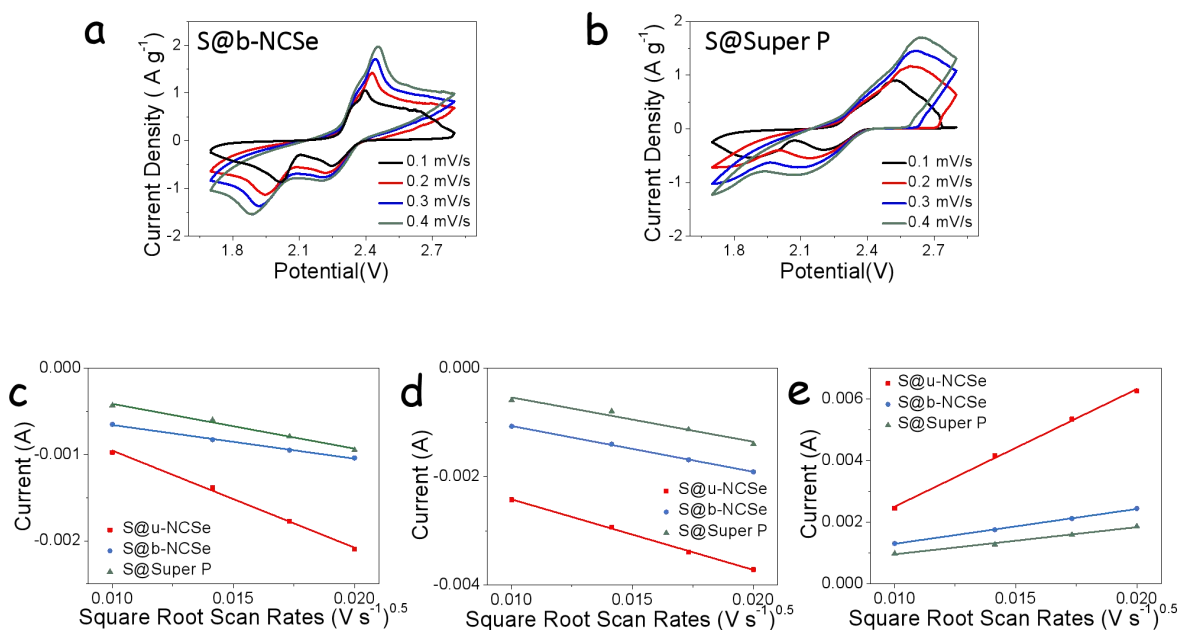


Figure 18. CV curves of (a) S@b-NCSe and (b) S@Super P at different scan rates. Plots of CV peak current for the (c) first cathodic reduction process (peak I: $\text{S}_8 \rightarrow \text{Li}_2\text{S}_x$), (d) second cathodic reduction process (peak II: $\text{Li}_2\text{S}_x \rightarrow \text{Li}_2\text{S}_2/\text{Li}_2\text{S}$), and (e) anodic oxidation process (peak III: $\text{Li}_2\text{S}_2/\text{Li}_2\text{S} \rightarrow \text{S}_8$) versus the square root of the scan rates.

During charge/discharge processes, the overpotential of LSBs was mainly caused by the sluggish kinetics of the oxidation/reduction of insulated solid Li_2S .^[41,42,53] To further demonstrate the catalytic effect of u-NCSe, Li_2S nucleation and dissolution experiments were conducted with a $\text{Li}_2\text{S}_8/\text{DOL-DME}$ solution (details can be found in experimental section).^[54] Figure 12g shows potentiostatic discharge profiles that demonstrate that CP/u-NCSe electrodes displayed faster responsivity toward Li_2S nucleation than CP/Super P. Based on the Faraday's law, CP/u-NCSe electrodes also exhibited larger capacities of Li_2S precipitation

(151.1 mAh g⁻¹) and shorter nucleation and growth times than CP/Super P electrodes (74.6 mAh g⁻¹). These results demonstrate that u-NCSe hosts can significantly reduce overpotential for the initial Li₂S nucleation and promote kinetics for subsequent Li₂S precipitation.^[55-57] A similar strategy was used to study the kinetics of Li₂S dissolution (Figure 12h). Potentiostatic charge curves of CP/u-NCSe exhibited higher current densities than CP/Super P, indicating a lower oxidation overpotential for Li₂S dissolution. Moreover, the calculated dissolution capacity of CP/u-NCSe (743 mAh g⁻¹) was much higher than for CP/Super P electrodes (389 mAh g⁻¹). Overall, these results verified the superior electrocatalytic effect of u-NCSe hosts in reducing polarization and promoting redox kinetics of LiPS conversion reaction.^[42]

Electrochemical performance was further analyzed through galvanostatic charge-discharge tests (**Figure 20**). Charge-discharge curves of S@Super P, S@b-NCSe and S@u-NCSe at 0.1 C showed one charge plateau and two discharge plateaus, consistently with CV. S@u-NCSe showed lower polarization potential ($\Delta E = 152$ mV) than S@b-NCSe ($\Delta E = 205$ mV) and S@Super P electrodes ($\Delta E = 222$ mV).^[17,49] The voltage gap ΔE between the oxidation and the second reduction plateaus introduced a hysteresis in the redox reaction.

Discharge curves showed two plateaus, corresponding to the reduction of sulfur to soluble LiPS ($S_8 \rightarrow S_6^{2-} \rightarrow S_4^{2-}$) and the subsequent conversion to insoluble products ($S_4^{2-} \rightarrow Li_2S_2 \rightarrow Li_2S$). The associated capacity of the two discharge plateaus was defined as Q1 and Q2, respectively (Figure 20a). The ratio between Q2 and Q1 (Q2/Q1) can be interpreted in terms of the catalytic ability for LiPS conversion reaction: sluggish kinetics during the solid \rightarrow liquid \rightarrow solid process and shuttle effect caused by diffusion of soluble LiPS give rise to capacity fading during Q2 stage. Thus, the higher Q2/Q1, the better catalytic ability.^[25,58] As shown in Figure 20b, the Q2/Q1 of S@u-NCSe was 2.8, much higher than that of S@b-NCSe (2.32) and S@Super P (1.88). This high ratio also proved the superior catalytic activity towards polysulfides redox reaction of u-NCSe.

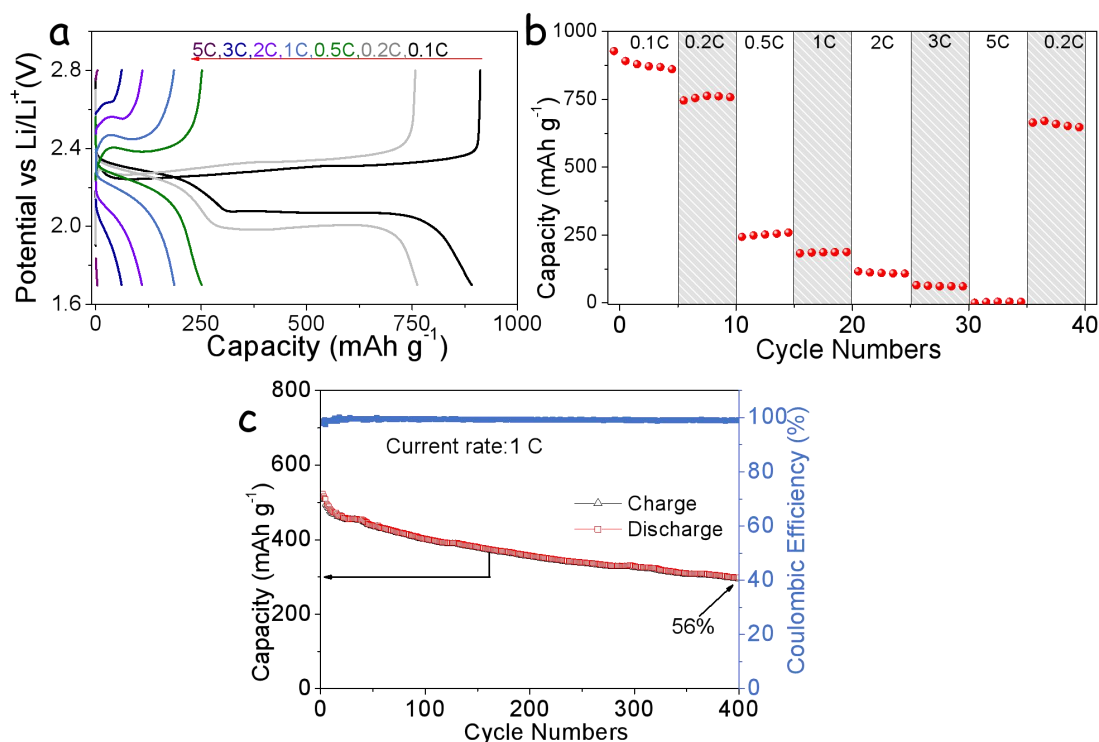


Figure 19. (a, b) Charge/discharge curves and rate capability of S@Super P at various C rates from 0.1 C to 5 C. (c) Stability test at 1 C showing 400 cycles.

Associated with the ability of u-NCSe to accelerate the charge transfer and promote conversion of polysulfides, S@u-NCSe showed the largest capacity among the different electrodes tested. All discharge curves at different current rates exhibited two evident discharge plateaus (Figure 20c). The electrochemical capacity of the cell with S@u-NCSe at various current densities from 0.1 C to 5 C is shown in Figure 20d. The initial discharge capacity was 1403 mAh g⁻¹, and stabilized to an average capacity of 1330 mAh g⁻¹ at 0.1 C. Even at high current rates of 5 C, the capacity still remained stable at 626 mAh g⁻¹, which is significantly higher than the one obtained for S@Super P electrodes (5 mAh g⁻¹, **Figure 19**) under the same conditions. Moreover, when the current rate was turned back to 0.2 C, the average capacity of the cell with S@u-NCSe returned to the same approximate value of 1060 mAh g⁻¹, implying a remarkable electrochemical stability.^[7,59]

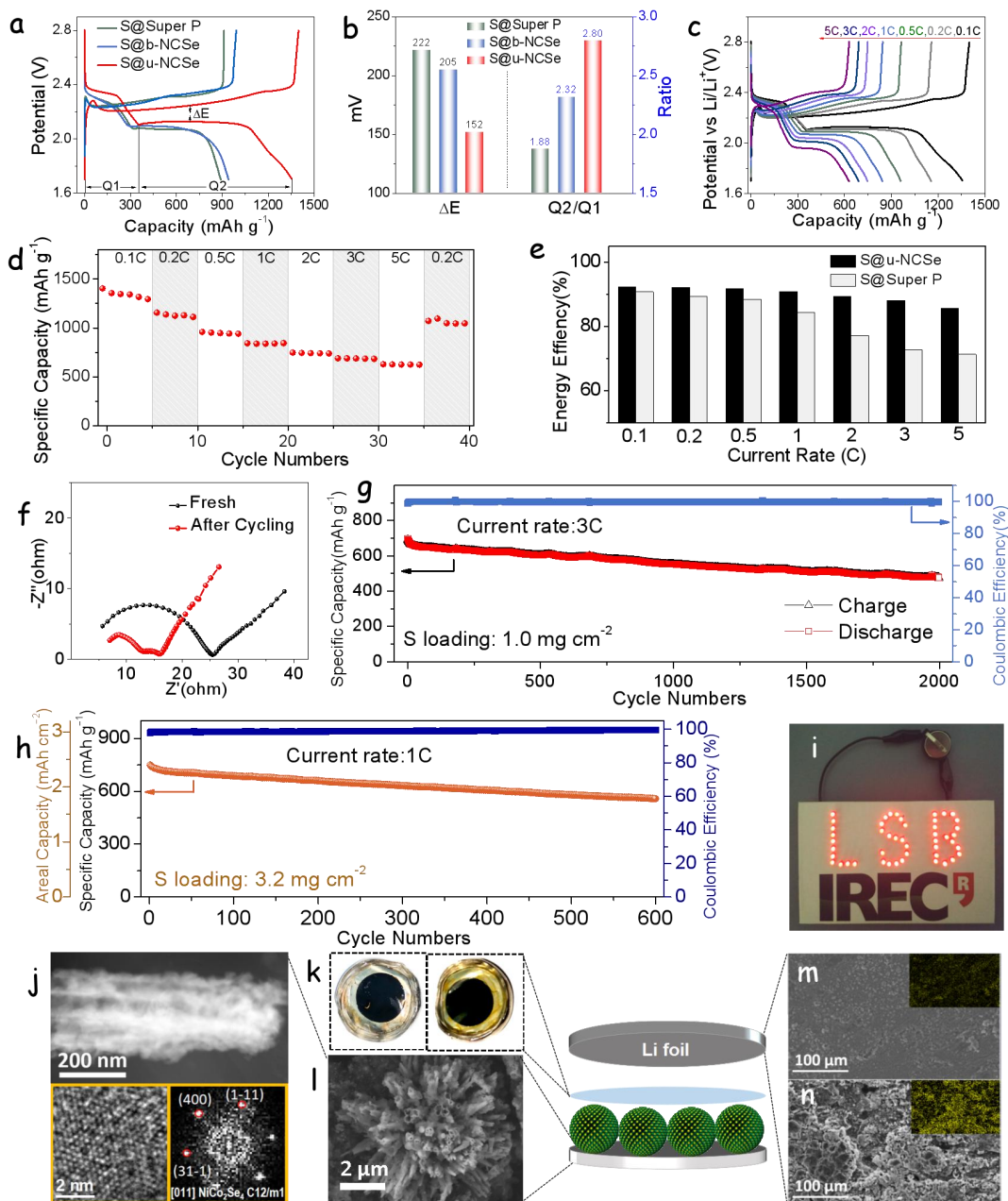


Figure 20. Electrochemical performance of coin cells (a) Charge/discharge curves of different electrodes at current rate of 0.1 C. (b) The value of ΔE and Q2/Q1 obtained from charge/discharge curves. (c, d) Charge/discharge curves and rate capability of the S@u-NCSe composite at various C rates from 0.1 C to 5 C. (e) Energy efficiency at different current densities. (f) EIS spectra of S@u-NCSe electrode before and after 100 cycles at 1 C. (g) capacity retention at 3 C. (h) Cycling performance of electrodes with a 3.2 mg cm⁻² sulfur-loading. (i) Digital photographs of 47 red LED lamps powered by one S@u-NCSe Li-S coin cell. After cycling at 1 C for 200 cycles, (j) HAADF-STEM and HRTEM micrographs of S@u-NCSe and corresponding FFT spectrum. (k) Separators of coin cells with S@u-NCSe

cathode (left) and S@Super P cathode (right), (l) SEM micrograph of S@u-NCSe electrode, and (m, n) surface of lithium foil from S@u-NCSe and S@Super P coin cells. Inset images in (m, n) are EDX mapping images showing sulfur signal.

Energy efficiency, the ratio of energy output/input ($E = \int UI dt$) upon voltage polarization cycles, is a pivotal parameter in large-scale electrochemical energy storage systems.^[17] S@u-NCSe electrodes were characterized with much higher and stable energy efficiencies than S@Super P, especially at high current rates (Figure 20e). As an example, S@u-NCSe retained 85.6% efficiency at 5 C, much higher than the 71.3% for S@Super P. The significant improvement in energy efficiency arised from the lower polarization potential, associated with the exceptional catalytic properties of u-NCSe, as discussed above.

EIS analyses were carried out to gain understanding of the enhanced electrochemical performance of S@u-NCSe electrodes. Figure 20f shows the Nyquist plot obtained from a fresh S@u-NCSe coin cell and the same cell after 100 cycles at 1 C. In the high frequency region, the fresh electrode showed a semicircle corresponding to the charge-transfer resistance, and a linear dependence in the low frequency region that reflected the diffusion of lithium ions into the electrode. After 100 cycles, the impedance plot changed to two poorly-resolved semicircles at high and middle frequencies and a lineal dependence at low frequencies.^[60,61] Apparently, the charge-transfer resistance decreased after cycling, which should be associated with the activation process. Moreover, comparing with the other two types of electrode tested, S@b-NCSe and S@Super P (Figure 21), S@u-NCSe electrodes showed the lowest charge-transfer resistance (R_{ct}).

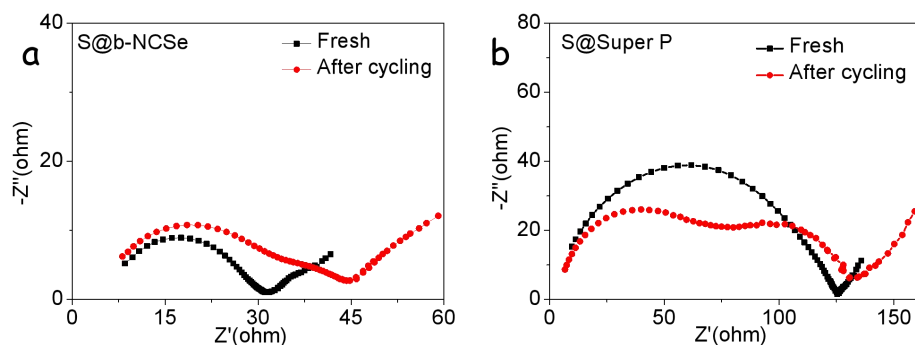


Figure 21. EIS spectra of coin cells (vs Li metal) of S@b-NCSe and S@Super P. Black trace corresponds to fresh cell and red trace to the same cell after cycling at 1 C for 100 cycles.

The long-term cycling stability of the NCSe-based batteries was evaluated at a high current density of 3C (Figure 20g). After 2000 cycles, S@u-NCSe electrodes delivered a capacity of 480 mAh g⁻¹, involving a 0.016% average capacity decay per cycle. Meanwhile, a high and steady Coulombic efficiency above 99.7% was obtained. It is worth mentioning that a negligible capacity was obtained from pure u-NCSe under the same measuring conditions, as shown in **Figure 22**. In contrast, S@Super P electrodes delivered a considerably low capacity after 400 cycles (294 mAh g⁻¹), suffering from a rapid capacity fading (0.11% average capacity decay per cycle), as well as a low Coulombic efficiency (average about 97.1%) at 1 C (Figure 19c).

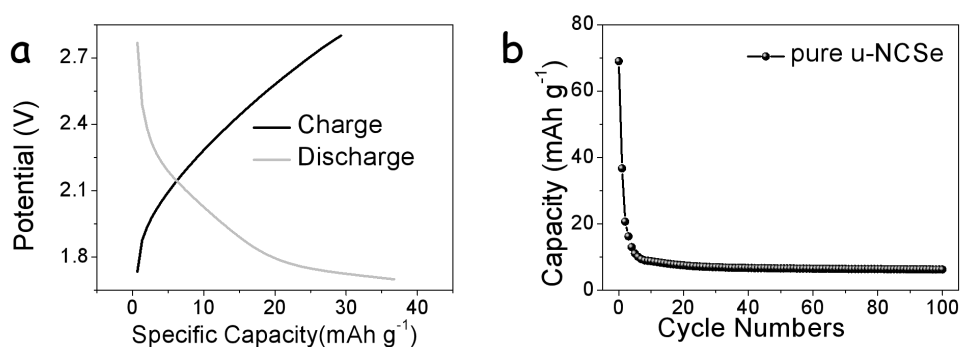


Figure 22. (a, b) Charge/discharge curves and cycling performance of pure u-NCSe tested using same electrochemical conditions as for S@u-NCSe composite.

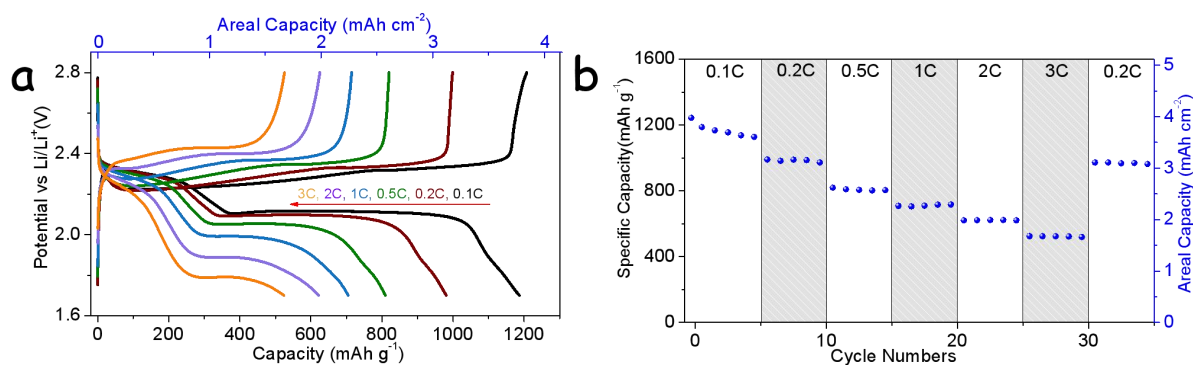


Figure 23. (a, b) Charge/discharge curves and rate capability of S@u-NCSe cathode loaded with 3.2 mg cm⁻² of sulfur at various C rates.

For practical applications, high energy density Li-S batteries require increasing the sulfur loading. Therefore, we studied the performance of S@u-NCSe electrodes at a higher sulfur loading, 3.2 mg cm⁻². **Figure 23a** displays galvanostatic charge-discharge curves of a S@u-NCSe electrode at different current rates. One charge plateau and two discharge plateaus were clearly observed at all current rates, up to 3 C, demonstrating the low polarization between charge and discharge processes. At this high sulfur loading, we measured average reversible capacities of S@u-NCSe electrodes from 1169 mAh g⁻¹ at 0.1 C to 522.8 mAh g⁻¹ at 3 C, which corresponded to areal capacities of 3.65 and 1.63 mAh cm⁻², respectively. This high rate performances even at high sulfur loadings was consistent with the high electrical conductivity and superior catalytic properties of this material. Long term cycling tests at 1 C showed S@u-NCSe electrodes loaded with 3.2 mg cm⁻² of sulfur to maintain 557 mAh g⁻¹ after 600 cycles, *i.e.* a 74.3% capacity retention, involving a 0.043% average capacity decay per cycle. Additionally, a high and steady Coulombic efficiency above 98.8% was consistently obtained (Figure 20h), indicating an excellent cycling stability.

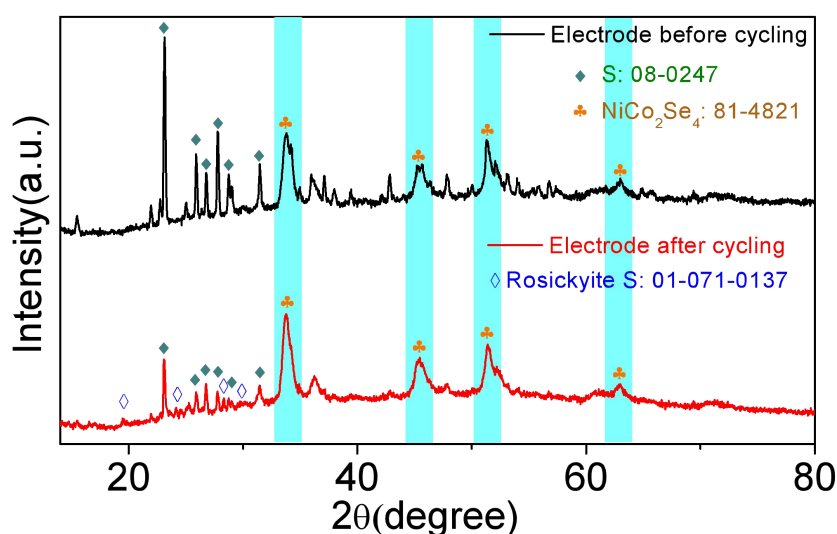


Figure 24. XRD patterns of electrode materials scraped from the Al foil before and after 200 cycles at 1C. After cycling test, the coin cells were charged to 3 V at 0.1 C, and then they were unpacked and washed by DOL/DME solution to remove Li-based salt. After drying and scraping them, XRD analyses of the recovered materials were conducted. It should be noted that the decrease of the S peaks with cycling was not only caused by the LiPS shuttle effect or some loss during washing, but also by possible phase changes of S.^[62–64]

Electrochemical results of S@u-NCSe cathodes for LSBs are compared to other state-of-art TM-based materials in Table 1. To illustrate the favorable electrochemical performance of S@u-NCSe cathodes and the promising practical application of related LSBs, one S@u-NCSe coin cell was used to light up a “LSB”-shaped LED panel containing 47 LEDs (voltage: 2-2.2V), as shown in Figure 20i.

Finally, to further demonstrate that u-NCSe effectively confines LiPS and minimizes the shuttle effect in LSBs, coin cells were disassembled after 200 cycles at 1C to inspect their membrane, cathodic integrity and anodic corrosion. Separators from S@u-NCSe coin cells exhibited much lighter color compared to those from S@Super P (Figure 20k). This observation probed that u-NCSe better confined LiPS, avoiding its diffusion during charge/discharge processes.^[7,69] Consistently with the lighter color of the separator, Li metal foils from S@u-NCSe coin cells showed less corrosion and fewer Li₂S species deposited at their surface than S@Super P coin cells, as shown by SEM and EDS analyses in Figure 20k and 20l.⁴⁸ Thus, the use of u-NCSe as host cathode material greatly relieved the LiPS shuttle effect and minimizes the irreversible losses of active sulfur in LSBs, leading to a superior stability during long term cycling, Figure 20g. Besides, the crystal structure and morphology of S@u-NCSe after cycling was analyzed. HAADF-STEM and SEM micrographs showed the original tubular nanostructure to be conserved after the cycling (Figure 20j and 20l). Additionally, HRTEM and XRD analysis probed the NCSe crystal structure to be conserved (Figure 20j and 24), indicating an excellent stability towards lithiation/delithiation cycles.

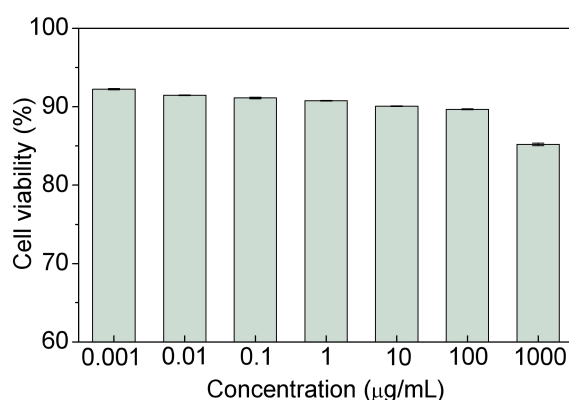


Figure 25. Cell viability with various concentration of S@u-NCSe.

Table 1. Comparison of u-NiCo₂Se₄ electrochemical performance as host cathode for LSBs with state-of-the-art TM-based materials.

Host material	Capacity (mAh g ⁻¹) (low current rate)	Capacity (mAh g ⁻¹) (high current rate)	Cycling stability(%) (times, current rate)	Decay rate (per cycle, %)	S content (wt%)	Reference
NiS@C-HS	1196 (0.1 C)	674 (2 C)	96% (300 cycles, 0.5 C)	0.013%	72%	65
C/Co ₃ O ₄	1036 (0.1 C)	428 (3 C)	64% (500 cycles, 0.5 C)	0.066%	66%	66
C@TiN	1149 (0.2 C)	373 (5 C)	86% (300 cycles, 2 C)	0.049%	70%	55
rGO/VS ₂	1198 (0.2 C)	401 (5 C)	79.6% (1200 cycles, 2 C)	0.017%	64%	24
TiB ₂	1232 (0.2 C)	752 (1 C)	71% (500cycles, 1 C)	0.058%	71%	67
1T-2H MoS ₂ -C	1195 (0.1 C)	677 (2 C)	78.7% (300 cycles, 0.5 C)	0.07%	79.6%	68
δ-MnO ₂	~1200 (0.06 C)	551 (0.6 C)	63% (200cycles, 0.06 C)	0.185%	72.5%	14
NiO-NiCo ₂ O ₄ @C	1063 (0.2 C)	698 (2 C)	70.5% (500cycles, 0.5 C)	0.059%	73%	69
u-NiCo₂Se₄	1330 (0.1C)	626 (5C)	68.6% (2000 cycles, 3C)	0.016%	70.1%	Our work

Biological security is an important parameter for application of energy storage materials. Thus, we analyzed the biocompatibility of S@u-NCSe by measuring through MTT assays the cytotoxicity of this material against the human hepatocellular carcinoma cell line HepG2.^[70] **Figure 25** showed the viability of the cultured cells in the presence of S@u-NCSe at concentrations ranging from 0.001 to 1000 µg/mL. Even though a gradual decreasing trend was observed with increasing concentrations, cell viabilities above 85% even at S@u-NCSe concentration of 1000 µg/mL were obtained, indicating that S@u-NCSe composites have a negligible cytotoxicity.

2.5. Conclusions

In summary, we developed urchin-like NiCo₂Se₄ nanostructures serving as polar host with catalytic effect for cathode of LSBs. Comprehensive kinetic investigations revealed that u-NCSe promoted redox kinetics of LiPS conversion reaction, and effectively decreased polarization during charging and discharging processes. A strong LiPS adsorbability was confirmed simultaneously by experimental results and DFT calculations. u-NCSe were characterized by a beneficial hollow structure to relieve volumetric expansion and a superior electrical conductivity to improve electron transfer. Owing to these excellent qualities, S@u-NCSe delivered impressive rate performance with 1330 and 626 mA h g⁻¹ at 0.1 C and 5 C, respectively. More significantly, a reversible capacity of 480 mA h g⁻¹ was retained after 2000 cycles at 3 C and, even at high sulfur loading (3.2 mg cm⁻²), 557 mA h g⁻¹ capacity was delivered after 600 cycles at 1 C. Additional cytotoxicity measurements demonstrated the u-NCSe biocompatibility. This work provides a strategy for the rational design and development of LSBs with long-life and high-rate performance in addition to insights into transition metal selenides as sulfur host material.

2.6 References

- [1] Z. W. Seh, Y. Sun, Q. Zhang, Y. Cui, *Chem. Soc. Rev.* **2016**, *45*, 5605.
- [2] X. Ji, K. T. Lee, L. F. Nazar, *Nat. Mater.* **2009**, *8*, 500.
- [3] H.-J. Peng, J.-Q. Huang, X.-B. Cheng, Q. Zhang, *Adv. Energy Mater.* **2017**, 1700260.
- [4] A. Manthiram, Y. Fu, S.-H. Chung, C. Zu, Y.-S. Su, *Chem. Rev.* **2014**, *114*, 11751.
- [5] Z. Li, H. B. Wu, X. W. (David) Lou, *Energy Environ. Sci.* **2016**, *9*, 3061.
- [6] J. Zhang, H. Huang, J. Bae, S.-H. Chung, W. Zhang, A. Manthiram, G. Yu, *Small Methods* **2018**, *2*, 1700279.
- [7] C. Dai, J.-M. Lim, M. Wang, L. Hu, Y. Chen, Z. Chen, H. Chen, S.-J. Bao, B. Shen, Y. Li, G. Henkelman, M. Xu, *Adv. Funct. Mater.* **2018**, *28*, 1704443.
- [8] C. Zu, A. Manthiram, *Adv. Energy Mater.* **2013**, *3*, 1008.
- [9] B. Zhang, X. Qin, G. R. Li, X. P. Gao, *Energy Environ. Sci.* **2010**, *3*, 1531.

- [10] J.-Q. Huang, Q. Zhang, S.-M. Zhang, X.-F. Liu, W. Zhu, W.-Z. Qian, F. Wei, *Carbon* **2013**, *58*, 99.
- [11] S. Evers, L. F. Nazar, *Acc. Chem. Res.* **2013**, *46*, 1135.
- [12] H.-J. Peng, G. Zhang, X. Chen, Z.-W. Zhang, W.-T. Xu, J.-Q. Huang, Q. Zhang, *Angew Chem Int Ed* **2016**, 15.
- [13] Z. Wei Seh, W. Li, J. J. Cha, G. Zheng, Y. Yang, M. T. McDowell, P.-C. Hsu, Y. Cui, *Nat. Commun.* **2013**, *4*.
- [14] K. Cao, H. Liu, Y. Li, Y. Wang, L. Jiao, *Energy Storage Mater.* **2017**, *9*, 78.
- [15] B.-Q. Li, S.-Y. Zhang, L. Kong, H.-J. Peng, Q. Zhang, *Adv. Mater.* **2018**, *30*, 1707483.
- [16] H. Lin, L. Yang, X. Jiang, G. Li, T. Zhang, Q. Yao, G. W. Zheng, J. Y. Lee, *Energy Environ. Sci.* **2017**, *10*, 1476.
- [17] Z. Yuan, H.-J. Peng, T.-Z. Hou, J.-Q. Huang, C.-M. Chen, D.-W. Wang, X.-B. Cheng, F. Wei, Q. Zhang, *Nano Lett.* **2016**, *16*, 519.
- [18] D. Liu, C. Zhang, G. Zhou, W. Lv, G. Ling, L. Zhi, Q.-H. Yang, *Adv. Sci.* **2018**, *5*, 1700270.
- [19] R. Lv, J. A. Robinson, R. E. Schaak, D. Sun, Y. Sun, T. E. Mallouk, M. Terrones, *Acc. Chem. Res.* **2015**, *48*, 56.
- [20] Q. H. Wang, K. Kalantar-Zadeh, A. Kis, J. N. Coleman, M. S. Strano, *Nat. Nanotechnol.* **2012**, *7*, 699.
- [21] R. R. Chianelli, G. Berhault, B. Torres, *Catal. Today* **2009**, *147*, 275.
- [22] C. Coughlan, M. Ibáñez, O. Dobrozhan, A. Singh, A. Cabot, K. M. Ryan, *Chem. Rev.* **2017**, *117*, 5865.
- [23] R. R. Chianelli, M. Daage, M. J. Ledoux, In *Advances in Catalysis* (Eds.: Eley, D. D.; Pines, H.; Haag, W. O.), Academic Press, **1994**, pp. 177–232.
- [24] Z. Cheng, Z. Xiao, H. Pan, S. Wang, R. Wang, *Adv. Energy Mater.* **2018**, *8*, 1702337.
- [25] C.-Y. Fan, Y.-P. Zheng, X.-H. Zhang, Y.-H. Shi, S.-Y. Liu, H.-C. Wang, X.-L. Wu, H.-Z. Sun, J.-P. Zhang, *Adv. Energy Mater.* **2018**, *8*, 1703638.
- [26] Z. Fang, L. Peng, Y. Qian, X. Zhang, Y. Xie, J. J. Cha, G. Yu, *J. Am. Chem. Soc.* **2018**, *140*, 5241.

- [27] Z. Fang, L. Peng, H. Lv, Y. Zhu, C. Yan, S. Wang, P. Kalyani, X. Wu, G. Yu, *ACS Nano* **2017**, *11*, 9550.
- [28] A. Travert, H. Nakamura, R. A. van Santen, S. Cristol, J.-F. Paul, E. Payen, *J. Am. Chem. Soc.* **2002**, *124*, 7084.
- [29] C. Tsai, F. Abild-Pedersen, J. K. Nørskov, *Nano Lett.* **2014**, *14*, 1381.
- [30] N. Gou, S. Yuan, J. Lan, C. Gao, A. N. Alshawabkeh, A. Z. Gu, *Environ. Sci. Technol.* **2014**, *48*, 8855.
- [31] X. Qian, H. Li, L. Shao, X. Jiang, L. Hou, *ACS Appl. Mater. Interfaces* **2016**, *8*, 29486.
- [32] M. Ibáñez, J. Fan, W. Li, D. Cadavid, R. Nafria, A. Carrete, A. Cabot, *Chem. Mater.* **2011**, *23*, 3095.
- [33] A. Cabot, M. Ibáñez, P. Guardia, A. P. Alivisatos, *J. Am. Chem. Soc.* **2009**, *131*, 11326.
- [34] Y. Li, L. Xu, M. Jia, L. Cui, J. Gao, X.-J. Jin, *J. Electrochem. Soc.* **2018**, *165*, E303.
- [35] Q. Wang, Y. Ma, Y. Wu, D. Zhang, M. Miao, *ChemSusChem* **2017**, *10*, 1427.
- [36] Z. Li, J. Zhang, B. Y. Guan, X. Wen, *Angew Chem* **2017**, *16*.
- [37] L. Long, X. Jiang, J. Liu, D. Han, M. Xiao, S. Wang, Y. Meng, *RSC Adv.* **2018**, *8*, 4503.
- [38] T. Lei, W. Chen, J. Huang, C. Yan, H. Sun, C. Wang, W. Zhang, Y. Li, J. Xiong, *Adv. Energy Mater.* **2017**, *7*, 1601843.
- [39] J. Song, Z. Yu, M. L. Gordin, D. Wang, *Nano Lett.* **2016**, *16*, 864.
- [40] X. Li, K. Ding, B. Gao, Q. Li, Y. Li, J. Fu, X. Zhang, P. K. Chu, K. Huo, *Nano Energy* **2017**, *40*, 655.
- [41] G. Zhou, H. Tian, Y. Jin, X. Tao, B. Liu, R. Zhang, Z. W. Seh, D. Zhuo, Y. Liu, J. Sun, J. Zhao, C. Zu, D. S. Wu, Q. Zhang, Y. Cui, *Proc. Natl. Acad. Sci.* **2017**, *114*, 840.
- [42] H. Yuan, H.-J. Peng, B.-Q. Li, J. Xie, L. Kong, M. Zhao, X. Chen, J.-Q. Huang, Q. Zhang, *Adv. Energy Mater.* **2018**, 1802768.
- [43] Y. Qiu, W. Li, W. Zhao, G. Li, Y. Hou, M. Liu, L. Zhou, F. Ye, H. Li, Z. Wei, S. Yang, W. Duan, Y. Ye, J. Guo, Y. Zhang, *Nano Lett.* **2014**, *14*, 4821.
- [44] C. Wu, Y. Wei, Q. Lian, C. Cui, W. Wei, L. Chen, C. Li, *Mater. Chem. Front.* **2017**, *1*, 2656.

- [45] C. Xia, H. Liang, J. Zhu, U. Schwingenschlögl, H. N. Alshareef, *Adv. Energy Mater.* **2017**, 7.
- [46] D. Luo, G. Li, Y.-P. Deng, Z. Zhang, J. Li, R. Liang, M. Li, Y. Jiang, W. Zhang, Y. Liu, W. Lei, A. Yu, Z. Chen, *Adv. Energy Mater.* **2019**, 1900228.
- [47] C. Xia, Q. Jiang, C. Zhao, M. N. Hedhili, H. N. Alshareef, *Adv. Mater.* **2016**, 28, 77.
- [48] J. Zhou, X. Liu, L. Zhu, J. Zhou, Y. Guan, L. Chen, S. Niu, J. Cai, D. Sun, Y. Zhu, J. Du, G. Wang, Y. Qian, *Joule* **2018**.
- [49] L. Zhang, X. Chen, F. Wan, Z. Niu, Y. Wang, Q. Zhang, J. Chen, *ACS Nano* **2018**, 12, 9578.
- [50] X. Zhu, W. Zhao, Y. Song, Q. Li, F. Ding, J. Sun, L. Zhang, Z. Liu, *Adv. Energy Mater.* **2018**, 8, 1800201.
- [51] L. Ma, W. Zhang, L. Wang, Y. Hu, G. Zhu, Y. Wang, R. Chen, T. Chen, Z. Tie, J. Liu, Z. Jin, *ACS Nano* **2018**, 12, 4868.
- [52] Z. Li, Q. He, X. Xu, Y. Zhao, X. Liu, C. Zhou, D. Ai, L. Xia, L. Mai, *Adv. Mater.* **2018**, 30, 1804089.
- [53] A. Berger, A. T. S. Freiberg, A. Siebel, R. Thomas, M. U. M. Patel, M. Tromp, H. A. Gasteiger, Y. Gorlin, *J. Electrochem. Soc.* **2018**, 165, A1288.
- [54] F. Y. Fan, Y.-M. Chiang, *J. Electrochem. Soc.* **2017**, 164, A917.
- [55] Y. Wang, R. Zhang, Y. Pang, X. Chen, J. Lang, J. Xu, C. Xiao, H. Li, K. Xi, S. Ding, *Energy Storage Mater.* **2019**, 16, 228.
- [56] F. Y. Fan, W. C. Carter, Y.-M. Chiang, *Adv. Mater.* **2015**, 27, 5203.
- [57] S. Huang, Y. V. Lim, X. Zhang, Y. Wang, Y. Zheng, D. Kong, M. Ding, S. A. Yang, H. Y. Yang, *Nano Energy* **2018**, 51, 340.
- [58] D. Su, M. Cortie, H. Fan, G. Wang, *Adv. Mater.* **2017**, 29, 1700587.
- [59] J. He, Y. Chen, A. Manthiram, *iScience* **2018**, 4, 36.
- [60] Z. Guo, H. Nie, Z. Yang, W. Hua, C. Ruan, D. Chan, M. Ge, X. Chen, S. Huang, *Adv. Sci.* **2018**, 5, 1800026.
- [61] W. Bao, D. Su, W. Zhang, X. Guo, G. Wang, *Adv. Funct. Mater.* **2016**, 26, 8746.
- [62] M. Cuisinier, P.-E. Cabelguen, S. Evers, G. He, M. Kolbeck, A. Garsuch, T. Bolin, M. Balasubramanian, L. F. Nazar, *J. Phys. Chem. Lett.* **2013**, 4, 3227.
- [63] Y. Chen, S. Lu, J. Zhou, X. Wu, W. Qin, O. Ogoke, G. Wu, *J. Mater. Chem. A* **2017**, 5, 102.

- [64] S. Huang, L. Liu, Y. Wang, Y. Shang, L. Zhang, J. Wang, Y. Zheng, O. G. Schmidt, H. Y. Yang, *J. Mater. Chem. A* **2019**, *7*, 6651.
- [65] C. Ye, L. Zhang, C. Guo, D. Li, A. Vasileff, H. Wang, S.-Z. Qiao, *Adv. Funct. Mater.* **2017**, *27*, 1702524.
- [66] F. Ma, J. Liang, T. Wang, X. Chen, Y. Fan, B. Hultman, H. Xie, J. Han, G. Wu, Q. Li, *9*.
- [67] C. Li, X. Liu, L. Zhu, R. Huang, M. Zhao, L. Xu, Y. Qian, *Chem. Mater.* **2018**, *30*, 6969.
- [68] Y. Zhang, Z. Mu, C. Yang, Z. Xu, S. Zhang, X. Zhang, Y. Li, J. Lai, Z. Sun, Y. Yang, Y. Chao, C. Li, X. Ge, W. Yang, S. Guo, *Adv. Funct. Mater.* **2018**, *28*, 1707578.
- [69] L. Hu, C. Dai, H. Liu, Y. Li, B. Shen, Y. Chen, S.-J. Bao, M. Xu, *Adv. Energy Mater.* **2018**, *8*, 1800709.
- [70] A. Dirany, I. Sirés, N. Oturan, A. Özcan, M. A. Oturan, *Environ. Sci. Technol.* **2012**, *46*, 4074.

Chapter 3

Hierarchical Nanoreactor with Multiple Adsorption and Catalytic Sites for Robust Lithium-Sulfur Batteries



3.1 Abstract

Developing high-performance cathode host materials is fundamental to solve the low utilization of sulfur, the sluggish redox kinetics, and the lithium polysulfide (LiPS) shuttle effect in lithium-sulfur batteries (LSBs). Here, a multifunctional Ag/VN@Co/NCNTs nanocomposite with multiple adsorption and catalytic sites within hierarchical nanoreactors is reported as a robust sulfur host for LSB cathodes. In this hierarchical nanoreactors, heterostructured Ag/VN nanorods serve as highly conductive backbone structure and provide internal catalytic and adsorption sites for LiPS conversion. Interconnected nitrogen-doped carbon nanotubes (NCNTs), *in Situ* grown from the Ag/VN surface, greatly improve the overall specific surface area for sulfur dispersion and accommodate volume change in the reaction process. Owing to their high LiPS adsorption ability, outer Co nanoparticles at the top of the NCNTs catch escaped LiPS, thus effectively suppressing the shuttle effect and enhancing kinetics. Benefiting from the multiple adsorption and catalytic sites of the developed hierarchical nanoreactors, Ag/VN@Co/NCNTs@S cathodes display outstanding electrochemical performances, including a superior rate performance of 609.7 mAh g⁻¹ at 4 C and a good stability with a capacity decay of 0.018% per cycle after 2000 cycles at 2 C. These

properties demonstrate the exceptional potential of Ag/VN@Co/NCNTs@S nanocomposites and approach LSBs closer to their real-world application.

3.2 Introduction

The lithium-sulfur battery (LSB) is considered to be a promising alternative to lithium-ion battery (LIB), as it offers advantages in terms of high energy density (2600 Wh kg^{-1}), low raw material cost, and environmental friendliness.¹⁻³ However, still huge challenges need to be overcome to bring LSBs to the market: First, the insulating properties of sulfur and lithium sulfide has associated an infra-utilization of the active material.⁴ Second, the drastic volumetric change ($\sim 80\%$) during charge/discharge processes rapidly damages the electrode structure.⁵ Third, the dissolution and diffusion of lithium polysulfides (LiPS) in the electrolyte seriously impair cycle stability and coulombic efficiency. Additionally, the sluggish redox kinetics of the LiPS conversion reaction limits the charge/discharge rate of LSBs.⁶ These critical drawbacks lead to rapid capacity attenuation, poor rate capability and low coulombic efficiency, which seriously limit the practical applications of LSBs.

Exploring high-performance sulfur host materials is an effective strategy toward solving the aforementioned problems. Carbon materials are usually characterized by high electrical conductivities, large specific surface areas, and good mechanical stabilities, which make them widely employed LSB cathode materials to improve sulfur usage and accommodate volume changes.⁷ However, the weak physical interaction of carbon materials with polar LiPS makes them not efficient to suppress the dissolution of LiPS and prevent the shuttle effect. In view of this point, a variety of polar materials have been investigated as sulfur hosts to more effectively capture LiPS. The list of tested polar materials includes metal oxides,⁸⁻¹⁰ sulfides,¹¹⁻¹³ phosphides,¹⁴ borides,^{15,16} carbides,^{17,18} nitrides,¹⁹⁻²² and their composites.^{23,24} Through strong polar-polar interaction with LiPS, these sulfur hosts effectively adsorb polysulfides and prolong to some extent the LSB cycle life. Nevertheless, if not prevented, the continuous accumulation of soluble LiPS within the cathode region inevitably leads to its diffusion into the electrolyte. To prevent this shuttle effect, it is critical not only to adsorb LiPS but also to ensure both their physical/chemical confinement and their rapid conversion

into insoluble $\text{Li}_2\text{S}_2/\text{Li}_2\text{S}$. In this second direction, the use of sulfur hosts with good electrocatalytic activity has been proven to effectively suppress the shuttle effect.^{12,13,17} Unfortunately, the so-far developed electrocatalytic host materials usually suffer from unsatisfactory adsorption ability toward LiPS.²⁵ Besides, a smooth deposition of Li_2S also requires hosts with huge surface areas which are not easy to produce.

Based on the above considerations, the ideal sulfur host possesses high electrical conductivity, very large surface area, strong LiPS affinity, and excellent electrocatalytic activity. Such a demanding combination of properties calls for multifunctional nanocomposites that integrate several different materials each of them with one or more of the required functionalities. Indeed, the challenging electrochemical performances demanded can be significantly improved through the synergistic contribution of different components. For example, Hu *et al.* proposed a $\text{NiO}/\text{NiCo}_2\text{O}_4@\text{C}$ nanocomposite as an efficient sulfur host, in which NiO strongly adsorbed LiPS, NiCo_2O_4 facilitated the conversion of LiPS, and the carbon layer improved electrical conductivity.²⁶ Very recently, multifunctional $\text{Co}/\text{CNT}@\text{MXene}$ ²⁷ and $\text{V}_2\text{O}_3/\text{V}_8\text{C}_7@\text{carbon}@\text{graphene}$ ¹⁷ nanocomposites have also demonstrated good rate performance and cycling stability even at high sulfur loadings. However, despite this progress, the engineering of multifunctional sulfur hosts is still at a very primary stage of development, and the integration of all the above-mentioned merits into one single material remains as a major challenge.

The structural design of the sulfur host also plays a critical role in defining the cathode electrochemical performance. In this direction, benefiting from the independent nanosized reaction space, abundant active sites, and depressed LiPS shuttle effect, nanoreactor-type host materials have very recently attracted much attention.²⁸⁻³¹ For example, Wu *et al.* prepared an ordered ladder-like carbon framework coupled with a built-in MoS_2 catalyst as nanoreactors for Li-S redox reactions.²⁹ Boyjoo *et al.* developed a simple one-step complexation modified Stöber method to synthesize Fe_{1-x}S electrocatalysts in N-doped porous carbon spheres as nanoreactors in LSBs.³⁰ Besides, Yang *et al.* proposed ZnSe/N -doped hollow carbon nanoreactor as sulfur hosts in LSBs.³¹ Although few nanoreactors loaded with different

catalysts have already been reported, the internal design of such nanoreactors is far from being optimized.

We believe that one key approach to significantly improve performance is through hierarchical structuration of the host. We hypothesize that through the synergetic combination of multiple components within hierarchical nanoreactors the LiPS conversion can be significantly accelerated for better LSB performance. Therefore, to overcome the present limitations of LSB cathodes, we designed a multifunctional composite containing abundant adsorption and catalytic sites. We first considered heterostructured Ag/VN nanorods both as a highly conductive backbone structure, and to provide internal catalytic and adsorption sites for LiPS conversion reaction. Besides, to improve the specific surface area for sulfur dispersion and to accommodate volume changes during the reaction process, we envisaged the presence of a high density of nitrogen-doped carbon nanotubes (NCNTs) on the surface of Ag/VN nanorods. Here we report on the synthetic realization of such a hierarchical Ag/VN@Co/NCNTs nanocomposite through the growth of ZIF-67 onto AgVO₃ nanorods and the subsequent annealing of the obtained product. Next, NCNTs arrays were *in Situ* grown on the surface of the produced Ag/VN nanorods. During the process, Co nanoparticles were formed at the top of NCNTs. These Co nanoparticles turned out to be highly convenient owing to their high capacity to adsorb escaped LiPS. We also thoroughly analyze here the electrochemical performance of the Ag/VN@Co/NCNTs nanocomposites produced. Besides, lithium-sulfur pouch cells based on these cathodes were manufactured and their potential toward practical applications is here demonstrated.

3.3 Experimental Section

Synthesis of β -AgVO₃ NWs. In a typical synthesis, 85 mg (0.5 mmol) of AgNO₃, 45 mg (0.25 mmol) of V₂O₅, and 39 mg (1.5 mmol) LiF were added to 30 mL of distilled water. The prepared yellow suspension was transferred to 50 mL Teflon-lined stainless steel autoclave and heated for 24 h at 180 °C in the oven. After cooling naturally, the bottle green precipitate

was obtained, then dried under an oven of 60 °C.

Synthesis of core-sheath β -AgVO₃@ZIF-67. With stirring, 30 mg of β -AgVO₃ NWs and 720 mg (2.5 mmol) of Co(NO₃)₂·6H₂O were added into 20 mL methanol, which is denoted as A. At the same time, 820 mg (10 mmol) of 2-MIM was dissolved in another 20 mL methanol, denoted as B. Afterwards, the solution B was added drop by drop into solution A, then stir for 30 minutes. The as-prepared products were washed thoroughly with anhydrous ethanol and finally dried under oven at 60 °C. The preparation of ZIF-67 is the same as that of β -AgVO₃@ZIF-67 without adding β -AgVO₃.

Synthesis of the Ag/VN@Co/NCNTs, VN@Co/NCNTs, Co/NCNTs and Ag/VN composite.

For the synthesis of Ag/VN@Co/NCNT, the nitriding process was conducted in a horizontal quartz tube furnace. The porcelain boat containing 300 mg of β -AgNO₃@ZIF-67 nanocomposite was placed at downstream position of the quartz tube furnace and another porcelain boat containing 3000 mg of melamine powder was placed at the upstream position. Then, β -AgVO₃@ZIF-67 precursor and melamine was calcining at 750 °C for 2 h with a heating rate of 5 °C min⁻¹ in mixture gas (95% Ar, 5% H₂). After cooling naturally, the Ag/VN@Co/NCNTs nanocomposite was obtained. The other composites (VN@Co/NCNTs, Co/NCNTs, and Ag/VN) were also synthesized by nitrogen treatment of precursors (V₂O₅@ZIF-67, ZIF-67, and β -AgNO₃) under the same condition, respectively. We have added this part in the revised manuscript.

Synthesis of host@S nanocomposites. For the synthesis of Ag/VN@Co/NCNTs@S, Ag/VN@Co/NCNTs and sulfur powder (1:3, weigh ratio) were mixed and heated at 155 °C for 24 h in a glass bottle under Ar atmosphere. VN@Co/NCNTs@S, Ag/VN@S, Co/NCNTs@S, and Super P@S were obtained using the same process.

Materials characterization. The morphology, structure and composition of the samples were tested by a high-resolution transmission electron microscope (HRTEM, Tecnai Talos F200i) and a field emission scanning electron microscope (FESEM, Zeiss Supra55, Germany) equipped with an energy dispersive X-ray spectrometer (EDX). Elemental mapping analysis

was conducted *via* high-angle annular dark-field scanning TEM energy-dispersive X-ray spectroscopy (HAADF-STEM-EDX). The crystallographic structural information of the materials was investigated using an X-ray diffractometer (XRD, Rigaku, D/max-Ultima III diffractometer, Cu K α radiation, $\lambda = 0.15418$ nm). The chemical composition and the valence states of the products were investigated by X-ray photoelectron spectroscopy (XPS, Thermo Fisher Scientific, ESCALAB 250). Thermogravimetric analysis (TGA) was performed to record the content of S within as-synthesized products by a synchronous thermal analyzer (NETZSCH, STA449-F5). UV-vis absorption spectra were recorded by a PerkinElmer LAMBDA 950 spectrophotometer. The Raman spectrum was recorded by a Raman Microscope (Thermo Electron Corporation, DXR2Xi). Nitrogen adsorption-desorption isotherms and BET surface area measurements were measured to acquire the specific surface area and the pore size distribution using the Brunauer–Emmett–Teller (Gemini VII2390).

Li-S Cell Assembly and Measurements. Host@S nanocomposites (Ag/VN@Co/NCNTs@S, VN@Co/NCNTs@S, Ag/VN@S, and Co/NCNTs@S), Super P, and PVDF binder (weight ratio = 8:1:1) were dispersed in *N*-methyl pyrrolidone (NMP, 99.9%, Aladdin) to form a slurry which was coated on aluminum foil and dried at 60 °C overnight. The coated aluminum foil was then punched into small disks with a diameter of 12.0 mm. Sulfur loading was about 1.0–1.3 mg cm⁻². In order to realize higher sulfur loadings, the mixed slurry was dropped on the carbon paper substrate to form Ag/VN@Co/NCNTs@S@CP electrodes. High-loading tests were applied using 2.8, 5.1, 7.2, and 10.3 mg cm⁻² of sulfur. Electrochemical measurements were conducted in standard 2032 coin-type cells. In LSBs assemblies, lithium foils were used as counter electrode and Celgard 2400 membranes as separators. The electrolyte used was 1.0 M lithium bis (trifluoromethanesulfonyl) imide (LiTFSI) (99.9%, Aladdin) dissolved in a mixture of 1,3-dioxolane (DOL, 99.5%, Alfa Aesar) and 1,2-dimethoxy ethane (DME, 99%, Honeywell) (v/v = 1/1) and containing 0.1 m of LiNO₃ (99.98%, Alfa Aesar). For each coin cell and punch cell, 20 μ L/mg S⁻¹ of electrolyte was used. High-loaded coin cells added 10–15 μ L/mg S⁻¹. Cells were galvanostatically cycled within a voltage range of 1.7–2.8 V using a battery-testing instrument (LAND CT2001A) at different

C rates. Cyclic voltammetry measurements were performed on the CHI660E instrument at a scan rate of 0.1–0.7 mV s⁻¹ and electrochemical impedance spectroscopy tests were performed using a sinusoidal voltage with an amplitude of 10 mV in the frequency range 100 kHz to 0.01 Hz.

Preparation of Li₂S_x (x=6 or 8) Solutions for Adsorption Test and Kinetic Study. Sulfur and Li₂S (99.9%, Alfa Aesar) in the molar ratio x-1:1 were added to appropriate amounts of DME and DOL (volume ratio of 1:1) under vigorous magnetic stirring overnight until a dark brown solution was formed. As-prepared host nanocomposites (24.8 mg of Ag/VN@Co/NCNTs, 20.5 mg of VN@Co/NCNTs, 103.6 mg of Ag/VN, 15.4 mg of Co/NCNTs, and 35.8 mg of Super P) with the same surface area were poured into 3.0 mL 10 mM Li₂S₆ solution and the mixtures were stirred 12 h for homogenization.

Symmetric cell fabrication and test. Electrodes for symmetric cells were fabricated in the same way as electrodes for LSBs. Two pieces of the same electrode (average loading about 0.5 mg cm⁻²) were used as identical working and counter electrodes with 40 μL of electrolyte containing 0.5 mol L⁻¹ Li₂S₆ and 1 mol L⁻¹ LiTFSI dissolved in DOL/DME (v/v=1/1). For comparison, symmetric cells with electrolyte 1 mol L⁻¹ LiTFSI dissolved in DOL/DME (v/v = 1/1) were also assembled and tested. In all cases, CV measurements were performed at a scan rate of 50 mV s⁻¹.

Measurement of Nucleation and Dissolution of Li₂S. The nucleation and dissolution of Li₂S were tested in 2032-coin cells. The host nanocomposite (Ag/VN@Co/NCNTs, VN@Co/NCNTs, Ag/VN, or Co/NCNTs) was dispersed in absolute ethyl alcohol to form a slurry which was coated on small carbon paper disks with a diameter of 12.0 mm and dried at 60 °C overnight. Host nanocomposite (Ag/VN@Co/NCNTs, VN@Co/NCNTs, Ag/VN, or Co/NCNTs) loading on carbon papers were about 1 mg cm⁻², and was applied as work electrode, respectively, Li foil worked as the counter electrode, 20 μL of 0.25 M Li₂S₈ dissolved in DOL/DME (v/v = 1:1) solution with 1.0 m LiTFSI was used as catholyte, and 20 μL of 1.0 m LiTFSI in DOL/DME (v/v = 1:1) solution as anolyte. The cells were held at 2.19 V for 2.5 h to reduce higher-order LiPS to Li₂S₄. Subsequently, they were held at a potential

of 2.05 V until the current decreased to 0.01 mA for Li₂S nucleation and growth. In order to analyze the Li₂S dissolution, fresh cells were first discharged at a current of 0.10 mA to 1.80 V, and subsequently discharged at 0.01 mA to 1.80 V for full transformation of S species into solid Li₂S. After this discharge, cells were potentiostatically charged at 2.40 V for the dissolution of Li₂S into LiPS until the charge current was below 10⁻² mA.

Pouch cell assembly and Measurements. Both the Ag/VN@Co/NCNTs@S cathode and lithium anode were cut into 6 × 4 cm pieces. The sulfur loading of the cathode in the pouch cell (6 × 4 cm) was 1.5 mg cm⁻² (total sulfur loading: 36 mg). The E/S ratio was about 13 mL g⁻¹_{Sulfur}, thickness of lithium belt anode was 0.4 mm. Separator and electrolyte were sandwiched between the tailored Ag/VN@Co/NCNTs@S and lithium belt. The test conditions for electrochemical performances are the same as that of the CR2032 coin cells.

Computational Details. All the spin-polarized computations were performed by using Vienna *ab initio* simulation package (VASP). The ion-electron interactions were described by the projector augmented wave method and the general gradient approximation in the Perdew–Burke–Ernzerhof (PBE) form was used. During the structure relaxation, the convergence criterion was set to 0.03 eV/Å and 10⁻⁵ eV for the residual force and energy, respectively. The 4 × 4 Co (111) slab, 3 × 3 VN (200) slab, and 3 × 2 Ag (200) stripe supported on 3 × 5 VN (200) slab were used as the models, and the corresponding Brillouin zones were sampled by Monkhorst-Pack 4 × 4 × 1, 4 × 4 × 1 and 4 × 2 × 1 k-point mesh. To avoid the interaction between two periodic units, a vacuum space of 15 Å was employed.

The adsorption energy of Li₂S₆ (E_{ad}) is calculated by:

$$E_{ad} = E_{total} - E_{clean} - E_{Li_2S_6}$$

where E_{total} and E_{clean} are the energies of systems with and without the adsorption of Li₂S₆, $E_{Li_2S_6}$ is the energy of a Li₂S₆ molecule. Therefore, more negative E_{ad} indicates stronger adsorption strength.

3.4 Results and Discussion

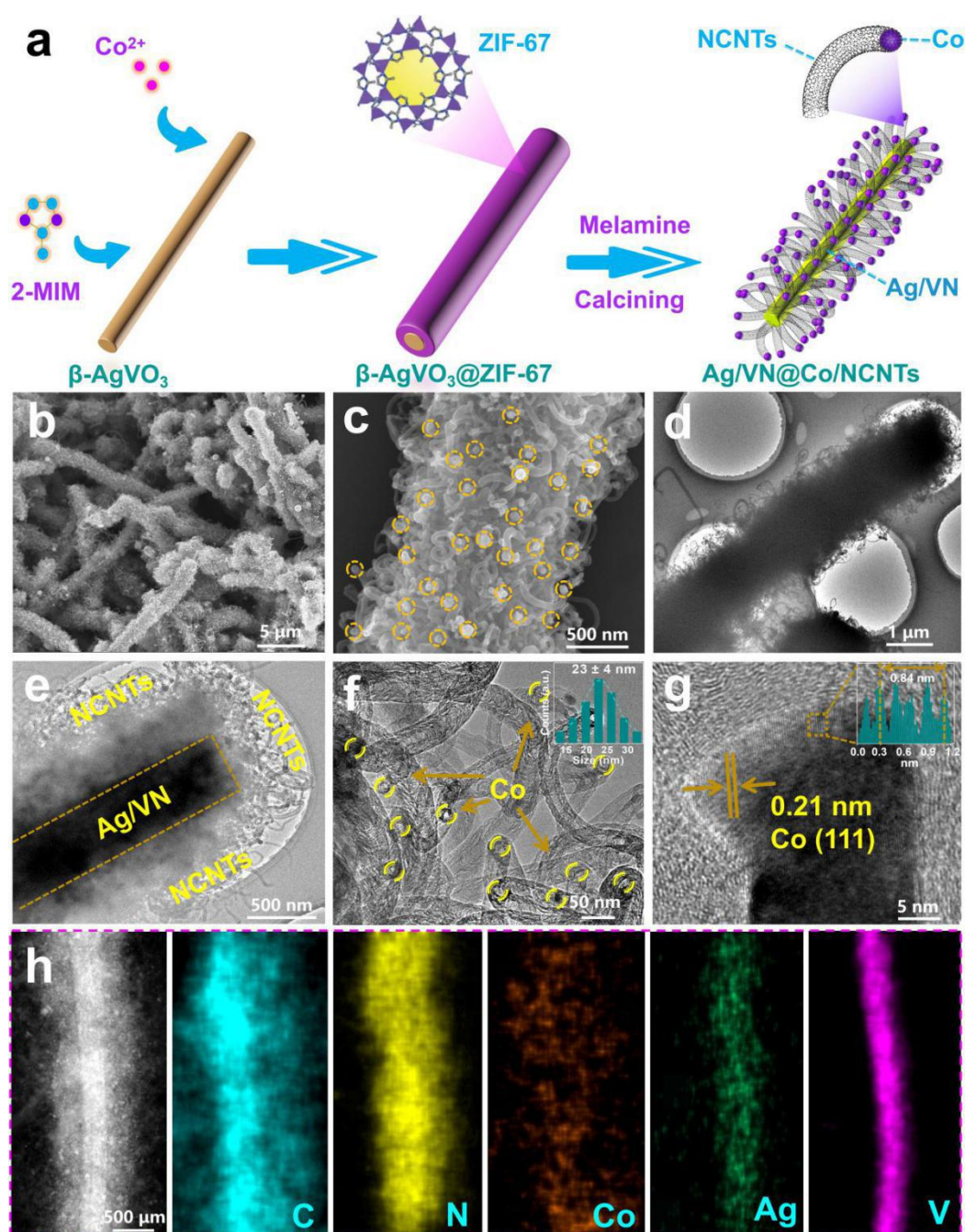


Figure 1. (a) Schematic illustration of the synthesis process. (b–h) Morphological and chemical characterization of Ag/VN@Co/NCNTs: (b,c) SEM images; (d–f) TEM images; (g) HRTEM image of the tip of a NCNT showing the presence of a Co nanoparticle; (h), HAADF-STEM image and EDS elemental maps. Yellow circles in (c) and (f) point at the presence of Co nanoparticles. The histogram in figure (f) corresponds to the diameter of the NCNTs.

The synthetic procedure used to produce Ag/VN@Co/NCNTs nanocomposites is schematically illustrated in **Figure 1a** (details can be obtained in the Experimental Section). First, β -AgVO₃ nanowires (NWs) were synthesized by a hydrothermal method (**Figure 2**).³² In a second step, the surface of β -AgVO₃ was coated with ZIF-67 *via* a solution method. Within the produced β -AgVO₃@ZIF-67 core@shell NWs, the ZIF-67 shell homogeneity and thickness can be easily tuned by adjusting the reaction time (**Figure 3** and **Figure 4**). To study the growth process of β -AgVO₃@ZIF-67, a series of time-dependent experiments were conducted. When the reaction time was set at 5 min, the surface of β -AgVO₃ NWs already appeared covered by small irregular ZIF-67 nanoparticles (Figure 4a,b). When the reaction time was extended to 15 min, these small ZIF-67 nanoparticles grow up (Figure 4c,d). At last, a dense shell of ZIF-67 nanoparticles on the surface of β -AgVO₃ NWs was obtained after 30 min (Figure 4e,f). Subsequently, melamine was added and the β -AgVO₃@ZIF-67 core@shell NWs were annealed under a reducing Ar/H₂ atmosphere (Figure 1b, 1d, and 5a,b). In this third step, the outer ZIF-67 was transformed into interwoven NCNTs (diameter ca. 23 ± 4 nm) decorated with Co nanoparticles at their tip (Figure 1c and 1f), as confirmed by high-resolution transmission electron microscopy (HRTEM, Figure 1g). In the same process, the inner β -AgVO₃ NWs were reduced into Ag/VN nanorods (Figure 1e). Chemical composition elemental maps obtained by energy dispersive spectroscopy (EDS, Figure 1h) show the distribution of Ag, Co, V, N, and C within the Ag/VN@Co/NCNTs nanocomposite; Ag/VN is found at the core of nanorods wrapped with NCNTs decorated by Co nanoparticles. Additional results from the morphological and compositional characterization of reference materials (VN@Co/NCNTs, Ag/VN, and Co/NCNTs) can be found in **Figure 6,7,8,9**.

X-ray diffraction (XRD) analysis (Figure 5c) of the Ag/VN@Co/NCNTs nanocomposite show all the diffraction peaks to be consistent with of the presence of VN (JCPDS No. 35-0768), Co (JCPDS No. 15-0806), and Ag (JCPDS No. 87-0719) crystal phases. Consistent results were also obtained from the XRD characterization of Ag/VN and Co/NCNTs reference samples (Figure 8f, 9c, and 10).

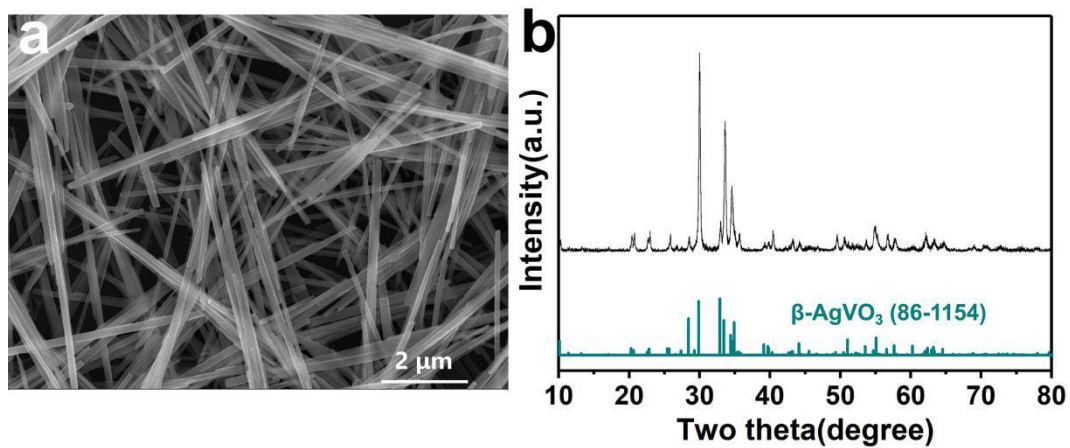


Figure 2. (a) SEM image and (b) XRD pattern of β -AgVO₃ nanowires.

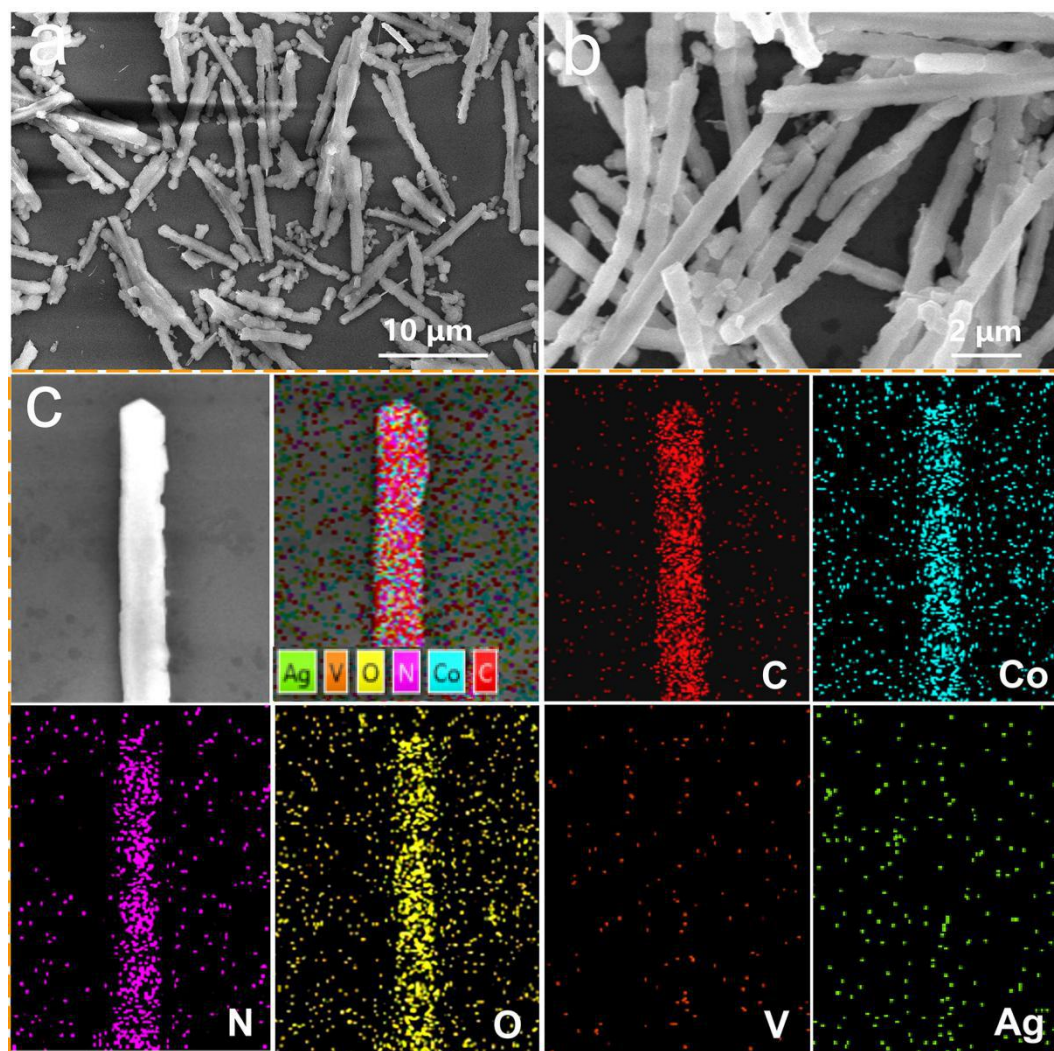


Figure 3. (a,b) SEM images, (c) SEM image and EDX elemental maps of β -AgVO₃@ZIF-67.

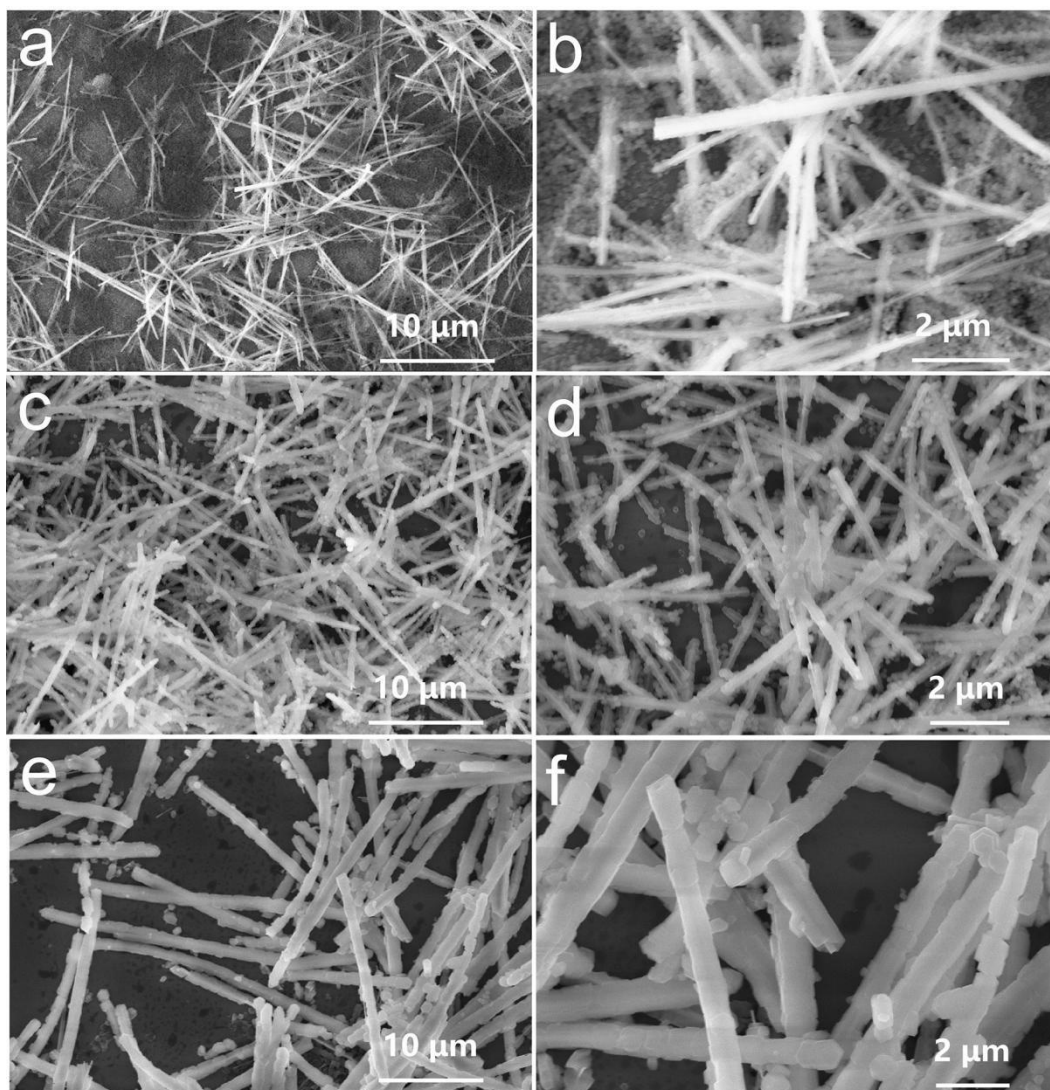


Figure 4. SEM images of β -AgVO₃@ZI-67 obtained after different reaction time: (a,b) 5 min, (c,d) 15 min (e,f) 30 min.

X-ray photoelectron spectroscopy (XPS) confirmed the presence of Co, V, Ag, N, and C within Ag/VN@Co/NCNTs nanocomposites (**Figure 11a**). High-resolution XPS spectra of Ag 3d, Co 2p, V 2p, and N 1s regions are displayed in Figure 11b and **Figure 12b-d**. The Ag 3d_{3/2} peak at 373.5 eV and the Ag 3d_{5/2} peak at 367.4 eV are ascribed to metallic Ag⁰ (Figure 2b).^{33,34} The Co 2p spectrum shows contributions from two chemical states: Co²⁺ at 796.8 eV (2p_{3/2}) and Co⁰ at 794.1 eV (2p_{3/2}) (Figure 2c).³⁵ The deconvolution of the V 2p_{3/2} band shows three well-resolved peaks at 513.9, 515.5, and 516.9 eV, which we ascribe to V³⁺, V⁴⁺, and V⁵⁺, respectively (Figure 12d). The presence of Co²⁺, V⁴⁺, and V⁵⁺ chemical states is related to the

partial oxidation of the surface when exposed to air during preparation and handling.²¹ The high-resolution N 1s XPS spectrum displays N in 4 different chemical environments that are identified as V-N at 397.4 eV, pyridinic N at 398.5 eV, pyrrolic N at 399.3 eV and graphitic N at 400.2 eV (Figure 11b).^{21,36,37}

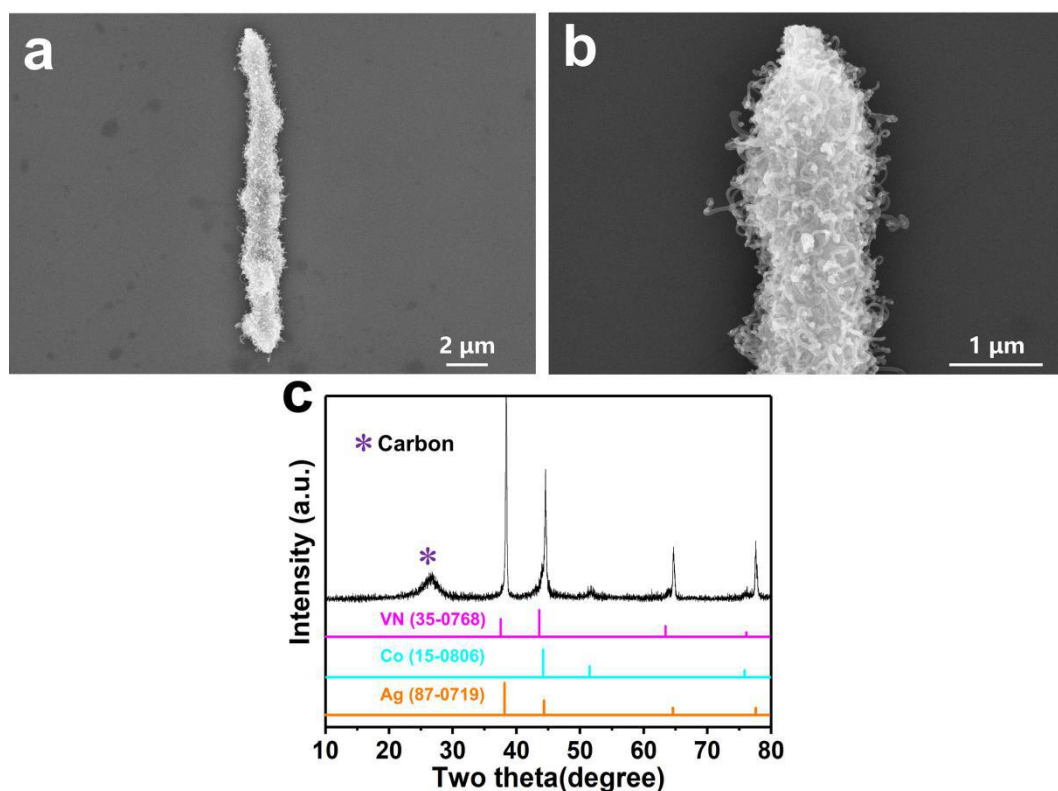


Figure 5. (a,b) SEM images at different magnifications and (c) XRD pattern of Ag/VN@Co/NCNTs.

Figure 13 displays the Raman spectra of Ag/VN@Co/NCNTs and the three reference nanocomposites. The peaks below 1000 cm^{-1} are attributed to VN and Co (Figure 13a).^{38,39} The two peaks located at 1345 cm^{-1} (D band) and 1589 cm^{-1} (G band) correspond to lattice defects and sp^2 -bonded carbon atoms, respectively.⁴⁰ Ag/VN@Co/NCNTs shows a higher intensity ratio I_D/I_G (1.05) than VN@Co/NCNTs (0.98) and Co/NCNTs (0.97) (Figure 13b), indicating that Ag/VN@Co/NCNTs contains more lattice defects. Ag/VN@Co/NCNTs is also characterized by a higher Brunauer–Emmett–Teller (BET) specific surface area, $80.7\text{ m}^2\text{ g}^{-1}$, when compared with VN@Co/NCNTs ($97.9\text{ m}^2\text{ g}^{-1}$), Ag/VN ($19.3\text{ m}^2\text{ g}^{-1}$), and Co/NCNTs ($130.2\text{ m}^2\text{ g}^{-1}$). Besides, Ag/VN@Co/NCNTs also displays a much larger porosity, with the

main contribution coming from mesopores in the 3–50 nm range (**Figure 14**).⁴¹

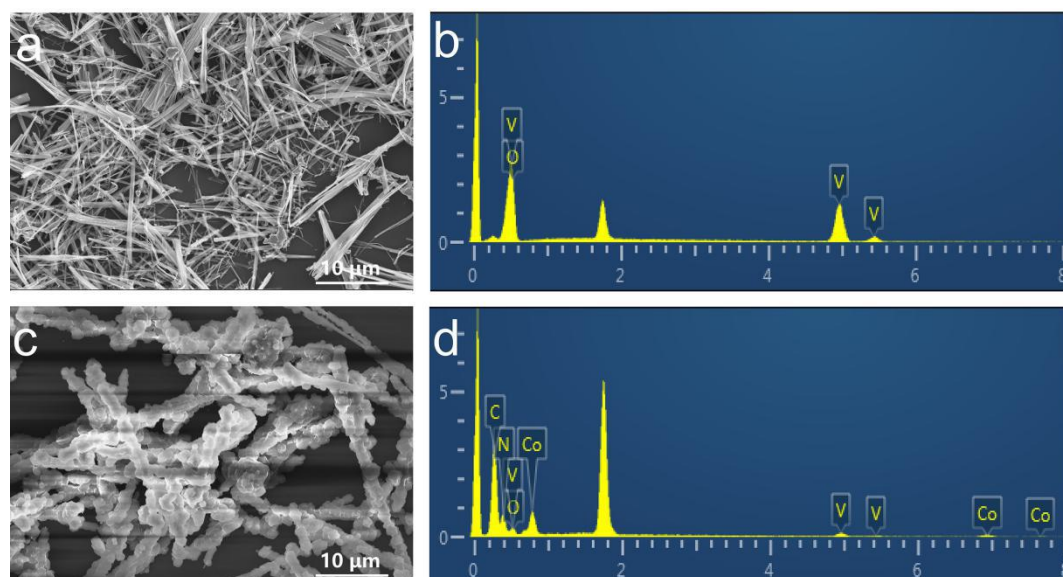


Figure 6. (a,b) SEM image and EDX spectrum of V_2O_5 nanowires. (c,d) SEM image and EDX spectrum of $V_2O_5@ZIF-67$.

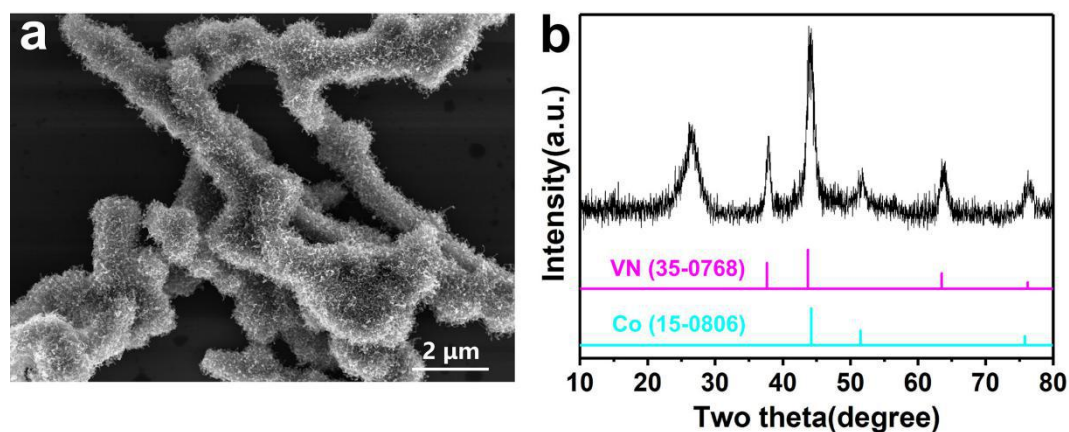


Figure 7. (a) SEM image and (b) XRD pattern of $VN@Co/NCNTs$.

Sulfur was introduced within the nanocomposites by a melt-diffusion process. SEM and TEM images of sulfur-filled $Ag/VN@Co/NCNTs$ ($Ag/VN@Co/NCNTs@S$) show the original nanocomposite morphology to be maintained (**Figure 15**). EDX chemical compositional maps display a homogeneous distribution of sulfur throughout the composite, with no independent sulfur aggregate being observed after extensive characterization (Figure 15e). These results suggest that most of the sulfur was confined within the $Ag/VN@Co/NCNTs$ nanocomposite

and with uniform dispersion. XRD and thermogravimetric analysis (TGA) of Ag/VN@Co/NCNTs@S nanocomposites confirmed the presence of crystalline cubic sulfur (JCPDS No. 08-0247) and quantified it at a 71.8 wt% mass fraction (**Figure 16** and 17). Similar results were obtained with the reference hosts (VN@Co/NCNTs, Ag/VN, and Co/NCNTs) as shown in **Figure 17-20**.

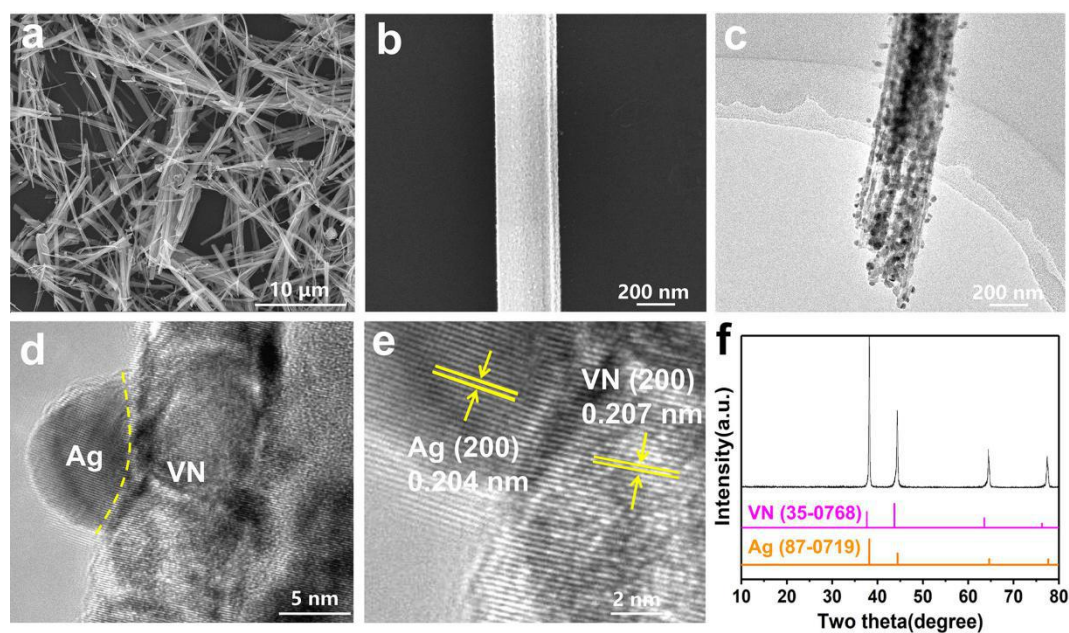


Figure 8. (a,b) SEM image, (c) TEM image, (d,e) HRTEM images and (f) XRD pattern of the Ag/VN nanowires.

The LiPS adsorption capacity of the host plays an important role in inhibiting the shuttling effect in a LSB. To identify the interaction between hosts and polysulfide, a series of adsorption experiments consisting on the direct observation of the color change of a Li_2S_6 solution in the presence of the different potential hosts were carried out (see the Experimental Section for details). In the presence of Ag/VN@Co/NCNTs, the initial dark yellow Li_2S_6 solution (10 mM) appears transparent after 12h, which indicates the complete adsorption of Li_2S_6 onto Ag/VN@Co/NCNTs (inset in Figure 12a). In contrast, in the presence of the same amount of VN@Co/NCNTs, Co/NCNTs, or Ag/VN, after 12h adsorption experiment the Li_2S_6 solution still presents a light yellow color. When using carbon black (Super P) as adsorber, the initial dark yellow color of the Li_2S_6 solution is maintained for the whole duration of the experiment (12 h), which indicates no LiPS adsorption by Super P. UV-vis absorption spectra

of the electrolyte solutions, particularly in the range 400–450 nm where Li_2S_6 has a strong absorption band, confirmed the lower amount of Li_2S_6 in the solution containing $\text{Ag}/\text{VN}@\text{Co}/\text{NCNTs}$ when compared with the solutions containing same surface area of the reference hosts (Figure 12a).⁴² The excellent Li_2S_6 adsorption differences confirmed the strong affinity between $\text{Ag}/\text{VN}@\text{Co}/\text{NCNTs}$ and LiPS .

Figure 12b–d exhibits the high-resolution Ag 3d, Co 2p, and V 2p XPS spectra obtained from $\text{Ag}/\text{VN}@\text{Co}/\text{NCNTs}$ before and after the Li_2S_6 adsorption. A clear shift to higher binding energies is observed from the metals spectra after Li_2S_6 adsorption, which demonstrates the strong interaction of S with surface Ag, Co, and V. Besides, after Li_2S_6 adsorption, the S 2p spectrum shows five doublets, which we ascribe to polythionate (168.7 eV), thiosulfate (167.1 eV), S^{2-} (161.5 eV), and the two species originated from the terminal sulfur (S_T^{-1} , 162.1 eV) and bridging sulfur (S_B^0 , 163.9 eV). (Figure 12e).^{12,17,42} Thus, overall, XPS analysis confirmed the strong interaction of LiPS with $\text{Ag}/\text{VN}@\text{Co}/\text{NCNTs}$.

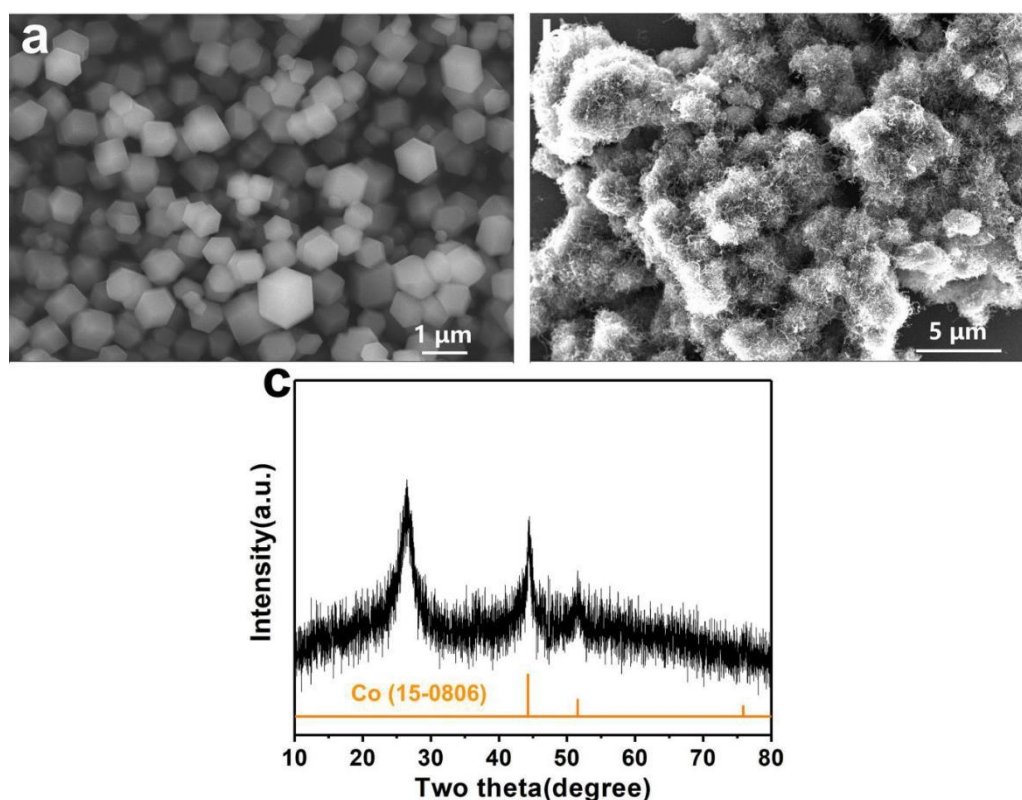


Figure 9. (a) SEM image of ZIF-67. (b) SEM image and (c) XRD pattern of the Co/NCNTs.

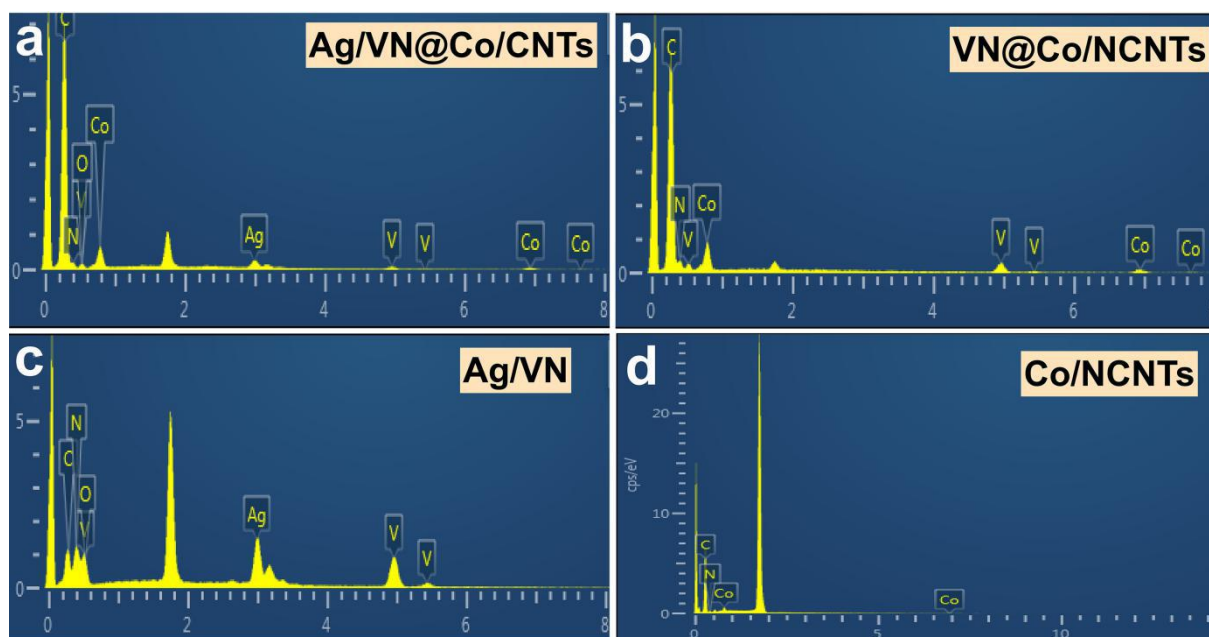


Figure 10. EDX spectrum of (a) Ag/VN@Co/NCNTs, (b) VN@Co/NCNTs, (c) Ag/VN, (d) Co/NCNTs.

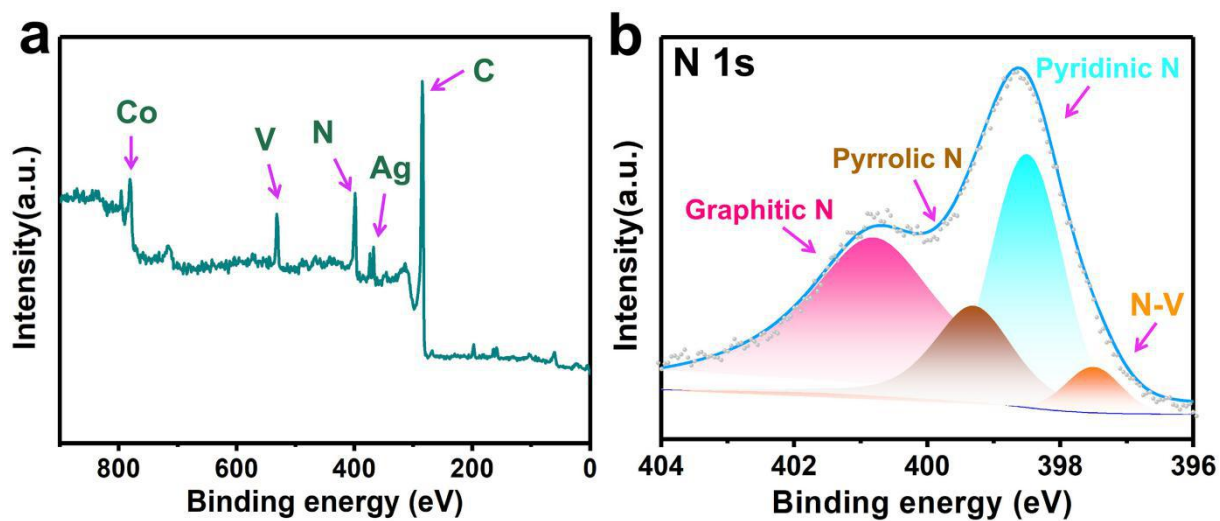


Figure 11. (a) XPS survey spectrum and (b) High-resolution N 1s XPS spectrum of Ag/VN@Co/NCNTs.

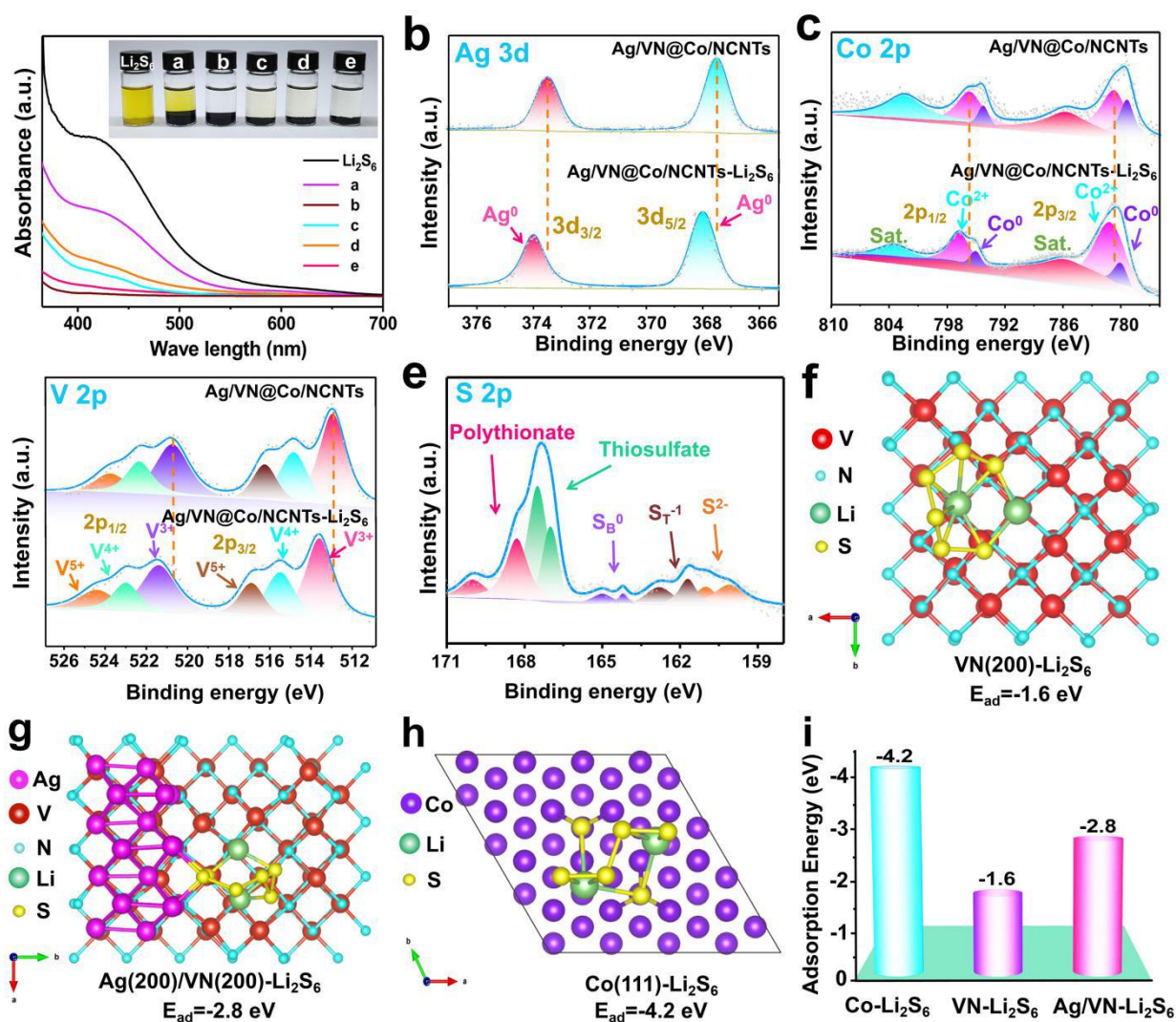


Figure 12. (a) UV-vis spectra of the polysulfide solutions 12 h after the introduction of the different adsorbents (a: Super P, b: Ag/VN, c: VN@Co/NCNTs, d: Co/NCNTs, and e: Ag/VN@Co/NCNTs). The inset shows optical photographs of the vials containing the solution and the adsorbents after 12 h test. (b–d) High-resolution XPS spectra of Ag 3d (b), Co 2p (c) and V 2p (d) of Ag/VN@Co/NCNTs before and after adsorption of Li_2S_6 . (e) S 2p XPS spectrum of Ag/VN@Co/NCNTs after Li_2S_6 adsorption for 0.5 h. (f–h) Top view of a Li_2S_6 molecule on VN (200), Ag (200)/VN (200), and Co (111) surfaces (V, N, Ag, Co, Li, and S atoms colored with red, cyan, magenta, violet, olive, and yellow, respectively). (i) Comparison of calculated energies of adsorption of Li_2S_6 on VN (200), Ag (200)/VN (200), and Co (111) surfaces.

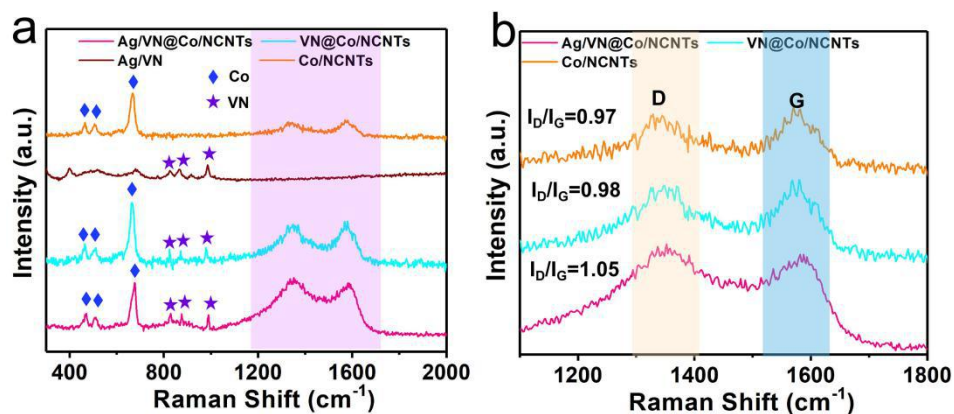


Figure 13. (a) Raman spectra of Ag/VN@Co/NCNTs, VN@Co/NCNTs, Ag/VN, Co/NCNTs. (b) Enlarged view of the violet squared area in (a).

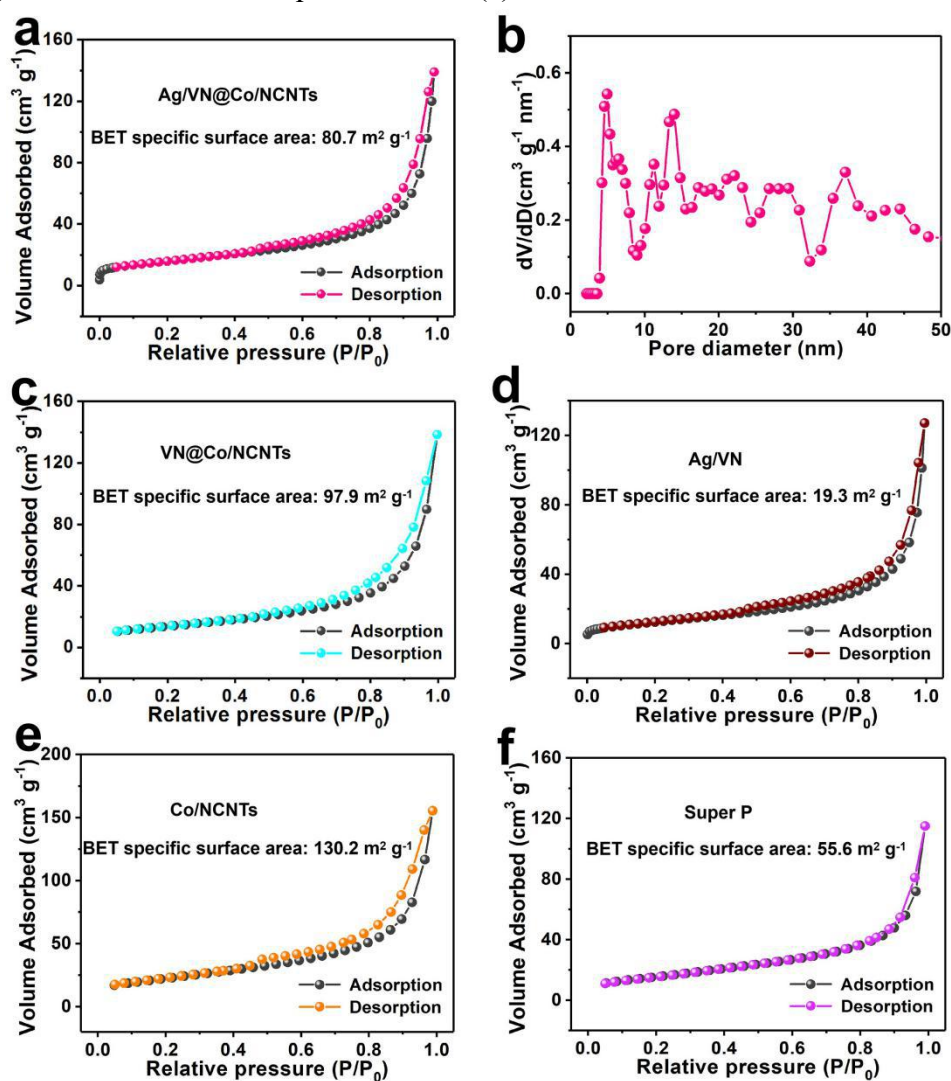


Figure 14. (a) Nitrogen adsorption/desorption isotherm and (b) pore-size distribution of Ag/VN@Co/NCNTs. Nitrogen adsorption/desorption isotherm of (c) VN@Co/NCNTs, (d) Ag/VN, (e) Co/NCNTs, and (f) Super P.

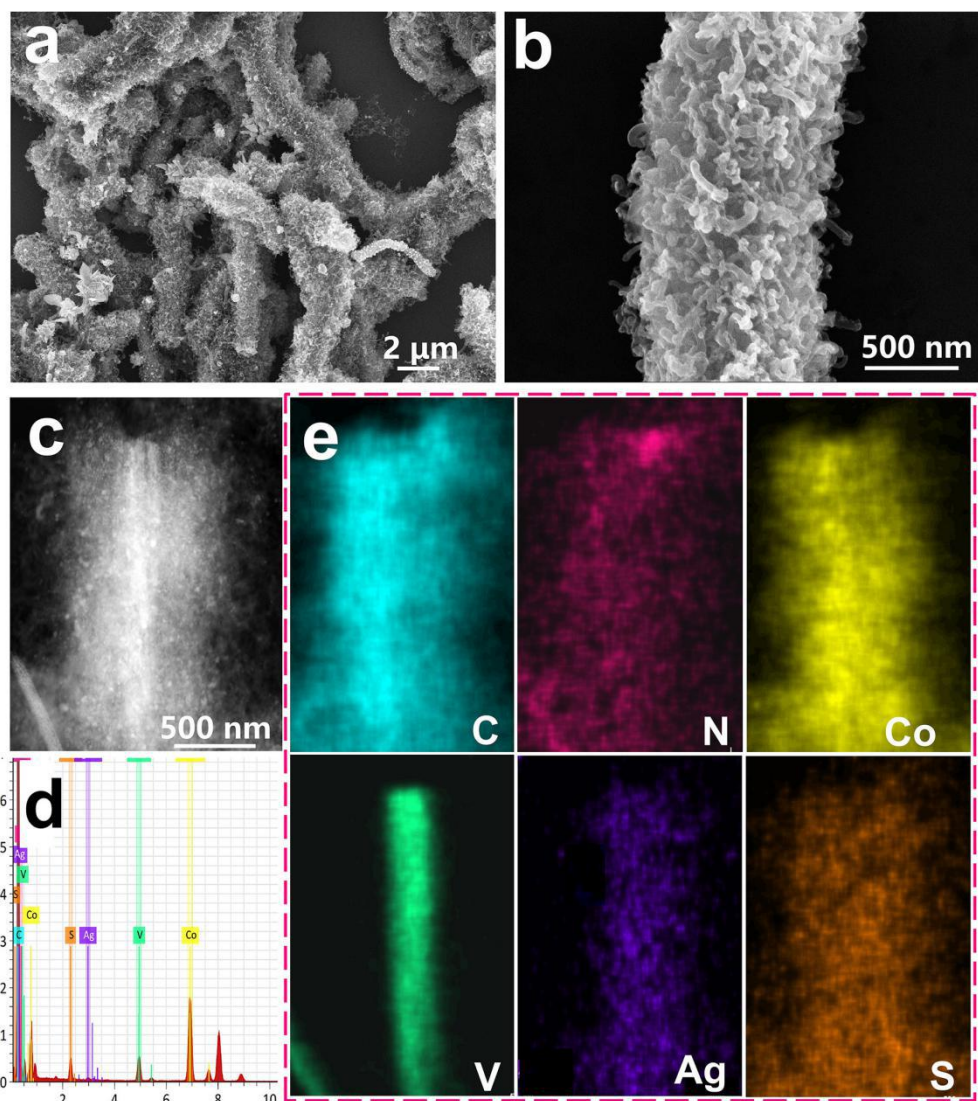


Figure 15. (a,b) SEM images, (c) STEM image, (d) EDX spectrum and (e) elemental maps of Ag/VN@Co/NCNTs@S.

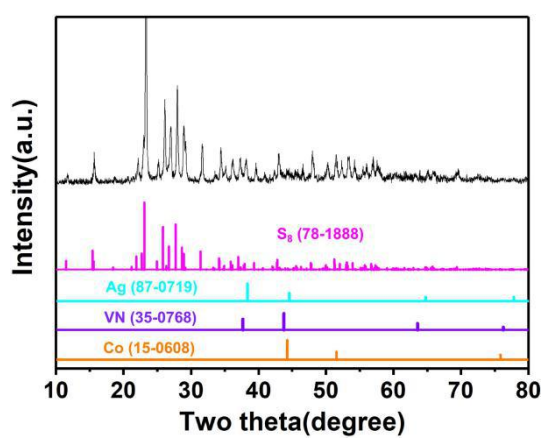


Figure 16. XRD pattern of Ag/VN@Co/NCNTs@S.

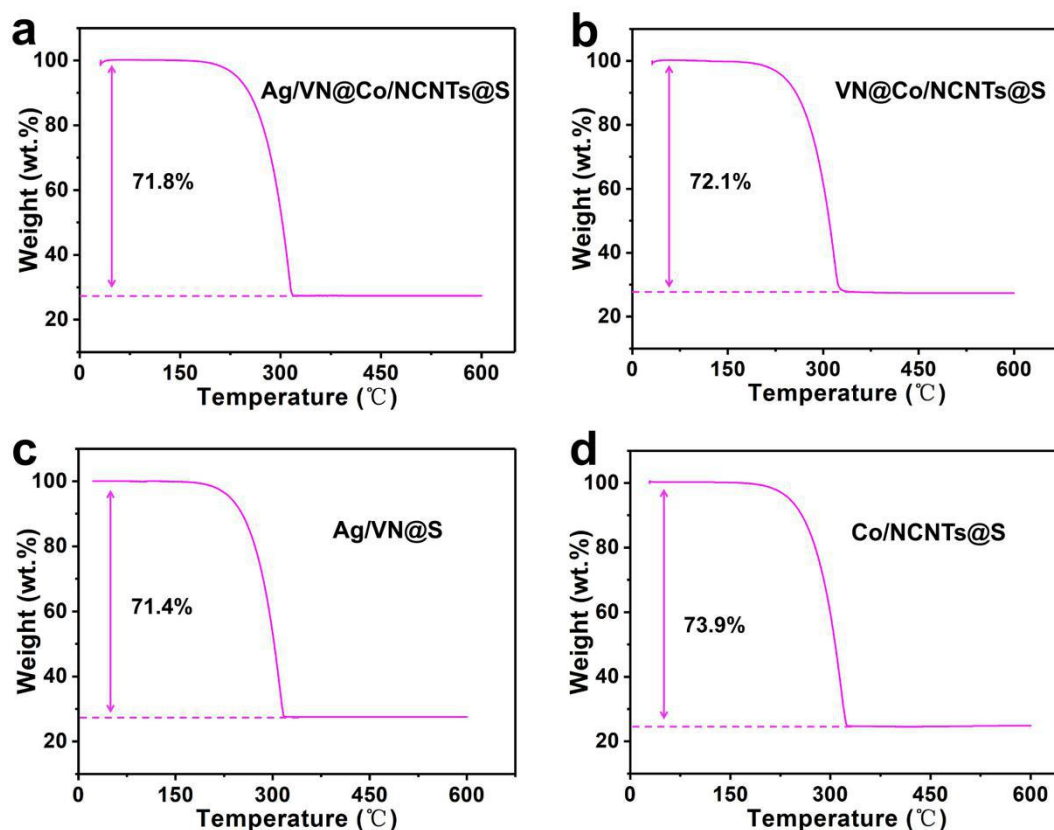


Figure 17. TGA curve of (a) Ag/VN@Co/NCNTs@S, VN@Co/NCNTs@S, Ag/VN@S, and Co/NCNTs@S measured in Ar, showing a weight loss of 71.8% 72.1 wt%, 71.4 wt%, and 73.9 wt% mass fraction respectively during heating, corresponding to the loss of sulfur.

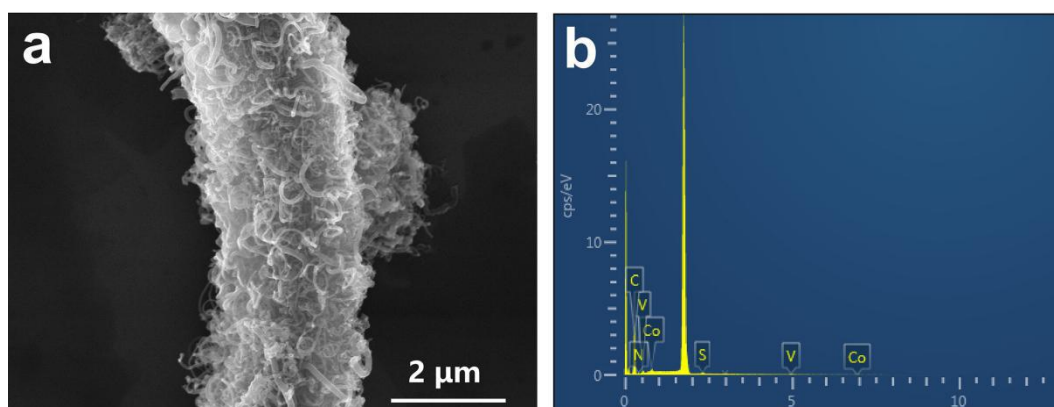


Figure 18. (a) SEM image and (b) EDX spectrum of VN@Co/NCNTs@S.

DFT calculations were used to gain atomic-level insight into the adsorption of LiPS on Ag/VN@Co/NCNTs. We specifically investigated the adsorption energy of LiPS on VN (200), Ag (200) and VN (200) heterojunction, and Co (111) slab models. Figure 12f-h and **Figure 21** exhibit the optimized configurations of Li₂S₆ adsorption on the surfaces of VN, Ag/VN, and Co. The adsorption energies of VN, Ag/VN, and Co are -1.6, -2.8, and -4.2 eV, respectively

(Figure 12i). Clearly, Ag/VN shows lower adsorption energy than VN alone, indicating that the Ag/VN heterojunction can effectively enhance LiPS adsorption. Besides, Co shows the strongest adsorption energy. This result is consistent with adsorption tests and XPS results showing the strong LiPS adsorption capacity of Ag/VN@Co/NCNTs through formation of metal-S bonds.

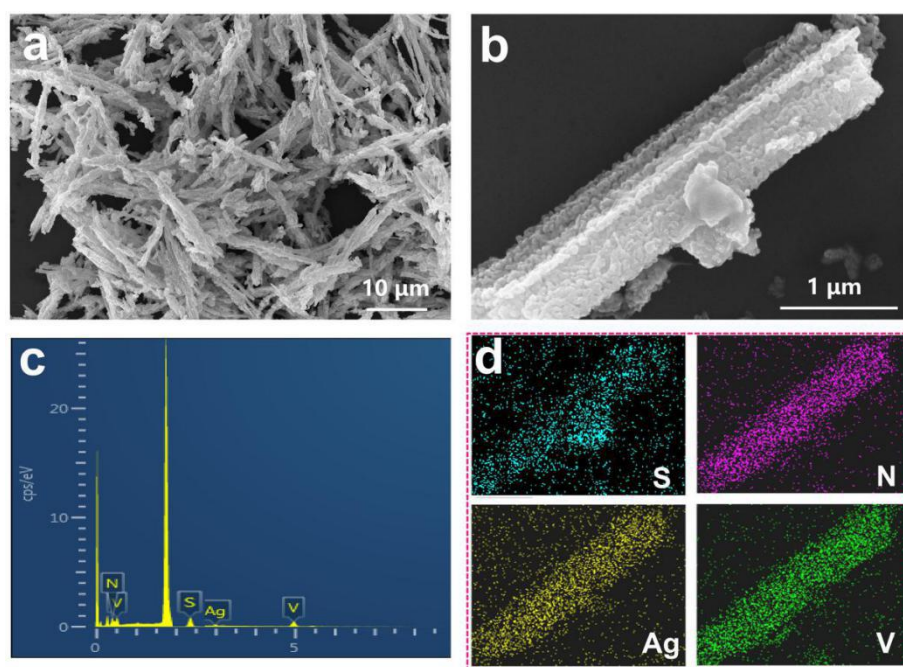


Figure 19. (a,b) SEM images, (c) EDX spectrum and (d) elemental maps of Ag/VN@S.

To explore synergistic merits of the different components and the hierarchical structure in LSBs, the electrochemical performance of Ag/VN@Co/NCNTs@S, VN@Co/NCNTs@S, Ag/VN@S, Co/NCNTs@S, and Super P@S cathodes were systematically investigated. Typical CV profiles for the five electrode types were obtained within a potential window of 1.7–2.8 V at a scan rate of 0.1 mV s⁻¹ (**Figure 22a** and **Figure 23a**). All the electrodes display two cathodic peaks and one anodic peak. The cathodic peak at the highest potential is attributed to the reduction of sulfur to long-chain LiPS (Li₂S_x, 4 ≤ x ≤ 8) and the cathodic peak at the lowest potential is related to the formation of insoluble short-chain Li₂S₂/Li₂S.^{7,43} When scanning back, the anodic peak originates from the oxidation of short-chain LiPS, eventually to sulfur. It is worth to note that the second reduction peak measured with the Ag/VN@Co/NCNTs@S cathode (2.03 V) appears at a higher potential than with the other

three electrodes (1.97, 2.01, and 2.02 V, Figure 22b) and Super P@S electrode (1.94 V, Figure 23a). The higher potentials of the reduction peaks obtained with Ag/VN@Co/NCNTs@S cathodes indicate a higher catalytic activity for polysulfide redox kinetics. This catalytic activity is confirmed by measuring the onset potentials, taken at a current density of $10 \mu\text{A cm}^{-2}$ beyond the baseline current (Figure 24).

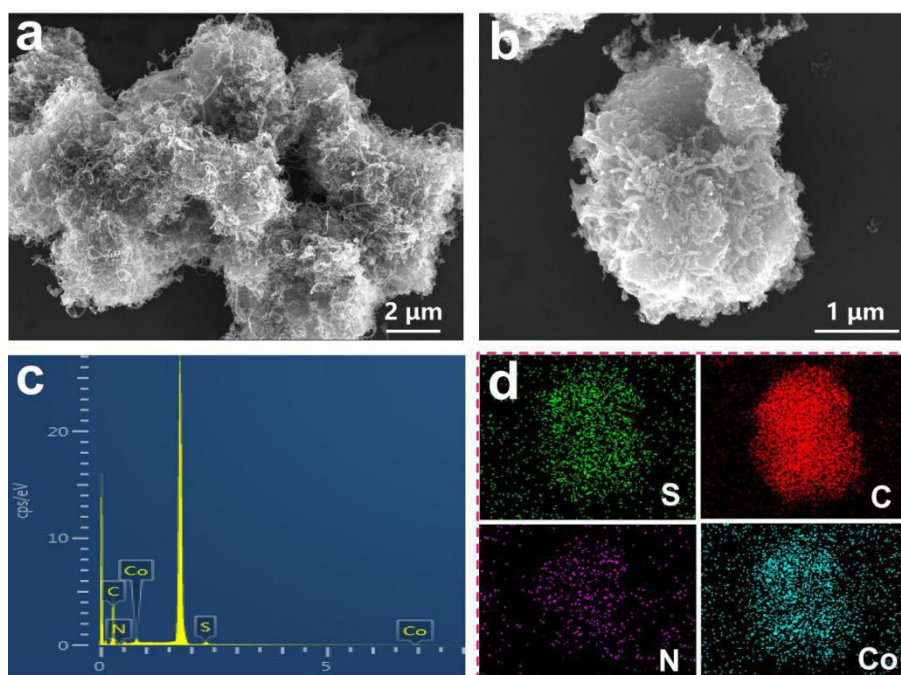


Figure 20. (a,b) SEM images, (c) EDX spectrum and (d) elemental maps of Co/NCNTs@S.

The electrochemical performance was further analyzed through galvanostatic charge/discharge tests. In Figure 22c, charge/discharge curves of Ag/VN@Co/NCNTs@S, VN@Co/NCNTs@S, Ag/VN@S, and Co/NCNTs@S cathodes at 0.1 C show one charge plateau and two discharge plateaus, consistently with CV analysis. The voltage gap ΔE between the oxidation and the second reduction plateaus denote a hysteresis in the redox reaction.^{31,44} Among the tested cathodes, Ag/VN@Co/NCNTs@S shows the lowest polarization potential ($\Delta E=170$ mV), significantly below those of VN@Co/NCNTs@S ($\Delta E=190$ mV), Ag/VN@S ($\Delta E=217$ mV), Co/NCNTs@S ($\Delta E=228$ mV), and Super P@S ($\Delta E=285$ mV) electrodes. All discharge curves show two plateaus, corresponding to the reduction of sulfur to soluble LiPS ($\text{S}_8 \rightarrow \text{S}_6^{2-} \rightarrow \text{S}_4^{2-}$) and the subsequent conversion to insoluble products ($\text{S}_4^{2-} \rightarrow \text{Li}_2\text{S}_2 \rightarrow \text{Li}_2\text{S}$).³ The capacities of the two discharge plateaus are

defined as Q₁ and Q₂, respectively (Figure 22c). The ratio between Q₂ and Q₁ (Q₂/Q₁) can be interpreted in terms of the catalytic ability for LiPS conversion reaction: sluggish kinetics during the solid→liquid→solid process and shuttle effect caused by the diffusion of soluble LiPS give rise to a capacity decrease between Q₁ and Q₂ stage. Thus, a high Q₂/Q₁ ratio indicates a good catalytic ability and *vice versa*.^{3,45} As shown in Figure 22d and Figure 23b, the Q₂/Q₁ of Ag/VN@Co/NCNTs@S is 2.33, well above that of VN@Co/NCNTs@S (2.12), Ag/VN@S (2.29), Co/NCNTs@S (1.88), and Super P@S (1.80), which proves the superior catalytic activity towards polysulfides redox reaction of Ag/VN@Co/NCNTs@S.

CV curves at different scan rates (0.1–0.7 mV s⁻¹) were measured to explore the Li⁺ ion diffusivity (Figure 22e). The anodic and cathodic peak currents display a linear relationship with the square root of the scan rate, which denotes a diffusion-limited reaction (Figure 22f). According to the fitting of this linear dependence, the diffusion constant of the rate-limiting species, *i.e.* lithium ions (D_{Li^+} , cm² s⁻¹), can be calculated using the Randles–Sevcik equation^{31,46}:

$$I_p = (2.69 * 10^5) n^{1.5} A D_{Li^+}^{0.5} C_{Li^+} \nu^{0.5}$$

Where I_p is the peak current density (A), n is the number of elemental charges transferred, A is the geometric area of the electrode (cm²), C_{Li⁺} is the concentration of lithium ions in the electrolyte (mol cm⁻³), and ν is the scan rate (V s⁻¹). According to the Randles–Sevcik equation, the values of D_{Li^+} calculated for Ag/VN@Co/NCNTs@S at peaks 1, 2, and 3 are 3.61 × 10⁻⁸, 3.97 × 10⁻⁸, and 1.06 × 10⁻⁷ cm² s⁻¹, respectively (Figure 22g). Among the four nanocomposites tested, the highest lithium ion diffusivities were obtained for Ag/VN@Co/NCNTs@S (Figure 22f, **Figure 25**), suggesting a facilitated ion transfer.^{29,31}

To gain insight into the importance of the catalytic effect in mitigating LiPS shuttle, *ex Situ* Raman spectroscopy test of Ag/VN@Co/NCNTs@S cathodes were conducted at different stages of the first discharge/charge process at 0.1 C (Figure 22h,i). As shown in Figure 22h, the characteristic peaks of S₈ can be clearly detected on the charged material at 155, 220, and

474 cm^{-1} . These peaks gradually disappear during the discharge process. The peaks of mid-chain LiPS (280, 396.5, and 457.0 cm^{-1}) appear when the electrode is charged to 2.0 V. But as the discharge time continues to increase, the intensity of these peaks gradually weakens to eventually disappear at the end of the discharge, which is consistent with reported works.^{17,47,48}

To further investigate the catalytic effect of Ag/VN@Co/NCNTs, Li_2S nucleation and dissolution experiments were conducted. The Li_2S nucleation capacity on these samples was calculated from the quantity of electric charge injected in term of Faraday's law. Results show that Li_2S nucleation capacity on Ag/VN@Co/NCNTs is 213.6 mAh g^{-1} , much higher than that on VN@Co/NCNTs (199.7 mAh g^{-1}), Ag/VN (171.2 mAh g^{-1}), and Co/NCNTs (149.7 mAh g^{-1}) (Figure 22j). It should be noted that a shorter nucleation time denotes a faster catalytic conversion and thus a lower diffusion of unused LiPS. Clearly, Ag/VN@Co/NCNTs shows a faster onset of nucleation (1010 s) compared to the other materials VN@Co/NCNTs (1375 s), Ag/VN (1629 s), and Co/NCNTs (2320 s), indicating a higher catalytic efficiency toward LiPS nucleation. A similar strategy was used to study the kinetics of Li_2S dissolution. Potentiostatic charge curves of Ag/VN@Co/NCNTs exhibit higher current than with the other nanocomposites, indicating a lower oxidation overpotential for Li_2S dissolution. Moreover, the calculated dissolution capacity of Ag/VN@Co/NCNTs (776.8 mAh g^{-1}) is much higher than for VN@Co/NCNTs (724.8 mAh g^{-1}), Ag/VN (672.4 mAh g^{-1}), and Co/NCNTs electrodes (586.0 mAh g^{-1}) (Figure 22k).

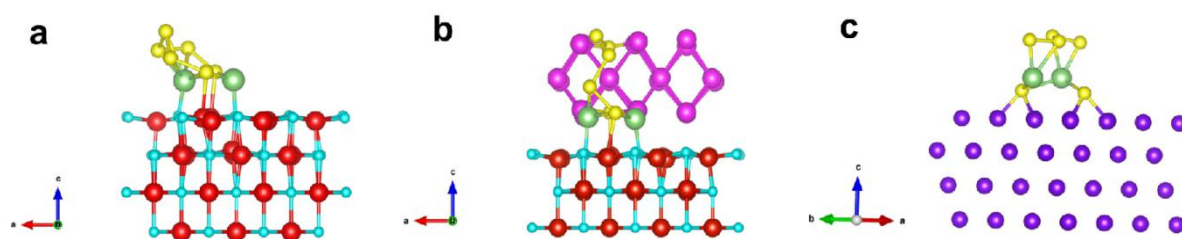


Figure 21. Side view of a Li_2S_6 molecule on (a) VN (200), (b) Ag (200)/VN (200), and (c) Co (111) surfaces. V, N, Ag, Co, Li, and S atoms are colored with red, cyan, magenta, violet, olive, and yellow, respectively.

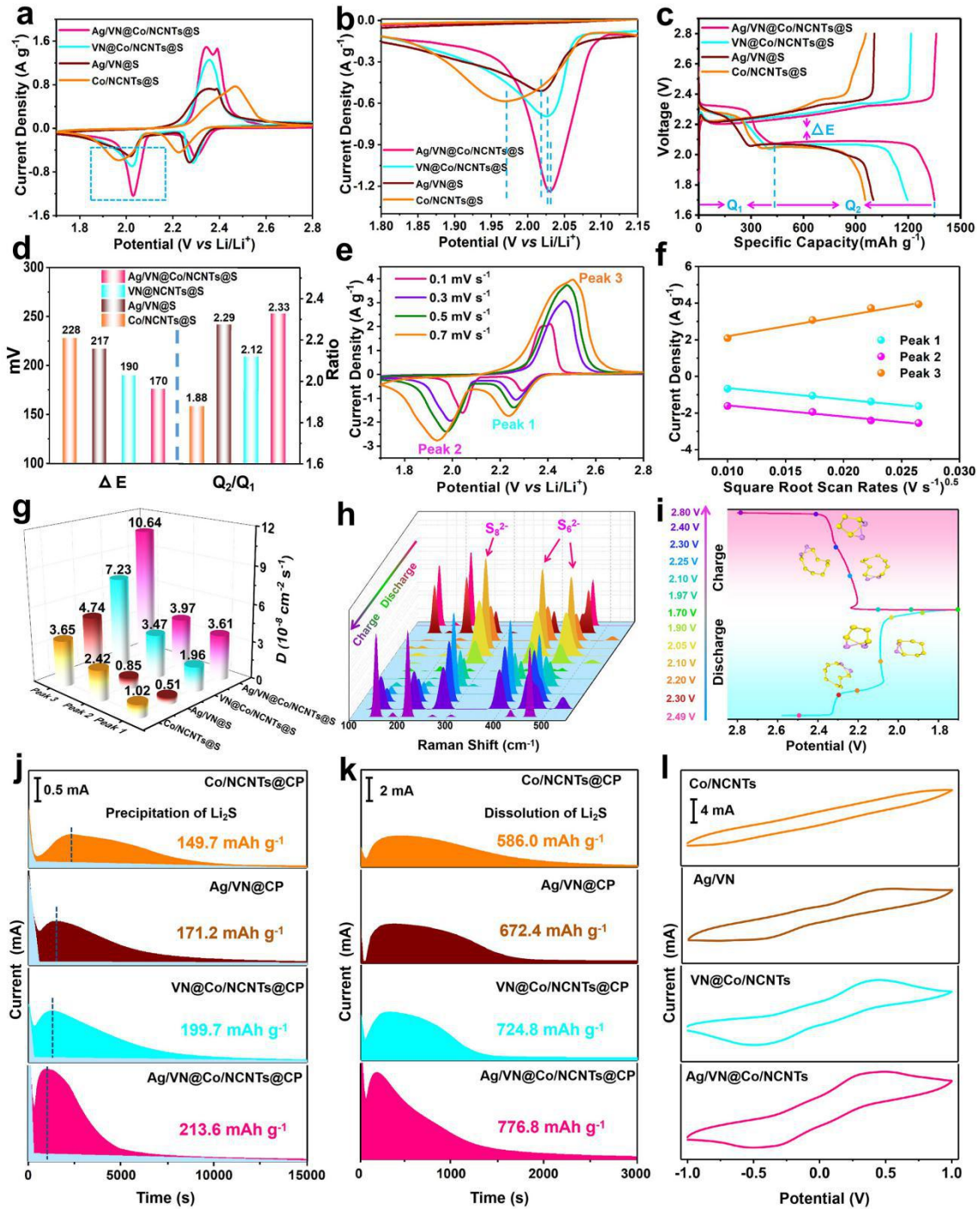


Figure 22. (a) CV profiles of the Ag/VN@Co/NCNTs@S, VN@Co/NCNTs@S, Ag/VN@S, and Co/NCNTs@S electrodes. (b) Enlarged view of the squared area in (a). (c) Charge/discharge curves of different electrodes at a current rate of 0.1 C. (d) Values of ΔE and Q_2/Q_1 obtained from charge/discharge curves, (e) CV curves of Ag/VN@Co/NCNTs@S at different scan rates in the range of 0.1–0.7 mV s^{-1} . (f) Currents for the peaks 1–3 shown in (e) as a function of the square root of the scan rate for Ag/VN@Co/NCNTs@S. (g) Li^+ diffusion coefficients calculated from the different CV redox peaks according to the Randles–Sevcik equation. (h) *Ex Situ* Raman spectra and (i) Voltage-capacity curve at 0.1 C for a

Ag/VN@Co/NCNTs@S electrode. (j) Potentiostatic discharge profiles at 2.05 V with Li_2S_8 catholyte to evaluate nucleation kinetics of Li_2S . (k) Potentiostatic charge profiles at 2.40 V to evaluate dissolution kinetics of Li_2S . (l) CV curves of symmetric cells at a scan rate of 50 mV s^{-1} .

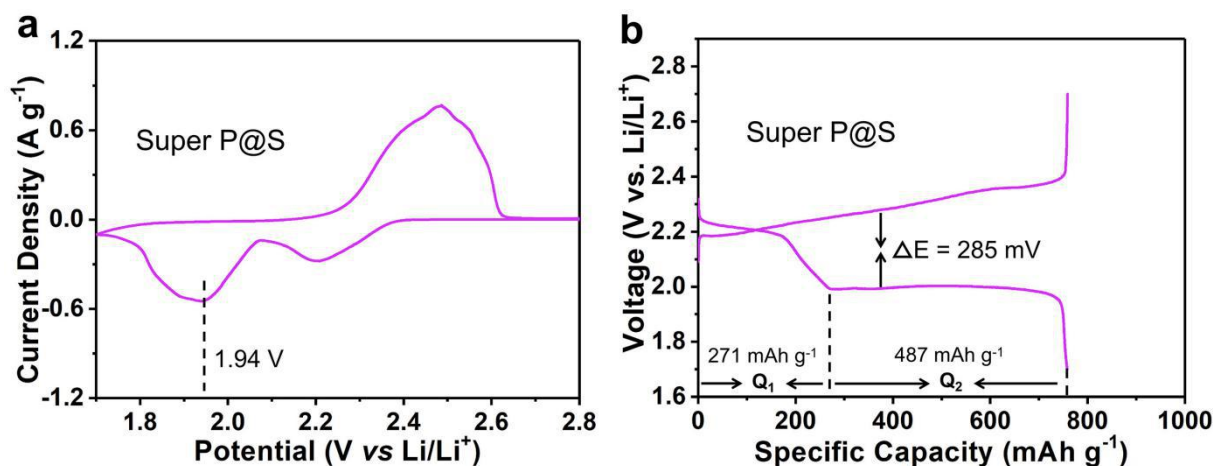


Figure 23. (a) CV profile at a scan rate of 0.1 mV s^{-1} and (b) charge/discharge curve of the Super P@S at a current rate of 0.1 C .

CV tests of symmetric cells were conducted to directly evaluate the LiPS catalytic reaction over host materials (Figure 22l). Among the tested samples, CV curve of Ag/VN@Co/NCNTs symmetrical cell show the largest current. Besides, Ag/VN@Co/NCNTs symmetric batteries with a Li_2S_6 -free electrolyte show a very weak current and a nearly rectangular charge/discharge curve associated to the capacitive behavior of a pure physical adsorption process (Figure 26). This result indicates that Li_2S_6 is the only active specie in the redox reaction system. Overall, these series of comprehensive experimental results verified the superior electrocatalytic effect of Ag/VN@Co/NCNTs hosts in reducing polarization and promoting kinetics of the LiPS redox reaction.⁴⁵

The electrochemical performance was evaluated by galvanostatic charge/discharge tests under different current rates. The charge/discharge curves of an Ag/VN@Co/NCNTs@S electrode are shown in Figure 27a. When increasing the current rate, the potential gap between the charge and discharge plateaus increases gradually, but two distinctive discharge plateaus are still obtained even at a high current density of 4 C , which confirms the fast LiPS reaction kinetics in Ag/VN@Co/NCNTs@S electrodes. CV curves of Ag/VN@Co/NCNTs@S almost

overlapped (**Figure 28**), showing no obvious peak shifts or current reduction, which indicates good stability and high reversibility.

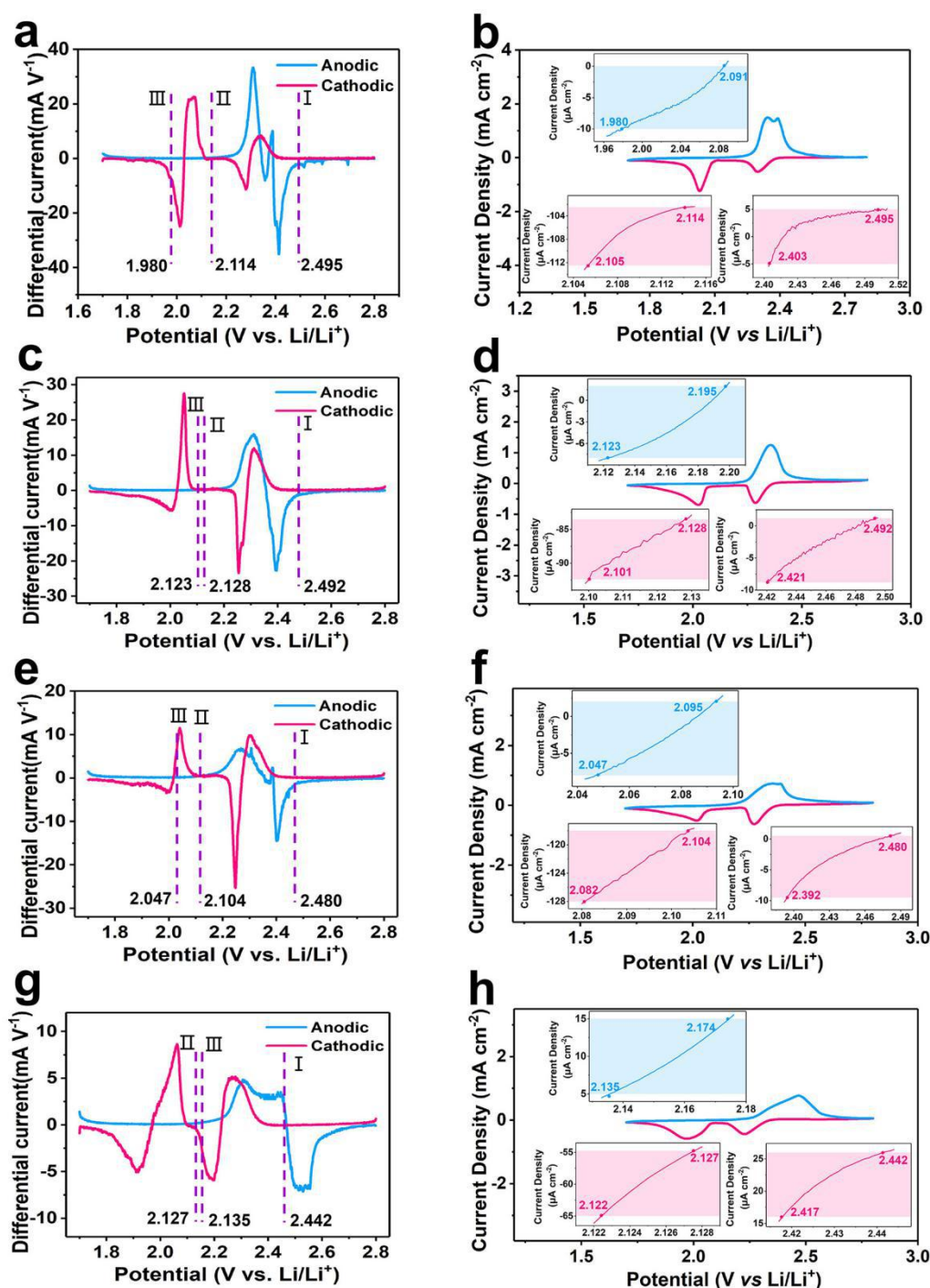


Figure 24. Onset potential for Li-S redox reactions. Differential CV curves of (a) Ag/VN@Co/NCNTs@S, (c) VN@Co/NCNTs@S, (e) Ag/VN@S and (g) Co/NCNTs@S. The baseline voltage and current density are defined as the value before the redox peak, where the variation on current density is the smallest, namely $dI/dV=0$. Baseline voltages are

denoted in red for cathodic peak I, II and in blue for anodic peak III, respectively. CV curves and corresponding onset potentials of redox peak I, II, and III (inset): (b) Ag/VN@Co/NCNTs@S, (d) VN@Co/NCNTs@S, (f) Ag/VN@S and (h) Co/NCNTs@S. The onset potential is determined when the current density is $10 \mu\text{A cm}^{-2}$ beyond the corresponding baseline current density (more specifically, $10 \mu\text{A cm}^{-2}$ more negative than baseline current density for cathodic peaks or $10 \mu\text{A cm}^{-2}$ positive than baseline current density for anodic peaks). As shown in the inset of b, d, f and h, the baseline voltages are the same as in a, c, e and g while the colored region indicates the gap in current density ($10 \mu\text{A cm}^{-2}$).

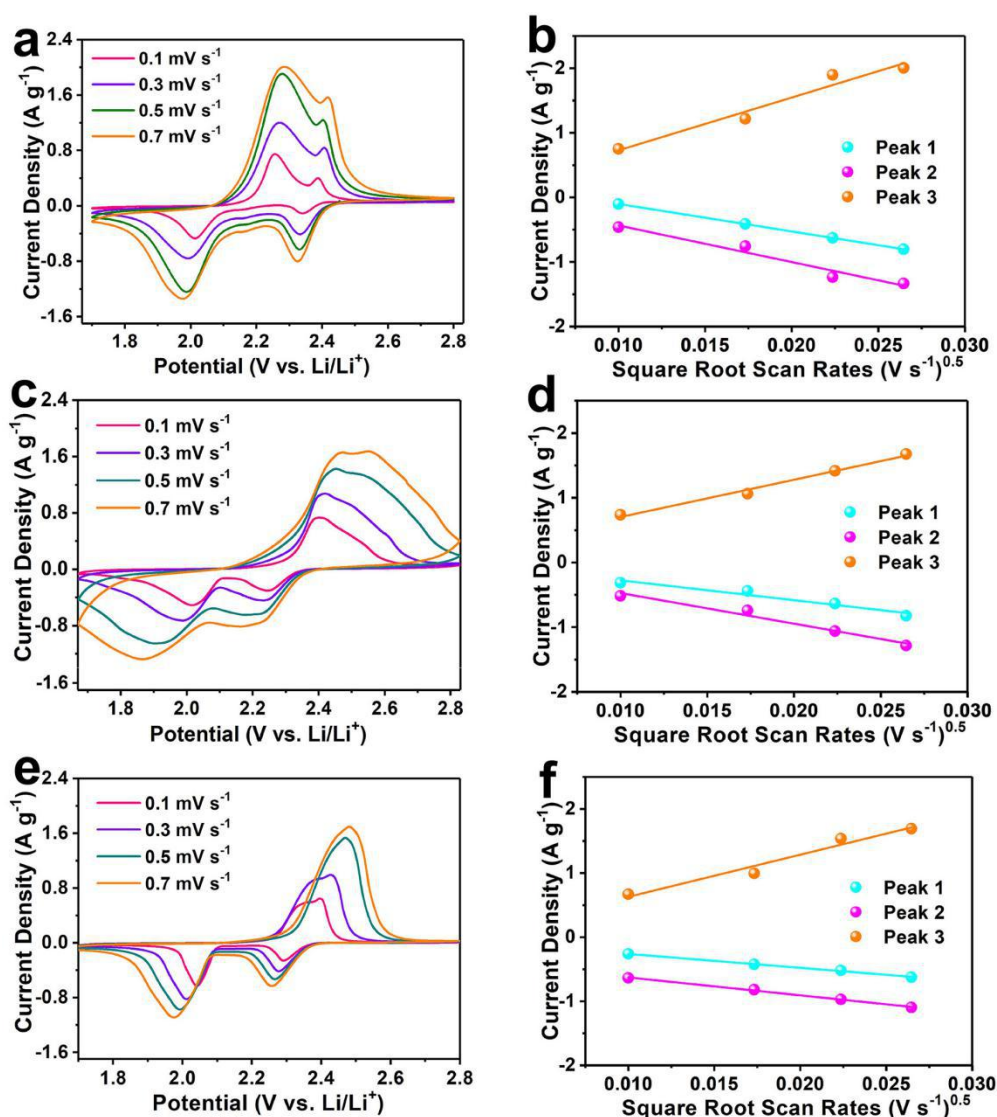


Figure 25. (a, c and e) CV curves of VN@Co/NCNTs@S, Ag/VN@S and Co/NCNTs@S in the range of 0.1–0.7 mV s^{-1} . (b, d and f) Peak currents *versus* square root of scan rates of VN@Co/NCNTs@S, Ag/VN@S and Co/NCNTs@S.

The rate performances of the four cathodes is shown in Figure 27b. Clearly, Ag/VN@Co/NCNTs@S electrodes show the best rate capability with average discharge capacities of 1350.0, 1204.7, 1131.9, 1019.9, 923.6, 800.5, and 767.7 mAh g⁻¹ at the current densities of 0.1, 0.2, 0.5, 1, 2, 3, and 4 C, respectively. A capacity retention rate of 57% at a current density of 4 C (Figure 27c) was obtained for Ag/VN@Co/NCNTs@S, which is much higher than that obtained for the reference electrodes, demonstrating a significantly higher sulfur utilization and LiPS conversion. This good rate performance is partially explained by the calculated density of states of Ag/VN (**Figure 29**), showing that the Fermi level is within a band of states, thus indicating a metallic character. Besides, results point out the important role played by interwoven Co/NCNTs to achieve fast electron transfer dynamics for Li-S conversion reaction.

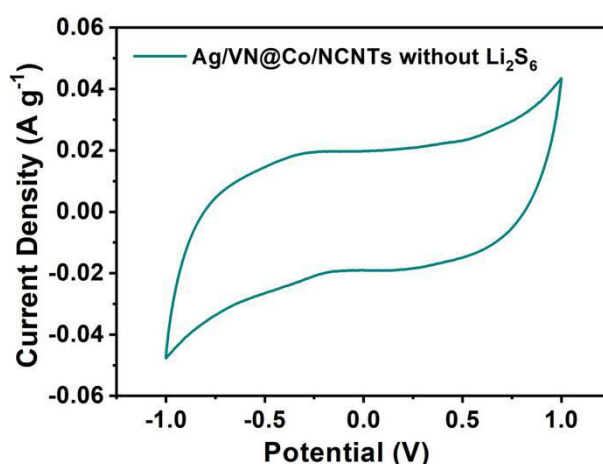


Figure 26. CV curve of Ag/VN@Co/NCNTs as electrode measured in symmetric coin cell configuration using an electrolyte containing 1 mol L⁻¹ LiTFSI dissolved in DOL/DME (v/v=1/1).

The cyclic stability of the four different electrodes is shown in Figure 27d. Among the four electrodes tested, the Ag/VN@Co/NCNTs@S electrode sustains the highest stabilized capacity at 1089.3 mAh g⁻¹ over 300 cycles at 0.1 C. This electrode also delivers the highest capacity retention at 85.6%, indicating excellent reaction kinetics and cycling stability. Furthermore, the Ag/VN@Co/NCNTs@S electrode preserves a very small potential hysteresis over 300 cycles, indicating limited LiPS shuttling and stabilized sulfur reaction kinetics (**Figure 30**).

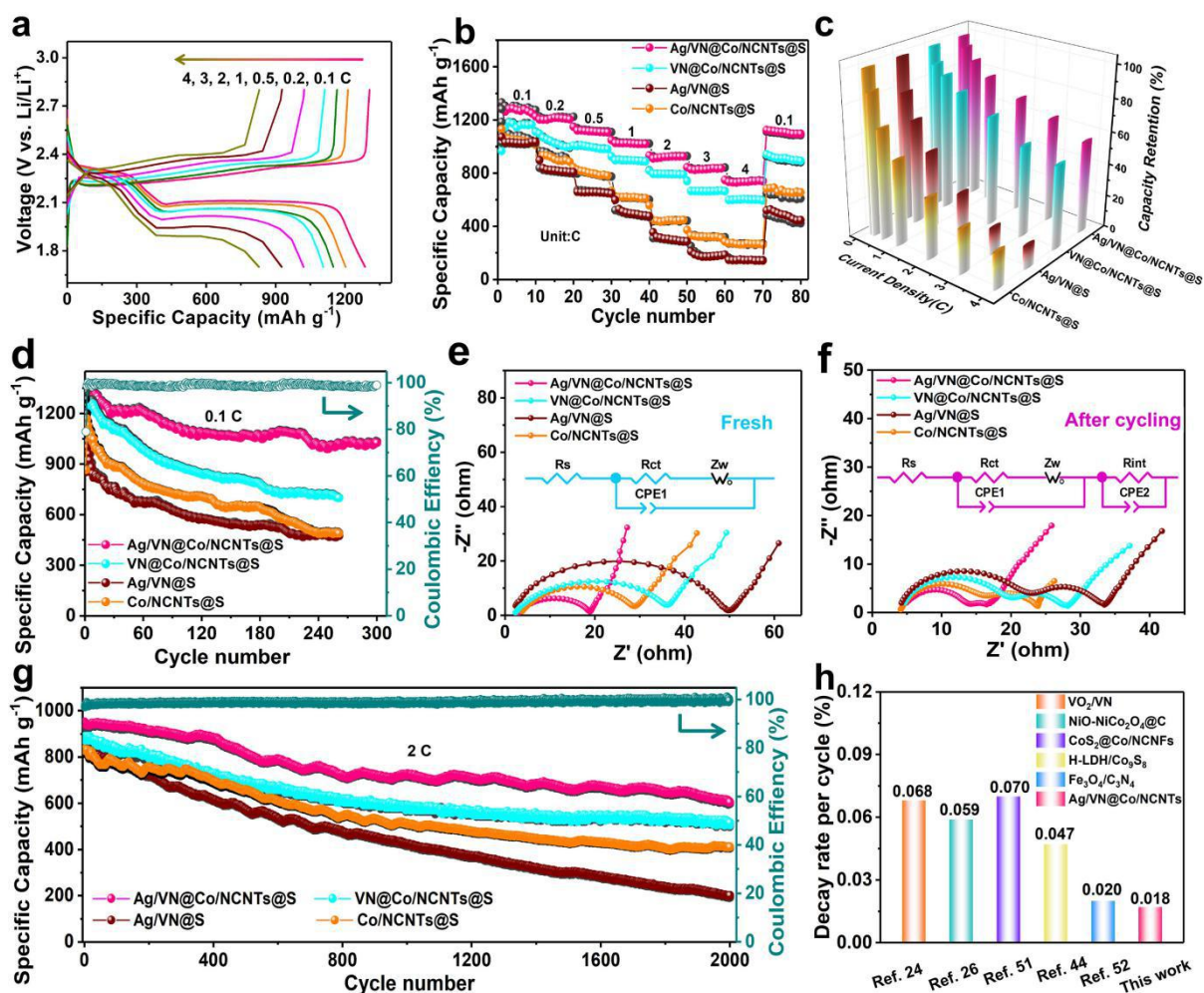


Figure 27 (a) Charge/discharge curves of a Ag/VN@Co/NCNTs@S nanocomposite at various rates from 0.1 C to 4 C. (b) Rate capability. (c) Corresponding capacity retention. (d) Cycle stability at 0.1 C for 300 cycles. (e) EIS spectra of the fresh electrodes. (f) EIS spectra of the electrodes after 300 cycles at 0.1 C. (g) Long-term cycling performance at 2 C for 2000 cycles. (h) Comparison of decay rate per cycle for Ag/VN@Co/NCNTs@S and other reported polar host materials.

Electrochemical impedance spectroscopy (EIS) analyses were carried out to gain a deeper understanding of the enhanced electrochemical performance of Ag/VN@Co/NCNTs@S electrodes. The EIS of the fresh cathodes were displayed in Figure 27e. In the equivalent circuit, R_{ct} is related to the charge transfer between the electrode and the electrolyte in the middle-frequency region. According to the fitting results (Table 1), the charge transfer resistance measured from Ag/VN@Co/NCNTs@S (16.71 Ω) is much smaller than the measured from Ag/VN (47.94 Ω), VN@Co/NCNTs (34.80 Ω), and Co/NCNTs (26.72 Ω). In Figure 27f and Table 2, Ag/VN@Co/NCNTs@S cells present considerably lower R_{int} (7.13 Ω)

than Co/NCNTs@S (7.25 Ω), VN@Co/NCNTs@S (13.63 Ω), and Ag/VN@S (19.85 Ω). The low R_{int} obtained from Ag/VN@Co/NCNTs@S cells is attributed to the inhibited formation of the insulating $\text{Li}_2\text{S}_2/\text{Li}_2\text{S}$ layer. This inhibition is related to the excellent catalytic activity towards LiPS conversion obtained from the synergistic contribution of Ag/VN, Co, and NCNTs within Ag/VN@Co/NCNTs.^{18,49}

The long-term cyclability of Ag/VN@Co/NCNTs@S electrodes is shown in Figure 27g. Ag/VN@Co/NCNTs@S electrodes are characterized by an outstanding cycling stability, with a capacity retention above 64% after 2000 cycles at 2 C, and a high and steady coulombic efficiency over 99.5%. This performance is well above that obtained from reference electrodes (Figure 27g). The high cycling stability of Ag/VN@Co/NCNTs@S electrodes suggests an effective inhibition of LiPS shuttling during LSBs charge and discharge. The comparison of LSB electrochemical results obtained for Ag/VN@Co/NCNTs@S with previously reported polar host materials and nanoreactors can be found in Figure 27h, **Table 3** and 4. Excitingly, Ag/VN@Co/NCNTs nanocomposites advantageously compare with previously developed host materials, *e.g.* VO_2/VN ,²⁴ $\text{NiO-NiCo}_2\text{O}_4/\text{C}$,²⁶ $\text{CoS}_2/\text{Co/NCFs}$,⁴⁸ $\text{H-LDH/Co}_9\text{S}_8$,⁵⁰ and $\text{Fe}_3\text{O}_4/\text{C}_3\text{N}_4$.⁴⁹

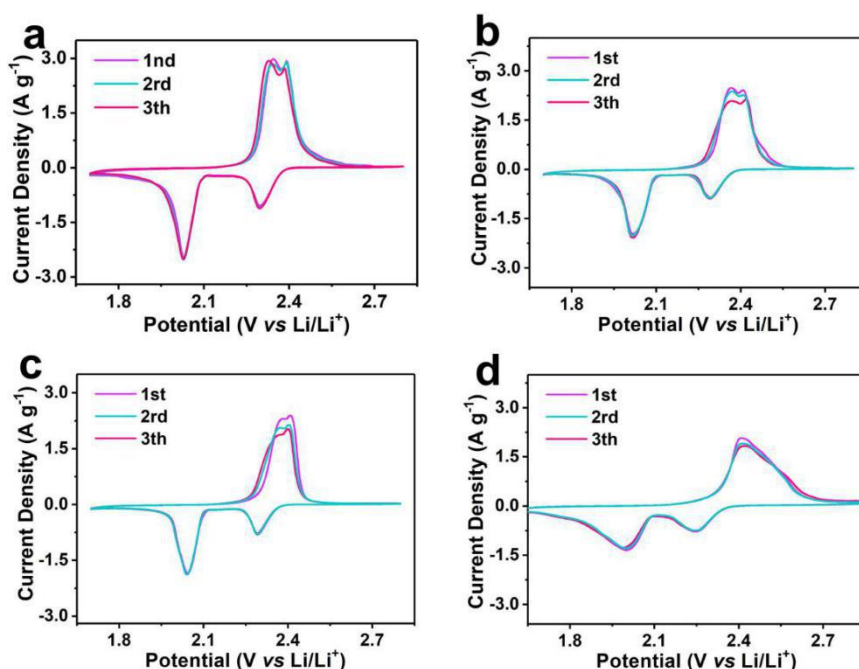


Figure 28. CV curves of (a) Ag/VN@Co/NCNTs@S, (b) VN@Co/NCNTs@S, (c) Ag/VN@S and (d) Co/NCNTs@S measured at 0.1 mV s^{-1} in the voltage range 1.7–2.8 V versus Li/Li^+ .

Disassembled cells after cycling provide another view to understand the chemical conversion in LSBs. The crystal structure and morphology of Ag/VN@Co/NCNTs@S after cycling was analyzed by SEM and XRD (**Figure 31**). After cycling, the hierarchical structure is maintained without obvious structural degradation, indicating excellent stability towards LiPS conversion reaction. **Figure 32** displays optical and SEM images of separators, lithium foil anodes, and cathode electrodes extracted from cells assembled with different cathode materials after 300 cycles. The separator extracted from the Ag/VN@Co/NCNTs@S cell showed the fewest yellowish-brown LiPS signs (Figure 32a). Additionally, thanks to the suppression of the shuttle effect, the surface of lithium foil in Ag/VN@Co/NCNTs@S cells was flat and very smooth, with minimal accumulation of lithium dendrites (Figure 32e). On the other hand, in Ag/VN@S and Co/NCNTs@S cells, shuttled LiPS clearly diffused across the separator and toward the surface of Li anode, severely corroding it (Figure 32 g,h).

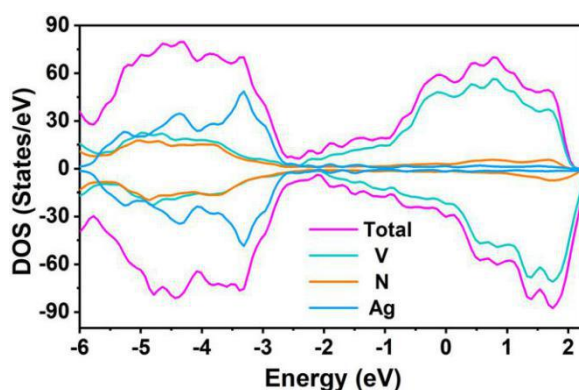


Figure 29. Calculated density of states of Ag/VN.

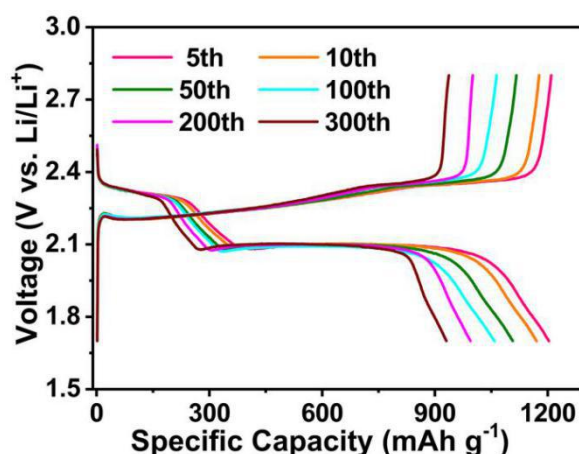


Figure 30. Charge/discharge curves of the Ag/VN@Co/NCNTs@S nanocomposite at the current rate of 0.1 C for the different cycles.

The cathode volume expansion was evaluated visually from the change in thickness before and after 300 cycles. The most serious cathode volume change among the four electrodes tested occurred for the composite containing no NCNTs, *i.e.* Ag/VN@S, which showed a 70.9% expansion (Figure 32k). This result evidences that the presence of NCNTs could certainly accommodate the volume change during the lithiation process (Figure 32 i, j, and l).

The above results demonstrate the important and different roles played by the different components within Ag/VN@Co/NCNTs electrodes and the synergism between them: Ag/VN heterostructures provide an excellent catalytic activity and act as a conductive backbone, realizing the rapid conversion of LiPS and inhibiting the shuttle effect. Co/NCNTs effectively inhibit volume expansion and suppress the diffusion of LiPS species out of the nanoreactors, thereby greatly increasing cycling stability. Through the synergistic cooperation between the components, hierarchical Ag/VN@Co/NCNTs nanocomposite achieve excellent electrochemical performances.

For practical applications, increasing the sulfur areal loading is essential to obtain high energy density LSBs. Therefore, the cycle performance of cells with different sulfur loading at the current density of 0.5 C was also tested (**Figure 33a**). Ag/VN@Co/NCNTs@S electrodes with a sulfur loading of 2.8 and 5.1 mg cm⁻² show excellent cycle performance, with a discharge capacity of 802.1 and 785.7 mAh g⁻¹ retained after 100 cycles and capacity retentions of 83.3% and 76.7%, respectively. At even higher sulfur loadings, 7.2 and 10.3 mg cm⁻², a good cycle performance is also achieved, with discharge capacities of 586.7 and 423.9 mAh g⁻¹, and relative areal capacities of 4.22 and 4.37 mAh cm⁻² after 100 cycles, which is comparable to commercial LIBs. These results show that Ag/VN@Co/NCNTs-based electrodes can effectively suppress the shuttling of LiPS and improve the cycling performance at high sulfur loading.

In view of the excellent electrochemical performance of Ag/VN@Co/NCNTs@S cathodes in coin cells, pouch cells were also fabricated according to the schematic diagram shown in Figure 33b. Ag/VN@Co/NCNTs@S-based pouch batteries have an initial discharge capacity of 1036 mAh g⁻¹ and maintain 724 mAh g⁻¹ at 0.5 C after 60 cycles (Figure 33d).

Table 1. Impedance (R_s and R_{ct}) of host materials before cycling.

Impedance	R_s (Ω)	R_{ct} (Ω)
Host material		
Co/NCNTs	4.17	26.72
Ag/VN	4.43	47.94
VN@Co/NCNTs	4.54	34.80
Ag/VN@Co/NCNTs	4.62	16.71

Table 2. Impedance (R_s , R_{ct} and R_{int}) of host materials after 300 cycles. The R_{int} is related to the charge transfer at the interface with the insulating Li_2S_2/Li_2S layer on the electrode surface.

Impedance	R_s (Ω)	R_{ct} (Ω)	R_{int} (Ω)
Host materials			
Co/NCNTs	4.57	10.79	7.25
Ag/VN	4.72	20.25	19.85
VN@Co/NCNTs	4.47	14.44	13.63
Ag/VN@Co/NCNTs	4.26	8.53	7.13

Table 3. Comparison of the electrochemical performance of Ag/VN@Co/NCNTs with other reported polar host materials.

Host materials	Capacity (mAh g ⁻¹)	Cycling stability	Decay rate (per cycle)	CE	Refs
MoN/VN	1436 (0.1 C) 636 (2 C)	72% (500 cycles, 1 C)	0.068%	99.0%	51 ⁵¹
C@SnO ₂ /1T-MoS ₂	1500 (0.2 C) 860 (5 C)	64% (4000 cycles, 5 C)	0.009%	99.0%	52 ⁵²
WS ₂ /WO ₃	1137 (0.3 C) 861 (3 C)	70% (500 cycles, 0.5C)	0.06%	99.5%	23 ²³
NCNT@Co-SnS ₂	1342 (3.2 mA cm ⁻¹)	52% (300 cycles, 2 C)	0.16%	100%	53 ⁵³
NiS ₂ /FeS	270 mAh cm ⁻³ (50 mA cm ⁻³)	52% (1000 cycles, 50 mA cm ⁻³)	0.01%	100%	54 ⁵⁴
V ₂ O ₃ /V ₈ C ₇	1348 (0.2 C) 788 (2 C)	83% (1000 cycles, 5 C)	0.017%	99.8%	17 ¹⁷
MoO ₂ -Mo ₃ N ₂	900 (0.5 C) 800 (1 C)	68% (1000 cycles, 1 C)	0.032%	100%	55 ⁵⁵
VSe ₂ -VG@CC	1480 (0.2 C) 450 (5 C)	69% (800 cycles, 5 C)	0.039%	100%	56 ⁵⁶
Sn _{0.063} MoO ₃	1390 (0.1 C) 903 (1 C)	80% (500 cycles, 1 C)	0.04%	99.7%	57 ⁵⁷
Fe _{3-x} C@C	1265 (0.2 C) 609 (5 C)	60% (1000 cycles, 1 C)	0.04%	99.0%	18 ¹⁸
TiO ₂ -Ni ₃ S ₂	893 (0.5 C) 534 (5 C)	66% (900 cycles, 5 C)	0.038%	99.0%	58 ⁵⁸
Ag/VN@Co/NCNTs	1307 (0.1 C) 609 (4 C)	64% (2000 cycles, 2 C)	0.018%	99.5%	This work

Table 4. Comparison of the electrochemical performance of hierarchical Ag/VN@Co/NCNTs nanoreactor with other reported nanoreactor-based host materials.

Host materials	Capacity (mAh g ⁻¹)	Cycling stability	Decay rate (per cycle)	CE	Refs
G-GCNs	1375 (0.1 C)	78.4%	0.021%	100%	59 ⁵⁹
	765 (5 C)	(1000 cycles, 1 C)			
C@MoS ₂	936 (0.2 C)	70%	0.030%	98.0%	29 ²⁹
	753 (2 C)	(1000 cycles, 2 C)			
Zn _{1-x} S-HNC	1180 (0.2 C)	89.5% (700 cycles, 5 C)	0.015%	100%	41 ⁴¹
3D-CNT/G	1217 (0.1 C)	83%	0.085%	91.0%	60 ⁶⁰
	653 (4 C)	(200 cycles, 0.2 C)			
Fe _{1-x} S-NC	1106 (0.5 C)	94%	0.003%	99.5%	30 ³⁰
	628 (5 C)	(200 cycles, 0.5 C)			
Fe-N/MHCS	1150 (0.1 C)	82.9%	0.018%	100%	61 ⁶¹
	949 (2 C)	(1000 cycles, 1 C)			
Ag/VN@Co/NCNTs	1307 (0.1 C)	64%	0.018%	99.5%	This work
	609 (4 C)	(2000 cycles, 2 C)			

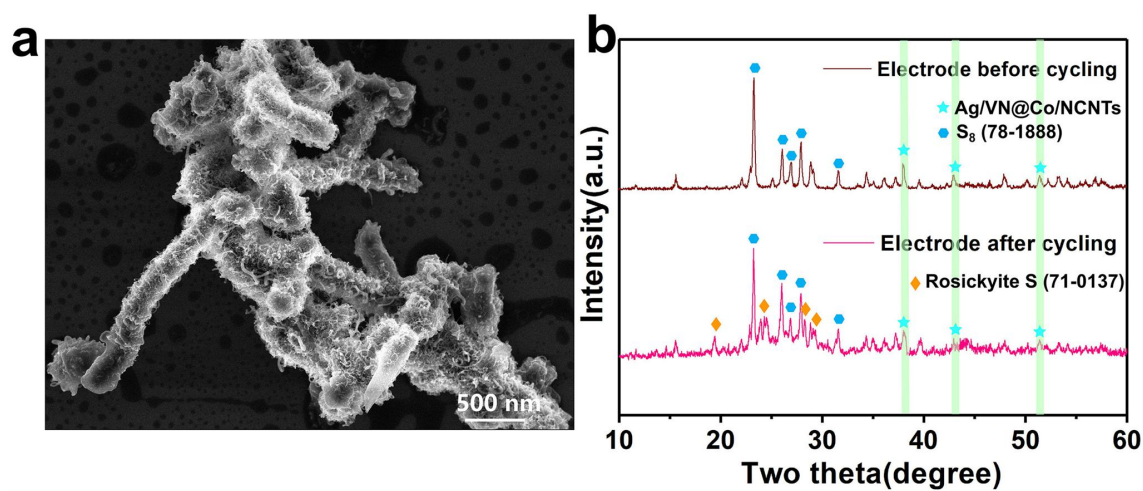


Figure 31. SEM and XRD patterns of electrode materials scraped from the Al foil before and after 300 cycles at 0.1 C.

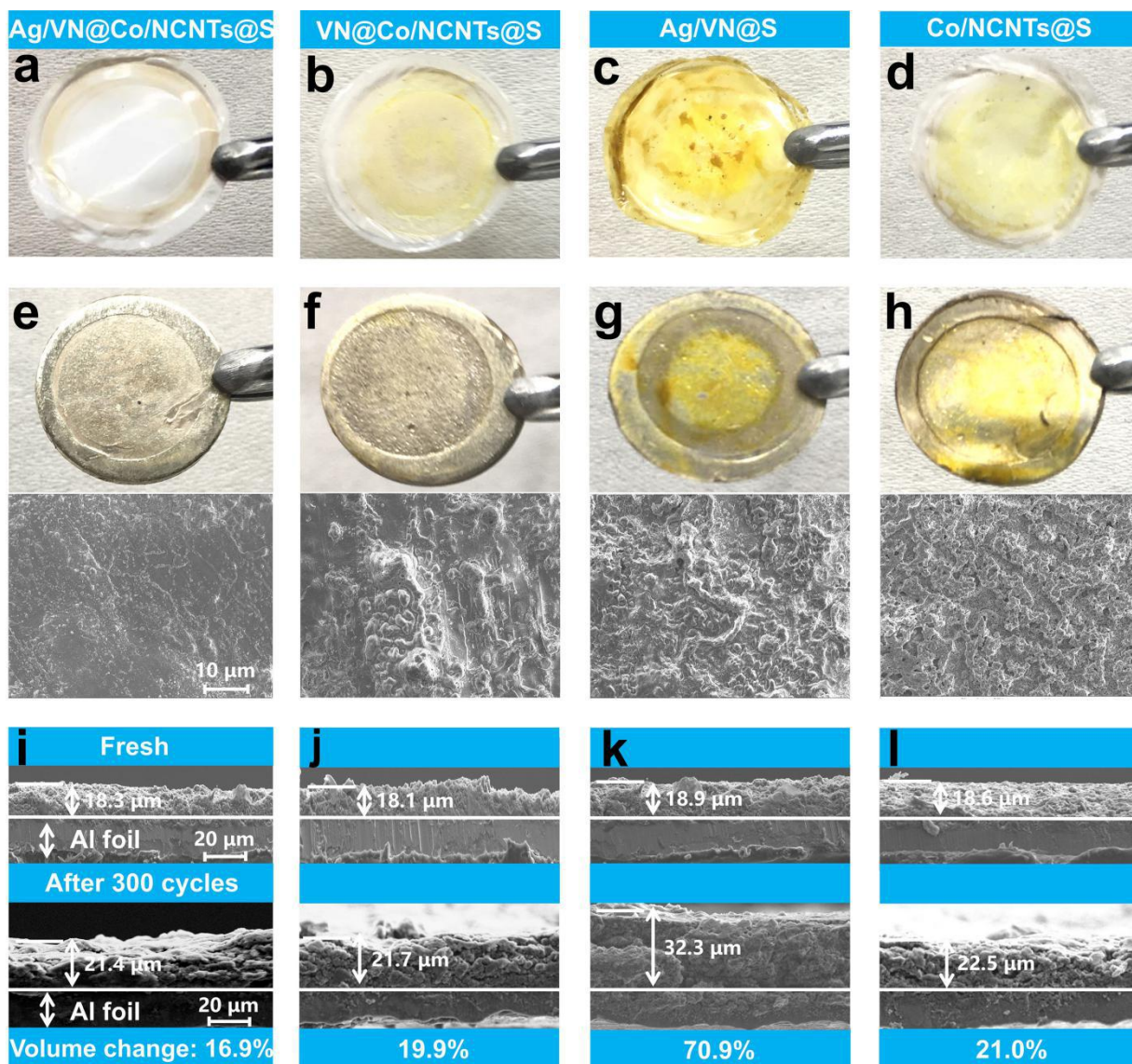


Figure 32. (a–d) Optical images of the separators recovered, after cycling, from cells containing the different cathode materials, as indicated on the top of each column. (e–h) Optical and SEM images of the recovered lithium foils. (i–l) Cross-sectional SEM images of the cathodes before (top) and after (bottom) 300 cycles at 0.1 C.

To demonstrate their potential, these pouch cells were used to power a wind car and even to charge a mobile phone (Figure 33c, Video 1). Even after 60 cycles, the pouch battery could easily light up the red diode shown in Figure 33d. All these results indicate that Ag/VN@Co/NCNTs@S electrodes can definitively help LSBs to reach practical applications.

Overall, the above characterization results prove that multifunctional Ag/VN@Co/NCNTs nanocomposites can deliver excellent electrochemical performance as cathode materials in

LSBs. Advantages are attributed both to the materials used and their structural properties (**Figure 34**). From the materials side, multicomponent Ag/VN@Co/NCNTs offer advantages in terms of: i) multiple adsorption sites in Ag/VN and Co to effectively confine LiPS and prevent their shuttle effect;⁶² ii) high electrical conductivity of Ag/VN heterostructures and NCNTs that ensure fast electron transfer;³⁵ and iii) excellent catalytic properties of Ag/VN toward Li-S reaction that enables a extensive sulfur usage and reduces LiPS shuttle effect.^{63–66} From the structural and organization side, electrochemical performance is promoted by: i) the independent nanosized reaction cavities acting as nanoreactors that allow the confinement of the Li-S reaction;^{49,67,68} ii) the hierarchical structure with an internal Ag/VN heterostructure backbone and an outer Co/NCNTs array that demonstrate an exceptional adsorption-catalysis synergistic effect; and iii) the large specific surface area of NCNTs habilitating a high sulfur dispersion and accommodating volume expansion.^{27,35,69–71}

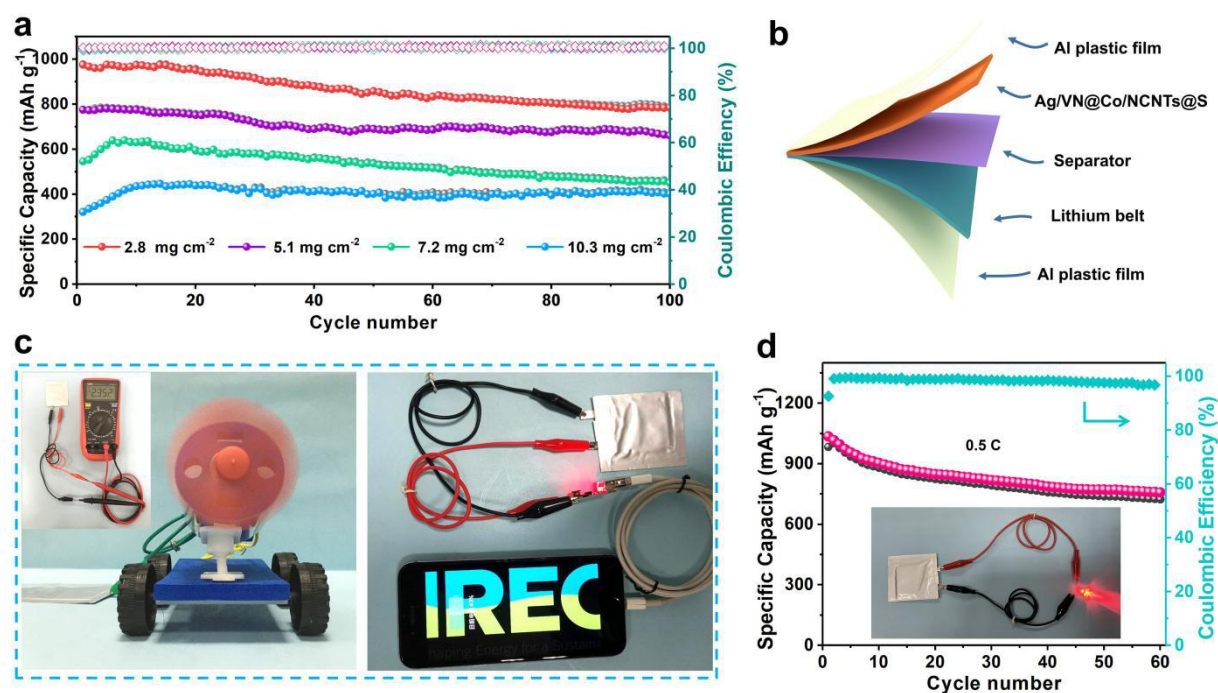


Figure 33. (a) Cycling performances at 0.5 C of Ag/VN@Co/NCNTs@S-based cells with different sulfur loads. (b) Schematic diagram of the Ag/VN@Co/NCNTs@S//Li pouch cell. (c) Digital photographs of a wind car powered by a pouch LSB (left) and of a pouch LSB used to charge a mobile phone (right). (d) Cycle stability of a pouch battery at 0.5 C for 60 cycles. Inset shows a red diode lighted by the pouch battery after 60 cycles.

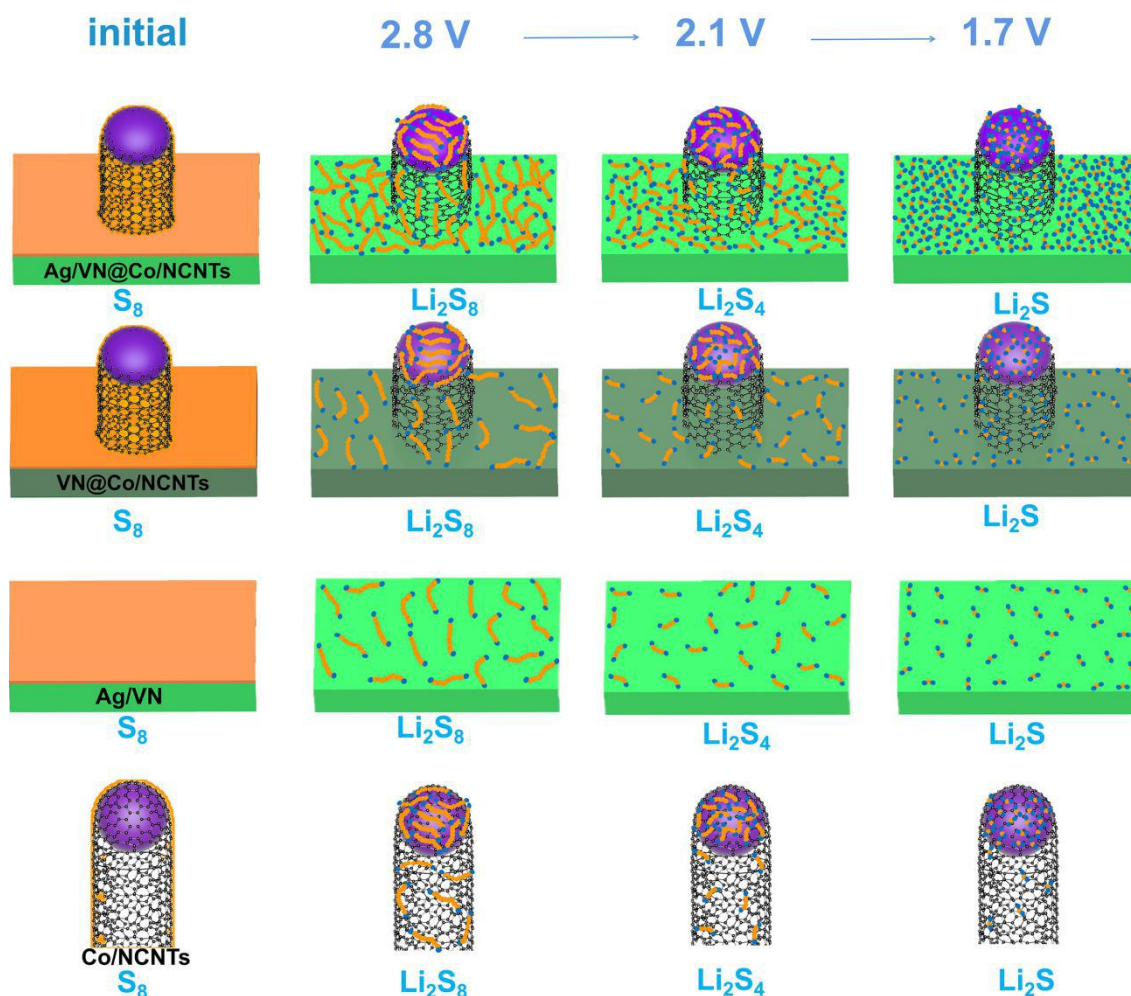


Figure 34. Schematic illustration of the mechanisms that allow Ag/VN@Co/NCNTs to inhibit the shuttle effect.

3.5 Conclusions

In summary, we reported a multifunctional Ag/VN@Co/NCNTs nanocomposite with multiple adsorption and catalytic sites within a hierarchical nanoreactor structure for robust LSBs. In the hierarchical nanoreactor, the internal Ag/VN heterostructure and outer Co nanoparticles serve as effective adsorption sites to confine the LiPS shuttle effect, as demonstrated by experimental results and DFT calculations. Metallic Ag/VN nanorods were used as the conductive backbone to assure fast electron transfer and to promote electrocatalytic activity. The interlinked NCNTs arrays allowed dispersion of sulfur and accommodated volume changes during charge/discharge processes. Besides, the nanoreactor structure not only served as a physical separation to provided independent Li-S reaction space, but also through the

coordination of the internal Ag/VN backbone and external Co/NCNTs array to deliver effective adsorption capacity and catalytic effect. Taking advantage from the synergistic effect of different components and structural merits of hierarchical nanoreactor, Ag/VN@Co/NCNTs@S cathodes revealed outstanding electrochemical performances. Besides, Ag/VN@Co/NCNTs@S cathodes within pouch cells demonstrated excellent potential for practical application. Overall, this work demonstrated the high potential of the hierarchical nanoreactor with multi-adsorption-catalytic sites in the field of LSBs.

3.6 References

- (1) Wei Seh, Z.; Sun, Y.; Zhang, Q.; Cui, Y. Designing High-Energy Lithium–Sulfur Batteries. *Chemical Society Reviews* **2016**, *45* (20), 5605–5634. <https://doi.org/10.1039/C5CS00410A>.
- (2) Chung, S.-H.; Manthiram, A. Current Status and Future Prospects of Metal–Sulfur Batteries. *Advanced Materials* **2019**, *31* (27), 1901125. <https://doi.org/10.1002/adma.201901125>.
- (3) Song, Y.; Cai, W.; Kong, L.; Cai, J.; Zhang, Q.; Sun, J. Rationalizing Electrocatalysis of Li–S Chemistry by Mediator Design: Progress and Prospects. *Advanced Energy Materials* **2020**, *10* (11), 1901075. <https://doi.org/10.1002/aenm.201901075>.
- (4) Wang, H.; Zhang, W.; Xu, J.; Guo, Z. Advances in Polar Materials for Lithium-Sulfur Batteries. *Advanced Functional Materials* **2018**, *28* (38), 1707520. <https://doi.org/10.1002/adfm.201707520>.
- (5) Zhou, L.; Danilov, D. L.; Eichel, R.; Notten, P. H. L. Host Materials Anchoring Polysulfides in Li–S Batteries Reviewed. *Advanced Energy Materials* **2020**, 2001304. <https://doi.org/10.1002/aenm.202001304>.
- (6) Bhargav, A.; He, J.; Gupta, A.; Manthiram, A. Lithium-Sulfur Batteries: Attaining the Critical Metrics. *Joule* **2020**, *4* (2), 285–291. <https://doi.org/10.1016/j.joule.2020.01.001>.
- (7) Ji, X.; Lee, K. T.; Nazar, L. F. A Highly Ordered Nanostructured Carbon–Sulphur Cathode for Lithium–Sulphur Batteries. *Nature Materials* **2009**, *8* (6), 500–506. <https://doi.org/10.1038/nmat2460>.
- (8) Zhu, J.; Tu, W.; Pan, H.; Zhang, H.; Liu, B.; Cheng, Y.; Deng, Z.; Zhang, H. Self-Templating Synthesis of Hollow Co₃O₄ Nanoparticles Embedded in

- N,S-Dual-Doped Reduced Graphene Oxide for Lithium Ion Batteries. *ACS Nano* **2020**, *14* (5), 5780–5787. <https://doi.org/10.1021/acsnano.0c00712>.
- (9) Kong, W.; Yan, L.; Luo, Y.; Wang, D.; Jiang, K.; Li, Q.; Fan, S.; Wang, J. Ultrathin MnO₂/Graphene Oxide/Carbon Nanotube Interlayer as Efficient Polysulfide-Trapping Shield for High-Performance Li–S Batteries. *Advanced Functional Materials* **2017**, *27* (18), 1606663. <https://doi.org/10.1002/adfm.201606663>.
- (10) Salhabi, E. H. M.; Zhao, J.; Wang, J.; Yang, M.; Wang, B.; Wang, D. Hollow Multi-Shelled Structural TiO_{2-x} with Multiple Spatial Confinement for Long-Life Lithium–Sulfur Batteries. *Angewandte Chemie* **2019**, *131* (27), 9176–9180. <https://doi.org/10.1002/ange.201903295>.
- (11) He, J.; Hartmann, G.; Lee, M.; S. Hwang, G.; Chen, Y.; Manthiram, A. Freestanding 1T MoS₂/Graphene Heterostructures as a Highly Efficient Electrocatalyst for Lithium Polysulfides in Li–S Batteries. *Energy & Environmental Science* **2019**, *12* (1), 344–350. <https://doi.org/10.1039/C8EE03252A>.
- (12) Liu, Y.; Ma, S.; Liu, L.; Koch, J.; Rosebrock, M.; Li, T.; Bettels, F.; He, T.; Pfnür, H.; Bigall, N. C.; Feldhoff, A.; Ding, F.; Zhang, L. Nitrogen Doping Improves the Immobilization and Catalytic Effects of Co₉S₈ in Li-S Batteries. *Advanced Functional Materials* **2020**, *30* (32), 2002462. <https://doi.org/10.1002/adfm.202002462>.
- (13) Xi, K.; He, D.; Harris, C.; Wang, Y.; Lai, C.; Li, H.; Coxon, P. R.; Ding, S.; Wang, C.; Kumar, R. V. Enhanced Sulfur Transformation by Multifunctional FeS₂/FeS/S Composites for High-Volumetric Capacity Cathodes in Lithium–Sulfur Batteries. *Advanced Science* **2019**, *6* (6), 1800815. <https://doi.org/10.1002/advs.201800815>.
- (14) Shen, J.; Xu, X.; Liu, J.; Liu, Z.; Li, F.; Hu, R.; Liu, J.; Hou, X.; Feng, Y.; Yu, Y.; Zhu, M. Mechanistic Understanding of Metal Phosphide Host for Sulfur Cathode in High-Energy-Density Lithium–Sulfur Batteries. *ACS Nano* **2019**, *13* (8), 8986–8996. <https://doi.org/10.1021/acsnano.9b02903>.
- (15) Wu, T.; Qi, J.; Xu, M.; Zhou, D.; Xiao, Z. Selective S/Li₂S Conversion via in-Built Crystal Facet Self-Mediation: Toward High Volumetric Energy Density Lithium–Sulfur Batteries. *ACS Nano* **2020**, *14* (11), 15011–15022. <https://doi.org/10.1021/acsnano.0c04933>.
- (16) He, J.; Bhargava, A.; Manthiram, A. Molybdenum Boride as an Efficient Catalyst for Polysulfide Redox to Enable High-Energy-Density Lithium–Sulfur Batteries. *Advanced Materials* **2020**, *32* (40), 2004741. <https://doi.org/10.1002/adma.202004741>.
- (17) Zhang, L.; Liu, Y.; Zhao, Z.; Jiang, P.; Zhang, T.; Li, M.; Pan, S.; Tang, T.; Wu, T.; Liu, P.; Hou, Y.; Lu, H. Enhanced Polysulfide Regulation via Porous Catalytic V₂O₃/V₈C₇ Heterostructures Derived from Metal–Organic Frameworks toward

- High-Performance Li–S Batteries. *ACS Nano* **2020**, *14* (7), 8495–8507. <https://doi.org/10.1021/acsnano.0c02762>.
- (18) Zhang, Y.; Li, G.; Wang, J.; Cui, G.; Wei, X.; Shui, L.; Kempa, K.; Zhou, G.; Wang, X.; Chen, Z. Hierarchical Defective Fe₃-XC@C Hollow Microsphere Enables Fast and Long-Lasting Lithium–Sulfur Batteries. *Advanced Functional Materials* **2020**, *30* (22), 2001165. <https://doi.org/10.1002/adfm.202001165>.
- (19) Ma, L.; Yuan, H.; Zhang, W.; Zhu, G.; Wang, Y.; Hu, Y.; Zhao, P.; Chen, R.; Chen, T.; Liu, J.; Hu, Z.; Jin, Z. Porous-Shell Vanadium Nitride Nanobubbles with Ultrahigh Areal Sulfur Loading for High-Capacity and Long-Life Lithium–Sulfur Batteries. *Nano Lett.* **2017**. <https://doi.org/10.1021/acs.nanolett.7b04084>.
- (20) Zhong, Y.; Chao, D.; Deng, S.; Zhan, J.; Fang, R.; Xia, Y.; Wang, Y.; Wang, X.; Xia, X.; Tu, J. Confining Sulfur in Integrated Composite Scaffold with Highly Porous Carbon Fibers/Vanadium Nitride Arrays for High-Performance Lithium-Sulfur Batteries. *Advanced Functional Materials* **2018**, *28* (38), 1706391. <https://doi.org/10.1002/adfm.201706391>.
- (21) Chen, W.; Jin, H.; Xie, S.; Xie, H.; Zhu, J.; Ji, H.; Wan, L.-J. TiN Nanocrystal Anchored on N-Doped Graphene as Effective Sulfur Hosts for High-Performance Lithium-Sulfur Batteries. *Journal of Energy Chemistry* **2021**, *54*, 16–22. <https://doi.org/10.1016/j.jechem.2020.05.007>.
- (22) Yao, Y.; Wang, H.; Yang, H.; Zeng, S.; Xu, R.; Liu, F.; Shi, P.; Feng, Y.; Wang, K.; Yang, W.; Wu, X.; Luo, W.; Yu, Y. A Dual-Functional Conductive Framework Embedded with TiN-VN Heterostructures for Highly Efficient Polysulfide and Lithium Regulation toward Stable Li–S Full Batteries. *Advanced Materials* **2020**, *32* (6), 1905658. <https://doi.org/10.1002/adma.201905658>.
- (23) Zhang, B.; Luo, C.; Deng, Y.; Huang, Z.; Zhou, G.; Lv, W.; He, Y.-B.; Wan, Y.; Kang, F.; Yang, Q.-H. Optimized Catalytic WS₂–WO₃ Heterostructure Design for Accelerated Polysulfide Conversion in Lithium–Sulfur Batteries. *Advanced Energy Materials* **2020**, *10* (15), 2000091. <https://doi.org/10.1002/aenm.202000091>.
- (24) Song, Y.; Zhao, W.; Kong, L.; Zhang, L.; Zhu, X.; Shao, Y.; Ding, F.; Zhang, Q.; Sun, J.; Liu, Z. Synchronous Immobilization and Conversion of Polysulfides on a VO₂–VN Binary Host Targeting High Sulfur Load Li–S Batteries. *Energy & Environmental Science* **2018**, *11* (9), 2620–2630. <https://doi.org/10.1039/C8EE01402G>.
- (25) Du, Z.; Chen, X.; Hu, W.; Chuang, C.; Xie, S.; Hu, A.; Yan, W.; Kong, X.; Wu, X.; Ji, H.; Wan, L.-J. Cobalt in Nitrogen-Doped Graphene as Single-Atom Catalyst for High-Sulfur Content Lithium–Sulfur Batteries. *J. Am. Chem. Soc.* **2019**, *141* (9), 3977–3985. <https://doi.org/10.1021/jacs.8b12973>.

- (26) Hu, L.; Dai, C.; Liu, H.; Li, Y.; Shen, B.; Chen, Y.; Bao, S.-J.; Xu, M. Double-Shelled NiO-NiCo₂O₄ Heterostructure@Carbon Hollow Nanocages as an Efficient Sulfur Host for Advanced Lithium-Sulfur Batteries. *Advanced Energy Materials* **2018**, *8* (23), 1800709. <https://doi.org/10.1002/aenm.201800709>.
- (27) Xiong, C.; Zhu, G. Y.; Jiang, H. R.; Chen, Q.; Zhao, T. S. Achieving Multiplexed Functionality in a Hierarchical MXene-Based Sulfur Host for High-Rate, High-Loading Lithium-Sulfur Batteries. *Energy Storage Materials* **2020**, *33*, 147–157. <https://doi.org/10.1016/j.ensm.2020.08.006>.
- (28) Cao, K.; Jiao, L.; Liu, Y.; Liu, H.; Wang, Y.; Yuan, H. Ultra-High Capacity Lithium-Ion Batteries with Hierarchical CoO Nanowire Clusters as Binder Free Electrodes. *Advanced Functional Materials* **2015**, *25* (7), 1082–1089. <https://doi.org/10.1002/adfm.201403111>.
- (29) Wu, Q.; Yao, Z.; Zhou, X.; Xu, J.; Cao, F.; Li, C. Built-In Catalysis in Confined Nanoreactors for High-Loading Li–S Batteries. *ACS Nano* **2020**, *14* (3), 3365–3377. <https://doi.org/10.1021/acsnano.9b09231>.
- (30) Boyjoo, Y.; Shi, H.; Olsson, E.; Cai, Q.; Wu, Z.-S.; Liu, J.; Lu, G. Q. (Max). Molecular-Level Design of Pyrrhotite Electrocatalyst Decorated Hierarchical Porous Carbon Spheres as Nanoreactors for Lithium–Sulfur Batteries. *Advanced Energy Materials* **2020**, *10* (20), 2000651. <https://doi.org/10.1002/aenm.202000651>.
- (31) Yang, D.; Zhang, C.; Biendicho, J. J.; Han, X.; Liang, Z.; Du, R.; Li, M.; Li, J.; Arbiol, J.; Llorca, J.; Zhou, Y.; Morante, J. R.; Cabot, A. ZnSe/N-Doped Carbon Nanoreactor with Multiple Adsorption Sites for Stable Lithium–Sulfur Batteries. *ACS Nano* **2020**, *14* (11), 15492–15504. <https://doi.org/10.1021/acsnano.0c06112>.
- (32) Han, C.; Pi, Y.; An, Q.; Mai, L.; Xie, J.; Xu, X.; Xu, L.; Zhao, Y.; Niu, C.; Khan, A. M.; He, X. Substrate-Assisted Self-Organization of Radial β -AgVO₃ Nanowire Clusters for High Rate Rechargeable Lithium Batteries. *Nano Lett.* **2012**, *12* (9), 4668–4673. <https://doi.org/10.1021/nl301993v>.
- (33) Chala, S. A.; Tsai, M.-C.; Su, W.-N.; Ibrahim, K. B.; Thirumalraj, B.; Chan, T.-S.; Lee, J.-F.; Dai, H.; Hwang, B.-J. Hierarchical 3D Architected Ag Nanowires Shelled with NiMn-Layered Double Hydroxide as an Efficient Bifunctional Oxygen Electrocatalyst. *ACS Nano* **2020**, *14* (2), 1770–1782. <https://doi.org/10.1021/acsnano.9b07487>.
- (34) Yan, D.-J.; Zhu, X.-D.; Wang, K.-X.; Gao, X.-T.; Feng, Y.-J.; Sun, K.-N.; Liu, Y.-T. Facile and Elegant Self-Organization of Ag Nanoparticles and TiO₂ Nanorods on V₂O₅ Nanosheets as a Superior Cathode Material for Lithium-Ion Batteries. *Journal of Materials Chemistry A* **2016**, *4* (13), 4900–4907. <https://doi.org/10.1039/C6TA01417H>.

- (35) Cao, Y.; Lu, H.; Hong, Q.; Xu, B.; Wang, J.; Deng, Y.; Yang, W.; Cai, W. Synthesis of Ag/Co@CoO NPs Anchored within N-Doped Hierarchical Porous Hollow Carbon Nanofibers as a Superior Free-Standing Cathode for LiO₂ Batteries. *Carbon* **2019**, *144*, 280–288. <https://doi.org/10.1016/j.carbon.2018.12.048>.
- (36) Li, Y.; Fan, J.; Zhang, J.; Yang, J.; Yuan, R.; Chang, J.; Zheng, M.; Dong, Q. A Honeycomb-like Co@N–C Composite for Ultrahigh Sulfur Loading Li–S Batteries. *ACS Nano* **2017**, *11* (11), 11417–11424. <https://doi.org/10.1021/acsnano.7b06061>.
- (37) Wang, J.; Yan, X.; Zhang, Z.; Ying, H.; Guo, R.; Yang, W.; Han, W.-Q. Facile Preparation of High-Content N-Doped CNT Microspheres for High-Performance Lithium Storage. *Advanced Functional Materials* **2019**, *29* (39), 1904819. <https://doi.org/10.1002/adfm.201904819>.
- (38) Ma, J.-L.; Meng, F.-L.; Xu, D.; Zhang, X.-B. Co-Embedded N-Doped Carbon Fibers as Highly Efficient and Binder-Free Cathode for Na–O₂ Batteries. *Energy Storage Materials* **2017**, *6*, 1–8. <https://doi.org/10.1016/j.ensm.2016.09.002>.
- (39) Yuan, J.; Hu, X.; Chen, J.; Liu, Y.; Huang, T.; Wen, Z. In Situ Formation of Vanadium Nitride Quantum Dots on N-Doped Carbon Hollow Spheres for Superior Lithium and Sodium Storage. *Journal of Materials Chemistry A* **2019**, *7* (15), 9289–9296. <https://doi.org/10.1039/C8TA12512K>.
- (40) Wei, Y.; Wang, B.; Zhang, Y.; Zhang, M.; Wang, Q.; Zhang, Y.; Wu, H. Rational Design of Multifunctional Integrated Host Configuration with Lithiophilicity-Sulfiphilicity toward High-Performance Li–S Full Batteries. *Advanced Functional Materials* **2021**, *31* (3), 2006033. <https://doi.org/10.1002/adfm.202006033>.
- (41) Shi, H.; Ren, X.; Lu, J.; Dong, C.; Liu, J.; Yang, Q.; Chen, J.; Wu, Z.-S. Dual-Functional Atomic Zinc Decorated Hollow Carbon Nanoreactors for Kinetically Accelerated Polysulfides Conversion and Dendrite Free Lithium Sulfur Batteries. *Advanced Energy Materials* **2020**, *10* (39), 2002271. <https://doi.org/10.1002/aenm.202002271>.
- (42) He, Y.; Li, M.; Zhang, Y.; Shan, Z.; Zhao, Y.; Li, J.; Liu, G.; Liang, C.; Bakenov, Z.; Li, Q. All-Purpose Electrode Design of Flexible Conductive Scaffold toward High-Performance Li–S Batteries. *Advanced Functional Materials* **2020**, *30* (19), 2000613. <https://doi.org/10.1002/adfm.202000613>.
- (43) Wang, J.; Luo, D.; Li, J.; Zhang, Y.; Zhao, Y.; Zhou, G.; Shui, L.; Chen, Z.; Wang, X. “Soft on Rigid” Nanohybrid as the Self-Supporting Multifunctional Cathode Electrocatalyst for High-Performance Lithium-Polysulfide Batteries. *Nano Energy* **2020**, *78*, 105293. <https://doi.org/10.1016/j.nanoen.2020.105293>.

- (44) Sun, Z.; Zhang, J.; Yin, L.; Hu, G.; Fang, R.; Cheng, H.-M.; Li, F. Conductive Porous Vanadium Nitride/Graphene Composite as Chemical Anchor of Polysulfides for Lithium-Sulfur Batteries. *Nature Communications* **2017**, *8*, 14627. <https://doi.org/10.1038/ncomms14627>.
- (45) Yuan, Z.; Peng, H.-J.; Hou, T.-Z.; Huang, J.-Q.; Chen, C.-M.; Wang, D.-W.; Cheng, X.-B.; Wei, F.; Zhang, Q. Powering Lithium–Sulfur Battery Performance by Propelling Polysulfide Redox at Sulfiphilic Hosts. *Nano Lett.* **2016**, *16* (1), 519–527. <https://doi.org/10.1021/acs.nanolett.5b04166>.
- (46) Qu, L.; Liu, P.; Yi, Y.; Wang, T.; Yang, P.; Tian, X.; Li, M.; Yang, B.; Dai, S. Enhanced Cycling Performance for Lithium–Sulfur Batteries by a Laminated 2D g-C₃N₄/Graphene Cathode Interlayer. *ChemSusChem* **2019**, *12* (1), 213–223. <https://doi.org/10.1002/cssc.201802449>.
- (47) He, J.; Bhargav, A.; Yaghoobnejad Asl, H.; Chen, Y.; Manthiram, A. 1T'-ReS₂ Nanosheets In Situ Grown on Carbon Nanotubes as a Highly Efficient Polysulfide Electrocatalyst for Stable Li–S Batteries. *Advanced Energy Materials* **2020**, *10* (23), 2001017. <https://doi.org/10.1002/aenm.202001017>.
- (48) Yao, S.; Zhang, C.; Guo, R.; Majeed, A.; He, Y.; Wang, Y.; Shen, X.; Li, T.; Qin, S. CoS₂-Decorated Cobalt/Nitrogen Co-Doped Carbon Nanofiber Networks as Dual Functional Electrocatalysts for Enhancing Electrochemical Redox Kinetics in Lithium–Sulfur Batteries. *ACS Sustainable Chem. Eng.* **2020**, *8* (36), 13600–13609. <https://doi.org/10.1021/acssuschemeng.0c02869>.
- (49) Kim, S.; Shirvani-Arani, S.; Choi, S.; Cho, M.; Lee, Y. Strongly Anchoring Polysulfides by Hierarchical Fe₃O₄/C₃N₄ Nanostructures for Advanced Lithium–Sulfur Batteries. *Nano-Micro Lett.* **2020**, *12* (1), 139. <https://doi.org/10.1007/s40820-020-00475-5>.
- (50) Chen, S.; Luo, J.; Li, N.; Han, X.; Wang, J.; Deng, Q.; Zeng, Z.; Deng, S. Multifunctional LDH/Co₉S₈ Heterostructure Nanocages as High-Performance Lithium–Sulfur Battery Cathodes with Ultralong Lifespan. *Energy Storage Materials* **2020**, *30*, 187–195. <https://doi.org/10.1016/j.ensm.2020.05.002>.
- (51) Ye, C.; Jiao, Y.; Jin, H.; Slattery, A. D.; Davey, K.; Wang, H.; Qiao, S.-Z. 2D MoN-VN Heterostructure to Regulate Polysulfides for Highly Efficient Lithium-Sulfur Batteries. *Angew. Chem. Int. Ed.* **2018**, *26*.
- (52) Wang, M.; Fan, L.; Tian, D.; Wu, X.; Qiu, Y.; Zhao, C.; Guan, B.; Wang, Y.; Zhang, N.; Sun, K. Rational Design of Hierarchical SnO₂/1T-MoS₂ Nanoarray Electrode for Ultralong-Life Li–S Batteries. *ACS Energy Lett.* **2018**, *3* (7), 1627–1633. <https://doi.org/10.1021/acsenerylett.8b00856>.

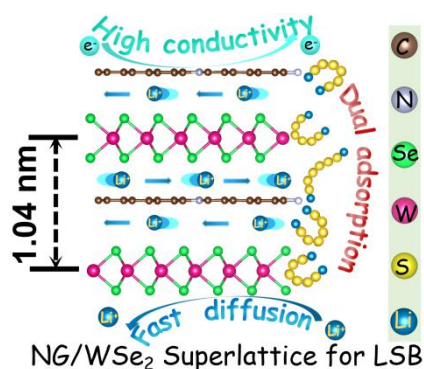
- (53) Gao, X.; Yang, X.; Li, M.; Sun, Q.; Liang, J.; Luo, J.; Wang, J.; Li, W.; Liang, J.; Liu, Y.; Wang, S.; Hu, Y.; Xiao, Q.; Li, R.; Sham, T.-K.; Sun, X. Cobalt-Doped SnS₂ with Dual Active Centers of Synergistic Absorption-Catalysis Effect for High-S Loading Li-S Batteries. *Advanced Functional Materials* **2019**, *29* (8), 1806724. <https://doi.org/10.1002/adfm.201806724>.
- (54) Liang, K.; Marcus, K.; Zhang, S.; Zhou, L.; Li, Y.; De Oliveira, S. T.; Orlovskaya, N.; Sohn, Y.-H.; Yang, Y. NiS₂/FeS Holey Film as Freestanding Electrode for High-Performance Lithium Battery. *Advanced Energy Materials* **2017**, *7* (22), 1701309. <https://doi.org/10.1002/aenm.201701309>.
- (55) Li, R.; Zhou, X.; Shen, H.; Yang, M.; Li, C. Conductive Holey MoO₂-Mo₃N₂ Heterojunctions as Job-Synergistic Cathode Host with Low Surface Area for High-Loading Li-S Batteries. *ACS Nano* **2019**, *13* (9), 10049-10061. <https://doi.org/10.1021/acsnano.9b02231>.
- (56) Ci, H.; Cai, J.; Ma, H.; Shi, Z.; Cui, G.; Wang, M.; Jin, J.; Wei, N.; Lu, C.; Zhao, W.; Sun, J.; Liu, Z. Defective VSe₂-Graphene Heterostructures Enabling In Situ Electrocatalyst Evolution for Lithium-Sulfur Batteries. *ACS Nano* **2020**, *14* (9), 11929-11938. <https://doi.org/10.1021/acsnano.0c05030>.
- (57) Yang, W.; Xiao, J.; Ma, Y.; Cui, S.; Zhang, P.; Zhai, P.; Meng, L.; Wang, X.; Wei, Y.; Du, Z.; Li, B.; Sun, Z.; Yang, S.; Zhang, Q.; Gong, Y. Tin Intercalated Ultrathin MoO₃ Nanoribbons for Advanced Lithium-Sulfur Batteries. *Advanced Energy Materials* **2019**, *9* (7), 1803137. <https://doi.org/10.1002/aenm.201803137>.
- (58) Wang, R.; Luo, C.; Wang, T.; Zhou, G.; Deng, Y.; He, Y.; Zhang, Q.; Kang, F.; Lv, W.; Yang, Q. Bidirectional Catalysts for Liquid-Solid Redox Conversion in Lithium-Sulfur Batteries. *Adv. Mater.* **2020**, 2000315. <https://doi.org/10.1002/adma.202000315>.
- (59) Zhang, J.; Yang, C.-P.; Yin, Y.-X.; Wan, L.-J.; Guo, Y.-G. Sulfur Encapsulated in Graphitic Carbon Nanocages for High-Rate and Long-Cycle Lithium-Sulfur Batteries. *Advanced Materials* **2016**, *28* (43), 9539-9544. <https://doi.org/10.1002/adma.201602913>.
- (60) He, J.; Chen, Y.; Li, P.; Fu, F.; Wang, Z.; Zhang, W. Three-Dimensional CNT/Graphene-Sulfur Hybrid Sponges with High Sulfur Loading as Superior-Capacity Cathodes for Lithium-Sulfur Batteries. *Journal of Materials Chemistry A* **2015**, *3* (36), 18605-18610. <https://doi.org/10.1039/C5TA04445F>.
- (61) Shao, Q.; Xu, L.; Guo, D.; Su, Y.; Chen, J. Atomic Level Design of Single Iron Atom Embedded Mesoporous Hollow Carbon Spheres as Multi-Effect Nanoreactors for Advanced Lithium-Sulfur Batteries. *Journal of Materials Chemistry A* **2020**, *8* (45), 23772-23783. <https://doi.org/10.1039/D0TA07010F>.

- (62) Zhang, C.; Biendicho, J. J.; Zhang, T.; Du, R.; Li, J.; Yang, X.; Arbiol, J.; Zhou, Y.; Morante, J. R.; Cabot, A. Combined High Catalytic Activity and Efficient Polar Tubular Nanostructure in Urchin-Like Metallic NiCo₂Se₄ for High-Performance Lithium–Sulfur Batteries. *Advanced Functional Materials* **2019**, *29* (34), 1903842. <https://doi.org/10.1002/adfm.201903842>.
- (63) Li, S.; Sun, X.; Yao, Z.; Zhong, X.; Cao, Y.; Liang, Y.; Wei, Z.; Deng, S.; Zhuang, G.; Li, X.; Wang, J. Biomass Valorization via Paired Electrosynthesis Over Vanadium Nitride-Based Electrocatalysts. *Advanced Functional Materials* **2019**, *29* (42), 1904780. <https://doi.org/10.1002/adfm.201904780>.
- (64) Gueon, D.; Hwang, J. T.; Yang, S. B.; Cho, E.; Sohn, K.; Yang, D.-K.; Moon, J. H. Spherical Macroporous Carbon Nanotube Particles with Ultrahigh Sulfur Loading for Lithium–Sulfur Battery Cathodes. *ACS Nano* **2018**, *12* (1), 226–233. <https://doi.org/10.1021/acsnano.7b05869>.
- (65) Park, S.-K.; Lee, J.-K.; Kang, Y. C. Yolk-Shell Structured Assembly of Bamboo-Like Nitrogen-Doped Carbon Nanotubes Embedded with Co Nanocrystals and Their Application as Cathode Material for Li-S Batteries. *Advanced Functional Materials* **2018**, *28* (18), 1705264. <https://doi.org/10.1002/adfm.201705264>.
- (66) Lee, B.-J.; Kang, T.-H.; Lee, H.-Y.; Samdani, J. S.; Jung, Y.; Zhang, C.; Yu, Z.; Xu, G.-L.; Cheng, L.; Byun, S.; Lee, Y. M.; Amine, K.; Yu, J.-S. Revisiting the Role of Conductivity and Polarity of Host Materials for Long-Life Lithium–Sulfur Battery. *Advanced Energy Materials* **2020**, *10* (22), 1903934. <https://doi.org/10.1002/aenm.201903934>.
- (67) Ye, Z.; Jiang, Y.; Li, L.; Wu, F.; Chen, R. A High-Efficiency CoSe Electrocatalyst with Hierarchical Porous Polyhedron Nanoarchitecture for Accelerating Polysulfides Conversion in Li–S Batteries. *Advanced Materials* **2020**, *32* (32), 2002168. <https://doi.org/10.1002/adma.202002168>.
- (68) Li, Y.; Wang, C.; Wang, W.; Eng, A. Y. S.; Wan, M.; Fu, L.; Mao, E.; Li, G.; Tang, J.; Seh, Z. W.; Sun, Y. Enhanced Chemical Immobilization and Catalytic Conversion of Polysulfide Intermediates Using Metallic Mo Nanoclusters for High-Performance Li–S Batteries. *ACS Nano* **2020**, *14* (1), 1148–1157. <https://doi.org/10.1021/acsnano.9b09135>.
- (69) Fang, D.; Wang, Y.; Qian, C.; Liu, X.; Wang, X.; Chen, S.; Zhang, S. Synergistic Regulation of Polysulfides Conversion and Deposition by MOF-Derived Hierarchically Ordered Carbonaceous Composite for High-Energy Lithium–Sulfur Batteries. *Advanced Functional Materials* **2019**, *29* (19), 1900875. <https://doi.org/10.1002/adfm.201900875>.

- (70) Xiao, Z.; Li, Z.; Li, P.; Meng, X.; Wang, R. Ultrahigh Volumetric Capacity Enabled by Dynamic Evolutions of Host-Guest Pairs in Self-Supporting Lithium-Sulfur Batteries. *Nano Energy* **2020**, *70*, 104522. <https://doi.org/10.1016/j.nanoen.2020.104522>.
- (71) Wang, Z.; Shen, J.; Liu, J.; Xu, X.; Liu, Z.; Hu, R.; Yang, L.; Feng, Y.; Liu, J.; Shi, Z.; Ouyang, L.; Yu, Y.; Zhu, M. Self-Supported and Flexible Sulfur Cathode Enabled via Synergistic Confinement for High-Energy-Density Lithium–Sulfur Batteries. *Advanced Materials* **2019**, *31* (33), 1902228. <https://doi.org/10.1002/adma.201902228>.

Chapter 4

Robust Lithium-Sulfur Batteries Enabled by Highly Conductive WSe₂-based Superlattices with Tunable Interlayer Space



4.1 Abstract

Superlattices are rising stars on the horizon of energy storage and conversion bringing new functionalities, but their complex synthesis limits their large-scale production and application. Herein, we report a simple solution-based method to produce organic-inorganic superlattices and demonstrate that the pyrolysis of the organic compound enables tuning their interlayer space. This strategy is exemplified here by combining polyvinyl pyrrolidone (PVP) with WSe₂ within PVP/WSe₂ superlattices. The annealing of such heterostructures results in N-doped graphene/WSe₂ (NG/WSe₂) superlattices with a continuously adjustable interlayer space in the range from 10.4 Å to 21 Å. Such NG/WSe₂ superlattices show a metallic electronic character with outstanding electrical conductivities. Both experimental results and theoretical calculations further demonstrate that these superlattices are excellent sulfur hosts at the cathode of lithium-sulfur batteries (LSB), being able to effectively reduce the lithium polysulfide shuttle effect by dual-adsorption sites and accelerating the sluggish Li-S reaction kinetics. Consequently, S@NG/WSe₂ electrodes enable LSBs characterized by high sulfur usages, superior rate performance, and outstanding cycling stability, even at high sulfur loadings, lean electrolyte conditions and at the pouch cell level. Overall, this work not only

establishes a cost-effective strategy to produce artificial superlattice materials but also pioneers their application in the field of LSBs.

4.2 Introduction

Since the discovery of graphene in 2004, the two-dimensional (2D) material family has grown rapidly.^[1,2] A plethora of monolayered 2D materials produced by exfoliating bulk layered materials have demonstrated fascinating physical and chemical properties.^[3] Besides, these monolayer nanosheets have been combined and stacked together with extraordinary control to form new 2D heterostructures and superlattice materials.^[4-6] These artificial structures further enrich the family of 2D materials with new functionalities, providing unprecedented performances when applied to the fields of light-emitting diodes, field-effect transistors, quantum devices, as well as energy storage and conversion, among others.^[7] Since the possible combinations are virtually unlimited, numerous new 2D superlattices with unique properties and functionalities are yet to be designed, engineered, and tested in different application fields.

Despite the advantages of 2D superlattice materials, their large-scale synthesis is still challenging, which limits their commercial application. Superlattice structures are generally produced by low throughput methodologies, such as layer-by-layer mechanical assembly or epitaxial growth by chemical vapour deposition, which makes them incompatible with material-intensive applications such as energy storage.^[8,9] Other proposed methodologies, such as the flocculating self-assembly of solution-dispersed nanosheets, still rely on the laborious precursor exfoliation step that limits the process scale-up.^[5,10] Thus the development of alternative cost-effective methods for the mass production of functional 2D superlattice materials is essential for their commercial implementation.

In the electrochemistry field, superlattice materials offer the unique advantages of tuneable interlayer spacing and improved conductivity on the base of an adjustable electronic band structure^[11,12]. The former can provide fast 2D diffusion channels for the transport of reactants,^[13] and the latter allows optimizing charge transport/injection and electrocatalytic activity.^[10,14] In the field of energy storage, proper tailoring of the interlayer spacing has great

potential for the engineering of the next generation of hybrid ion supercapacitors and secondary batteries based on Mg/K/Zn for instance.^[7] However, effective optimization of the material functional properties requires a precise tuning of its structural and chemical properties that has remained elusive. While superlattice materials with enlarged interlayer spacing have been reported,^[5] a continuous and precise adjustment of the interlayer spacing to provide ion-selective 2D channels is yet to be accomplished.

Among other exciting applications, the unique characteristics of superlattice materials have the potential to solve the current limitations of lithium-sulfur batteries (LSBs). Recently, the Sasaki group reported Nb₃O₈/graphene superlattice as a three-in-one cathode host to prevent the lithium polysulfide (LiPS) shuttle effect, accelerate LiPS conversion, and promote Li₂S nucleation, delivering superior electrochemical performance.^[15] In terms of host material design, carbon materials and transitional metal dichalcogenides have been extensively investigated as cathode sulfur hosts to boost the performance of LSBs, but a single component host cannot meet the strict requirements of LSBs^[16–19] While graphene and other carbon supports can provide high specific surface area and electrical conductivity, their nonpolar surfaces are unable to anchor the soluble LiPS and catalyze their reaction.^[20,21] On the other hand, dichalcogenides provide polar surfaces to effectively anchor LiPS and catalyze LiPS conversion,^[22–25] but are characterized by moderate electrical conductivities, especially those characterized by layered structures with weak van der Waals interlayer bonding that shields electron transport between layers.^[26] Because graphene and metal dichalcogenides show highly complementary properties and limitations as sulfur hosts in LSB cathodes, the development of graphene-transition metal dichalcogenide superlattices that combine the complementary advantages of the two materials would have great potential to improve LSB performance. Nevertheless, surprisingly, such superlattice materials have never been designed, engineered, optimized, or tested within an LSB.

Herein, we report a simple two-step method for the cost-effective production of highly conductive N-doped graphene/WSe₂ (NG/WSe₂) superlattices. First, a scalable solvothermal method is employed to produce hybrid organic-inorganic polymer-WSe₂ superlattices with intercalated polyvinyl pyrrolidone (PVP). After a subsequent calcination step, NG/WSe₂

superlattices with an adjustable bandgap and WSe₂ layer spacing are obtained. Both experimental results and theoretical calculations are used to demonstrate that such composites can accelerate the Li⁺ transport during Li-S reaction, improve the electrical conductivity, and optimize the Li-S redox catalysis reaction. Moreover, dual LiPS adsorption sites at the superlattice interface effectively inhibit the shuttle effect and boost the cycling stability.

4.3 Experimental Section

Preparing r-WSe₂, WSe₂-800, p-WSe₂ and NG/WSe₂. p-WSe₂ nanosheets were prepared by a one-pot solvothermal method. NG/WSe₂ nanosheets were obtained by the calcination of p-WSe₂ within a controlled atmosphere. Typically, 158 mg of selenium powder and 80 mg of sodium borohydride (NaBH₄) were dissolved in 15 mL N, N-dimethylformamide (DMF), and the mixture was continuously stirred for about 30 minutes until a dark brown solution (Solution A) was obtained. Solution B was obtained by dissolving 248 mg of ammonium metatungstate (AMT) and 350 mg polyvinyl pyrrolidone (PVP) in 15 mL DMF with 15 minutes of stirring. Subsequently, Solution B was poured into Solution A and the mixture was stirred for 5 minutes. Then, the resultant solution was transferred into an autoclave, which was sealed, and heated at 240 °C for 24 h. After cooling down naturally, the black product was washed with DMF, ethanol and deionized water several times to remove the precursor residues. The obtained produce was then freeze-dried for 24 h to obtain p-WSe₂ nanosheets. For calcination, the obtained black powder was sealed in a small quartz tube filled with Ar gas, and heated for 2 hours at 800 °C with a 5 °C/min heating rate to obtain ca. 290 mg NG/WSe₂ nanosheets with a yield of 84.8% (calculated based on the quantity of W and Se precursor used). Other calcined products were prepared by the same process but varying the calcination temperatures and they were named p-WSe₂-X (X=calcination temperature). The r-WSe₂ and WSe₂-800 nanosheets were obtained by the same process but without adding PVP. N-carbon was prepared by annealing PVP powder under 800°C with Ar gas protection with a 5 °C/min heating rate.

Preparing of XX-WSe₂ and XX-WSe₂-800 nanosheets (XX=CTAB, SDS, F127, GLU).

XX-WSe₂ and XX-WSe₂-800 samples were obtained by the same methods of p-WSe₂ and NG/WSe₂ nanosheets preparation, but employing another organic/polymer to replace PVP.

Synthesis of S@NG/WSe₂, S@WSe₂-800, S@GLU-WSe₂ and S@G. Typically, NG/WSe₂, WSe₂-800, GLU-WSe₂ and graphene (G, Sigma Aldrich, 99.5%) were mixed with sulfur powder (Sigma Aldrich, 99.98%) separately with a weight ratio of 1:3, and then the mixture was heated to 155 °C overnight in a sealed glass bottle under Ar protection. The redundant sulfur was removed by 3 mL CS₂ (99.9%, Alfa Aesa) and ethanol solution (1:4, volume ratio).

Materials Characterization: The crystallographic structural information of the as-prepared products was characterized by X-ray diffraction (XRD, Miniflex 600) with Cu K radiation ($\lambda = 1.5106 \text{ \AA}$) operating at 40 kV and 15 mA. The morphology and microstructure of samples were investigated by field emission scanning electron microscopy (FESEM, ZEISS Auriga) equipped with an energy-dispersive X-ray spectroscopy (EDS) detector operated at 15-20 kV. High-resolution transmission electron microscopy (HRTEM) and scanning TEM (STEM) studies were carried out using a field emission gun FEI Tecnai F20 microscope at 200 kV with a point-to-point resolution of 0.19 nm. Elemental mapping analysis was conducted via high-angle annular dark-field scanning TEM energy-dispersive X-ray spectroscopy (HAADF-STEM-EDS). The chemical composition and the valence states of the products were observed by employing an X-ray photoelectron spectroscopy (XPS, Thermo Fisher Scientific, ESCALAB 250). The content of sulfur in the composites was estimated by thermogravimetric analysis (TGA, NETZSCH, STA449-F5) experiments under N₂ atmosphere. The specific surface area and analysis of the pore size distribution were obtained from nitrogen adsorption-desorption isotherms on Gemini VII2390 system. UV-vis absorption spectra were identified by the PerkinElmer LAMBDA 950 UV-vis spectrophotometer. The Raman spectrum was recorded by a Raman Microscope (Thermo Electron Corporation, DXR2Xi). Electrical conductivities were measured using a four-point probe technique (Keithley 2400, Tektronix), and all of the samples before the test were pressed into $\Phi 12$ mm disks with ca. 1 mm thickness.

Li-S cell assembly and measurements: Li-S batteries performance was tested at room temperature in CR2032 coin-type cells. Lithium foils were used as the anode, Celgard 2400 membranes as separators, and S@host composites as the cathode. The assembly process was conducted in a glovebox filled with argon. The cathode was obtained by doctor blading.

Briefly, S@host composites (S@NG/WSe₂; S@WSe₂-800 and S@G), conductive carbon, and PVDF binder (weight ratio = 80:10:10) were mixed within N-methyl pyrrolidone (NMP, 99.5%, Acros Organics) to form a black slurry, which was coated on Al foils and dried at 60 °C overnight. After drying, the foil was punched into small disks with 1.0 mg cm⁻² sulfur loading. The electrolyte was prepared by dissolving 1.0 M lithium bis(trifluoromethanesulfonyl)imide (LiTFSI) (99%, Acros Organics) into a solution of 1,2-dimethoxy ethane (DME, 99%, Honeywell) and 1,3-dioxolane (DOL, 99.5%, Alfa Aesar) (v/v = 1/1) and containing 0.2 M of LiNO₃ (99.98%, Alfa Aesar). For each coin cell, 15 mL g⁻¹_{Sulfur} of electrolyte was used. To realize higher sulfur loadings, the mixed slurry was coated on a carbon paper with 5.2 mg cm⁻² sulfur-loading, and the electrolyte was added with the ratio of 11.6, 7.8, and 4.8 mL g⁻¹_{Sulfur}. The Li-S cells were galvanostatically cycled within a voltage window of 1.7-2.8 V on a LAND CT2001A battery tester with different C rates. Low current activation was conducted before the cycling test. Cyclic voltammetry (CV) measurements were performed on an electrochemical tester Gamry Interface 5000E at a scan rate of 0.1-0.4 mV s⁻¹. Electrochemical impedance spectroscopy (EIS) tests were conducted to fresh cells after 10 hours standing and cycled cells under charge state, the voltage amplitude of 10 mV was selected with the frequency range 100 kHz to 10 mHz.

Preparation of Li₂S₄ solutions for adsorption test: Sulfur and Li₂S (99.9%, Alfa Aesar) were mixed with the molar ratio of 3:1, and then the powder was poured into appropriate amounts of DME/DOL (volume ratio of 1:1) solution under vigorous magnetic stirring overnight until a dark brown solution was obtained. 20 mg of NG/WSe₂, WSe₂-800 and G were poured into 3.0 mL 10 mM Li₂S₄ solution, respectively. All the steps were conducted under Ar atmosphere.

Measurement of nucleation and dissolution of Li₂S: Nucleation and dissolution of Li₂S were conducted in CR2032 coin cells. 1 mg of host materials was loaded on the carbon papers applied as working electrodes. Li foil worked as the counter electrode. 20 μL catholyte was added in the positive side, in which 0.25 M Li₂S₈ was dissolved in tetraglyme with 1.0 M LiTFSI added. 20 μL of 1.0 M LiTFSI in tetraglyme solution was used as anolyte. The cells

were first discharged at a current of 0.112 mA to 2.06 V and then hold the voltage at 2.05 V until the current decreased to 10^{-2} mA for Li_2S nucleation and growth.

Pouch cell assembly and measurements: Both the S@NG/WSe₂ cathode and lithium anode were cut into 6×5 cm pieces. The sulfur loading of the cathode in the pouch cell (6×5 cm) was 2 mg cm^{-2} (total sulfur loading: 60 mg). The E/S ratio was about $15 \text{ mL g}^{-1}_{\text{Sulfur}}$, the thickness of the lithium belt anode was 0.4 mm. The pouch cell with high-sulfur loading (4.3 mg cm^{-2}) and low electrolyte usage ($5.8 \text{ mL g}^{-1}_{\text{Sulfur}}$) employed 4×3 cm carbon paper as the cathode current collector. The separator and electrolyte were sandwiched between the tailored S@NG/WSe₂ and lithium belt. The pouch cell was galvanostatically cycled within a voltage range of 1.7–2.8 V.

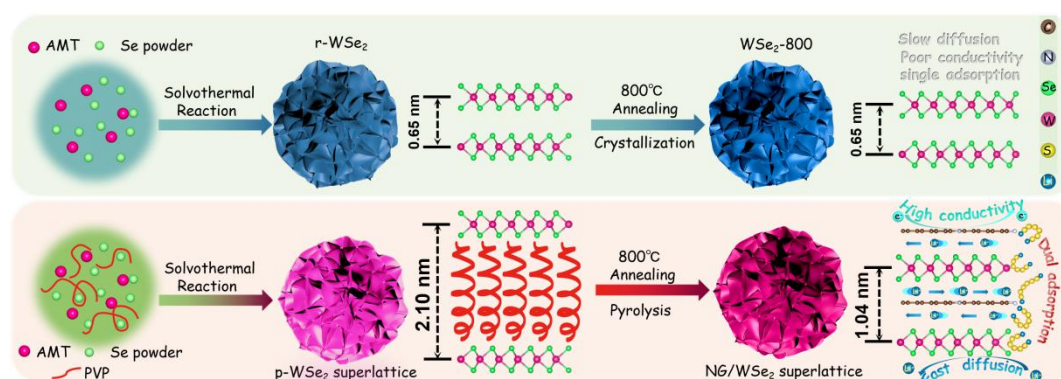
Theoretical calculations: All DFT calculations were performed using the VASP [27] package with VASPKIT code for post-processing the calculated data. Generalized gradient approximation (GGA) with the Perdew-Burke-Ernzerhof functional [28] was employed to treat the exchange-correlation energy. The interaction between core and valence electrons was described by the projected augmented wave (PAW) [29] basis set. A converged cutoff was set to 500 eV. Zero damping DFT-D3 method was used to investigate weak intermolecular interactions.[30] These heterointerfaces were built in a relatively low crystal parameter mismatch level by less than 5.0%. In the geometry optimization step, the force convergence standard was set below 0.02 eV/\AA . The density of Monkhorst-Pack K-point mesh (threshold: 0.04) and k-path for band calculation was used according to VASPKIT code's suggestion. A 20 \AA vacuum layer was constructed along the z-axis for each model regardless of the periodic layer effect.

The binding energy of LiPS intermediate species was calculated by the following equations: $E_{\text{LiS}_x} = E_{\text{slab}} + E_{\text{LiS}_x} - E_{\text{LiS}_x - \text{slab}}$ where E_{LiS_x} , E_{slab} , E_{LiS_x} and $E_{\text{LiS}_x - \text{slab}}$ are the energies of the binding energy of the LiPS species, the DFT energy of the slab, the corrected energy (300 K) of isolated LiPS molecules in vacuum, and the total energy after slab absorbing the intermediate Li-S_x species, respectively; x is the stoichiometry number of S atom in a Li-S_x-like molecule. Besides, to get an accurate bandgap near the Fermi level, all the projected-to-element band structures in this work were calculated in a mix-type basis of

SCAN^[31] functional because it is a large system, and then the partial density of states (pDOS) was obtained by the band calculation. Transition states of interest were searched by CI-NEB method.^[32] Charge density difference was obtained from the charge difference between the substrate and the adsorbent.

4.4 Results and discussion

2D NG/WSe₂ superlattices were produced in two steps, as schematized in **Scheme 1**. The first step involves the solvothermal reaction of ammonium metatungstate (AMT) and selenium powder in the presence of PVP. In the second step, the obtained powder is annealed at 800 °C within an inert atmosphere.



Scheme 1. Schematic illustration of the synthetic procedure used to produce NG/WSe₂ superlattice.

Figure 1a and **2a** display scanning electron microscopy (SEM) and high-angle annular dark-field scanning transmission electron microscopy (HAADF-STEM) images of the product obtained when no PVP was added to the reaction mixture. Without PVP, the obtained product, named raw-WSe₂ (r-WSe₂), was composed of nanosheet-based 330±40 nm quasi-spherical particles. Energy-dispersive X-ray spectroscopy (EDS) analysis of the r-WSe₂ particles showed a W:Se atomic ratio of 1:2.1 (Figure 2b). The small Se excess was related to residual Se from the synthesis process, and it could be removed in the subsequent annealing step.

When the solvothermal reaction was carried out in the presence of PVP, the obtained product was referred to as PVP-WSe₂ (p-WSe₂). The morphology of the p-WSe₂ particles was similar to that of r-WSe₂, with an average particle size of 320±30 nm (Figure 1b). EDS mapping analysis showed a uniform distribution of C, N, O, W, and Se, with a W:Se atomic ratio of

1:2.3 (Figure 3a). Fourier transform infrared (FTIR) spectroscopy analysis displayed the absorption fingerprints of the -C-N and carbonyl groups of PVP at 1650 cm^{-1} and 1286 cm^{-1} , respectively,^[33] demonstrating the formation of a hybrid PVP-WSe₂ organic-inorganic composite (Figure 3b).

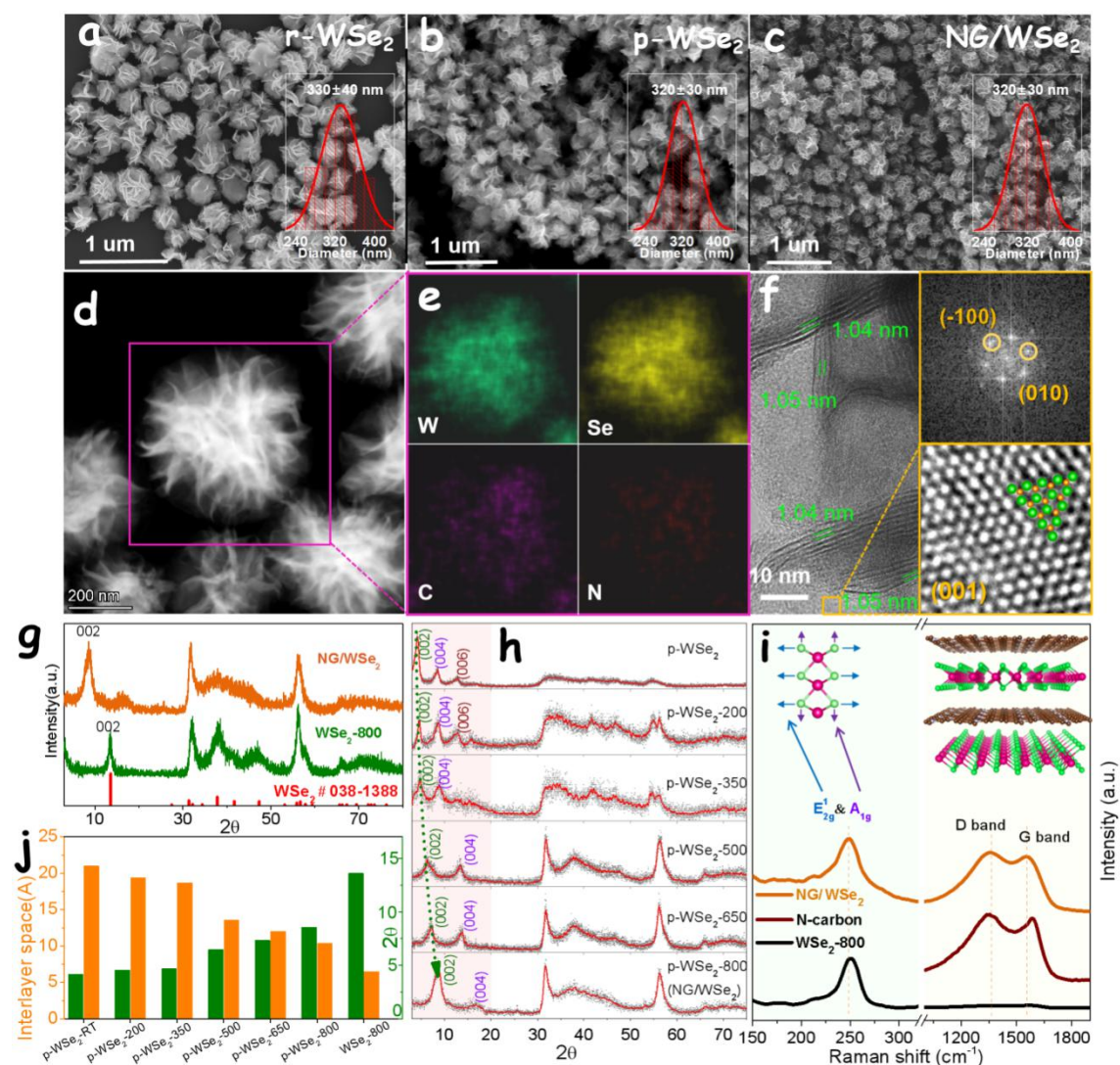


Figure 1. (a-c) SEM images of r-WSe₂ (a), p-WSe₂ (b), and NG/WSe₂ (c). Inset histograms show the particle diameter distributions. (d) HADDF-STEM image of NG/WSe₂ superlattice and (e) EDX element maps. (f) HRTEM image of an NG/WSe₂ superlattice with FFT spectrum and enlarged image of the yellow frame. (g) XRD patterns of WSe₂-800 and NG/WSe₂ samples. (h) XRD patterns of p-WSe₂ annealed at different temperatures. (j) (002) XRD peak position and the corresponding interlayer space calculated from Bragg's law. (i) Raman spectra of N-carbon, WSe₂-800 and NG/WSe₂ samples.

The thermogravimetric analysis (TGA) of p-WSe₂ showed a weight profile similar to that of PVP (Figure 3c), confirming the presence of PVP molecules or their derivatives within the

p-WSe₂ composite. The minor weight loss below 300 °C is associated with the removal of water or small organic molecule (e.g., DMF) and residual Se. The more drastic weight loss at 350-450 °C is related to the decomposition and carbonation of the PVP molecular chains. The moderate mass loss at higher temperatures, in the range of 450-800°C, is associated with a further graphitization process that enhances crystallinity.^[34]

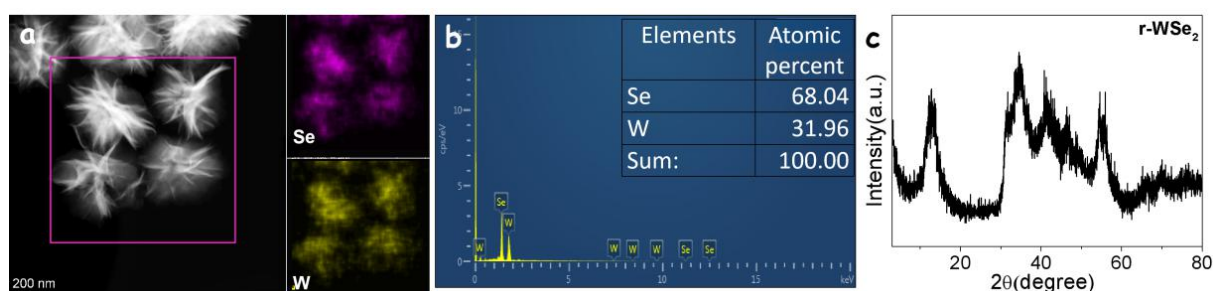


Figure 2. (a) SEM image and EDS elemental maps of r-WSe₂. (b) EDS elemental contents from r-WSe₂. (c) XRD pattern of r-WSe₂.

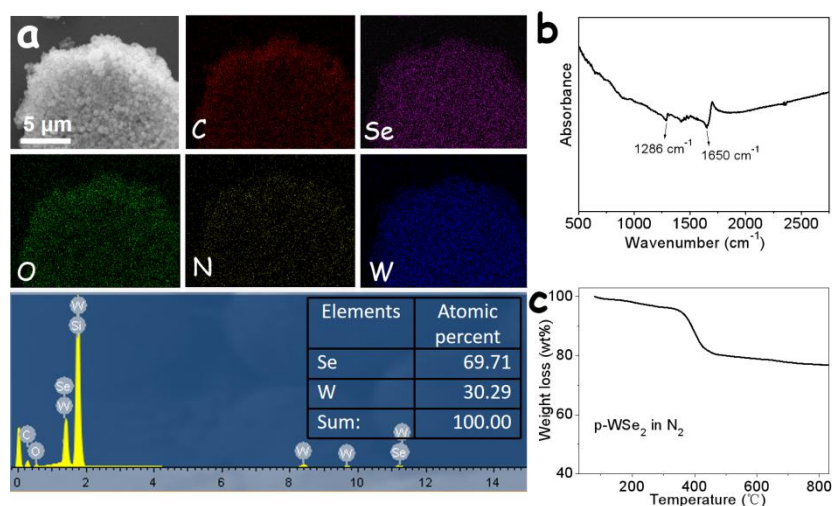


Figure 3. (a) EDS elemental maps, (b) FT-IR spectrum and (c) TGA curves of p-WSe₂.

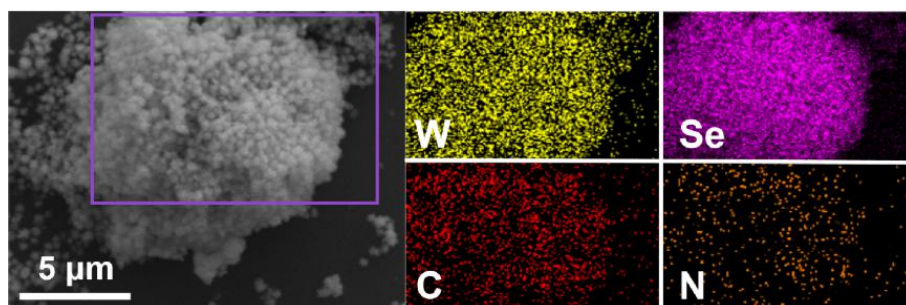


Figure 4. SEM image and EDX compositional maps of NG/WSe₂.

In the second step, the p-WSe₂ was annealed at 800 °C in an inert atmosphere to decompose interlaminar PVP into N-doped graphitic carbon.^[35] As observed by SEM, the annealed material, named NG/WSe₂, displayed a similar morphology to that of r-WSe₂ and p-WSe₂, with 320±30 nm quasi-spherical particles made of nanosheets (Figure 1c). HADDF-STEM micrographs and EDS elemental maps more clearly displayed the nanosheet-based structure of the spherical particles and their uniform W, Se, C, and N composition (Figure 1d,e, and Figure 4). High-resolution transmission electron microscope (HRTEM) images displayed the NG/WSe₂ (002) interlayer spacing to be 1.04 nm (Figure 1f), well above the 0.65 nm measured from r-WSe₂ annealed at the same temperature (WSe₂-800, Scheme 1 and Figure 5a) and approximately equal to the sum of the layer spacings of graphite carbon (0.34 nm) and WSe₂ (0.65). The enlarged HRTEM image of the NG/WSe₂ nanosheets and the related FFT diffraction pattern display an atomic W distribution that is consistent with hexagonal WSe₂ belonging to the p63/mmc space group, as it corresponds to the 2H phase of WSe₂ (Figure 1f inset). While the large atomic number difference between W and C did not allow observing the isolated graphite layers within the WSe₂ layered structure, we hypothesize that the enlarged interlayer space is related to the presence of graphitic carbon in the WSe₂ interlayers.

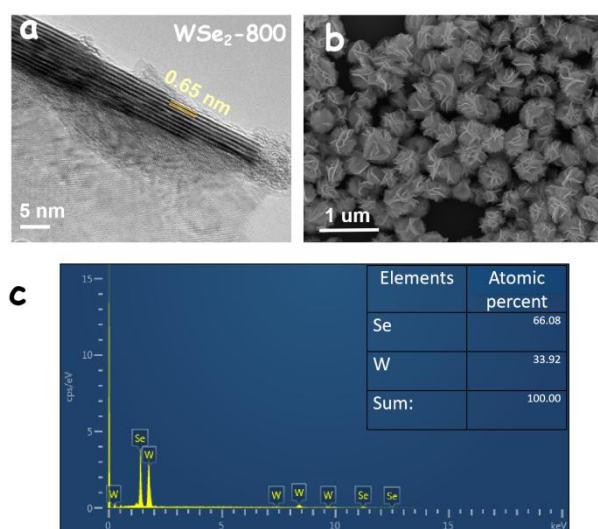


Figure 5. (a) HRTEM image and (b) SEM image of WSe₂-800. (c) Elements contents of WSe₂-800 from EDS results.

The X-ray diffraction (XRD) pattern of WSe₂-800 (Figure 1g) showed stronger diffraction peaks at 13.6°, 31.4°, 37.8° and 55.9° than the precursor r-WSe₂ (Figure 2c), which were indexed with the (002), (100), (103) and (110) planes of WSe₂ (JCPDS No. 038-1388).^[36]

Most XRD peaks of NG/WSe₂ coincided with those of WSe₂-800, except for the (002) family planes, which was significantly shifted from 13.6° to 8.5°. This shift revealed an interlayer distance increase from 6.5 Å to 10.4 Å, which matches well with the results obtained by HRTEM (Figure 1f and 5a). We further simulated the XRD pattern of a NG/WSe₂ superlattice configuration. As shown in Figure 6, the two peaks at 8.5° and 17.0° in the experimental XRD pattern of NG/WSe₂ (Figure 1g) match well with the simulated (002) and (004) diffraction peaks of the superlattice.^[10,37] Interestingly, we investigated the 2H stacking and 3R stacking configuration of transition metal dichalcogenides in the superlattice structure. The best fit was obtained considering the 2H stacking. Thus, simulation results point towards the NG/WSe₂ superlattice maintaining the inversion symmetry of the original WSe₂ crystal.^[38]

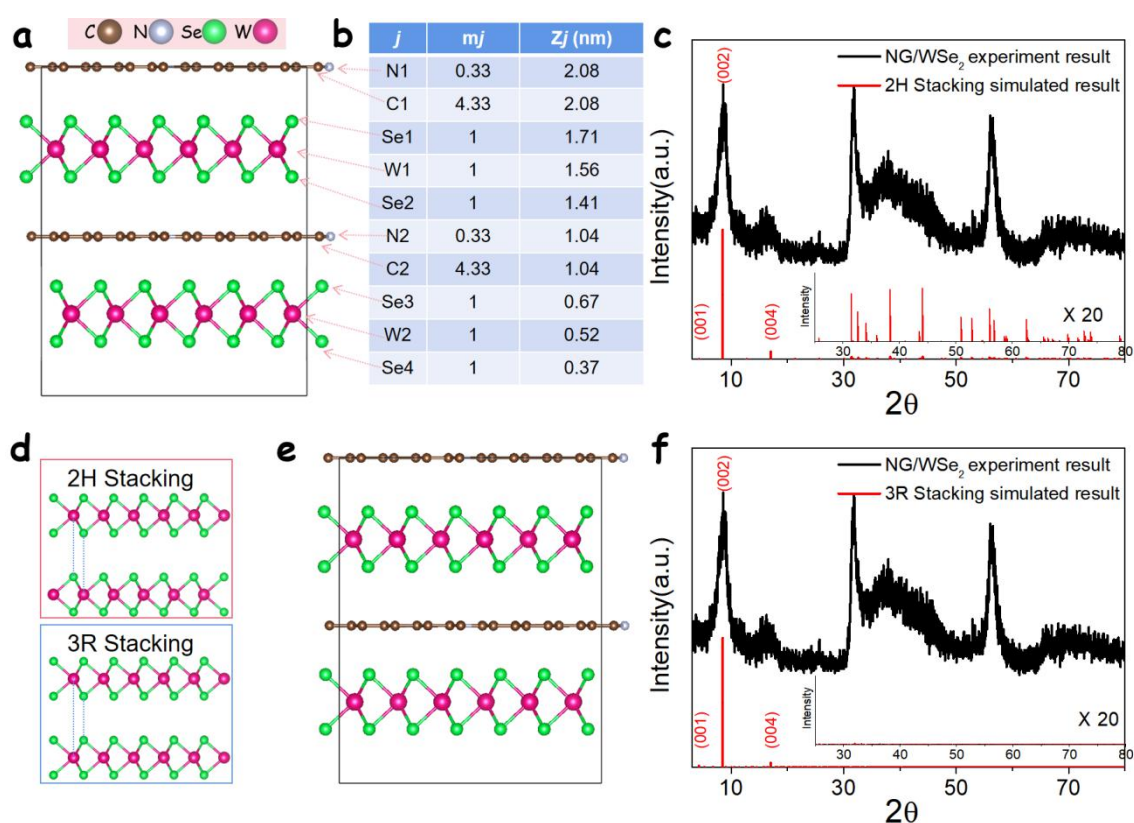


Figure 6. (a) Scheme of the superlattice structure of NG/WSe₂ with 2H stacking configuration. (b) Table of superlattice structural parameters. (c) Experimental XRD pattern of NG/WSe₂ superlattice and 2H stacking simulated result. The XRD simulations were calculated based on a reported method.^[10,37] The thickness of one unit cell was assumed to be ca. 2.08 nm based on the sum of double nanosheet thickness. (d) Scheme of the two stacking configurations: 2H stacking with two layers mirrored with respect to one another, and 3R stacking with alignment of the layers.^[38] (e) Scheme of the superlattice structure of NG/WSe₂ with 3R stacking configuration. (f) Experimental XRD pattern of NG/WSe₂ superlattice and 3R stacking simulated result.

On the other hand, the adjustment of the calcination temperature enabled us to control the interlayer spacing in an unprecedented wide range. According to XRD results, the (002) diffraction peak located at 4.2°, 4.5°, 4.7°, 6.5°, 7.3°, 8.5° as the calcination temperature increased from room temperature (RT) to 200, 350, 500, 650, and 800 °C, and thus the interlayer spacing of p-WSe₂ decreased from 21 to 19.4, 18.7, 13.6, 12, and 10.4 Å, respectively (Figure 1h, j). In addition to the strongest second-order diffraction peak (002) at 4.2°, p-WSe₂ clearly showed a series of higher-order diffraction peaks, (004) and (006), as labelled in Figure 1h and simulated in Figure 7 (see details in the SI). To the best of our knowledge, this is the widest continuous adjustable range of interlayer spacing reported for a 2D material, which opens the door to a wide range of applications not only in the field of rechargeable batteries but also in other fields like ionic sieves.^[7]

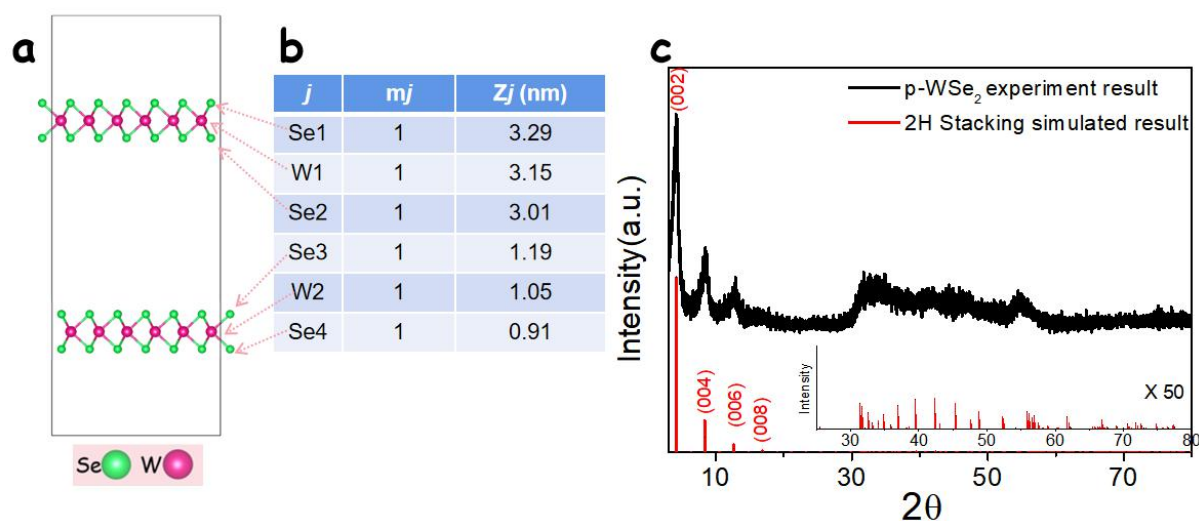


Figure 7. (a) Scheme of the superlattice structure of p-WSe₂ with 2H stacking configuration. Considering the weak crystal structure of PVP molecules, it is reasonable to ignore the existence of PVP molecules in the superlattice XRD simulation. (b) Table of the superlattice structural parameters. (c) Experimental XRD pattern of p-WSe₂ superlattice and 2H stacking simulated result. The thickness of one unit cell was assumed to be ca. 4.2 nm based on the sum of double nanosheet thickness. The XRD intensity of the superlattice structure was simulated according to the above method.

As obtained with the four-point probe method, the NG/WSe₂ superlattices annealed at 800 °C displayed a high electrical conductivity, up to 6.47 S cm⁻¹, which was two orders of magnitude above that of WSe₂-800 (Figure 8). As expected, the electrical conductivity significantly increased with the calcination temperature. The high electrical conductivity of

the NG/WSe₂ samples is consistent with the graphitization of the WSe₂ interlayer polymer and it is critical for the effective use of the composite material as sulfur host in LSB cathodes.^[15]

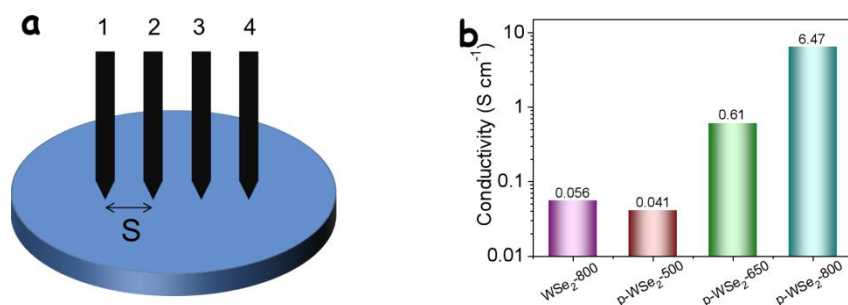


Figure 8. (a) Schematic plot of four-point probe technique used to measure the electrical conductivity. (b) Electrical conductivity of the different samples. The four probes are equidistant with a distance of S , and a constant current was input from probe 1 to probe 4, and the resistivity could be calculated by measuring the voltage between probe 2 and probe 3 with the equation of $\rho = 2\pi S \cdot V_{23} / (I \cdot B_0)$, where B_0 is the correction factor, and then the conductivity σ can obtain through the equation of $\sigma = 1/\rho$.

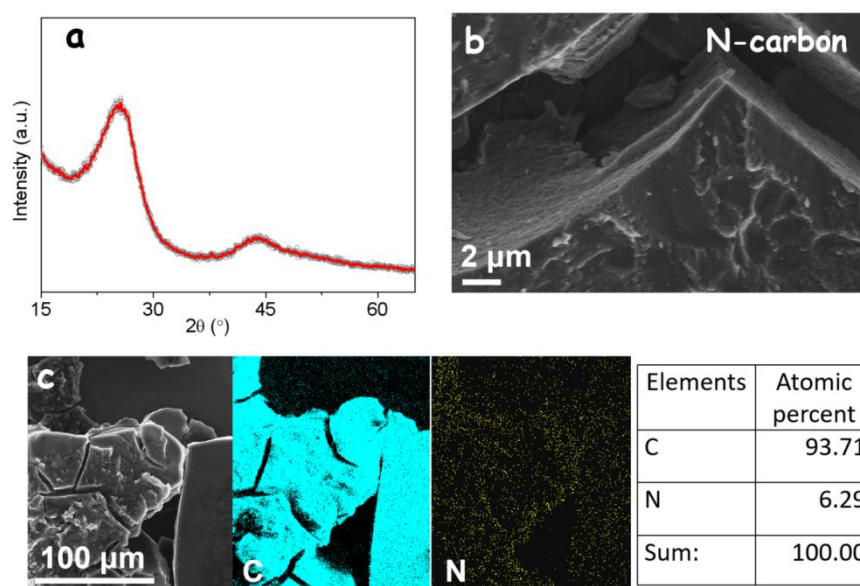


Figure 9. (a) XRD pattern, (b) SEM image, and (c) EDS mapping of N-carbon derived from annealing of PVP.

Figure 1i shows the Raman spectra of NG/WSe₂ and WSe₂-800 samples. A peak at ca. 250 cm⁻¹ was observed in the two samples and it was attributed to the E_{12g}¹ and A_{1g} modes of the WSe₂ 2H phase, which correspond to the axial and lateral stretching, respectively.^[39] The presence of interlayer product slightly affects the axial and lateral stretching of the WSe₂ layer,

resulting in a minor shift of the peak, from 249 to 251 cm^{-1} .^[40,41] Meanwhile, NG/WSe₂ displayed two additional peaks at around 1358 cm^{-1} and 1560 cm^{-1} that were assigned to the D band (disordered carbon) and G band (sp^2 -hybridized graphitic carbon) of carbon materials, respectively.^[41,42] Compared with the graphitic N-doped carbon obtained by calcination of PVP (N-carbon, Figure 9, see details in the experimental section), the shift of the G band in the Raman spectrum of NG/WSe₂ reflects that the interlayer NG was significantly affected by the sandwiched WSe₂ layer. The intensity ratio of the two peaks (I_D/I_G) in the NG/WSe₂ spectrum was estimated at 1.08 (close to the value of N-carbon, 1.05), indicating a defective carbon structure that we associated with the formation of N-doped carbon.^[43]

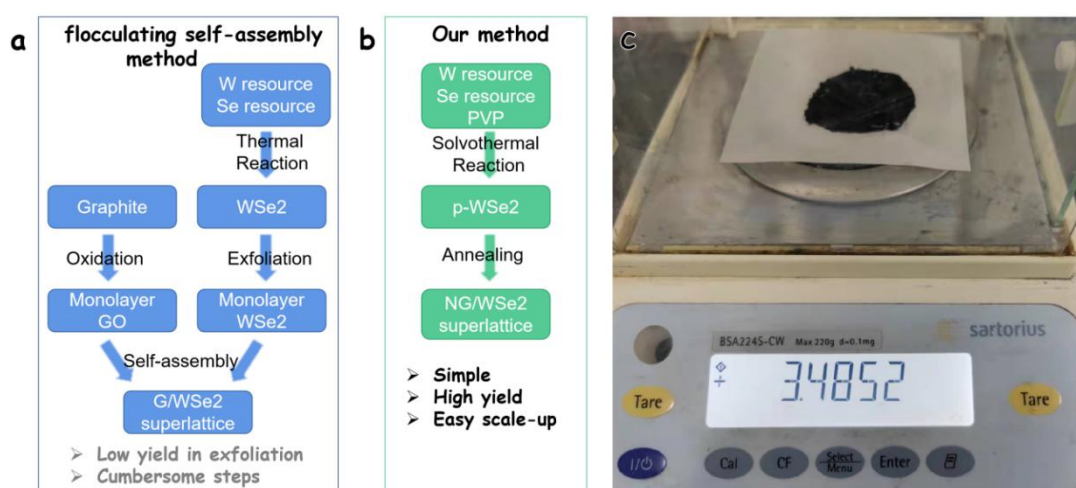


Figure 10. Comparison of experimental process between (a) flocculating self-assembly method and (b) our method. Our method effectively reduces the number of steps and avoids the low yield exfoliation process. (c) Optical photograph of the 3.485 g NG/WSe₂ superlattice obtained from one synthesis batch using 0.36 L of reactants (12 times scale-up experiment) with a high yield of 85 %.

Notice that while the fingerprint of carbon was clearly observed in the Raman spectrum of NG/WSe₂, no carbon/graphite-related XRD peaks were obtained, and no graphene layer could be identified by extensive HRTEM characterization, which is consistent with graphene layers intercalated within the WSe₂ structure to form an NG/WSe₂ superlattice, as illustrated in Figure 1i.

Overall, the above data demonstrate the formation of a high electrical conductivity NG/WSe₂ superlattice with a tunable WSe₂ interlayer distance by a simple (only 2 steps) and easily scalable procedure that provided a high material yield of ca. 85% (a detailed comparison can

be found in Figure 10. These composites were obtained using PVP as a structure-directing agent. We speculate that in DMF solvent PVP couples with the (001) surface of the nucleating WSe₂, inhibiting continuous growth in the [001] direction but promoting a stable 2D growth of WSe₂ monolayer. As the reaction progresses, PVP forms a coating layer on the surface of WSe₂. The other side of the PVP molecules bind to the WSe₂ monolayer are used as heterogeneous nucleation sites for the growth of an additional WSe₂ nanosheet. This layer-by-layer growth results in the formation of -WSe₂-PVP-WSe₂-PVP- superlattice nanosheets. The presence of the PVP molecular layer effectively separates the WSe₂ stack, shifting the (002) peak/spot in the XRD and electron diffraction patterns.^[44,45]

A priori, the same procedure should allow obtaining hybrid organic-inorganic composites that contain other organic molecules/polymers that have some affinity for the surface of metal chalcogenide nanostructures. To test this hypothesis, PVP was replaced by other organics/surfactants commonly used to direct the synthesis of chalcogenide nanoparticles, such as cetyltrimethylammonium bromide (CTAB), pluronic (F127), sodium dodecyl sulfate (SDS), and glucose (GLU). Figure 11 shows SEM images and XRD patterns of the obtained materials. As observed by SEM, all the obtained materials showed a nanosheet-based morphology, similar to that of p-WSe₂. Besides, XRD analysis showed the product obtained from the solvothermal reaction to display the characteristic XRD peaks of WSe₂ with a clear shift of the (002) interlayer spacing, confirming the successful intercalation of the organic within the WSe₂ layered structure. However, this shift of the (002) XRD peak disappeared after the calcination treatment. Thus, none of these alternative organics could be stably pyrolyzed into interlayer graphene at high temperatures to yield the NG/WSe₂ superlattice material. We hypothesize that the successful use of PVP is related to its robust molecular chain structure and its high intercalation content, which guarantee the graphitization transformation during the pyrolysis process rather than its volatilization from the interlayer.

The electronic band structure and the associated density of state (DOS) of NG, WSe₂, and NG/WSe₂ were determined using density functional theory (DFT). As expected, NG exhibited a typical conductor band structure and DOS, with the Fermi level lying within a continuous band of states (**Figure 12a**). On the other hand, WSe₂ displayed a semiconductor structure

with a bandgap of 1.68 eV (Figure 12b).^[46] The combination of both within the NG/WSe₂ superlattice showed no gap of states at the Fermi level (Figure 12c), which is consistent with a metallic character and the high electrical conductivity measured by the four-probe method.

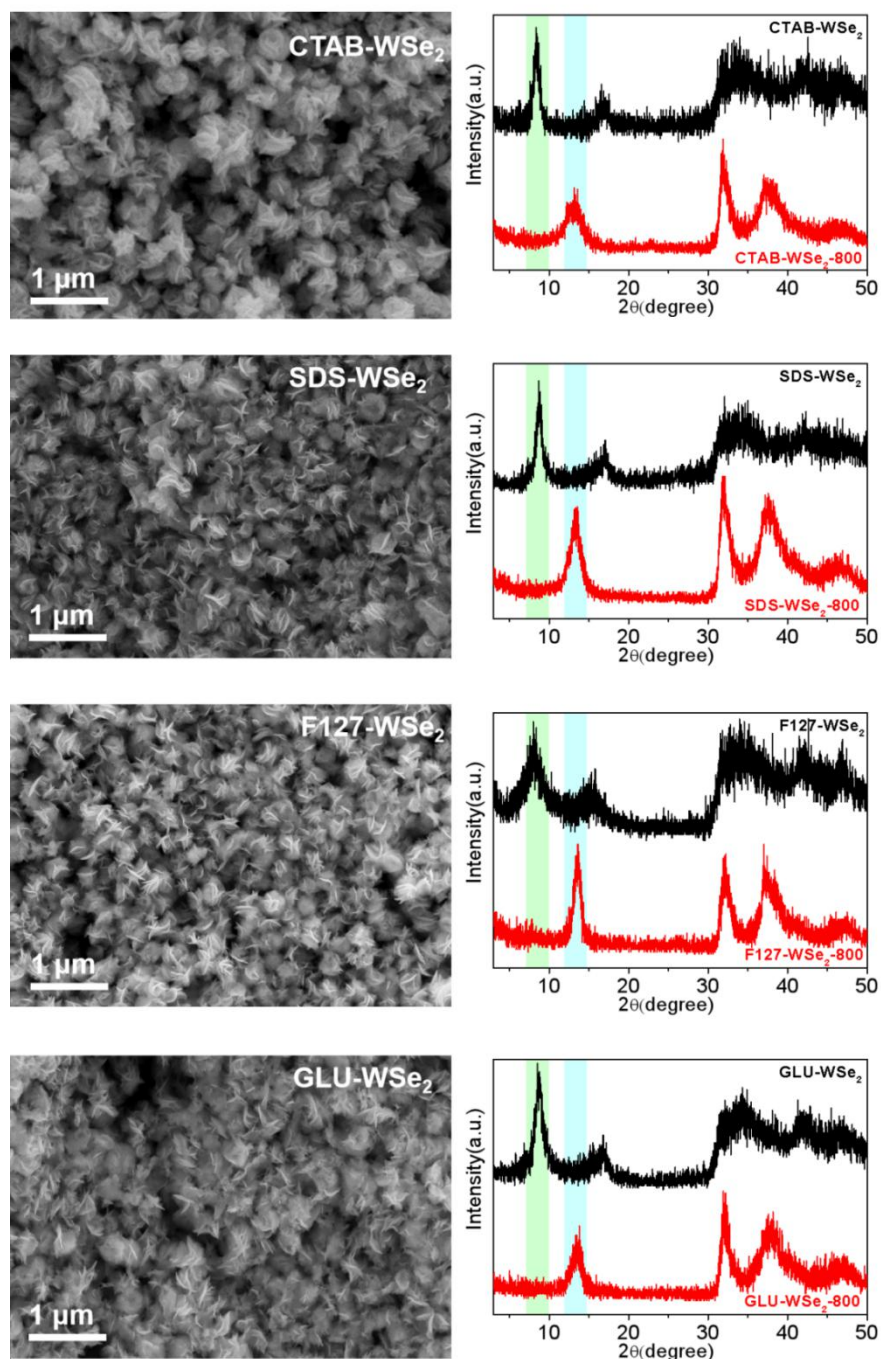


Figure 11. SEM image of XX-WSe₂ and XRD patterns of XX-WSe₂ and XX-WSe₂-800, with XX=cetyltrimethylammonium bromide (CTAB), pluronic (F127), sodium dodecyl sulfate (SDS), and glucose (GLU).

X-ray photoelectron spectroscopy (XPS) analysis was used to experimentally corroborate the Fermi level position and study the chemical state of the different elements. As observed in Figure 13a, the Fermi level of the NG/WSe₂ superlattice at ambient temperature is located within a band of states, delimiting the occupied and unoccupied states, consistent with DFT calculations. The high-resolution Se 3d XPS spectrum of WSe₂-800 and the NG/WSe₂ composite displayed one doublet associated with Se²⁻ anions within a WSe₂ chemical environment (Figure 12e).^[24] This Se 3d doublet was located at 55.64 eV (Se 3d_{3/2}) and 54.79 eV (3d_{5/2}) for WSe₂-800, but it was slightly shifted (~ 0.15 eV) to lower binding energies in NG/WSe₂. The high-resolution W 4f XPS spectra of WSe₂-800 and NG/WSe₂ were also fitted with one doublet, associated with W⁴⁺ within a WSe₂ environment (Figure 12f).^[24] The W 4f XPS spectrum of NG/WSe₂ was also red-shifted ca. 0.15 eV with respect to that of WSe₂-800. We hypothesize that the coincident redshift of the binding energies of both anions and cations within WSe₂ was related to a transfer of charge between NG and WSe₂ layers.

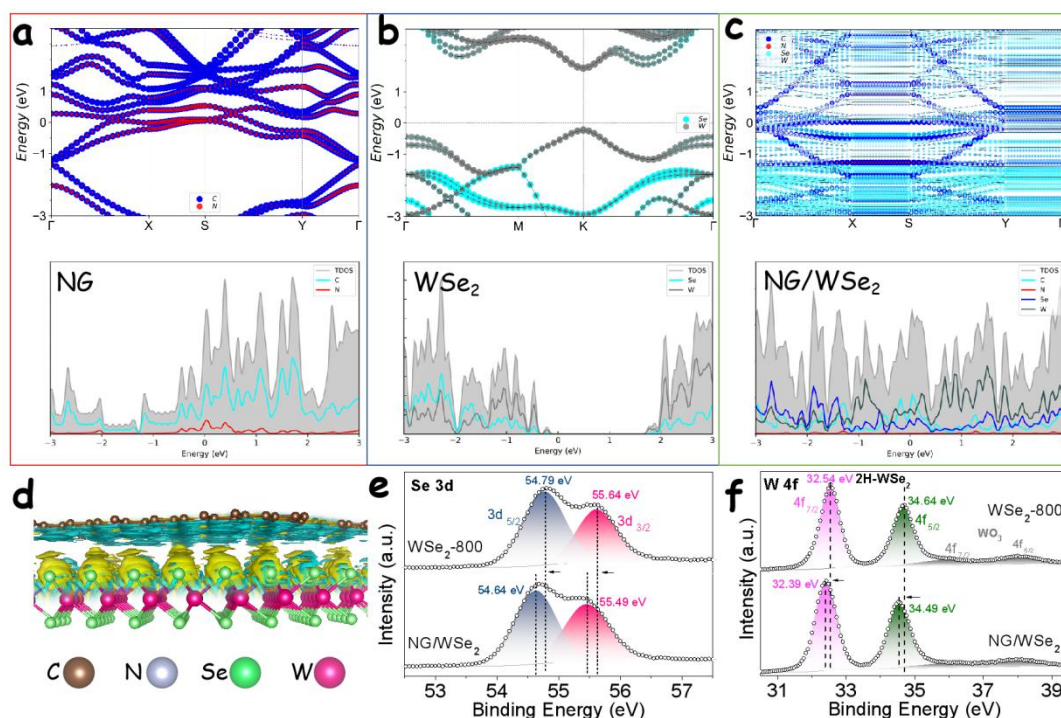


Figure 12. (a-c) HSE06 band structure and density of states of NG (a), WSe₂ (b), and NG/WSe₂ superlattice (c). (d) Charge density differential plot of the NG/WSe₂ superlattice. The yellow and blue regions represent increased and decreased electron density, respectively. (e) Se 3d and (f) W 4f high-resolution XPS spectra from WSe₂-800 and NG/WSe₂ samples.

DFT calculations of the three-dimensional (3D) charge density difference at the NG/WSe₂ heterojunction was employed to analyze the charge transfer between NG and WSe₂ layers. Calculations demonstrated a reduction of the electron density in the NG layer, as shown by the blue areas in Figure 12d, and an accumulation of the electron density in the WSe₂ layer, as represented by the yellow areas. The accumulation of negative charge in the WSe₂ layer facilitates the extraction of electrons from the W and Se levels, as observed by XPS analysis. Thus, experimental and computational evidence demonstrate that the charge transfer occurs at the atomic interface between the two materials, with the negative charge being transferred from the NG layer to the WSe₂ layer. A Bader analysis quantified the charge transfer in 0.038 electrons per supercell. This differential accumulation of charge is associated with a built-in electric field that can promote the adsorption of LiPS, which is crucial for inhibiting the shuttle effect and improving the cycle performance of LSBs. [20,47,48][49]

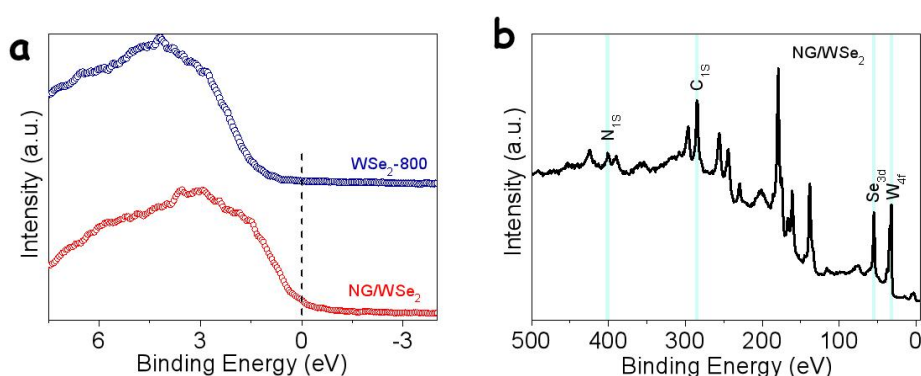


Figure 13. (a) Valence band of WSe₂-800 and NG/WSe₂, (b) XPS survey spectra of NG/WSe₂.

The LiPS-adsorption ability of NG/WSe₂ was experimentally compared with that of WSe₂-800 and graphene (G) by immersing 20 mg of each material in 5 mM Li₂S₄ solutions overnight and observing their colour change. As observed from the optical images in **Figure 14a**, the original 5 mM Li₂S₄ solution had an orange colour. In the presence of graphene, the colour of the solution remained unchanged, as expected from the very low LiPS adsorption ability of the nonpolar graphene surface. The solution containing WSe₂-800 became more pallid, consistent with the WSe₂ ability to chemisorb LiPS. But the solution containing NG/WSe₂ was completely decoloured, demonstrating the much stronger affinity of this material towards Li₂S₄ adsorption. This stronger affinity could be in part related to the built-in

electric field between NG and WSe₂. The adsorption ability could be quantified by analyzing the supernatant using UV-vis spectroscopy (Figure 14b). Li₂S₄ presents a strong absorption band in the range of 400-500 nm.^[49] The absorbance in this region strongly decreased in the presence of WSe₂ and especially NG/WSe₂, indicating that most of the Li₂S₄ in the solution had been captured by the adsorber.

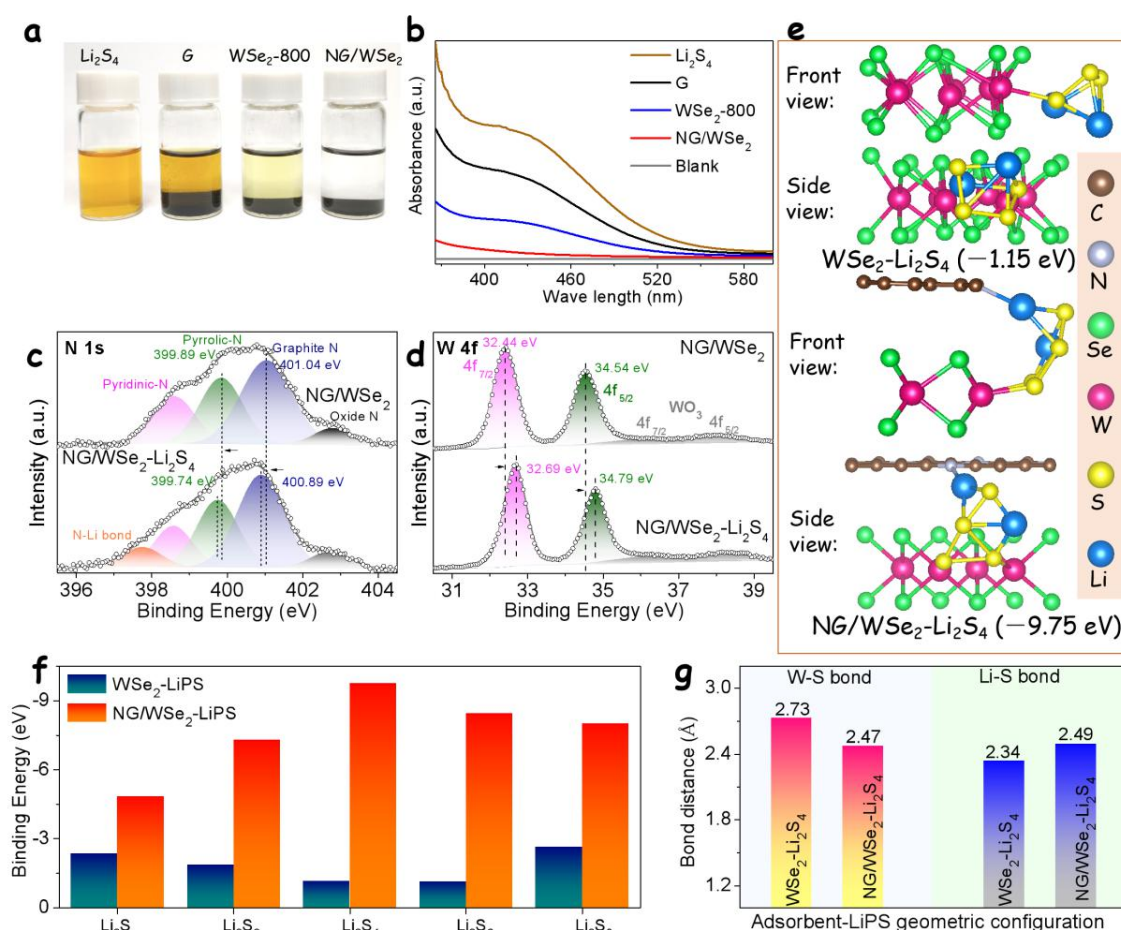


Figure 14. (a) Optical photograph and (b) UV-vis spectra of Li₂S₄ solutions containing the different adsorbents overnight. (c) N 1s and (d) W 4f XPS spectra of NG/WSe₂ before and after Li₂S₄. (e) Relaxed Li₂S₄-adsorbed configurations on the edge of WSe₂ and NG/WSe₂. (f) Binding energies between LiPS (Li₂S, Li₂S₂, Li₂S₄, Li₂S₆ and Li₂S₈) and WSe₂ and NG/WSe₂. (g) W-S bond and Li-S bond distances in WSe₂-Li₂S₄ and NG/WSe₂-Li₂S₄ configurations. The Li-S bond distance was selected as the closest distance to the adsorbent structure.

The NG/WSe₂ chemical states after the Li₂S₄ adsorption test were analyzed by XPS. From the comparison of the N 1s spectra of the superlattices before and after Li₂S₄ adsorption (Figure 14c), a shift of the pyridinic-N band from 399.89 eV to 399.74 eV and of the graphite-N band from 401.04 eV to 400.89 eV, was observed.^[50] This shift of the N 1s electronic states toward lower binding energies is related to a decrease of the chemical

environment electronegativity that we associate with the interaction of N with Li-ions. Besides, a small N 1s band at 397.74 eV was observed in the XPS spectrum of the material after Li_2S_4 adsorption. This additional band was attributed to the N-Li bond formation during the adsorption process. The strong influence of the Li_2S_4 adsorption process on the N 1s XPS spectra is related to the anchoring of the Lewis acid Li atoms of LiPS on Lewis base nitrogen sites through dipole-dipole interactions.^[20,51] On the other hand, after the Li_2S_4 adsorption test, the high-resolution W 4f XPS spectrum shifted in the opposite direction than N 1s, i.e. towards higher binding energies (Figure 14d). This shift is related to an increase of the chemical environment electronegativity, which is associated with the interaction of W in the WSe_2 lattice with S atoms in LiPS.

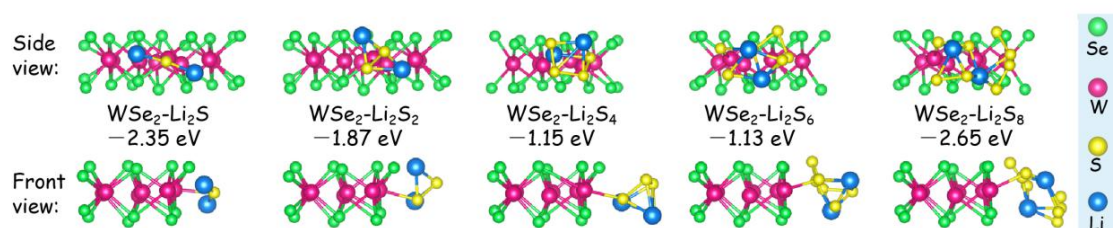


Figure 15. Binding energies and adsorbed structures of LiPS on the edge of WSe_2 calculated by DFT.

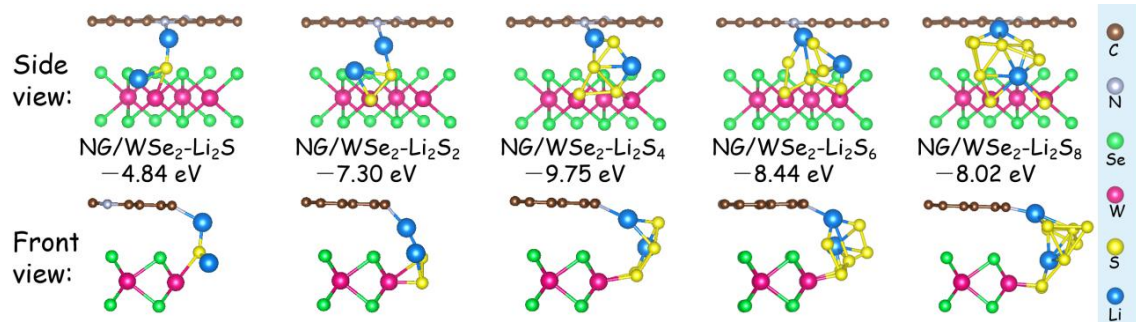


Figure 16. Binding energies and adsorbed structures of LiPS on the edge of NG/WSe_2 calculated by DFT.

DFT calculations were used to further investigate the adsorption of LiPS at WSe_2 and NG/WSe_2 sites. According to previous reports, in 2D transition metal dichalcogenides, LiPS preferentially adsorb at edge-exposed metal sites sandwiched between two chalcogen layers.^[17,22,52] Thus, we focused on the calculation of the binding energy (E_b) and adsorption configuration of different LiPS molecules adsorbed on the edge sites of WSe_2 and NG/WSe_2 . Figure 15 displays the optimized geometric configuration of WSe_2 -LiPS species with five

different lithiation levels (Li_2S_8 , Li_2S_6 , Li_2S_4 , Li_2S_2 , Li_2S). The $\text{WSe}_2\text{-Li}_2\text{S}_4$ adsorption configuration employed W-S bonds to immobilize the soluble Li_2S_4 species with an Eb of -1.15 eV (Figure 14e), which is higher (in absolute value) than the Eb reported for graphene (< -1 eV).^[53,54] This higher absolute value of Eb correlates well with the experimental data on Li_2S_4 adsorption discussed above. A much higher absolute value of Eb was obtained for the $\text{NG/WSe}_2\text{-Li}_2\text{S}_4$ adsorption, -9.75 eV. This very high absolute value of Eb is related to the adsorption of LiPS at two sites, as shown in the optimized geometric configuration displayed in Figure 14f. This optimized configuration consisted of a Li_2S_4 anchored by Li-N and W-S bonds on the NG-WSe_2 surface. Besides, DFT calculations showed the W-S bond within the $\text{NG/WSe}_2\text{-Li}_2\text{S}_4$ system to be shorter than within $\text{WSe}_2\text{-Li}_2\text{S}_4$, while the distance of the Li-S bond within the LiPS increases when Li_2S_4 is adsorbed on NG/WSe_2 instead of WSe_2 (Figure 14g). The optimized configurations and Eb of $\text{NG/WSe}_2\text{-LiPS}$ at other lithiation stages are illustrated in Figures 16 and Figure 14f, respectively. Overall, the DFT results demonstrated that the NG-WSe_2 superlattice can employ dual-adsorption sites in sublattice layers to deliver robust LiPS chemisorption, which is consistent with experimental results from XPS analysis and adsorption test. The combination of DFT calculations and experimental data demonstrate that NG/WSe_2 contains very effective lithiophilic/sulfurophilic adsorption sites able to trap polysulfides, which should allow minimizing the shuttle effect and enable a uniform deposition of the sulfur-based reaction products.

Sulfur was loaded within the porous structure of the host materials by a melting method (see details in the experimental section), to obtain S@NG/WSe_2 , $\text{S@WSe}_2\text{-800}$, and S@G . After S loading, the specific surface area of NG/WSe_2 decreased from 59.6 to 0.86 m^2 g^{-1} (Figure 17a). XRD patterns of the S-loaded host clearly showed the diffraction peaks associated with the cubic sulfur phase (JCPDS No. 08-0247, Figure 17b), together with the (002) peak of NG/WSe_2 . TGA allowed quantifying the sulfur content within S@NG/WSe_2 in a 73.8 wt% (Figure 17c). Besides, SEM and EDX elemental maps showed a uniform distribution of sulfur within S@NG/WSe_2 . Similar results were obtained from the reference samples, $\text{S@WSe}_2\text{-800}$ and S@G , which contained 73.2-73.4 wt% of S, as displayed in Figure 18.

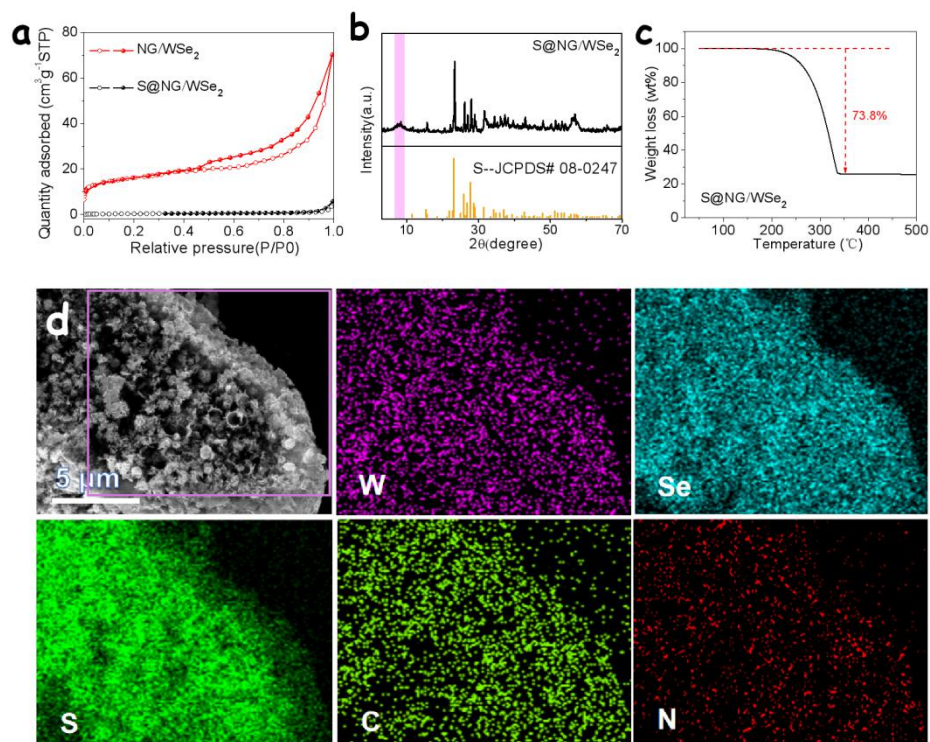


Figure 17. (a) N₂ adsorption-desorption isotherms of NG/WSe₂ and S@NG/WSe₂. (b) XRD pattern and (c) TGA curve measured in N₂ atmosphere from S@NG/WSe₂. (d) SEM image and EDS compositional maps of S@NG/WSe₂ sample.

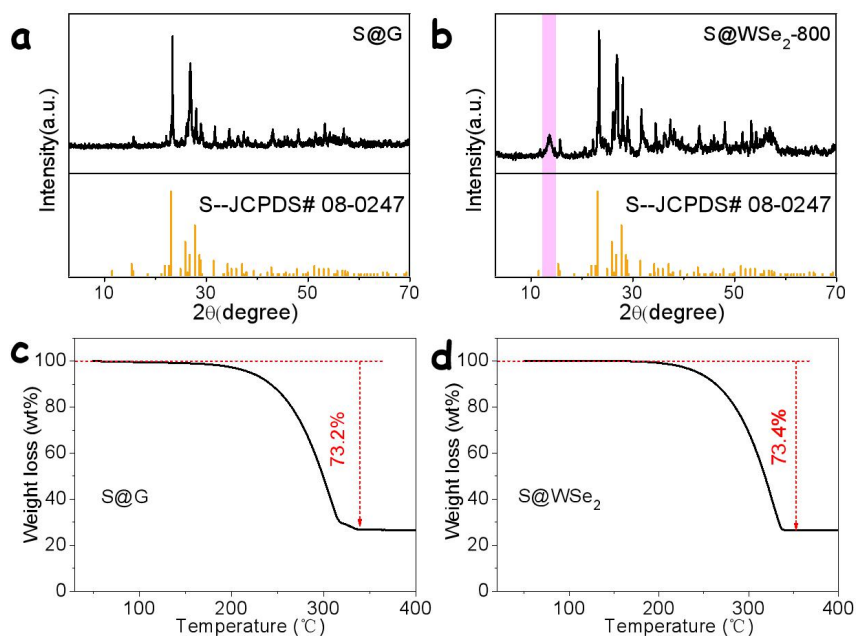


Figure 18. XRD patterns (a,b) and TGA curves measured in N₂ atmosphere (c,d) obtained from S@G and S@WSe₂-800.

The sulfur cathodes were assembled into coin cells to evaluate their electrochemical performance. **Figure 19a** displays the galvanostatic charge/discharge curves of the three electrodes, S@NG/WSe₂, S@WSe₂-800, and S@G, at a 0.1 C current rate. All the tested electrodes showed one charging and two discharging plateaus, associated with the relatively complex sulfur redox reaction. The two discharge plateaus reflect the 4-electron reduction of sulfur to soluble long-chain LiPS ($S_8 + 4Li^+ + 4e^- \rightarrow 2Li_2S_4$) and the subsequent 12-electron reaction to insoluble lithium sulfide ($2Li_2S_4 + 12Li^+ + 12e^- \rightarrow 8Li_2S$). The anodic plateau obtained during the charging process is attributed to a reverse multi-step sulfur oxidation process in which short-chain sulfides are converted to LiPS and eventually to sulfur.^[55] The S@NG/WSe₂ electrode showed a significantly higher discharge capacity (up to 1513 mAh g⁻¹) than S@WSe₂-800 (1239 mAh g⁻¹) and S@G (995 mAh g⁻¹) electrodes. This capacity was contributed mainly by sulfur, since the sulfur-free NG/WSe₂ electrode showed a very low capacity to store lithium ions within the voltage range 1.7-2.8 V, as displayed in Figure 20.

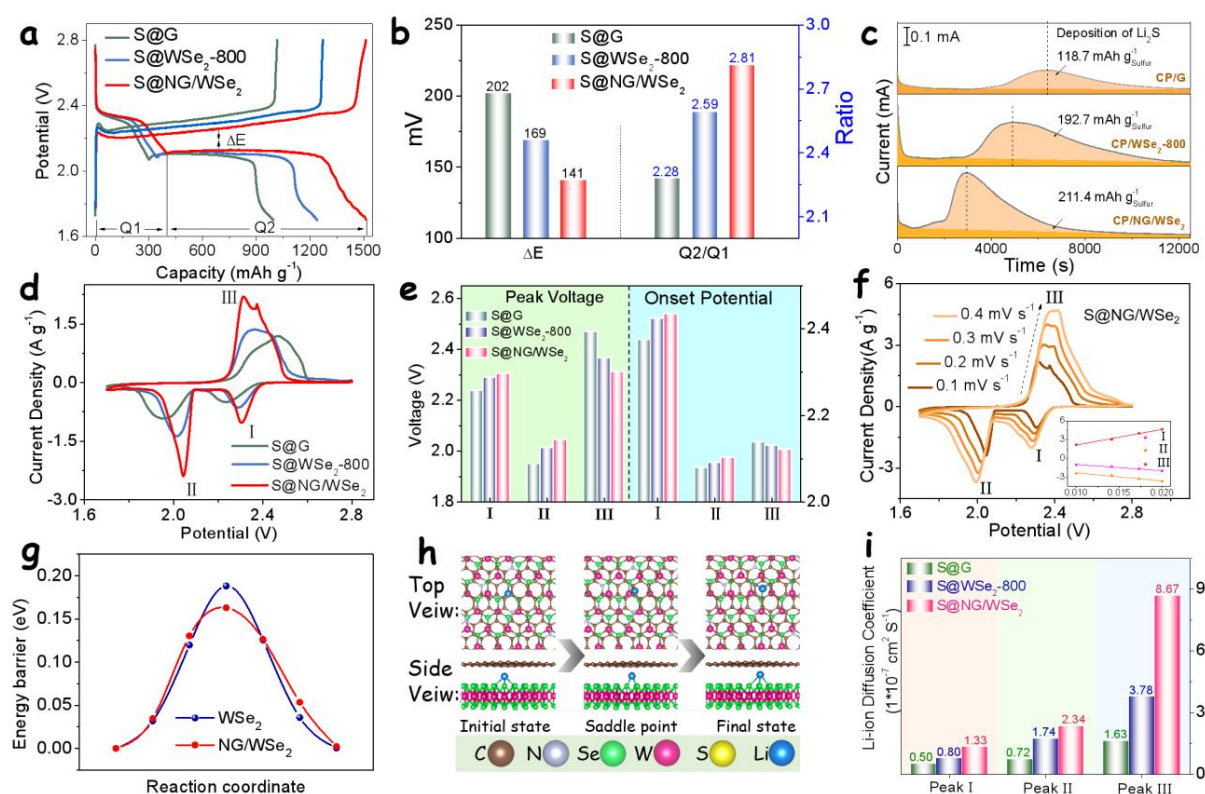


Figure 19. (a) Charge/discharge curves of different electrodes at 0.1 C current rate. (b) ΔE and Q2/Q1 values obtained from charge/discharge curves. (c) Potentiostatic discharge profile of Li₂S nucleation at 2.05 V on different electrodes with Li₂S₈ catholyte. (d) CV profiles of lithium-sulfur coin cells with different electrodes. (e) Peak voltages and onset potentials

obtained from CV curves of different electrodes. (f) CV curves of the S@NG/WSe₂ electrode at various scan rates. Inset shows the CV peak current density ($A\ g^{-1}$) for peaks I, II, and III versus the square root of the scan rate ($V\ s^{-1}$). The oxidation peak current was selected as the highest current point in CV curves. (g) Energy profiles of Li ion migration in the interlayer of NG/WSe₂. (h) Illustration of stages of Li ion diffusing in the interlayer of NG/WSe₂. (i) Li-ion diffusion coefficient value at CV peaks I, II, and III.

The voltage gap between the oxidation platform and the second reduction platform at 50% discharge capacity, ΔE , is considered as the polarization potential in the Li-S reaction, which is a measure of the LiPs transformation kinetics.^[49] The polarization potential obtained with the S@NG/WSe₂ electrode ($\Delta E = 141\ mV$) was significantly lower than that obtained with S@WSe₂-800 ($\Delta E = 169\ mV$) and S@G ($\Delta E = 202\ mV$). Besides, the overpotentials obtained with the S@NG/WSe₂ electrode, associated with the phase transition between soluble Li₂S₄ and insoluble Li₂S₂/Li₂S,^[52] were much lower than those obtained with the S@WSe₂-800 and S@G electrodes (Figure 21).

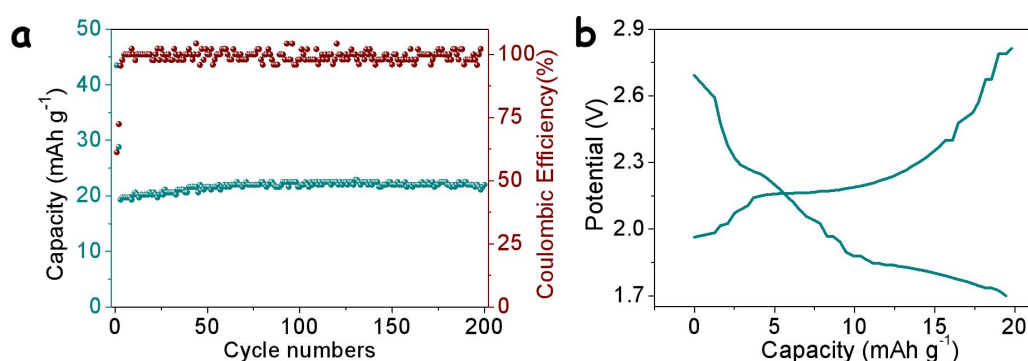


Figure 20. (a) Cycling performance and (b) charge/discharge curves of an NG/WSe₂ electrode containing no sulfur tested at 0.5 C.

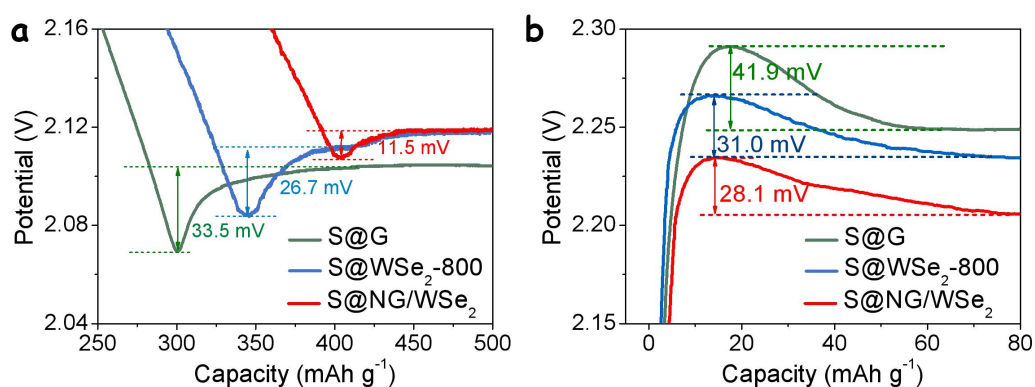


Figure 21. (a) Discharging and (b) charging profiles of S@NG/WSe₂, S@WSe₂-800, and S@G electrodes showing the overpotentials for conversion between soluble LiPS and insoluble Li₂S₂/Li₂S.

The ratio of the capacities of the first (Q1) and second (Q2) discharge plateaus can be used as an additional quantitative measure of the catalytic activity of the host materials toward the LiPS conversion reaction.^[20] As the first discharge plateau involves 4 electrons and the second one involves 12 electrons, the theoretical Q2/Q1 ratio is 3. However, in practice, this ratio is significantly reduced because of an incomplete sulfur reduction to a combination of Li₂S and Li₂S₂ instead of pure Li₂S. This incomplete reduction is the result of the slow reaction kinetics of the liquid to solid transition. Besides, the Q2/Q1 ratio is also reduced because part of the soluble LiPS is lost during the second plateau (Q2). Therefore, the Q2/Q1 ratio provides a measure of the degree of completion of the reduction reaction, associated with the host catalytic ability, and the inhibition of the shuttle effect. Figure 19b displays the Q2/Q1 ratios of the three host materials. The S@NG/WSe₂ electrode showed the highest Q2/ Q1 ratio at 2.81, close to the theoretical value and well above that of S@WSe₂-800 (2.59) and S@G (2.28).

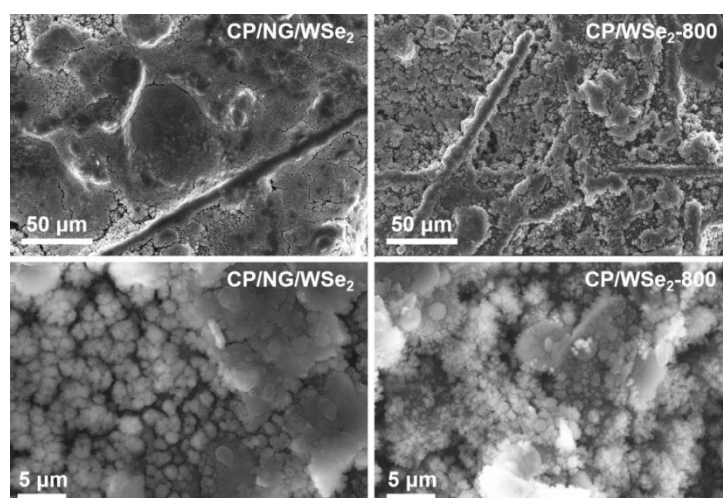


Figure 22. SEM images of CP/NG/WSe₂ and CP/WSe₂-800 electrodes after the nucleation test.

The final reaction step, the conversion of Li₂S₂ to Li₂S ($4\text{Li}_2\text{S}_2 + 8\text{Li}^+ + 8\text{e}^- \rightarrow 8\text{Li}_2\text{S}$) accounts for 50% of the capacity associated with the Li-S reaction. This step is at the same time the one with the more sluggish reaction kinetics and thus the most demanding for the catalytic material. Thus, Li₂S nucleation tests were used to quantitatively evaluate the impact of host materials in this transformation process.^[56] As can be seen from the potentiostatic discharge curves in Figure 19c, the NG/WSe₂-based electrode obtained by loading NG/WSe₂ on carbon

paper (CP/NG/WSe₂) showed the sharpest nucleation peak and the fastest Li₂S nucleation response when compared with CP/WSe₂-800 and CP/G electrodes. According to Faraday's Law, by integrating the area of the current-time curve a nucleation capacity of 211.4 mAh g⁻¹ was obtained for the CP/NG/WSe₂, well above that CP/WSe₂-800 (192.7 mAh g⁻¹) and CP/G (118.7 mAh g⁻¹). The cathode surface morphology after the nucleation test was studied by SEM (Figure 22). The SEM image of CP/NG/WSe₂ electrode obtained from the disassembled cell showed a more uniform and denser Li₂S layer than the CP/WSe₂-800 electrode, which further demonstrated that NG/WSe₂ could significantly boost the Li₂S nucleation process.

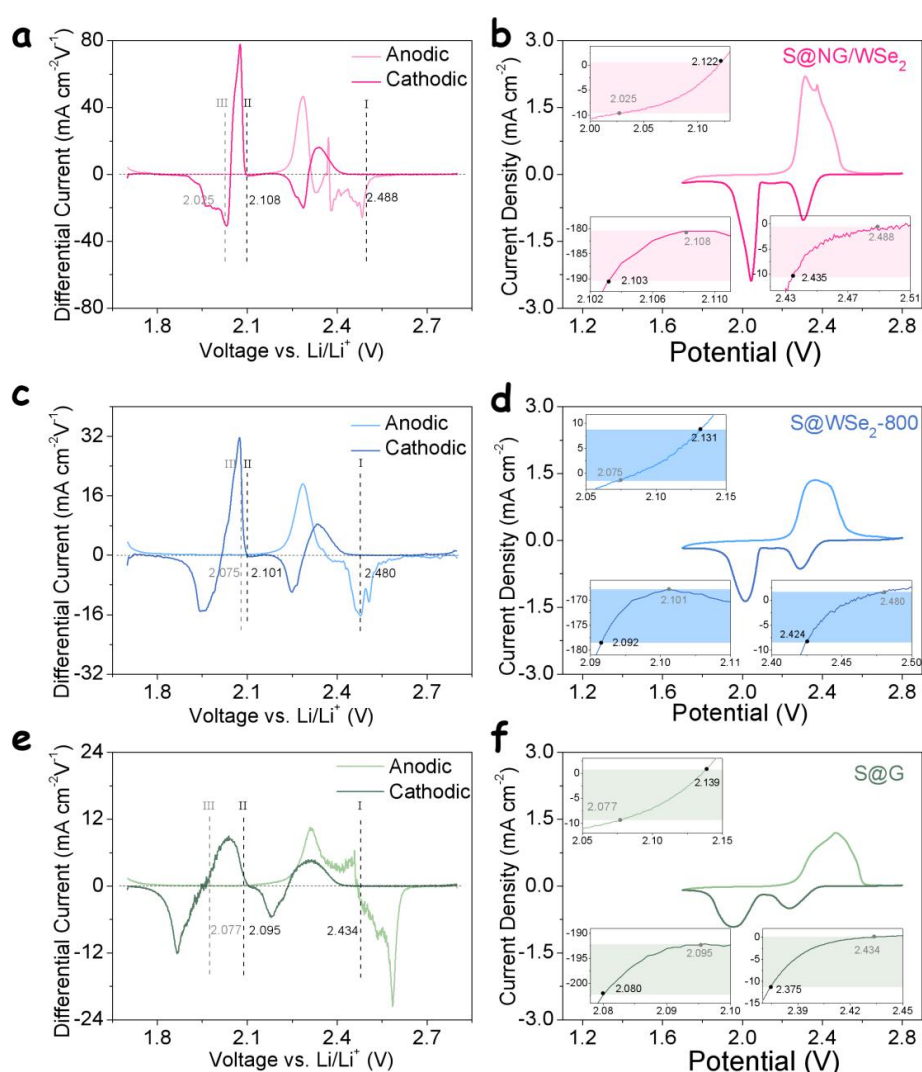


Figure 23. Onset potentials for Li-S redox reactions. (a, c, e) Differential CV curves of (a) S@NG/WSe₂, (c) S@WSe₂-800, and (e) S@G. The baseline voltage and current density are defined as the value before the redox peak, where the variation on current density is the smallest, namely $dI/dV = 0$. Baseline voltages are denoted in black for cathodic peaks I, II, and in grey for the anodic peak III, respectively. (b, d, f) CV curves and corresponding onset potentials of redox peaks I, II, and III (inset): (b) S@NG/WSe₂, (d) S@WSe₂-800, and (f)

S@G. Following a common definition employed in electrocatalysis, the onset potential is determined when the current density is $10 \mu\text{A cm}^{-2}$ beyond the corresponding baseline current density (more specifically, $10 \mu\text{A cm}^{-2}$ more negative than baseline current density for cathodic peaks or $10 \mu\text{A cm}^{-2}$ more positive than the baseline current density for anodic peaks). As shown in the inset of b, d, and f, the baseline voltages are the same as in a, c, and e while the coloured region indicates the gap in current density ($10 \mu\text{A cm}^{-2}$).

Overall, the above data demonstrate that the NG/WSe₂-based electrode can effectively reduce the Li-S redox reaction overpotential, minimize the LiPS shuttle effect and promote the nucleation reaction of Li₂S.

Figure 19d shows the cyclic voltammetry (CV) curves obtained from S@NG/WSe₂, S@WSe₂-800, and S@G electrodes. All curves display two cathodic peaks (peaks I and II) and one anodic peak (peak III), which is consistent with the measured charge/discharge plateaus. Also consistent with the above results, among the three tested electrodes, S@NG/WSe₂ showed the highest peak current densities and the most positive/negative potential of the cathode/anode peaks (Figure 19e). The S@NG/WSe₂ electrode also displayed the highest/lowest reduction/oxidation onset potentials at a current density of $10 \mu\text{A cm}^{-2}$ (Figure 23).^[56,57] Thus, CV curves further evidenced NG/WSe₂ to be the most effective electrocatalyst to promote the kinetics of polysulfide redox reaction.

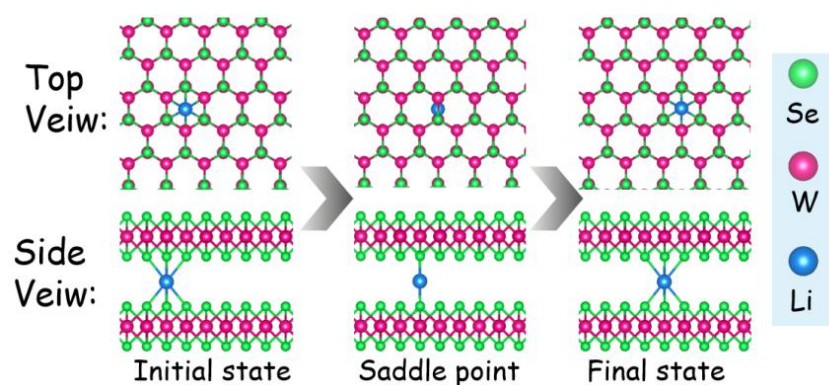


Figure 24. Diffusion of a Li-ion within a WSe₂ interlayer as obtained from DFT calculations

Besides electron transport/transfer properties and catalytic activity, the reactant diffusivity is an additional key parameter determining the dynamics of an electrochemical reaction.^[58] In the particular case of LSBs, the low electrical conductivity of S₈, polysulfides, and Li₂S demands for very effective and rapid diffusion of Li⁺ within the sulfur host.^[59] DFT calculations were used to determine the Li-ion diffusion pathways and diffusion barriers in

the interlayer space of WSe₂ and NG/WSe₂ (Figure 19g,h, and Figure 24). Both materials present effective channels for Li⁺ diffusion with a low energy barrier. However, the presence of NG within the WSe₂ interlayer in NG/WSe₂ allowed reducing the energy barrier for Li⁺ diffusion from 0.188 eV to 0.163 eV, thus pointing towards a faster Li-ion diffusion capability and stronger interfacial ions transfer dynamics.^[60,61]

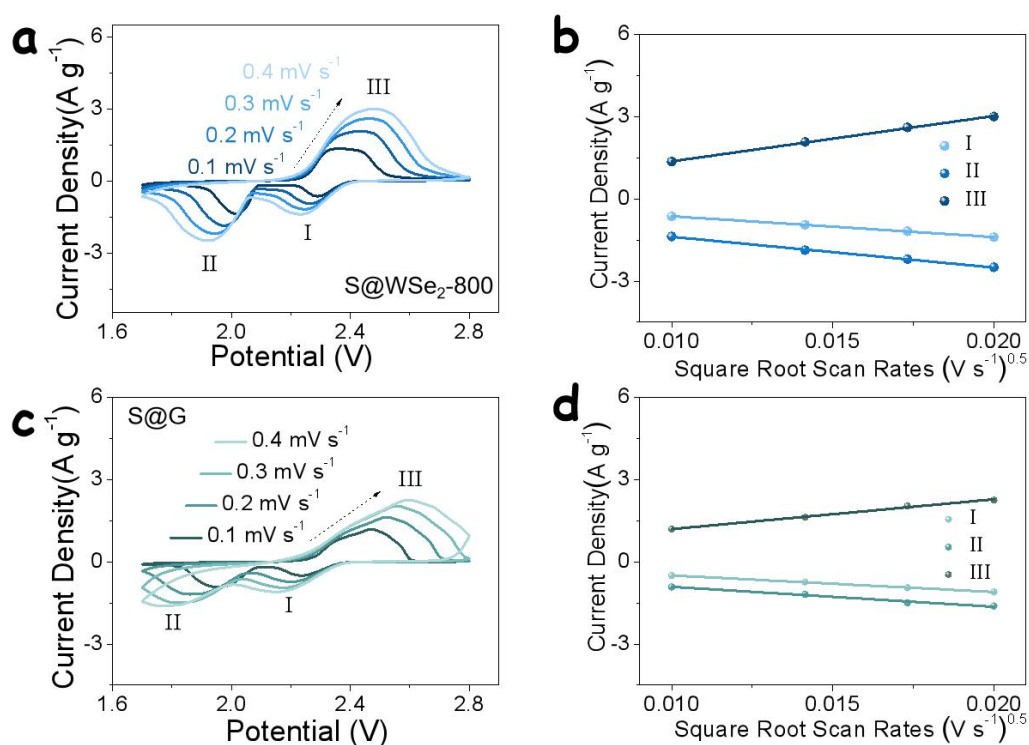


Figure 25. CV curves of (a) S@WSe₂-800 and (c) S@G electrode at different scan rates. Plots of CV peak current versus the square root of the scan rates with (b) S@WSe₂-800 and (d) S@G electrodes.

The Li⁺ ion diffusivity was experimentally determined by measuring CV curves at different scan rates (0.1 to 0.4 mV s⁻¹). As observed in Figure 19f and Figure 25, for all the electrodes, when increasing the scan rate, the reduction (oxidation) peaks shifted towards lower (higher) potentials, the peak current density increased and the polarization voltage (voltage gap between peak I and peak III) augmented. Among the different electrodes, S@NG/WSe₂ showed the highest current densities and the lowest polarization voltage at all scanning rates, indicating the fastest LiPS conversion kinetics. Besides, a linear relationship was observed between the peak current and the square root of the scanning rate for the three peaks, which denotes diffusion-controlled reduction and oxidation reactions (inset of Figure 19f). Thus, the

Randles-Sevcik equation was applied to calculate the Li⁺ diffusion coefficient in the process:^[49,62]

$$I_p = (2.69 * 10^5) n^{1.5} A D_{Li^+}^{0.5} C_{Li^+} v^{0.5}$$

where I_p is the peak current (A), n is the number of charge transfer, A is the geometric electrode area (cm²), D_{Li^+} is the Li⁺ diffusion coefficient, C_{Li^+} is the concentration of Li⁺ in the electrolyte (mol cm⁻³), and v is the scan rate (V s⁻¹). Being n , A , and C_{Li^+} constants, a steeper $I_p/v^{0.5}$ slope indicates a faster Li⁺ diffusion. The S@NG/WSe₂ electrode was characterized by the steepest slopes, involving the highest Li⁺ diffusivities during the Li-S redox reaction.^[20] Quantitatively, the D_{Li^+} calculated from peaks I, II, and III were 1.3, 2.3, and 8.7×10^{-7} cm² s⁻¹, respectively (Figure 19i). The Li⁺ diffusion rate is influenced by the electrode structure, i.e. the density and effectiveness of the Li⁺ transport channels, the electrolyte viscosity, which depends on the amount of dissolved LiPS, and the rate of formation/dissolution of the Li₂S/Li₂S₂ layer.^[63] The high Li⁺ diffusion rate of the S@NG/WSe₂ electrode is related to the large interlayer spacing promoting a rapid transport of Li ions within the host material and a promoted adsorption and catalytic conversion of LiPS that decrease the LiPS electrolyte concentration and accelerates the kinetics of Li₂S/Li₂S₂ formation/dissolution. This improved Li⁺ diffusivity should be reflected in a superior rate capability.

Rate performance tests were carried out in the current density range of 0.1 C to 5 C (**Figure 26a**). The S@NG/WSe₂ electrode showed the highest discharge capacities at all current rates, with an initial discharge capacity of 1597.5 mAh g⁻¹ at 0.1 C that indicates a high utilization of sulfur in the cathode. When the current was increased to 5 C, the S@NG/WSe₂ electrode still maintained a high average capacity of 569.5 mAh g⁻¹, well above that of S@WSe₂-800 (197.5 mAh g⁻¹) and S@G (9.2 mAh g⁻¹). Besides, S@NG/WSe₂ recovered an average capacity of 1131 mAh g⁻¹ when the current rate was returned to 0.2 C. Figure 26b displays the galvanostatic charge/discharge curves under different current rates. All discharge curves show two discharge plateaus, even at 5 C. In contrast, the S@WSe₂-800 cell showed a high increase of the polarization voltage and a reduced capacity in the charge/discharge profiles when

increasing the current rate, and the S@G electrode was almost unable to release capacity at 5 C (Figure 27).

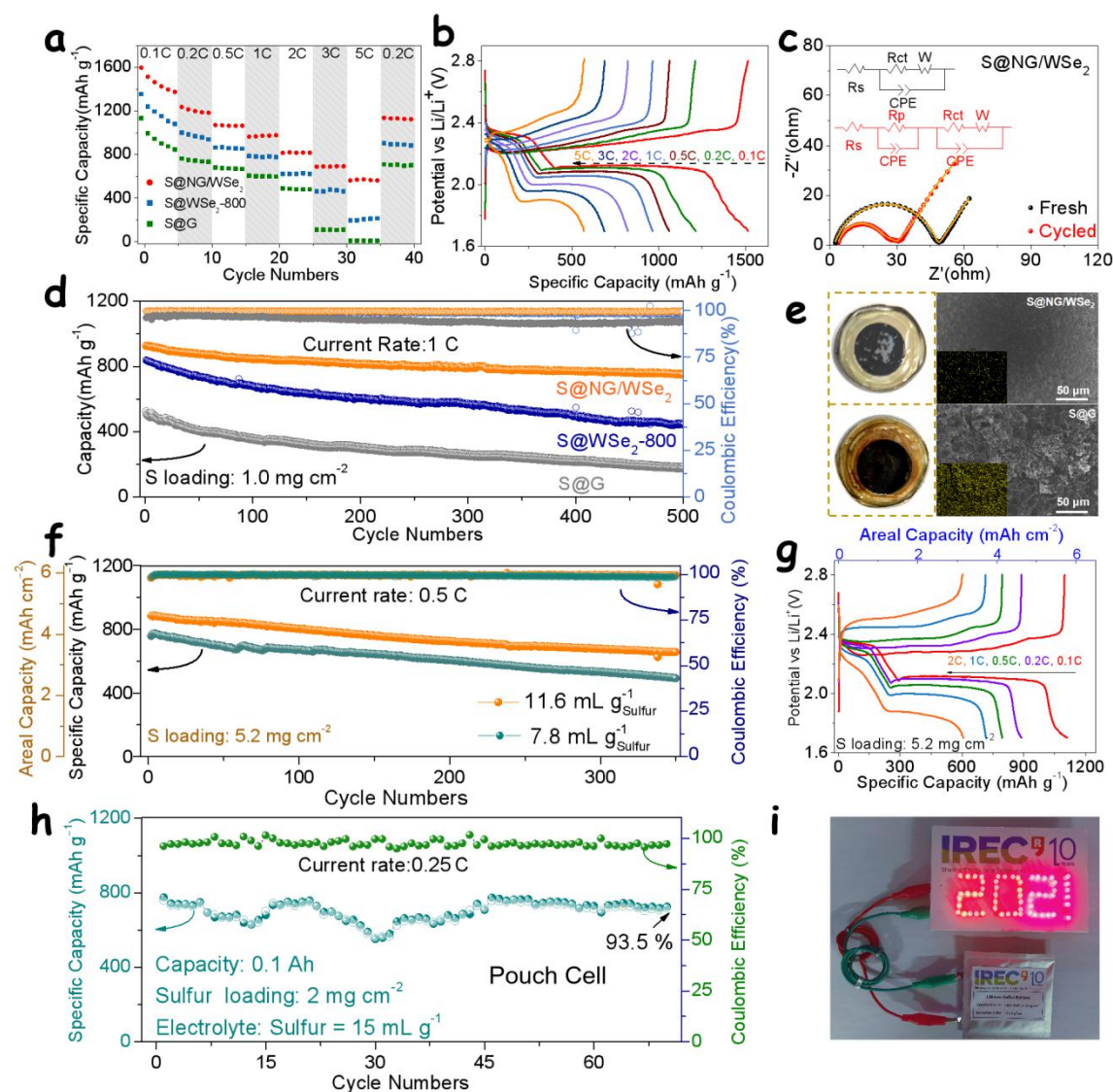


Figure 26. (a) Rate performances of S@NG/WSe₂, S@WSe₂-800, and S@G electrodes. (b) Charging/discharging curves of the S@NG/WSe₂ electrode at current rates from 0.1 to 5 C. (c) Nyquist plot of the EIS results obtained from a S@NG/WSe₂ electrode before and after 100 cycles at 1 C. The Nyquist curves were fitted considering the equivalent circuits shown as inset, where R_s, R_p, R_{ct}, and W stand for the resistances of the electrolyte, the insoluble Li₂S₂/Li₂S precipitation layer, the interface charge-transport, and the semi-infinite Warburg diffusion, respectively; and CPE stands for the corresponding capacitances. (d) Capacity retention of different electrodes at 1 C over 500 cycles. (e) Optical images of membranes and SEM image of lithium foil recovered from cycled coin cells containing a S@NG/WSe₂ electrode (top) and a S@G electrode (down). The inset images show the map of the sulfur signal detected by EDX. (f) Cycling stability of a S@NG/WSe₂ electrode with a high sulfur loading (5.2 mg cm⁻²) and a lower electrolyte usage (11.6 and 7.8 mL g⁻¹_{Sulfur}) at 0.5 C over 350 cycles. (g) Charge/discharge curves of S@NG/WSe₂ electrodes with a 5.2 mg cm⁻² sulfur

loading at various current rates. (h) Cycling performances at 0.25 C of a pouch cell based on a S@NG/WSe₂ cathode. (i) Optical photograph of a “2021” panel contained 58 red LEDs powered by a pouch cell based on a S@NG/WSe₂ electrode.

Figure 26d displays 500 continuous cycles of the three different electrodes at 1 C. During cycling, the S@G electrode suffered a drastic capacity decay because of its lack of effective catalytic-adsorption sites, retaining just 34.4 % (173 mAh g⁻¹) of its initial capacity after 500 cycles. In contrast, the S@WSe₂-800 electrode provided a larger initial capacity, 839 mAh g⁻¹, and it was able to retain 54.0% of it (453.3 mAh g⁻¹) after 500 cycles. But best results were obtained with the S@NG/WSe₂ electrode, which provided an initial discharge capacity at 1 C of 923 mAh g⁻¹, and it retained 81.3% of its capacity (750.4 mAh g⁻¹) after 500 cycles, which corresponds to a much lower capacity decay rate of just 0.037% per cycle.

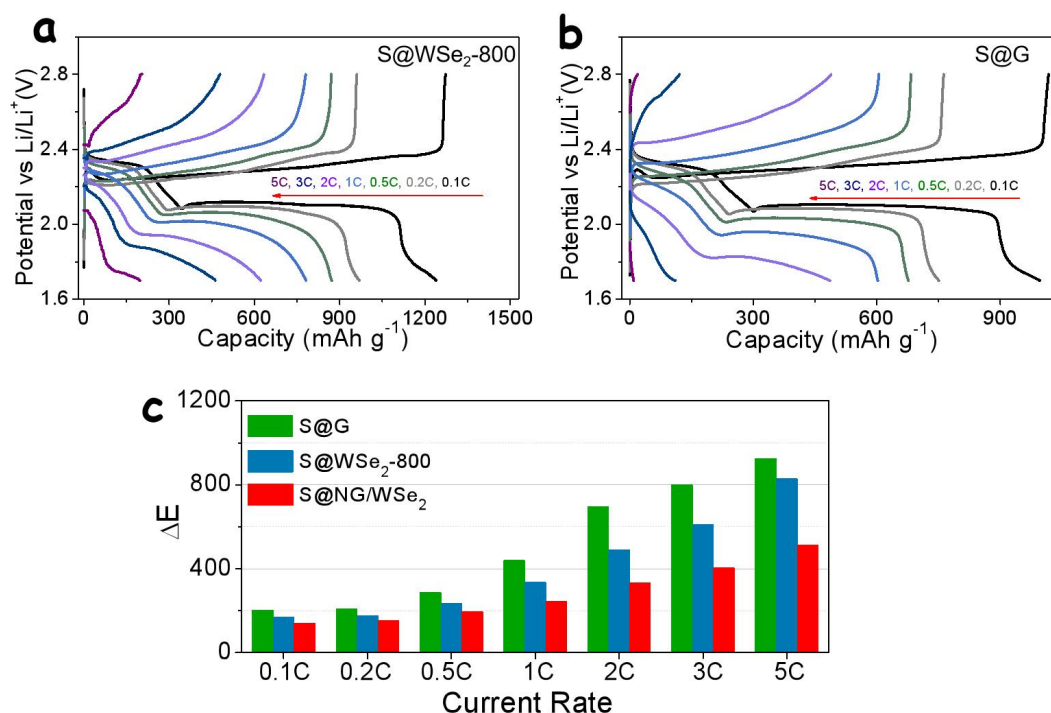


Figure 27. Galvanostatic charge/discharge curves of (a) S@WSe₂-800 and (b) S@G at various C rates. (c) ΔE change with the three electrodes at different current rates.

Interestingly, we investigated the effect of other carbonaceous materials as intercalators on the electrochemical performance of the formed superlattice. Figure 28 shows the results obtained using the GLU-WSe₂ superlattice (not annealed) as the sulfur host material. Indeed, the S@GLU-WSe₂ electrode was also characterized by a superior rate performance and cycle

stability which can be in part related to the small amount of residual Se present in the unannealed material,^[64,65]

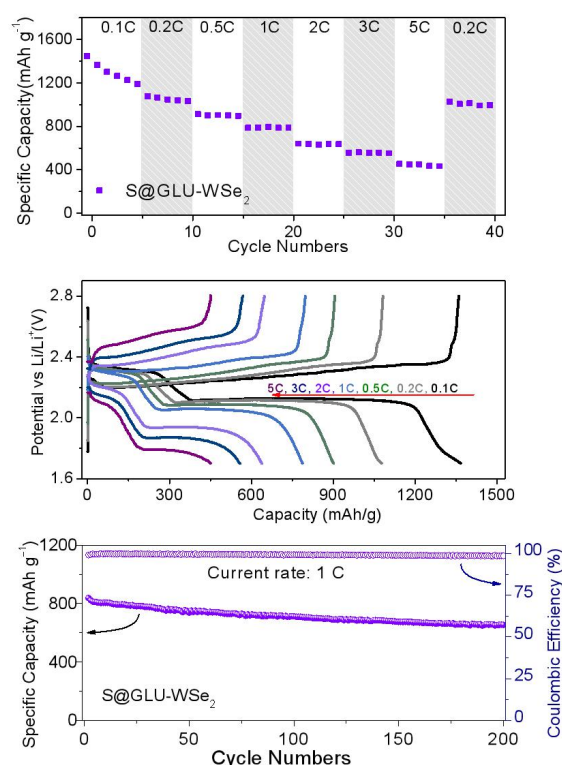


Figure 28. (a) Rate performance of a S@GLU-WSe₂ electrode and (b) the corresponding charge/discharge curves at various C rates. (c) Cycling performance at a current rate of 1 C.

Figure 26c and Figure 29 show the impedance changes of S@NG/WSe₂, S@WSe₂-800, and S@G electrodes before and after cycling at 1 C, and the equivalent circuits used to fit the data (inset in Figure 26c). The Nyquist plots of the electrochemical impedance spectroscopy (EIS) result obtained from the fresh batteries show a semicircle at the high-frequency range related to the charge-transfer resistance (R_{ct}), and a sloping straight line at lower frequencies related to the lithium ions diffusion.^[66,67] The S@NG/WSe₂ fresh electrode showed the lowest R_{ct} (46.6 Ω) compared with S@WSe₂-800 (69.2 Ω) and S@G (77.9 Ω), which confirms the enhanced charge transferability of the superlattice cathode. After 100 cycles and keeping the cells in the charged state for the EIS test, all R_{ct} values were significantly reduced due to the activation of the process.^[20,49] Besides, the fitting of the Nyquist plots required a new element to account for the additional semicircle appearing in the high-frequency range. This new feature is related to the impedance of the passivating layer in the cathode and anode created during the cycling (R_p in the equivalent circuit) and that was generated from the electrolyte

decomposition,^[68,69] Li_2S corrosion in the anode surface caused by LiPS diffusion from cathode to anode,^[69] and residues of unoxidized $\text{Li}_2\text{S}/\text{Li}_2\text{S}_2$ in the cathode during the fast charge/discharge process.^[70,71] After cycling, the S@NG/WSe_2 electrode was characterized by the smallest resistances ($R_{\text{ct}} = 6.9 \ \Omega$ and $R_{\text{p}} = 19.5 \ \Omega$), well below that of cycled $\text{S@WSe}_2\text{-800}$ ($R_{\text{ct}} = 25.9 \ \Omega$ and $R_{\text{p}} = 40.4 \ \Omega$) and S@G ($R_{\text{ct}} = 75.2 \ \Omega$ and $R_{\text{p}} = 44.8 \ \Omega$). The small R_{p} values obtained with S/NG/WSe_2 suggest that NG/WSe_2 effectively inhibited the shuttle effect and promoted faster conversion kinetics of Li_2S , which effectively reduces the Li_2S corrosion in the anode and the residue of unoxidized $\text{Li}_2\text{S}/\text{Li}_2\text{S}_2$ in the cathode. The comparison of the slopes measured in the low-frequency range (Figure S24 d), confirmed the faster diffusion of Li^+ within the S@NG/WSe_2 electrode, which displayed the highest slopes both before and after cycling.

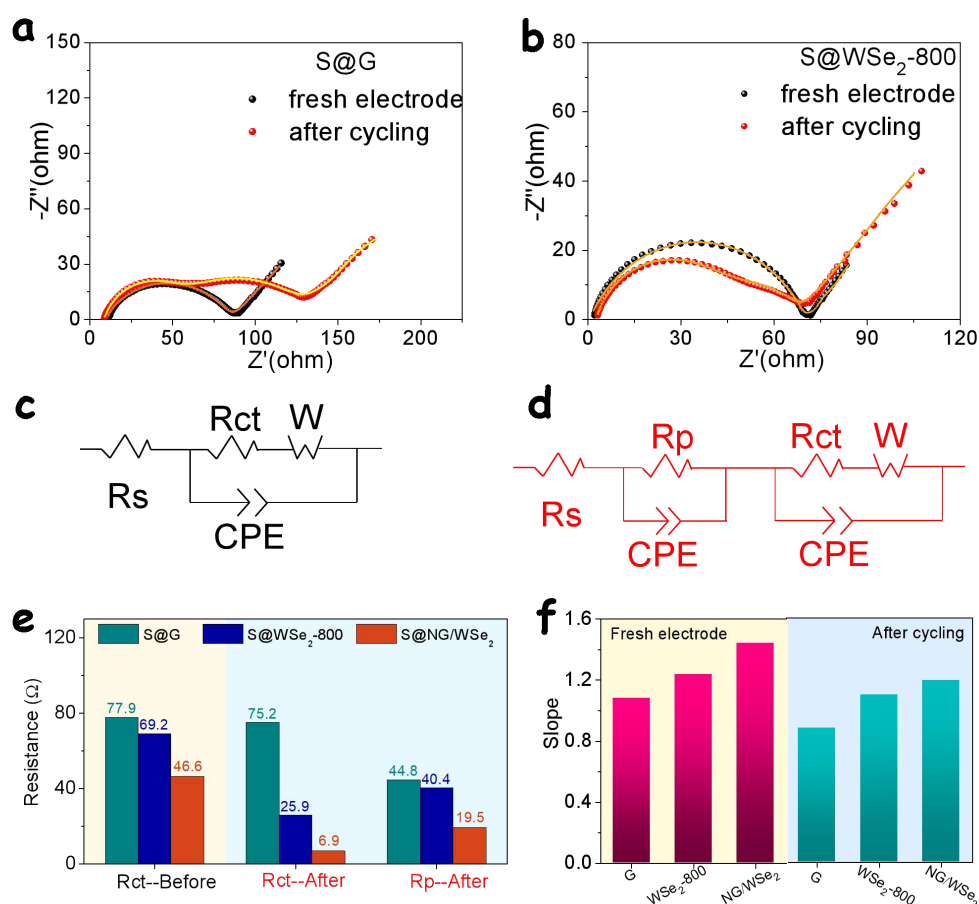


Figure 29. EIS spectra of (a) S@G and (b) $\text{S@WSe}_2\text{-800}$ electrodes before and after 100 cycles. The black data points correspond to a fresh cell and the red data points to the same cell after cycling at 1 C for 100 cycles. The solid line corresponds to the fitting result using the equivalent circuits (c) and (d), where R_{s} , R_{p} , R_{ct} , and W stand for the resistances of the electrolyte, insoluble $\text{Li}_2\text{S}_2/\text{Li}_2\text{S}$ layer, interfacial charge-transportation, and semi-infinite

Warburg diffusion, respectively; and CPE stands for the corresponding capacitances. (e) Resistances of the three coin cells as obtained from the equivalent circuit. (f) Slope of Nyquist plot at the range of low frequency.

After 100 cycles, coin cells were disassembled to quantitatively assess the amount of LiPS diffusing to the anode material and the structural stability of the host material. After 100 cycles, the membranes of the NG/WSe₂ and S/NG cells showed a sharp colour contrast (Figure 26e). The yellowish colour of the membrane extracted from the S@NG/WSe₂ cell indicates a low LiPS diffusion and thus an effective capture of polysulfide species. In contrast, the dark brown colour of the membrane obtained from the S@G cell indicated significant contamination with LiPS species not properly anchored to the cell cathode. Besides, the lithium anode of the cycled S@G coin cell displayed serious corrosion, multiple cracks, and notable contamination with sulfur (Figure 26e). In contrast, the lithium anode of the cycled S@NG/WSe₂ coin cell displayed a smooth and compact Li surface and low intensity of the EDS sulfur signal (Figure 26e), suggesting a negligible amount of LiPS reaching the anode.^[20,49] At the other side of the cell, despite the incorporation of conductive/binder additives and the grinding processes used for the slurry preparation, the nanosheet structure of NG/WSe₂ is still recognizable in the SEM image of the cycled S@NG/WSe₂ cathode (Figure 30), indicating good mechanical stability of the superlattice during the lithiation/delithiation cycles.

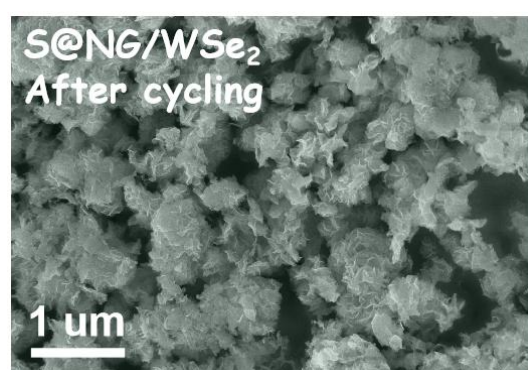


Figure 30. SEM image of the S@NG/WSe₂ electrode after 100 cycles at 1 C.

The commercial application of high energy density LSBs requires maximizing the sulfur areal load and reducing the electrolyte volume. In this direction, we prepared S@NG/WSe₂ electrodes with a 5.2 mg cm⁻² sulfur load and tested them within cells containing just 11.6 mL

$\text{g}^{-1}_{\text{Sulfur}}$ of electrolyte. When cycled at a 0.5 C current rate, these cathodes achieved an initial discharge capacity of 885.3 mAh g^{-1} , which is equivalent to an areal capacity of 4.6 mAh cm^{-2} (Figure 26f), well above that of commercial lithium-ion batteries (4 mAh cm^{-2}). After 350 cycles, the discharge capacity remained at 656.0 mAh g^{-1} , which corresponds to a 74.1% capacity retention. Figure 31a displays the change of charge/discharge curves during the cycling process, exhibiting a steady decay process with the same charge/discharge plateaus. Figure 26g and 31b display the rate performance of the high sulfur loading electrodes. The S@NG/WSe₂ electrode containing 5.2 mg cm^{-2} of sulfur showed a high initial capacity of 1188 mAh g^{-1} at a current rate of 0.1 C. Even at a high current rate of 2 C, a stable discharge capacity of 607 mAh g^{-1} was achieved. Besides, the capacity recovered well when the current rate was reduced back to 0.2 C. The charge/discharge curves at all different current rates clearly show one charging plateau and two discharge plateaus (Figure 26g), demonstrating that even at high sulfur loadings, the NG/WSe₂ host is able to effectively reduce polarization and achieve a very notable sulfur transformation.

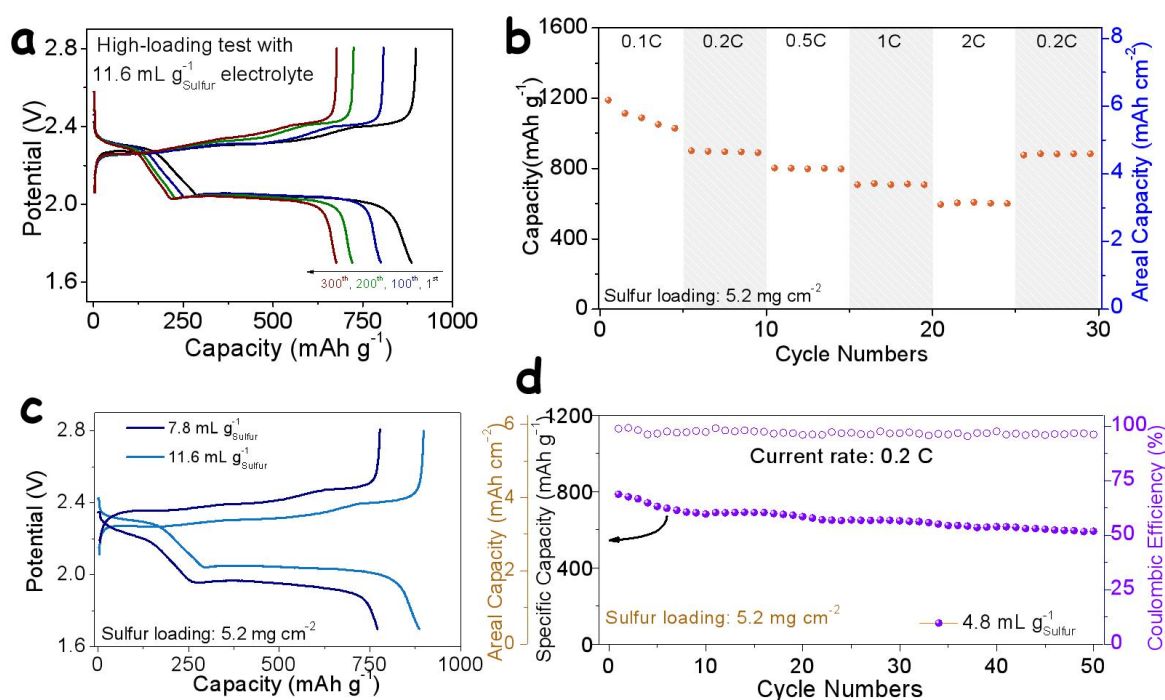


Figure 31. (a) Charge/discharge profiles of S@NG/WSe₂ electrode with high-loading sulfur at various cycles during the cycling test. (b) Rate capability of a S@NG/WSe₂ cathode loaded with 5.2 mg cm^{-2} of sulfur at various C rates. (c) Initial charge/discharge curves of S@NG/WSe₂ electrodes cycling at 0.5 C with different electrolyte usage. (d) Cycling test under $4.8 \text{ mL g}^{-1}_{\text{Sulfur}}$ electrolyte condition.

S@NG/WSe₂ cathodes were also tested within cells containing even lower volumes of electrolyte (7.8 mL g⁻¹_{Sulfur}) to increase the overall LSB energy density. In these lean electrolyte conditions, the high electrolyte viscosity usually reduces the Li-ion mobility and thus increases the polarization voltage (Figure 31c). Nevertheless, the S@NG/WSe₂ electrode tested with just 7.8 mL g⁻¹_{Sulfur} electrolyte endured 350 cycles with notable stability, showing capacity retention of 65.4%. In addition, the more rigorous electrolyte usage condition, 4.8 mL g⁻¹_{Sulfur}, was also tested, and the results showed that the lean-electrolyte cell could also run steadily (Figure 31d). For comparison, the key LSB performance parameters of several state-of-the-art sulfur hosts are listed in Table 1. Among the numerous sulfur hosts developed as cathode materials in LSBs, NG/WSe₂ exhibits an outstanding capacity and stability.

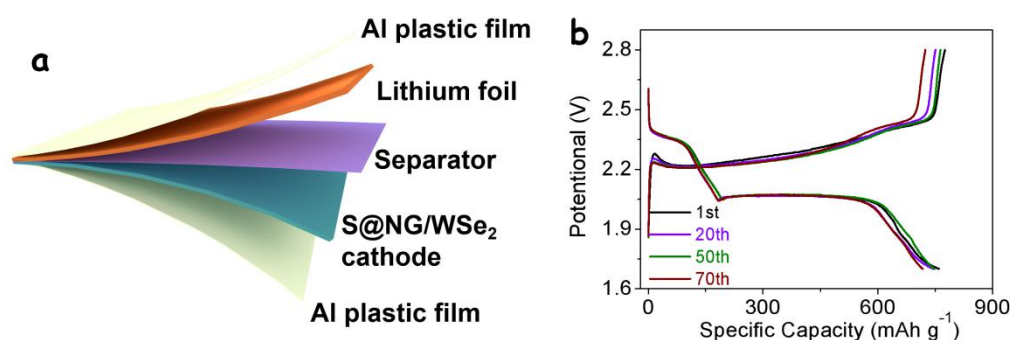


Figure 32. (a) Schematic diagram of a S@NG/WSe₂//Li pouch cell. (b) Charge/discharge profiles of pouch cell based on S@NG/WSe₂ electrode at various cycles during cycling test.

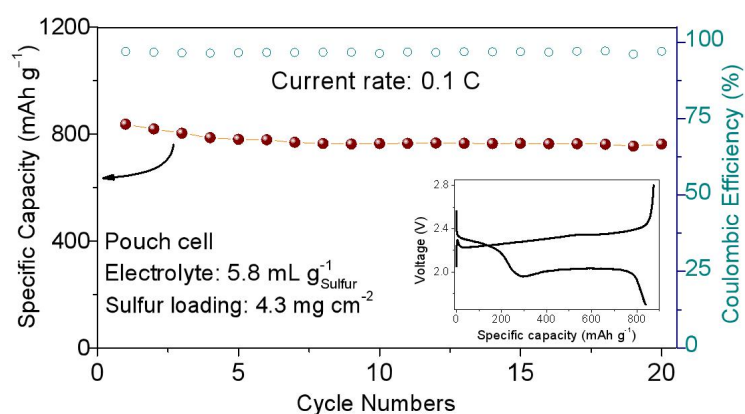


Figure 33. (a) Cycling performance of a pouch cell based on S@NG/WSe₂ electrode at lean electrolyte condition of 5.8 mL g⁻¹_{Sulfur}. The inset plot shows the charge/discharge profile.

Finally, to demonstrate the potential for practical use of S@NG/WSe₂ cathodes, we scaled them up to the production of pouch cells (see fabrication details and schematic diagram in

Figure 32a). The initial capacity of the pouch cell based on an S@NG/WSe₂ cathode at 0.25 C was ca. 800 mAh g⁻¹, and it retained 93.5% of its capacity after 70 cycles (Figure 26h and 32b). As a demonstration of its power, the pouch cell was able to light a "2021" panel composed of 58 red LED bulbs (Figure 26i). High-sulfur loading and lean electrolyte test were also conducted at the pouch cell level. As displayed in Figure 33, the S@NG/WSe₂ cathode maintained a stable capacity under 4.3 mg cm⁻² sulfur loading and 5.8 mL g⁻¹_{Sulfur} electrolyte usage, illustrating the potential for practical application of sulfur cathodes based on NG/WSe₂ superlattice hosts.

Table 1. Comparison of NG/WSe₂ electrochemical performance as host cathode for LSBs with state-of-the-art cathodes based on 2D transition metal chalcogenides.

Host material	Capacity (mAh g ⁻¹)	Cycling stability(%)	Decay rate (per cycle, %)	S content (wt%)	Ref
	(low/high current rate)	(cycles, current rate)			
rGO/MoS ₂	1100 (0.2 C)	55%	0.15%	80%	72
	660 (2 C)	(300 cycles, 1 C)			
MXene/1T-2H MoS ₂ -C	1195 (0.1 C)	79%	0.07%	79.6%	73
	677 (2 C)	(300 cycles, 0.5 C)			
MoSe ₂ @MCHS	1708 (0.2 C)	61%	0.26%	60%	74
	293 (5 C)	(150 cycles, 0.2 C)			
WS ₂ /C	911 (0.5 C)	68.8%	0.078%	60%	75
	440 (8 C)	(400 cycles, 0.5 C)			
rGO/WS ₂	1531 (0.05 C)	68.8%	0.086%	70%	76
	823 (1 C)	(500 cycles, 1 C)			
NbS ₂ @IG	1190 (0.2 C)	75.5%	0.07%	72%	77
	182 (40 C)	(350 cycles, 0.5 C)			
rGO/1T'-ReS ₂	1027 (0.1 C)	67%	0.082%	63.2%	78
	577 (2 C)	(400 cycles, 1 C)			
VS ₂	~1420 (0.1 C)	33.5%	0.133%	71%	79
	~380 (2 C)	(500 cycles, 0.2 C)			
G-VS ₂	1323 (0.2 C)	64%	0.12%	70%	62
	812 (2 C)	(300 cycles, 5 C)			
VSe ₂ -VG@CC	1480 (0.2 C)	68.8%	0.039%	68%	80
	450 (5 C)	(800 cycles, 5 C)			
NG/WSe₂	1598 (0.1 C)	81.3%	0.037%	73%	Our work
	821 (2 C)	(500 cycles, 1 C)			
	570 (5 C)				

4.5 Conclusion

In summary, we reported the scalable synthesis of a superlattice material (NG/WSe₂) by a simple two-step method and its application as sulfur host in LSBs. The synthesis method involved a first solvothermal process that resulted in hybrid organic-inorganic polymer-WSe₂ superlattices. A subsequent thermal treatment pyrolyzed the polymer to yield NG/WSe₂ superlattices. The temperature of the calcination step allowed a continuous adjustment of the WSe₂ interlayer space, from 10.4 Å to 21 Å. Compared with WSe₂, NG/WSe₂ superlattices showed a metallic character with no gap of states at the Fermi level, a highly enhanced conductivity (over 100 times), and much faster ion diffusion. NG/WSe₂ superlattices also provided accelerated reaction kinetics of LiPS conversion, with lower overpotentials and higher Li₂S nucleation capacity. Moreover, both experimental results and theoretical calculations proved that NG/WSe₂ superlattices greatly improve the affinity to LiPS at the heterostructure interface by the formation of Li-N and W-S bonds, which effectively inhibits the soluble LiPS shuttle effect. As a result, S@NG/WSe₂ electrodes allowed a high sulfur utilization, a superior rate performance (569.5 mAh g⁻¹ at 5 C), and improved cycling stability with 81.3% capacity retention after 500 cycles. Even at high sulfur loading, lean electrolyte conditions, and in up-scaled 0.1 Ah capacity pouch cells, robust Li-S performances were demonstrated. All these results demonstrate the excellent qualities of heterostructured superlattices as sulfur hosts in LSB cathodes. Thus, this work not only established a simple, cost-effective, and scalable procedure to produce these materials, but also pioneered their use and demonstrated their great potential in the LSB technological field.

4.6 References

- [1] K. S. Novoselov, A. K. Geim, S. V. Morozov, D. Jiang, Y. Zhang, S. V. Dubonos, I. V. Grigorieva, A. A. Firsov, *Science* **2004**, *306*, 666.
- [2] Q. Yun, L. Li, Z. Hu, Q. Lu, B. Chen, H. Zhang, *Advanced Materials* **2020**, *32*, 1903826.
- [3] C. Tan, X. Cao, X.-J. Wu, Q. He, J. Yang, X. Zhang, J. Chen, W. Zhao, S. Han, G.-H. Nam, M. Sindoro, H. Zhang, *Chem. Rev.* **2017**, *117*, 6225.
- [4] K. S. Novoselov, A. Mishchenko, A. Carvalho, A. H. Castro Neto, *Science* **2016**, *353*, aac9439.
- [5] P. Xiong, B. Sun, N. Sakai, R. Ma, T. Sasaki, S. Wang, J. Zhang, G. Wang, *Advanced Materials* **2020**, *32*, 1902654.

- [6] Y. Huang, J. Liang, C. Wang, S. Yin, W. Fu, H. Zhu, C. Wan, *Chem. Soc. Rev.* **2020**, *49*, 6866.
- [7] A. Khan, J. Azadmanjiri, B. Wu, L. Liping, Z. Sofer, J. Min, *Advanced Energy Materials* **2021**, *11*, 2100451.
- [8] G. Jin, C.-S. Lee, O. F. N. Okello, S.-H. Lee, M. Y. Park, S. Cha, S.-Y. Seo, G. Moon, S. Y. Min, D.-H. Yang, C. Han, H. Ahn, J. Lee, H. Choi, J. Kim, S.-Y. Choi, M.-H. Jo, *Nat. Nanotechnol.* **2021**, *16*, 1092.
- [9] C. Forsythe, X. Zhou, K. Watanabe, T. Taniguchi, A. Pasupathy, P. Moon, M. Koshino, P. Kim, C. R. Dean, *Nature Nanotech* **2018**, *13*, 566.
- [10] P. Xiong, X. Zhang, H. Wan, S. Wang, Y. Zhao, J. Zhang, D. Zhou, W. Gao, R. Ma, T. Sasaki, G. Wang, *Nano Lett.* **2019**, *19*, 4518.
- [11] Y. Guo, Q. Chen, A. Nie, H. Yang, W. Wang, J. Su, S. Wang, Y. Liu, S. Wang, H. Li, Z. Liu, T. Zhai, *ACS Nano* **2020**, *14*, 1635.
- [12] J. Zhuang, C. Liu, Q. Gao, Y. Liu, H. Feng, X. Xu, J. Wang, J. Zhao, S. X. Dou, Z. Hu, Y. Du, *ACS Nano* **2018**, *12*, 5059.
- [13] Y. Shen, Y. Wang, Y. Miao, M. Yang, X. Zhao, X. Shen, *Advanced Materials* **2020**, *32*, 1905524.
- [14] Md. S. Islam, M. Kim, X. Jin, S. M. Oh, N.-S. Lee, H. Kim, S.-J. Hwang, *ACS Energy Lett.* **2018**, *3*, 952.
- [15] C. Wang, N. Sakai, Y. Ebina, T. Kikuchi, M. R. Snowdon, D. Tang, R. Ma, T. Sasaki, *J. Mater. Chem. A* **2021**, *9*, 9952.
- [16] L. Ji, M. Rao, H. Zheng, L. Zhang, Y. Li, W. Duan, J. Guo, E. J. Cairns, Y. Zhang, *J. Am. Chem. Soc.* **2011**, *133*, 18522.
- [17] H. Wang, Q. Zhang, H. Yao, Z. Liang, H.-W. Lee, P.-C. Hsu, G. Zheng, Y. Cui, *Nano Letters* **2014**, *14*, 7138.
- [18] Z. A. Ghazi, X. He, A. M. Khattak, N. A. Khan, B. Liang, A. Iqbal, J. Wang, H. Sin, L. Li, Z. Tang, *Advanced Materials* **2017**, *29*, 1606817.
- [19] B. Fei, C. Zhang, D. Cai, J. Zheng, Q. Chen, Y. Xie, L. Zhu, A. Cabot, H. Zhan, *ACS Nano* **2021**, *15*, 6849.
- [20] C. Zhang, R. Du, J. J. Biendicho, M. Yi, K. Xiao, D. Yang, T. Zhang, X. Wang, J. Arbiol, J. Llorca, Y. Zhou, J. R. Morante, A. Cabot, *Advanced Energy Materials* **2021**, *11*, 2100432.
- [21] Z. Liang, D. Yang, P. Tang, C. Zhang, J. J. Biendicho, Y. Zhang, J. Llorca, X. Wang, J. Li, M. Heggen, J. David, R. E. Dunin-Borkowski, Y. Zhou, J. R. Morante, A. Cabot, J. Arbiol, *Advanced Energy Materials* **n.d.**, *n/a*, 2003507.
- [22] G. Babu, N. Masurkar, H. Al Salem, L. M. R. Arava, *Journal of the American Chemical Society* **2017**, *139*, 171.
- [23] H. Lin, L. Yang, X. Jiang, G. Li, T. Zhang, Q. Yao, G. W. Zheng, J. Y. Lee, *Energy & Environmental Science* **2017**, *10*, 1476.
- [24] H.-J. Li, K. Xi, W. Wang, S. Liu, G.-R. Li, X.-P. Gao, *Energy Storage Materials* **2021**, DOI 10.1016/j.ensm.2021.11.024.
- [25] P. Wang, F. Sun, S. Xiong, Z. Zhang, B. Duan, C. Zhang, J. Feng, B. Xi, *Angewandte Chemie* **n.d.**, *n/a*, e202116048.

- [26]S. Zhou, S. Liu, W. Chen, Y. Cheng, J. Fan, L. Zhao, X. Xiao, Y.-H. Chen, C.-X. Luo, M.-S. Wang, T. Mei, X. Wang, H.-G. Liao, Y. Zhou, L. Huang, S.-G. Sun, *ACS Nano* **2021**, *15*, 13814.
- [27]P. Hohenberg, W. Kohn, *Phys. Rev.* **1964**, *136*, B864.
- [28]J. P. Perdew, K. Burke, M. Ernzerhof, *Phys. Rev. Lett.* **1996**, *77*, 3865.
- [29]P. E. Blöchl, *Phys. Rev. B* **1994**, *50*, 17953.
- [30]S. Grimme, S. Ehrlich, L. Goerigk, *Journal of Computational Chemistry* **2011**, *32*, 1456.
- [31]J. Sun, A. Ruzsinszky, J. P. Perdew, *Phys. Rev. Lett.* **2015**, *115*, 036402.
- [32]G. Henkelman, B. P. Uberuaga, H. Jónsson, *J. Chem. Phys.* **2000**, *113*, 9901.
- [33]R. Bryaskova, D. Pencheva, S. Nikolov, T. Kantardjiev, *J Chem Biol* **2011**, *4*, 185.
- [34]L. Mo, Z. Guo, Z. Wang, L. Yang, Y. Fang, Z. Xin, X. Li, Y. Chen, M. Cao, Q. Zhang, L. Li, *Nanoscale Research Letters* **2019**, *14*, 197.
- [35]Y. Liu, Y. Qiao, W.-X. Zhang, Z. Li, X.-L. Hu, L.-X. Yuan, Y.-H. Huang, *J. Mater. Chem.* **2012**, *22*, 24026.
- [36]P. D. Antunez, D. H. Webber, R. L. Brutchey, *Chem. Mater.* **2013**, *25*, 2385.
- [37]P. Xiong, R. Ma, N. Sakai, L. Nurdiwijayanto, T. Sasaki, *ACS Energy Lett.* **2018**, *3*, 997.
- [38]D. Bennett, B. Remez, *npj 2D Mater Appl* **2022**, *6*, 1.
- [39]X. Luo, Y. Zhao, J. Zhang, M. Toh, C. Kloc, Q. Xiong, S. Y. Quek, *Phys. Rev. B* **2013**, *88*, 195313.
- [40]H. Liu, B. Liu, H. Guo, M. Liang, Y. Zhang, T. Borjigin, X. Yang, L. Wang, X. Sun, *Nano Energy* **2018**, *51*, 639.
- [41]X. Hu, Y. Liu, J. Li, G. Wang, J. Chen, G. Zhong, H. Zhan, Z. Wen, *Advanced Functional Materials* **2020**, *30*, 1907677.
- [42]C. Zhang, Q. Chen, H. Zhan, *ACS Appl. Mater. Interfaces* **2016**, *8*, 22977.
- [43]F. Han, J. Yue, X. Fan, T. Gao, C. Luo, Z. Ma, L. Suo, C. Wang, *Nano Lett.* **2016**, *16*, 4521.
- [44]Z. Lin, Z. Wan, F. Song, B. Huang, C. Jia, Q. Qian, J. S. Kang, Y. Wu, X. Yan, L. Peng, C. Wan, J. Zhou, Z. Sofer, I. Shakir, Z. Almutairi, S. Tolbert, X. Pan, Y. Hu, Y. Huang, X. Duan, *Chem* **2021**, *7*, 1887.
- [45]W. Yu, Z. Dong, I. Abdelwahab, X. Zhao, J. Shi, Y. Shao, J. Li, X. Hu, R. Li, T. Ma, Z. Wang, Q.-H. Xu, D. Y. Tang, Y. Song, K. P. Loh, *ACS Nano* **2021**, *15*, 18448.
- [46]J. Ni, W. Wang, M. Quintana, F. Jia, S. Song, *Applied Surface Science* **2020**, *514*, 145911.
- [47]Y. Wang, R. Zhang, Z. Sun, H. Wu, S. Lu, J. Wang, W. Yu, J. Liu, G. Gao, S. Ding, *Advanced Materials Interfaces* **2020**, *7*, 1902092.
- [48]D. Sun, K. Liu, J. Hu, J. Zhou, *Small n.d.*, *n/a*, 2006374.
- [49]C. Zhang, J. J. Biendicho, T. Zhang, R. Du, J. Li, X. Yang, J. Arbiol, Y. Zhou, J. R. Morante, A. Cabot, *Advanced Functional Materials* **2019**, *29*, 1903842.
- [50]J. Liu, Y. Zhang, L. Zhang, F. Xie, A. Vasileff, S.-Z. Qiao, *Advanced Materials* **2019**, *31*, 1901261.
- [51]X. Hong, J. Jin, T. Wu, Y. Lu, S. Zhang, C. Chen, Z. Wen, *J. Mater. Chem. A* **2017**, *5*, 14775.

- [52]D. Yang, Z. Liang, C. Zhang, J. J. Biendicho, M. Botifoll, M. C. Spadaro, Q. Chen, M. Li, A. Ramon, A. O. Moghaddam, J. Llorca, J. Wang, J. R. Morante, J. Arbiol, S.-L. Chou, A. Cabot, *Advanced Energy Materials* **2021**, *11*, 2101250.
- [53]Z. Yi, F. Su, L. Huo, G. Cui, C. Zhang, P. Han, N. Dong, C. Chen, *Applied Surface Science* **2020**, *503*, 144446.
- [54]J. He, G. Hartmann, M. Lee, G. S. Hwang, Y. Chen, A. Manthiram, *Energy & Environmental Science* **2019**, *12*, 344.
- [55]D. Yang, C. Zhang, J. J. Biendicho, X. Han, Z. Liang, R. Du, M. Li, J. Li, J. Arbiol, J. Llorca, Y. Zhou, J. R. Morante, A. Cabot, *ACS Nano* **2020**, *14*, 15492.
- [56]Z. Yuan, H.-J. Peng, T.-Z. Hou, J.-Q. Huang, C.-M. Chen, D.-W. Wang, X.-B. Cheng, F. Wei, Q. Zhang, *Nano Lett.* **2016**, *16*, 519.
- [57]L. Ma, W. Zhang, L. Wang, Y. Hu, G. Zhu, Y. Wang, R. Chen, T. Chen, Z. Tie, J. Liu, Z. Jin, *ACS Nano* **2018**, *12*, 4868.
- [58]F. Liu, G. Sun, H. B. Wu, G. Chen, D. Xu, R. Mo, L. Shen, X. Li, S. Ma, R. Tao, X. Li, X. Tan, B. Xu, G. Wang, B. S. Dunn, P. Sautet, Y. Lu, *Nat Commun* **2020**, *11*, 5215.
- [59]S. Wang, S. Feng, J. Liang, Q. Su, F. Zhao, H. Song, M. Zheng, Q. Sun, Z. Song, X. Jia, J. Yang, Y. Li, J. Liao, R. Li, X. Sun, *Advanced Energy Materials* **2021**, *11*, 2003314.
- [60]X. Tao, J. Wang, C. Liu, H. Wang, H. Yao, G. Zheng, Z. W. Seh, Q. Cai, W. Li, G. Zhou, C. Zu, Y. Cui, *Nature Communications* **2016**, *7*, DOI 10.1038/ncomms11203.
- [61]W. Chen, T. Lei, W. Lv, Y. Hu, Y. Yan, Y. Jiao, W. He, Z. Li, C. Yan, J. Xiong, *Advanced Materials* **2018**, *30*, 1804084.
- [62]X. Zhu, W. Zhao, Y. Song, Q. Li, F. Ding, J. Sun, L. Zhang, Z. Liu, *Advanced Energy Materials* **2018**, *8*, 1800201.
- [63]G. Zhou, H. Tian, Y. Jin, X. Tao, B. Liu, R. Zhang, Z. W. Seh, D. Zhuo, Y. Liu, J. Sun, J. Zhao, C. Zu, D. S. Wu, Q. Zhang, Y. Cui, *Proceedings of the National Academy of Sciences* **2017**, *114*, 840.
- [64]X. Chen, L. Peng, L. Wang, J. Yang, Z. Hao, J. Xiang, K. Yuan, Y. Huang, B. Shan, L. Yuan, J. Xie, *Nat Commun* **2019**, *10*, 1021.
- [65]S. Li, W. Zhang, Z. Zeng, S. Cheng, J. Xie, *Electrochem. Energ. Rev.* **2020**, *3*, 613.
- [66]Z. Guo, H. Nie, Z. Yang, W. Hua, C. Ruan, D. Chan, M. Ge, X. Chen, S. Huang, *Advanced Science* **2018**, *5*, 1800026.
- [67]W. Bao, D. Su, W. Zhang, X. Guo, G. Wang, *Advanced Functional Materials* **2016**, *26*, 8746.
- [68]Y. Lu, J.-L. Qin, T. Shen, Y.-F. Yu, K. Chen, Y.-Z. Hu, J.-N. Liang, M.-X. Gong, J.-J. Zhang, D.-L. Wang, *Advanced Energy Materials* **2021**, *11*, 2101780.
- [69]S. Waluś, C. Barchasz, R. Bouchet, F. Alloin, *Electrochimica Acta* **2020**, *359*, 136944.
- [70]A. Schneider, C. Weidmann, C. Suchomski, H. Sommer, J. Janek, T. Brezesinski, *Chem. Mater.* **2015**, *27*, 1674.
- [71]J. Wang, Z. Zhang, X. Yan, S. Zhang, Z. Wu, Z. Zhuang, W.-Q. Han, *Nano-Micro Lett.* **2019**, *12*, 4.
- [72]Y. You, Y. Ye, M. Wei, W. Sun, Q. Tang, J. Zhang, X. Chen, H. Li, J. Xu, *Chemical Engineering Journal* **2019**, *355*, 671.

- [73] Y. Zhang, Z. Mu, C. Yang, Z. Xu, S. Zhang, X. Zhang, Y. Li, J. Lai, Z. Sun, Y. Yang, Y. Chao, C. Li, X. Ge, W. Yang, S. Guo, *Advanced Functional Materials* **2018**, *28*, 1707578.
- [74] L. Meng, Y. Yao, J. Liu, Z. Wang, D. Qian, L. Zheng, B.-L. Su, H.-E. Wang, *Journal of Energy Chemistry* **2020**, *47*, 241.
- [75] S. Majumder, M. Shao, Y. Deng, G. Chen, *J. Electrochem. Soc.* **2019**, *166*, A5386.
- [76] X. Li, Z. Pan, Z. Li, X. Wang, B. Saravanakumar, Y. Zhong, L. Xing, M. Xu, C. Guo, W. Li, *Journal of Power Sources* **2019**, *420*, 22.
- [77] Z. Xiao, Z. Yang, L. Zhang, H. Pan, R. Wang, *ACS Nano* **2017**, *11*, 8488.
- [78] H. Liu, B. Chen, H. Qin, N. Wang, E. Liu, C. Shi, N. Zhao, *Applied Surface Science* **2020**, *505*, 144586.
- [79] X. Chen, G. Du, M. Zhang, A. Kalam, S. Ding, Q. Su, B. Xu, A. G. Al-Sehemi, *Energy Technology* **2020**, *8*, 1901163.
- [80] H. Ci, J. Cai, H. Ma, Z. Shi, G. Cui, M. Wang, J. Jin, N. Wei, C. Lu, W. Zhao, J. Sun, Z. Liu, *ACS Nano* **2020**, *14*, 11929.

Result and Discussions

Over the past three decades, the lithium-ion battery (LIB) technology has revolutionized portable electronics and electric mobility. In recent years, with the rapid penetration of rechargeable battery technology into many consumer products and industrial systems, the development of more advanced rechargeable batteries to meet the needs of social development has become an urgent matter. Especially, the traditional LIB has almost reached the theoretical limit of energy density, and the unprecedented development of electric vehicles is in urgent need for researchers to explore the next-generation battery system with higher energy density and lower price.

Due to the high energy density and low cost and environmental friendliness, lithium-sulfur batteries (LSBs) have attracted tremendous attention and are considered as the most promising next-generation energy storage technology. The development of LSBs needs to overcome a series of challenges, such as the shuttle effect of soluble lithium polysulfides (LiPS), the insulation character of S/Li_2S , huge volume expansion during charge and discharge, and the sluggish reaction kinetics. In view of the above challenges, rational design of cathode host materials can effectively alleviate these severe problems and achieve outstanding Li-S electrochemical performance. In this thesis, I detail the progress I have done beyond the state of the art on the design and engineering of a variety of cathode hosts from the perspective of materials, architectures, and interfaces. Although different host materials have certain differences in crystal phase and morphology, they are closely related to design ideas. Through careful analysis, the design rules of host materials for advanced LSB can be understood.

In Chapter 2, I proved the great potential of selenides as a cathode host by developing $u\text{-NCSe}$ with a hollow tubular structure, excellent conductivity, surface polarity, and high catalytic activity, which can effectively inhibit the shuttle effect of LiPS and enhance the transformation kinetics. In the comparison of the performance from $NiCo_2Se_4$ with different structures, hollow urchins-shaped nanostructure and bulk structure, we found that the nanostructure also plays an important role in LSB performance. This report demonstrated for subsequent researchers that well-designed selenides are good candidates for advanced hosts.

At the same time, considering that the combination of multi-component materials will produce a more advantageous complementary effect, in Chapter 3, I designed and engineered the $Ag/VN@Co/NCNT$ nanoreactor to achieve the physical limitation and chemisorption of

LiPS at the same time, accommodate the volume expansion, and also promote the catalytic effect. In a series of electrochemical characterization and disassembly experiments, I verified that the construction of the nanoreactor can effectively promote the Li-S reaction conversion and prolong cycling lifespan.

In the case of Ag/VN@Co/NCNT, through theoretical analysis and experimental verification, I demonstrated that the heterojunction effect constructed between different components has a very strong positive effect on LSB. The 2D superlattice structure can achieve the maximum heterojunction effect, but the current synthesis technology is very complicated and has a low yield, which greatly limits its application in the field of energy storage. In Chapter 4, I deeply considered the advantages and disadvantages of 2D metal selenide and graphene, and explored a more simple way to mass-produce NG/WSe₂ superlattice structures. The obtained NG/WSe₂ superlattice exhibited much stronger LiPS adsorption ability at the edge side and more rapid Li⁺ diffusion in the expanded interlayers.

Based on the results of this study, the reasonable design of cathode host is expected to achieve high-performance LSB by fully understanding the cathode challenges and considering the multiple influencing factors from material, architecture, and interface. These efforts and attempts not only provide an understanding of the design of energy storage materials, but also explore a possible successful road for the commercial application of LSBs.

Conclusions

In this thesis, from the point of materials, architecture, and interface, I designed various cathode hosts to meet the critical challenges of lithium-sulfur battery(LSB), including the insulating character of S/Li₂S, the shuttle effect of lithium polysulfide (LiPS), and the sluggish Li-S reaction kinetics. In each chapter, the physico-chemical properties of the proposed host materials were studied in detail, including crystal phase, morphology, surface chemistry, *etc.* Moreover, the LiPS catalytic and adsorption effects of hosts were emphatically verified. Both theoretical calculation and experiment were employed to prove that the optimized hosts play a great role in inhibiting the shuttle effect and boosting transformation kinetics, thus realizing the advanced LSBs.

In the study of urchin-shaped NiCo₂Se₄ as the cathode host, this work probed that transition metal selenides with high conductivity, high catalytic activity, adjustable morphology, and polar surface have the great potential to regulate the LiPS in Li-S reactions. Subsequently, in the study of Ag/VN@Co/NCNT host, this work proved that the electrochemical performance of LSBs can be effectively enhanced by designing hierarchical nanoreactors with multiple components. In the NG/WSe₂ superlattice investigation, this work not only established a simple, cost-effective, and scalable procedure to produce superlattice materials, but also demonstrated significant effects on LiPS regulation at the interface, including high adsorption capacity, high catalytic conversion, and rapid diffusion of lithium ions, pioneered their use and demonstrated their great potential in the LSB technological field.

In conclusion, this thesis detailed the design and engineering of several advanced cathode hosts through optimizing material and nanostructure, employing the heterogeneous interface effects, to effectively regulate LiPS and improve Li-S reaction electrochemical performance. It is important to note that in order to achieve a more advanced host for LSBs, composite materials are required and synergistically multiple factors need to be optimized because a single approach is hard to adequately address the complex challenges arising from LSBs. In addition, particularly interesting was the exploration of superlattice architectures, which not only opened a door to develop new 2D materials, but also allows obtaining more unique physical and chemical properties.

Future work

Lithium-sulfur batteries (LSBs) are considered the most promising next-generation energy storage devices to replace existing lithium-ion batteries. Although the design of advanced cathode host materials from materials, architecture, and interfaces carried out in this thesis effectively helped to solve a series of cathode problems of LSBs, including the conductivity of sulfur and lithium sulfide, the shuttle effect of polysulfide compounds, and the slow kinetics of Li-S reactions, there are still a series of serious challenges to be solved for the commercialization of LSBs.

1. The problems associated with the use of a lithium anode are still serious. Lithium dendrite growing on the anode surface could pierce the membrane during a long time charging/discharging process, causing serious safety problems. Inspired by the cathode host material, advanced anode hosts need to be explored in future experiments to inhibit lithium dendrite growth and reduce the polarization phenomenon during the plating and stripping of lithium anode. Only building the stable and reliable lithium-sulfur full batteries by improving both cathode and anode could realize the possibility of future LSB commercialization

2. Although we can effectively achieve good Li-S electrochemical properties at the coin cell level, there is a significant discount at the level of pouch cells. In the process of the practical application of LSBs, it is necessary to explore the production process of pouch cells in the lab for future factory manufacture. Therefore, in future work, more stable and efficient pouch cell preparation parameters need to be developed to achieve a high energy density Ah-level pouch cell product, which will be the key exploration of the practical application of LSBs.

3. In addition, in terms of nanomaterial synthesis, superlattice structure greatly enriched two-dimensional (2D) material family and exhibited huge potential in the field of energy storage and conversion, which aroused my great interest. At present, I have developed a series of 2D organic-inorganic superlattices represented by transition metal selenide-based materials, which show very unique physical/chemical properties and enhanced electrochemical performance compared to the original selenide. In the coming years, I will focus on the development and utilization of new superlattice materials with more unique features.

CURRICULUM VITAE

Chaoqi Zhang

Date of Birth: 20th January, 1994

Phone Number: +34 615073412

ORCID: 0000-0002-0357-235X

Google scholar: [click here](#)

Email: chaoqi.zhang2017@gmail.com / czhang@irec.cat



Address: Catalonia Institute for Energy Research, Sant Adrià de Besòs, Barcelona, Spain

Education

- **University of Barcelona, Catalonia Institute for Energy Research, Barcelona, Spain**
Ph.D. Candidate, Nanoscience 2017.10-2022.5
Supervisor: Prof. Andreu Cabot
Keywords: lithium-sulfur battery, electrocatalysis, transition metal selenide, superlattice
- **Fuzhou University, Fuzhou, China**
M.S., Materials Physics and Chemistry 2014.9-2017.3
Supervisor: Prof. Hongbing Zhan
Keywords: transition metal hydroxide/sulfide, supercapacitor
- **Fuzhou University, Fuzhou, China**
B.S., Materials Science and Engineering 2010.9-2014.7

Research interest

- **Synthesis and characterization of functional nanomaterials**
Wet chemical synthesis of transition metal chalcogenides, carbon materials, superlattice
- **Rechargeable batteries**
Lithium/sodium-sulfur battery, lithium/sodium/potassium ion battery, supercapacitor

Research Experience

1. **Catalonia Institute for Energy Research, Barcelona, Spain** 2017.10-present
 - ✧ *Developed urchin-shaped bimetallic selenides NiCo_2Se_4 as an effective sulfur host with the hollow tubular structure, excellent conductivity, surface polarity, and high catalytic activity.*
 - ✧ *Designed the $\text{Ag}/\text{VN}@\text{Co}/\text{NCNT}$ nanoreactor with multi-components as the sulfur host.*
 - ✧ *Synthesized the NG/WSe_2 superlattice in a simple and mass-produced way for LSB cathode.*

✧ *Developed the C_3N_4 -TMSe based superlattices obtained by a one-step approach to fully activate the inert base plane for effective LiPS catalyst.*

2. **Fuzhou University**, Fuzhou, China

2014.9-2017.3

✧ *Prepared the reduced graphene oxide nanofibers (rGONF) as a substrate for $Ni(OH)_2$ nanoplates growing with enhanced electrochemical performance.*

✧ *Synthesized the core-shell structural Prussian blue-cobalt sulfide nanocubes derived from Metal-Organic Frameworks for supercapacitor.*

Working Experience

Contemporary Amperex Technology Co. Limited (CATL), NingDe, China

Product Engineer

2017.4-2017.8

Keywords: lithium-ion battery, large scale manufacturing, yield improvement

Responsibility: Participate in the production and testing of power batteries, responsible for the introduction of new technologies and the improvement of the production line; responsible for the stable output of 95Ah LPF batteries of 300 K per month with a yield of 90.6%; and complete the urgent task of from production line adjustment to 60 K 102Ah batteries out of the factory in 30 days.

Awards

Chinese Graduate Student National Scholarship, 2017

Chinese Scholarship Council, 2017

Conferences

Poster presentation: Combined High Catalytic Activity and Efficient Polar Tubular Nanostructure in Urchin-Like Metallic $NiCo_2Se_4$ for High-Performance Lithium-Sulfur Batteries. 2019.07

Summer School of Exciting nanostructures at the Physikzentrum Bad Honnef, Germany.

Publications

[1] **Chaoqi Zhang**, Ban Fei, Dawei Yang, Hongbing Zhan*, Jiaao Wang*, Jiefeng Diao, Junshan Li, Graeme Henkelman, Daoping Cai, Jordi Jacas Biendicho, Joan Ramon Morante, Andreu Cabot*. Robust Lithium-Sulfur Batteries Enabled by Highly Conductive WSe_2 -based Superlattices with Tunable Interlayer Space. *Advanced Functional Materials*, 2022, 2201322. (IF= 18.808)

[2] **Chaoqi Zhang**[†], Ruifeng Du[†], Jordi Jacas Biendicho, Mingjie Yi, Ke Xiao, Dawei Yang, Ting Zhang, Xiang Wang, Jordi Arbiol, Jordi Llorca, Yingtang Zhou*, Joan Ramon Morante, Andreu Cabot*. Tubular $CoFeP@CN$ as a Mott-Schottky Catalyst with Multiple Adsorption Sites for Robust Lithium-Sulfur Batteries. *Advanced Energy Materials*, 2021, 2100432. (IF= 29.368)

[3] **Chaoqi Zhang**, Jordi Jacas Biendicho*, Ting Zhang, Ruifeng Du, Junshan Li, Xuhui Yang, Jordi Arbiol, Yingtang Zhou*, Joan Ramon Morante, Andreu Cabot*. Combined High Catalytic Activity and Efficient Polar Tubular Nanostructure in Urchin-Like Metallic $NiCo_2Se_4$ for High-Performance

Lithium-Sulfur Batteries. *Advanced Functional Materials*, 2019, 29, 34, 1903842. (IF= 18.808)

[4] **Chaoqi Zhang**, Qidi Chen, and Hongbing Zhan*. Supercapacitors Based on Reduced Graphene Oxide Nanofibers Supported Ni(OH)₂ Nanoplates with Enhanced Electrochemical Performance. *ACS Applied Materials & Interfaces*, 2016, 8, 35, 22977. (IF= 9.229)

[5] Ban Fei†, **Chaoqi Zhang**†, Daoping Cai*, Jingying Zheng, Qidi Chen, Yulan Xie, Longzhen Zhu, Andreu Cabot*, Hongbing Zhan*. Hierarchical Nanoreactor with Multiple Adsorption and Catalytic Sites for Robust Lithium-Sulfur Batteries. *ACS Nano*, 2021, 15, 4, 6849-6860. (IF=15.881)

[6] Xiaoting Yu †, **Chaoqi Zhang** †, Zhishan Luo*, Ting Zhang, Junfeng Liu, Junshan Li, Yong Zuo, Jordi Jacas Biendicho, Jordi Llorca, Jordi Arbiol, Joan Ramón Morante, Andreu Cabot*. A Low Temperature Solid State Reaction to Produce Hollow Mn_xFe_{3-x}O₄ Nanoparticles as Anode for Lithium-ion Batteries. *Nano Energy*, 2019, 66, 104199. (IF= 17.881)

[7] Dawei Yang, Zhifu Liang, **Chaoqi Zhang***, Jordi Jacas Biendicho, Marc Botifoll, Maria Chiara Spadaro, Qiulin Chen, Mengyao Li, Alberto Ramon, Ahmad Ostovari Moghaddam, Jordi Llorca, Jiaao Wang*, Joan Ramon Morante, Jordi Arbiol, Shu - Lei Chou*, Andreu Cabot*. NbSe₂ Meets C₂N: A 2D-2D Heterostructure Catalysts as Multifunctional Polysulfide Mediator in Ultra - Long - Life Lithium-Sulfur Batteries. *Advanced Energy Materials*, 2021, 11, 36, 2101250. (IF= 29.368)

[8] Dawei Yang, **Chaoqi Zhang***, Jordi Jacas Biendicho, Xu Han, Zhifu Liang, Ruifeng Du, Mengyao Li, Junshan Li, Jordi Arbiol, Jordi Llorca, Yingtang Zhou*, Joan Ramon Morante, and Andreu Cabot*. ZnSe/N-Doped Carbon Nanoreactor with Multiple Adsorption Sites for Stable Lithium-Sulfur Batteries. *ACS Nano*, 2020, 14, 11, 15492. (IF=15.881)

[9] Dawei Yang †, Zhifu Liang †, Pengyi Tang †, **Chaoqi Zhang**, Mingxue Tang, Qizhen Li, Jordi Jacas Biendicho, Junshan Li, Marc Heggen, Rafal E. Dunin-Borkowski, Ming Xu*, Jordi Llorca, Jordi Arbiol*, Joan Ramon Morante, Shu-Lei Chou*, Andreu Cabot*. A High Conductivity One-Dimensional π -d Conjugated Metal-Organic Framework with Efficient Polysulfide Trapping-Diffusion-Catalysis in Lithium-Sulfur Batteries. *Advanced Materials*, 2022, 2108835. (IF= 30.849)

[10] Mengyao Li, Dawei Yang,* Jordi Jacas Biendicho, Xu Han, **Chaoqi Zhang**, Kun Liu, Jiefeng Diao, Junshan Li, Jing Wang, Marc Heggen, Rafal E. Dunin-Borkowski, Jiaao Wang,* Graeme Henkelman, Joan Ramon Morante, Jordi Arbiol, Shu-Lei Chou,* and Andreu Cabot* Enhanced Polysulfide Conversion with Highly Conductive and Electrocatalytic Iodine-Doped Bismuth Selenide Nanosheets in Lithium-Sulfur Batteries. *Advanced Functional Materials*, 2022, 2200529. (IF= 18.808)

[11] Zhifu Liang†, Dawei Yang†, Pengyi Tang†, **Chaoqi Zhang**, Jordi Jacas Biendicho, Yi Zhang, Jordi Llorca, Xiang Wang, Junshan Li, Marc Heggen, Jeremy David, Rafal E. Dunin-Borkowski, Yingtang Zhou*, Joan Ramon Morante, Andreu Cabot*, Jordi Arbiol*, Atomically Dispersed Fe in C₂N based Catalyst as Sulfur Host for Efficient Lithium-Sulfur Batteries. *Advanced Energy Materials*, 2021, 11, 5, 2003507. (IF= 29.368)

[12] Daoping Cai*, Yaxuan Zhuang, Ban Fei, **Chaoqi Zhang**, Yaguang Wang, Qidi Chen, Hongbing Zhan*. Self-supported VN arrays coupled with N-doped carbon nanotubes embedded with Co nanoparticles as a multifunctional sulfur host for lithium-sulfur batteries. *Chemical Engineering Journal*, 2021, 132931. (IF=13.273)

[13] Yong Zuo†, Xijun Xu†, **Chaoqi Zhang**, Junshan Li, Ruifeng Du, Xiang Wang, Xu Han, Jordi Arbiol, Jordi Llorca, Jun Liu, Andreu Cabot*. SnS₂/g-C₃N₄/graphite Nanocomposites as Durable

Lithium-ion Battery Anode with High Pseudocapacitance Contribution. *Electrochimica Acta*. 2020, 349, 136369. (IF= 6.901)

[14] Junfeng Liu, Xiaoting Yu, Ruifeng Du, **Chaoqi Zhang**, Ting Zhang, Jordi Llorca, Jordi Arbiol, Ying Wang*, Michaela Meyns, Andreu Cabot*. Chromium phosphide CrP as highly active and stable electrocatalysts for oxygen electroreduction in alkaline media. *Applied Catalysis B: Environmental*, 2019, 256, 117846. (IF= 19.503)

[15] Mingjie Yi, **Chaoqi Zhang**, Cong Cao, Chao Xu, Baisheng Sa, Daoping Cai, Hongbing Zhan. MOF-derived Hybrid Hollow Submicrospheres of Nitrogen-doped Carbon-encapsulated Bimetallic Ni-Co-S Nanoparticles for Supercapacitors and Lithium Ion Batteries. *Inorganic Chemistry*, 2019, 58, 6, 3916. (IF= 5.165)

[16] Junshan Li, Xijun Xu, Zhishan Luo, **Chaoqi Zhang**, Yong Zuo, Ting Zhang, Pengyi Tang, Maria F Infante - Carrió, Jordi Arbiol, Jordi Llorca, Jun Liu, Andreu Cabot Co-Sn Nanocrystalline Solid Solutions as Anode Materials in Lithium-Ion Batteries with High Pseudocapacitive Contribution. *ChemSusChem*, 2019, 12, 7, 1451. (IF= 8.928)

[17] Junshan Li, Zhishan Luo*, Feng He*, Yong Zuo, **Chaoqi Zhang**, Junfeng Liu, Xiaoting Yu, Ruifeng Du, Ting Zhang, Maria F Infante-Carrió, Pengyi Tang, Jordi Arbiol, Jordi Llorca, Andreu Cabot*. Colloidal Ni-Co-Sn Nanoparticles as Efficient Electrocatalysts for the Methanol Oxidation Reaction. *Journal of Materials Chemistry A*, 2018, 6, 45, 22915. (IF=12.732)

Reference

Prof. Andreu Cabot
Functional Nanomaterials
Research Department,
Catalonia Institute for
Energy Research (IREC)
acabot@irec.cat

Prof. Joan Ramon Morante
Director of IREC
Energy Storage, Harvesting and
Catalysis Research Department,
IREC and University of
Barcelona
jrmorante@irec.cat

Prof. Hongbing Zhan
College of Materials Science and
Engineering, Fuzhou University
hbzhan@fzu.edu.cn

Annex

Collection of Publications Presented in This Thesis